Study on 2002 Sudden Stratospheric Warming, Mesosphere-Lower Thermospheric wind structure and dynamics and middle atmospheric temperature structure, based on SuperDARN HF RADAR, LIDAR, Riometer, Satellites and Models

by

Nkanyiso Bongumusa Mbatha

A thesis submitted in partial fulfilment of the academic
requirements for the degree of
Doctor of Philosophy
in the School of Physics,
University of KwaZulu-Natal
Durban

As the candidate's supervisor I have/have not approved this thesis for submission

Signed: .... Name: .... Date: ....

As the candidate's co-supervisor I have/have not approved this thesis for submission

Signed: .... Name: .... Date: ....

PREFACE

The experimental work described in this thesis was carried out at the Hermanus Magnetic Observatory, Hermanus, and at the School of Physics, University of KwaZulu-Natal, Durban, from October 2007 to December March 2012 under the supervision of Professor Sivakumar Venkataraman and under the co-supervision of Dr Sandile Malinga, Professor Sadhasivan Pillay and Professor Hassan Bencherif.

These studies represent original work by the author and have not otherwise been submitted in any form for any degree or diploma to any tertiary institution. Where use has been made of the work of others it is duly acknowledged in the text.

Nkanyiso Bongumusa Mbatha

DECLARATION 1 - PLAGIARISM

I, Nkanyiso Bongumusa Mbatha, declare that

1. The research reported in this thesis, except where otherwise indicated, is my original research.
2. This thesis has not been submitted for any degree or examination at any other university.
3. This thesis does not contain other persons' data, pictures, graphs or other information, unless specifically acknowledged as being sourced from other persons.
4. This thesis does not contain other persons writing, unless specifically acknowledged as being sourced from other researchers. Where other written sources have been quoted, then: (a) Their words have been re-written but the general information attributed to them has been referenced (b) Where their exact words have been used, then their writing has been placed in italics and inside quotation marks, and referenced.
5. This thesis does not contain text, graphics or tables copied and pasted from the Internet, unless specifically acknowledged, and the source being detailed in the thesis and in the References sections.

Signed:..

DECLARATION 2 - PUBLICATIONS

DETAILS OF CONTRIBUTION TO PUBLICATIONS that form part and/or include research presented in this thesis (include publications in preparation, submitted, in press and published and give details of the contributions of each author to the experimental work and writing of each publication)

Publication 1

- Mbatha, N., Sivakumar, V., Malinga, S., Bencherif, H., and Pillay, S. R.: Study on the impact of sudden stratosphere warming in the upper mesosphere-lower thermosphere regions using satellite and HF radar measurements, Atmos. Chem. Phys, 10. 1-8, 2010.

Publication 2

- Mbatha, N., Sivakumar, V., Bencherif, H., Malinga, S. B., Pillay S. R., Moorgawa, A., and Michaelis, M. M.: DURBAN RAYLEIGH LIDAR MEASUREMENTS OF THE STRATOSPHERE-MESOSPHERE TEMPERATURE STRUCTURE, 25th International Laser Radar Conference, 987-990, 2010.

Publication 3

- Mbatha, N., Sivakumar, V., Bencherif, H., Malinga, S. B., Pillay S. R., Moorgawa, A., and Michaelis, M. M.: Observations of a middle atmosphere thermal structure over Durban using a ground-based Rayleigh LIDAR and satellite data, South African Journal of Science, 108(1/2), Art. #612, 9 pages. http:// dx.doi.org/10.4102/sajs.v108i1/2.612, 2012.

Publication 4

- Mbatha, N., Malinga, S., Sivakumar, V., Bencherif, H., Mthembu, S., Pillay, S. R., and Khanyile, S.: Extracting gravity waves parameters during the September 2002 Southern Hemisphere stratospheric major warming using a SANAE imaging riometer. To be submitted to Atmos. Chem. Phys, 2012.

Signed:..

Abstract

In this thesis, the dynamics and coupling in the middle atmosphere over the Southern Hemisphere are investigated using SuperDARN high frequency (HF) radar wind data, satellites, light detection and ranging (LIDAR), the South African National Antarctic Expedition (SANAE) imaging riometer and models. In particular, the study focuses on the unprecedented 2002 major stratospheric warming and its role in coupling the middle atmosphere. The dynamics of the middle atmosphere is investigated in terms of mean wind, temperature, gravity waves and planetary wave activity.

Studying the middle atmospheric thermal structure over Southern Africa is an important activity to improve the understanding of atmospheric dynamics of this region. Observation of a middle atmosphere thermal structure over Durban (29.9°S, 31.0°E, South Africa) using LIDAR data collected from April 1999 to July 2004 (277 nights), including closest overpasses of the Sounding of the Atmosphere using Broadband Emission Radiometry (SABER) and Halogen Occultation Experiments (HALOE) satellites, and the COSPAR International Reference Atmosphere (CIRA-86) are presented in this thesis. The observations from the LIDAR instrument, satellites and CIRA-86 exhibit the presence of annual oscillation in the stratosphere, whereas in the mesosphere the semi-annual oscillation seems to dominate the annual oscillation at some levels. The stratopause is observed in the height range of ∼40-55 km for all the instruments, with the stratopause temperatures being 260-270 K for the LIDAR, 250-260 K for the SABER, and 250-270 K for the HALOE. Data from the LIDAR, satellites and CIRA-86 model indicate almost the same thermal structure of the middle atmosphere over Durban. This indicates a good agreement between LIDAR, satellites and the CIRA-86 model.

Mean wind and planetary waves are investigated on a climatological scale in this study. Mean wind observations from the SANAE SuperDARN HF radar are compared with observations from Halley SuperDARN HF radar. There is a good agreement between the observations from the two stations both in the zonal and meridional wind components. Zonal wind is observed to be consistently larger than the meridional wind. The zonal wind is also consistently more eastward at both stations with maxima occurring during the solstice months. High latitude summer zonal mean flow at ∼94 km is observed to be weaker and more variable compared to the eastward winter mean circulation owing to tropospherically forced planetary waves propagating through the middle atmosphere. The zonal mean wind shows greater seasonal variability than does the meridional mean wind. This seasonal behaviour is reasonably well understood in terms of the upward propagating planetary waves and gravity waves interacting with the mean flow. The Coriolis force also plays an important role in the case of meridional wind component.

The climatology of planetary waves both in the zonal and meridional wind components indicates an amplification of planetary waves of shorter wavenumbers ($s = \pm 3$) in the winter months. During summer, long period oscillations (e.g. >10 days) which are dominant in winter disappear, and oscillations with shorter period (e.g. <10 days) become dominant.

There is a strong planetary wave coupling between the stratosphere and mesosphere-lower thermospheric (MLT) during the year 2002 winter season, whilst the coupling is observed to be relatively weak during the other years. The strong planetary wave coupling in 2002 is understandable because during this year the middle atmosphere winter months were characterised by strong planetary wave activity which led to the first ever detection of the SSW in the Southern Hemisphere.

In the year 2002 winter period the mean circulation in the stratosphere is characterized by a series of planetary wave events that weakened the polar vortex and triggered the sudden stratospheric warming in late September. In particular, in the stratosphere there is a presence of a quasi 10-day eastward propagating planetary wave of wavenumber s=1, while in the MLT a quasi 14-day eastward propagating planetary wave of wavenumber s=1 is observed to be dominant. The Eliassen Palm flux (E-P) flux shows that strong planetary wave activity observed in the middle atmosphere originates from the troposphere. Zonal winds at the MLT show reversal approximately 7 days before the reversal at stratosphere, indicating a downwards propagation of circulation disturbance in the middle atmosphere. Eastward zonal winds dominate the winter MLT, but during the 2002 winter there are many periods of westward winds observed compared to the other years. The SABER vertical temperature profiles indicate cooling of the MLT region during the SSW occurrence. Gravity wave horizontal phase velocities and horizontal wavelengths as seen by the SANAE imaging riometer are observed to reduce dramatically over SANAE during the occurrence of the stratospheric warming. The disturbance of the middle atmosphere during the Southern Hemisphere stratospheric warming in year 2002 winter preconditioned the region for gravity waves to propagate upward to the MLT. The potential energy of these gravity waves is observed to increase with height up until they reach the lower thermosphere. At the MLT they lose their energy, thus depositing their momentum, leading to the MLT cooling and mean wind reversal.

Keywords: SSW, Planetary waves, Gravity waves, Stratosphere, MLT, SuperDARN radar, Mean wind, Temperature, Middle atmosphere, SANAE.

Acknowledgements

I am greatly indebted to the following for the role they played in making this thesis and my academic career possible:

1. Prof. Sivakumar Venkataraman, supervisor, for guidance and support throughout the duration of this project. I wish that you will continue to be a good and very friendly supervisor to your future students.
2. Dr. Sandile Malinga, co-supervisor, for guidance and support throughout the duration of this project. And I would like to thank him for always accommodating me on his very limited time.
3. Prof. Sadhasivan Pillay, co-supervisor, for guidance, suggestions and support during the course of this investigation.
4. Prof. Hassan Bencherif, for guidance, suggestions and support during the course of this investigation.
5. Elda Saunderson and Dr Zama Katamzi for evaluating the grammar and spelling of this thesis.
6. The South African National Space Agency (SANSA) Space Science group; Sibusiso Mthembu, Dr. Patrick Sibanda, Stefan Lotz and others, for always supporting and giving me useful ideas thoughout the study period.
7. The National Research Foundation (NRF) for their financial support.

This work is specifically dedicated to my family: Mbatha (Shandu-kaNdaba), Ntombela (Mpangazitha), Mdluli (Skhandzisa) and Lesala. Nonke niyisibani kimi, futhi ngiyanithanda kakhulu. Lena yimiphumela yokungesekela kwenu kuyoyonke impilo yami, ngakhoke lomsebenzi ungowenu. Ukuba ngiyazenzela ngabe lomsebenzi nguwubhale nangolwimi lwesiZulu, ukuze nesinedolo sikwazi ukuwufunda. Ngibonga noMvelinqangi ngokungigada nokungesekela kuyoyonke lempilo yalapha emhlabeni engelula nezeneze. Ngiyabonga.

Contents

List of Figures

List of Tables

Chapter 1

Introduction

The atmosphere including the troposphere, stratosphere, mesosphere-lower thermosphere (MLT) and ionosphere are linked by energy and momentum transfer (Holton, 2004). Thus, this whole region forms a coupled system in which influences that originate at one height or in one region can have profound influence elsewhere in the system. The middle and upper atmosphere is widely regarded as very important and sensitive indicators of the health of the atmosphere as a whole. In particular, the polar middle atmosphere is important because it is a region which is used to study global climate change and its accompanying processes.

The main objective of this thesis is to study the dynamics of the middle atmosphere over Antarctica and the Southern Hemisphere region. This includes specifically studying the coupling between the MLT and the region below. There have been many studies of the Arctic middle atmosphere in the Northern Hemisphere due to availability of different types of instruments (e.g. radars, LIDARs, rockets, models, satellites), with relatively few such studies in the Southern Hemisphere. Some aspects of the dynamics of the middle atmosphere over Antarctica and in the whole Southern Hemisphere have been described in previous studies. But, there are still many issues and unanswered questions.

An instrument which is usually used to study the dynamics of the middle atmosphere is the medium frequency (MF) radar. This is primarily due to their relatively good time and height resolutions and their continuous operation, which permits a wide variety of atmospheric processes to be studied, including different types of atmospheric waves and the mean flow in the atmosphere. However, this instrument is not available at the South African station in Antarctica. Although there are a number of MF radars in Antarctica at other stations, any available wind measurements, especially from a global network of identical instruments like Super Dual Auroral Radar Network (SuperDARN), is a desirable option for studying wind variations, atmospheric waves and associated characteristics in the MLT region. Thus, one of the motivations of the present work is to utilise neutral wind data retrieved from the South African National Antarctic Expedition (SANAE, 72°S, 3°W) to study the dynamics of MLT over Antarctica.

Originally, SuperDARN radars were designed to study plasma flow in the high-latitude ionosphere. However, Hall et al. (1997) demonstrated that echoes at ranges close to the SuperDARN radars are actually due to scatter from meteor trails near 94 km altitude. Therefore, the near-range scatters can be utilised to study neutral winds at meteor heights. In recent years there have been an increase in a number of studies which utilise the SuperDARN HF radar wind data to study the MLT dynamics (e.g. Bristow et al. (1999); Hussey et al. (2000); Espy et al. (2005); Malinga and Ruohoniemi (2007); Mbatha et al. (2010b)).

The basic vertical structure of the temperature distribution in the neutral atmosphere can be understood on radiative-convective grounds (e.g. Andrews et al. (1987); Shepherd (2000); Holton (2004)). Moreover, the basic information which has been known for sometime about the middle atmosphere is the absorption of the solar ultraviolet radiation by ozone leading to the temperature maximum around 50 km, which defines the stratopause. At a height above approximately 85 km there is an increase in temperature with height primarily due to the absorption of solar radiation by molecular oxygen. However, detailed measurements both in situ and from satellites have shown that there are many other major processes taking place in the middle atmosphere. Some of the examples of these processes are sudden stratospheric warmings (SSW), semi-annual oscillations (SAO), quasi-biennial oscillations (QBO) and others.

In this study, the main focus is the unprecedented late winter Southern Hemisphere major SSW in the year 2002. In generally, the major SSW occur about once every two years in the Northern Hemisphere (Hoffmann et al., 2002), presumably due to the topography of the area. The primary cause of the SSW is thought to be planetary waves originating from the troposphere and propagating upwards to the stratosphere and mesosphere lower-thermosphere region (Matsuno, 1971; Holton, 1983; Andrews et al., 1987). These planetary waves interact with the mean-flow and due to that interaction an upward and pole-ward directed heat and momentum flux leads to decreasing eastward winds and increasing temperature in the polar region in winter (Matsuno, 1971; Hoffmann et al., 2002). The unprecedented major SSW during 2002 caused many disturbances in the lower and middle atmosphere over the Southern Hemisphere polar region. In spite of existing studies of this unusual stratospheric warming in the Southern Hemisphere, there are still many unanswered questions regarding this event.

Due to the unusual behaviour of the Antarctica stratosphere in 2002, it is expected that the MLT wind field measured by the SANAE HF radar also exhibits similar behaviour. Thus, this thesis presents the first detailed study of the influence of the SSW in the MLT using the SuperDARN HF radar. Data from the National Centre for Environmental Prediction (NCEP), UK Met Office (UKMO) and the European Centre for Medium-Range Weather Forecast Re-Analysis for 40 years (ECMWF ERA-40) are also utilised to study the dynamics of stratosphere and the lower mesosphere. The Sounding of the Atmosphere using Broadband Emission Radiometry (SABER) instrument on board the

Thermosphere–Ionosphere–Mesosphere-Energetics and Dynamics (TIMED) satellite is capable of taking measurements from the stratosphere to the lower thermosphere. Thus, in this thesis it is used to study the dynamics of the whole middle atmosphere region in terms of temperature and potential energy. There are very few instruments that can sample the MLT at a sufficient resolution to study gravity waves. Considering the importance of gravity waves in the dynamics of the MLT (e.g. Fritts and Alexander (2003)), the study of gravity waves during the SSW period is an important subject. Thus, in this thesis a technique outlined by Moffat-Griffin et al. (2008) is used for the first time to extract parameters of short scale gravity waves during the period of the 2002 major SSW in the Southern Hemisphere.

Temperature monitoring in the atmosphere is important as temperature controls the rate of chemical reaction and thus ozone abundance. The middle atmospheric temperature is an important parameter because it is a combined manifestation of the dynamical, radiative, and chemical processes occurring in the middle atmosphere (Singh et al., 1996). Thus, this thesis also utilises the Durban Rayleigh LIDAR temperature data to study the middle atmosphere temperature climatology over Durban (29.9°S, 30°E), South Africa. LIDAR measurements made from April 1999 to July 2004 are used for the first time to study the stratosphere-mesospheric thermal structure over Durban. LIDAR monthly temperature mean profiles are also compared to SABER observations, temperature data from Halogen Occultation Experiment (HALOE), and the COSPAR International Reference Atmosphere (CIRA-86) model. Seasonal variations of temperature measured by the Durban LIDAR system are obtained and compared with a similar Rayleigh LIDAR system situated in Reunion Island (20.8°S, 55.5°E).

Basically, this chapter presents the background information about middle atmosphere, in terms of temperature and mean circulation. A special focus is given to relevant information such as theoretical background of atmospheric waves and stratospheric warmings.

1.1 Structure of the Atmosphere

A simplest method used within the scientific community to classify the Earth's atmosphere is its vertical temperature structure. This is because the temperature of the atmosphere alternates from the Earth's surface upwards. Figure 1.1 is a simple diagram showing the different layers of the Earth's atmosphere. It basically shows the vertical temperature profile from the Committee on Space Research (COSPAR) International Reference atmosphere (CIRA-86) model plotted for the month of January at 50°S. Moving vertically upwards the temperature decreases and increases giving rise to four distinct regions named the troposphere, stratosphere, mesosphere and thermosphere.

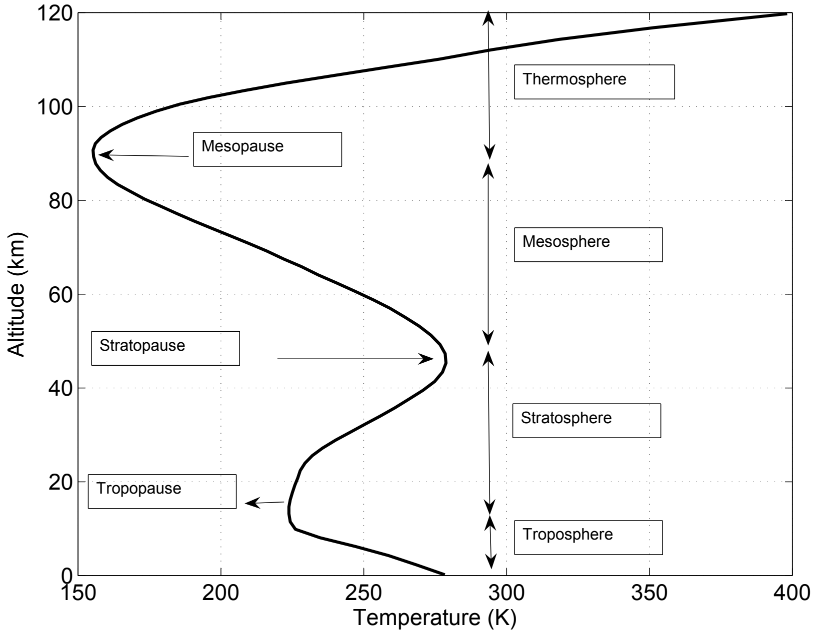

Figure 1.1: Vertical structure of the atmosphere.

Vertical structure of the atmosphere also varies with density and pressure. Moving upwards these two parameters of the atmosphere decrease exponentially by the factor of $e^{-z/H}$, where H is the scale height given by $H = RT/g$, and z the height above sea level . In this equation R is the gas constant for dry air, T is the mean planetary surface temperature in kelvins, g is acceleration due to gravity on planetary surface ($\mathrm{m/s^2}$). The main cause of the alternating shape of the vertical temperature profile of the Earth's atmosphere is the combination of the atmospheric dynamics, atmospheric chemistry and solar radiation effects. At the Earth's surface the sunlight is absorbed and re-emitted towards the space at infrared wavelengths, leading to the high temperature at the lower part of the troposphere region. Troposphere region of the atmosphere extends from the surface upwards to about 10-16 km, depending on geographical location, season and other factors. The temperature of the troposphere decreases with a lapse rate of 6.5 $\mathrm{K.km^{-1}}$ of the altitude. A height at which this temperature stops decreasing is termed the tropopause, and this is a layer which separates this region from the stratosphere. Tropopause height also varies directly with the troposphere. The tropopause heights are the highest over the equator because strong vertical motions raise the base of the ozone layer and force it to spread horizontally to higher latitudes.

Above the tropopause is the stratosphere. The stratosphere is defined as the height above the troposphere where the temperature starts to increase with altitude. This region extends up to an altitude of about 48-50 km. Temperature starts to increase in this region because of the absorption of solar ultraviolet (UV) radiation by ozone. The vertical temperature structure of the stratosphere ranges from about 225 K at ~20 km, up to ~275 K at ∼50 km. A region where the stratospheric temperature reaches its maximum is termed the stratopause, and it is a layer which separates the stratosphere from the mesosphere.

Mesosphere region is the region above the stratopause where the temperature decreases. This region extends from ∼50 km to ∼90 km. Within this region, a small fraction of the neutral particles are ionised by the radiation from the sun forming the bottom side ionospheric region named the D-region (∼55-90 km). A thin layer where this region reaches its lowest temperature (the coldest part of the atmosphere) is termed the mesopause, and it is the region where the thermosphere starts.

The thermosphere is the region extending from the mesopause upwards, where temperature starts to increase again all the way into space. In this region temperature increases with height from 180 K at the mesopause up to a maximum of 600-2000 K, depending on the level of solar activity. This temperature increase is mainly due to the absorption of solar radiation by molecular oxygen and other chemical species in the thermosphere.

The middle atmosphere (region extending from the stratosphere to the mesosphere-lower thermosphere) is the principal region of interest for this thesis.

1.1.1 The Middle Atmosphere

Of all the regions of the atmosphere, the troposphere may be regarded as an important region because it is responsible for weather disturbances and climate variability. However, the middle atmosphere is equally important. The middle atmosphere is the region extending upwards from the tropopause to the mesopause. This whole region consists of two main layers, the stratosphere and the mesosphere. The troposphere and middle atmosphere are linked through radiative and dynamical processes that can be represented in global forecast scale and climate model (Holton, 2004). Within the troposphere and middle atmosphere there is also an exchange of trace substances that are important for the photochemistry of the ozone layer. Thus, this section focuses primarily on the dynamical processes in the troposphere and the middle atmosphere.

1.1.1.1 Zonal Mean Temperature and Zonal Wind

The contour plots in Figure 1.2 and 1.3 show CIRA-86 zonal mean temperature and zonal mean zonal wind cross sections in the troposphere and middle atmosphere for January and July, respectively. Due to little solar radiation reaching the troposphere, the thermal structure of the troposphere is maintained by an approximate balance among infrared radiative cooling, vertical transport of sensible and latent heat away from the surface by small-scale eddies, and large-scale heat transport by synoptic-scale eddies (Holton, 2004). This results in the mean temperature structure being high in the equatorial region and decreasing towards the winter and summer poles, as well as a rapid decrease in altitude with a lapse rate of about 6°C.km^{-1}.

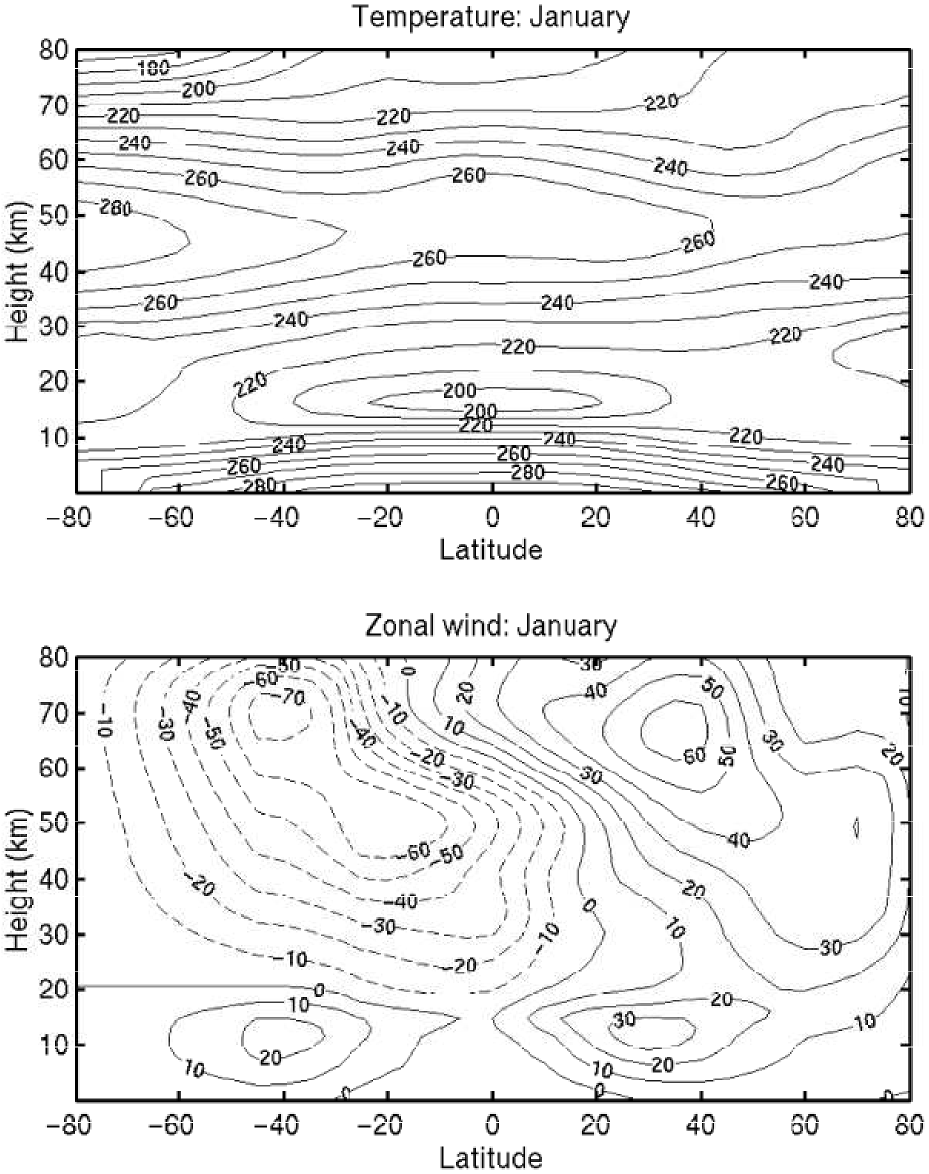

Figure 1.2: Monthly averaged zonal temperature (K) and zonal wind (m.s^{-1}) for January (from on Fleming et al. (1990)).

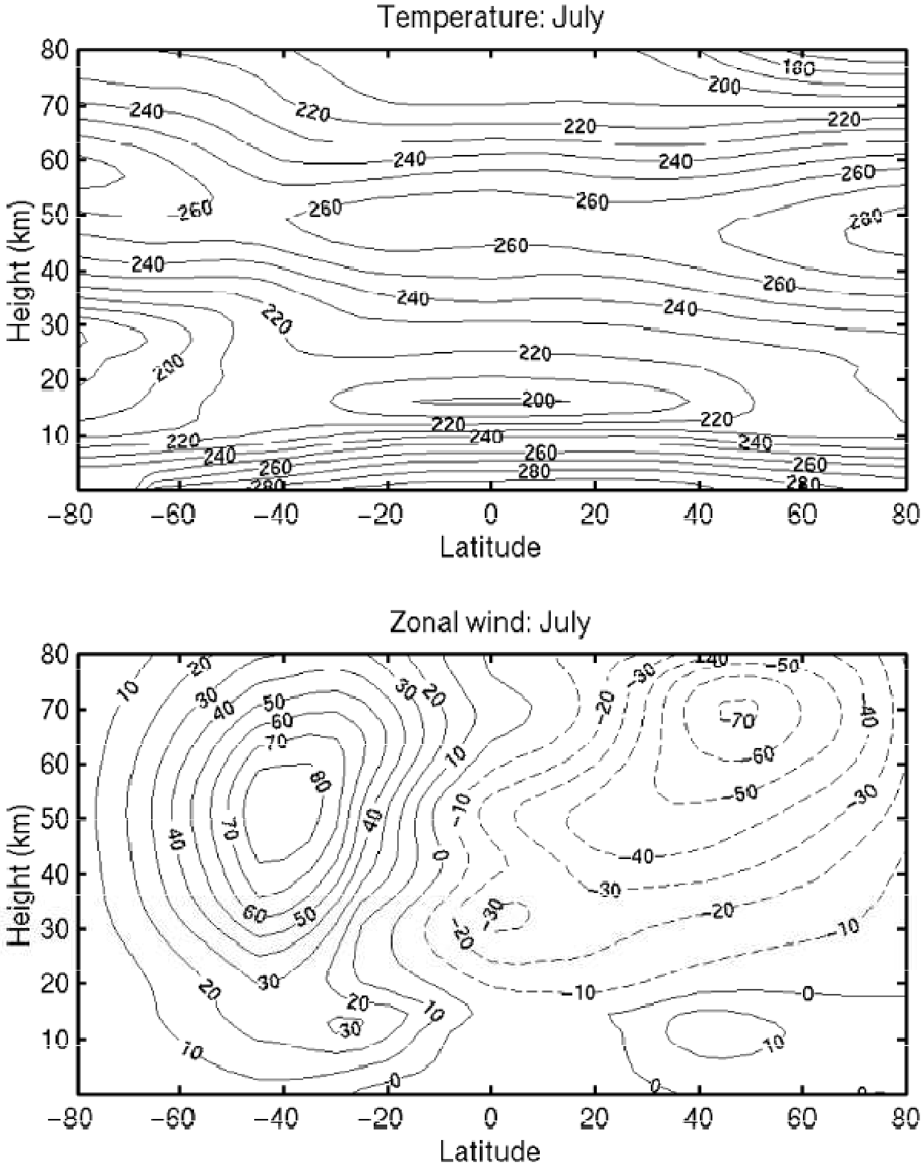

Figure 1.3: Monthly averaged zonal temperature (K) and zonal wind (m.s^{-1}) for July (from on Fleming et al. (1990)).

There are some features present in the zonal temperature means in the two figures that cannot be explained by radiative equilibrium only, such as the temperature distribution in the mesosphere with higher temperature at the winter poles and colder temperature at the summer poles. This rather complex behaviour of temperature is primarily due to gravity waves which deposit energy and momentum in the region, changing the dynamics including the meridional flow and forcing the temperature away from the equilibrium conditions (Dowdy, 2005).

The contour plots in the lower panels of Figure 1.2 and 1.3 show the CIRA-86 mean zonal wind for January and July, respectively. Some of the outstanding features are a westward jet in the summer hemisphere and an eastward jet in the winter hemisphere, with maxima in the wind speeds occurring near the 60 km altitude. These polar night jets provide wave guides for the vertical propagation of quasi stationary planetary waves (Holton, 2004).

Generally, during the winter seasons there is an absence of sunlight in the polar regions which creates low pressure systems over the poles. During this period the stratospheric zonal wind can become very strong, and this is commonly known as the polar vortex or polar night jet. The polar vortex is a very strong eastward wind. The mid-winter stratospheric temperatures inside the polar vortex are about 20 K cooler in the Southern Hemisphere compared to the Northern Hemisphere . This is one of the significant differences in the processes occurring in the Antarctic and Arctic (Andrews et al., 1987). The cooler mid-winter stratospheric temperatures in Antarctica supports the formation of the polar stratospheric clouds (PSC), leading to a regular hole in the ozone layer over the south pole (Farman et al., 1985). Thus, the PSCs are essential in the depletion of ozone because they support chemical reactions that produce active chlorine.

In the mesosphere, clouds known as the polar mesospheric clouds (PMC) can form due to the extremely low temperatures which occur during the summer seasons (Shettle et al., 2002). However, this may be a surprise considering the radiative equilibrium during summer seasons. Basically, PMCs are water ice particles which form as the temperature becomes less than the frost point for upper mesosphere water vapour concentrations (about$\sim$140 K) (Dowdy, 2005).

1.1.1.2 The Meridional Circulation in the Atmosphere

If planet Earth was not rotating the circulation driven by the pole-equator temperature difference would be straightforward, with warm air rising in low latitudes and cold air sinking at high latitudes. But, due to the rotation of the Earth the air does not move directly from high to low pressure areas but it deflects to the right in the Northern Hemisphere and to the left in the Southern Hemisphere.

Using several observations from sailing ships Hadley (1735) was able to show the general features of the meridional circulation in the atmosphere for the first time. The pioneering work by Brewer (1949) and Dobson (1956) also recognised that the meridional and seasonal distributions of stratospheric tracers imply that tropospheric air ascends into and within the tropical stratosphere, and spreads poleward and downward from there into the winter hemisphere (see Figure 1.4). The above mentioned studies by Brewer and Dobson lead to what is nowadays known as the Brewer-Dobson Circulation, which is known to be responsible for the transport of all the long-lived trace elements, such as, ozone and CFCs. In the mesosphere, the summer hemisphere air parcel originating from the lower atmosphere is observed to be transported to the winter hemisphere where it sinks at high latitudes.

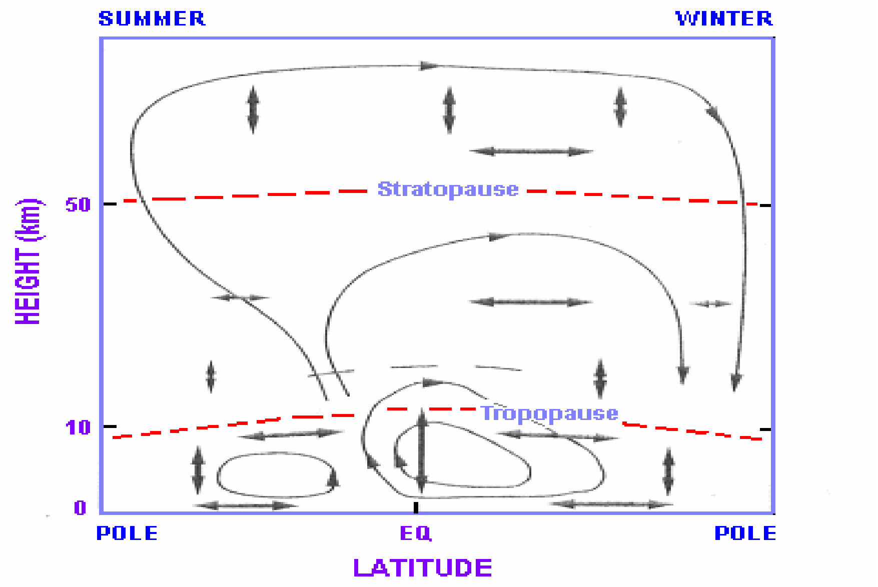

Figure 1.4: Meridional circulation in the atmosphere (WMO., 1985).

1.2 The Atmospheric Dynamics

In order to discuss the results presented in this thesis it is necessary to look at the basics of atmospheric dynamics. Thus, this section introduces the basics of atmospheric dynamics. The section will specifically concentrate on the equations describing the basis of atmospheric motion and the derivations that lead to the perturbation equations for planetary waves and gravity waves.

1.2.1 Basic Equations

The following theoretical discussion of the basic equations of the atmosphere is largely based on Andrews (2000) and Baumgaertner (2007). Basically, atmospheric motions are governed by three fundamental physical principles, namely, conservation of mass, conservation of momentum and conservation of energy (Holton, 2004). Thus, to explain the atmospheric motions it is necessary to look at fundamental fluid equations. Due to the complexity of these equations in the atmospheric point of view, one can use spherical coordinates where several approximations can be made to simplify these equations. One example of the approximations can be to neglect the Coriolis force associated with the horizontal component of the Earth's rotation, and distance from a point in the atmosphere to the centre of the Earth can be replaced by a mean radius a. The set of output equations are termed the primitive equations.

In the present thesis, and due to the purpose of this work, the primitive equations are introduced in the log-pressure and the Cartesian system. Similar to the studies by Holton (2004) and Baumgaertner (2007), in log-pressure coordinates on a sphere the zonal and meridional momentum equations, the mass continuity equation, the thermodynamic energy equation, and the equation for hydrostatic balance which approximates the vertical momentum equation can be mathematically written as

$$\frac{\partial}{\partial t} + \frac{u}{a\cos\phi}\frac{\partial u}{\partial\lambda} + \frac{v}{a\cos\phi}\frac{\partial v}{\partial\phi}(u\cos\phi) + w\frac{\partial u}{\partial z} - fv + \frac{1}{a\cos\phi}\frac{\partial\Phi}{\partial\lambda} = X \tag{1.1}$$

$$\frac{\partial v}{\partial t} + \frac{u}{a\cos\phi}\frac{\partial v}{\partial\lambda} + \frac{v}{a}\frac{\partial v}{\partial\phi} + w\frac{\partial v}{\partial z} + \frac{u^2\tan\phi}{a} + fu + \frac{1}{a}\frac{\partial\Phi}{\partial\phi} = Y \tag{1.2}$$

$$\frac{1}{a\cos\phi}\frac{\partial u}{\partial\lambda} + \frac{1}{a\cos\phi}\frac{\partial}{\partial\phi}(v\cos\phi) + \frac{\partial w}{\partial z} - \frac{w}{H} = 0 \tag{1.3}$$

$$\frac{\partial T}{\partial t} + \frac{u}{a\cos\phi}\frac{\partial T}{\partial\lambda} + \frac{v}{a}\frac{\partial T}{\partial\phi} + w\left(\frac{\partial T}{\partial z} + \frac{\kappa T}{H}\right) = \frac{Q}{c_p} \tag{1.4}$$

$$\frac{\partial\Phi}{\partial z} = \frac{RT}{H}, \tag{1.5}$$

where t is the time, ϕ the latitude, λ the longitude, z the log-pressure height given by $(-H\ln(p/p_0))$, u the zonal velocity, v the meridional velocity, w the vertical velocity given by dz/dt, H the scale height, f Coriolis force $(= 2\Omega\sin\phi)$, p the pressure at height z, p_0 pressure at the sea level, Ω the angular velocity of the Earth, Φ geopotential, T the temperature, c_p the specific heat at constant pressure, κ gas constant $(= R/c_p)$, R the gas constant for dry air, a the radius of the Earth, Q the heating rate per unit mass, and X and Y the horizontal components of unspecified non-conservative forcings.

The work by Andrews (2000) and Baumgaertner (2007) showed that in Cartesian coordinates, with height as a vertical coordinate, and small increment distances $dx = a\cos\phi d\lambda$ in the eastwards direction and $dy = ad\phi$ in the northward direction, the momentum equations becomes

$$\frac{du}{dt} - \left(2\Omega + \frac{u}{a\cos\phi}\right)(v\sin\phi - w\cos\phi) + \frac{1}{\rho}\frac{\partial p}{\partial x} = X \tag{1.6}$$

$$\frac{dv}{dt} + \frac{wv}{a} + \left(2\Omega + \frac{u}{a\cos\phi}\right)u\sin\phi + \frac{1}{\rho}\frac{\partial p}{\partial y} = Y \tag{1.7}$$

$$\frac{dw}{dt} - \frac{u^2+v^2}{a} - 2\Omega u\cos\phi + \frac{1}{\rho}\frac{\partial p}{\partial z} + g = Z, \tag{1.8}$$

where d/dt is the total derivative, the rate of change of a variable following the motion given by $\frac{\partial}{\partial t} + u\frac{\partial}{\partial x} + v\frac{\partial}{\partial y} + w\frac{\partial}{\partial z}$. Z is the vertical component of unspecified non-conservative forcings, p is the $\rho$the mass density. Now if one uses the approximations (Baumgaertner, 2007)

$$\frac{\mid u \mid}{c \cos \phi} \ll 2\Omega$$

$$\mid w \cos \phi \mid \ll \mid v \sin \phi \mid$$

$$\mid wv \mid /r \ll 2\Omega \mid u \sin \phi \mid$$

equations 1.6 to 1.8 become

$$\frac{du}{dt} - fv + \frac{1}{\rho}\frac{\partial p}{\partial x} = X \tag{1.9}$$

$$\frac{dv}{dt} + fu + \frac{1}{\rho}\frac{\partial p}{\partial y} = Y \tag{1.10}$$

$$\frac{dw}{dt} + \frac{1}{\rho}\frac{\partial p}{\partial z} + g = 0 \tag{1.11}$$

in the Cartesian coordinate system. c is the speed of light. The representation of the continuity equation and the thermodynamic energy equation in a Cartesian coordinate system can thus be given by

$$\frac{1}{\rho}\frac{d\rho}{dt} + \frac{\partial u}{dx} + \frac{\partial v}{dy} + \frac{\partial w}{dz} = 0 \tag{1.12}$$

$$\frac{d\theta}{dt} = Q, \tag{1.13}$$

where the potential temperature θ is given by $T\left(p_0/p\right)^k$, and κ is gas constant. Using scale analysis equations 1.9 to 1.11 can be simplified and become equations known as the geostrophic (equation 1.14 and 1.15) and hydrostatic (equation 1.16) approximations

$$fv = \frac{1}{\rho}\frac{\partial p}{\partial x} \tag{1.14}$$

$$-fu = \frac{1}{\rho}\frac{\partial p}{\partial y} \tag{1.15}$$

$$\frac{\partial p}{\partial z} = -g\rho. \tag{1.16}$$

Air behaves more or like as an ideal gas. The ideal gas equation is given by

$$p = \rho R T. \tag{1.17}$$

Using the ideal gas law and the geostrophic approximation equations 1.14 and 1.16, the thermal wind-shear equations can be derived to form

$$f \frac{\partial v}{\partial z} = \frac{g}{T} \frac{\partial T}{\partial x} \tag{1.18}$$

$$f \frac{\partial u}{\partial z} = \frac{g}{T} \frac{\partial T}{\partial y}. \tag{1.19}$$

1.2.2 Theory of Planetary Waves

In general, all atmospheric waves are periodic disturbances in the field of atmospheric variables such as wind, temperature, geopotential height, etc. This subsection will focus on planetary waves (atmospheric waves with periods from 2 to about 35 days), or sometimes called Rossby waves. These planetary waves are forced modes generated in the troposphere by flow over continental scale topography, by continent-ocean heating contrasts, and by nonlinear interactions among transient tropospheric wave disturbances. They are known to propagate both horizontally and vertically carrying momentum into the middle and upper atmosphere. Most importantly, these waves are responsible for setting up the polar stratosphere to conditions which favour the occurrence of the stratospheric warming. This leads to the breakdown of the polar vortex and the split of the ozone hole.

Planetary waves have large horizontal scales, thus for the better understanding of these waves it is also necessary to consider the effects of the rotating spherical Earth, which leads to a common mathematical description. The details of the theory of planetary waves have been studied extensively (e.g. Charney and Drazin (1961); Volland (1988); Andrews et al. (1987); Garcia et al. (2005)). In the present work, the theory of planetary waves will be discussed based on the work by Holton (1975), Volland (1988), and Forbes (1995).

In order to understand the theory of planetary waves better, there are important approximations which need to be applied to the primitive equations. The first step is to consider only equations 1.9 to 1.11. These equations can be approximated by the so-called Boussinesq equations where density variations are ignored except when they are coupled to gravity. The next step is to approximate the Boussinesq equations by restricting the flow to a quasi-geostrophic flow. These approximations yield a quasi-geostrophic vorticity equation

$$D_g q = 0, \tag{1.20}$$

where D_g is the time derivative following the geostrophic flow (u_g, v_g),

$$D_g = \frac{\partial}{\partial t} + u_g \frac{\partial}{\partial x} + v_g \frac{\partial}{\partial y}. \tag{1.21}$$

The parameter q is the quasi-geostrophic potential vorticity given by

$$q = f_0 + \beta y + \frac{\partial^2 \psi}{\partial^2 x} + \frac{\partial^2 \psi}{\partial^2 y} + \frac{\partial}{\partial z}\left(\frac{f_0^2}{N^2}\frac{\partial \psi}{\partial z}\right) \tag{1.22}$$

for the geostrophic stream-function $\psi \equiv p/f_0\rho_0$. Parameter f_0 is the Coriolis parameter defined in the centre of the beta planen and N is the bouyancy frequency. The quasi-geostrophic potential vorticity equation above uses the β-plane approximation, $f(y) \approx f_0 + \beta y$. If one assumes a uniform zonal background flow $(U, 0, 0)$ with small amplitudes, the disturbances produce the stream-function,

$$\psi = -Uy + \psi^{'} \tag{1.23}$$

and thus, the quasi-geostrophic potential vorticity equation 1.22 becomes

$$\left(\frac{\partial}{\partial t} + U\frac{\partial}{\partial x}\right)\left(\nabla^2 \psi + \frac{f_0^2}{N^2}\frac{\partial^2 \psi}{\partial z^2}\right) + \beta\frac{\partial \psi}{\partial x} = 0. \tag{1.24}$$

The planetary wave solutions are assumed to be

$$\psi = Re\left(\psi_0 \exp\left[i\left(\omega t + kx + ly + mz\right)\right]\right), \tag{1.25}$$

where k, l and m are the zonal, meridional, and vertical wave number, ψ_0 is the amplitude, and ω is the angular frequency. When combining the above solutions with the quasi-geostrophic potential vorticity equation it forms the dispersion relation

$$m^2 = \frac{N}{f_0}\left(\frac{\beta}{U - (\omega/k)} - \left(k^2 + l^2\right)\right). \tag{1.26}$$

If $\beta > 0$ this means that the zonal phase speed of the waves

$$c = \frac{\omega}{k} = U - \frac{\beta}{k^2 + l^2 + f_0^2 m^2/N^2} \tag{1.27}$$

satisfies

$$U - c > 0. \tag{1.28}$$

Equation 1.28 implies that the planetary waves always propagate westwards with respect to the background mean flow in the atmosphere. An upwards propagation of waves can only occur if m is real and non-zero, thus m^2 must be greater than zero. This means that from the dispersion relation one can deduce

$$U - c = \frac{\beta}{k^2 + l^2 + f_0^2 m^2/N^2} < U_c \equiv \frac{\beta}{k^2 + l^2}. \tag{1.29}$$

The Charney-Drazin criterion (Charney and Drazin, 1961) is satisfied when the wave is a stationary wave ($c = 0$), which implies that $0 < U < U_c$, where U_c depends on the vertical wavelength. Basically, the Charney-Drazin criterion signifies that vertical propagation of the wave will not be allowed if the background wind has a very large eastward component. The Charney-Drazin criterion is very important for this thesis, as it will help to explain the planetary wave coupling in the middle atmosphere, and will be referred to in several chapters of this thesis.

1.2.3 Theory of Gravity Waves

Gravity waves are mesoscale phenomena that have important global effects on the circulation, temperature structure, chemistry, and composition of the entire atmosphere (Alexander and Dunkerton, 1999). Gravity waves are formed when a parcel of air in the atmosphere has a different density to surrounding air. This can be primarily caused by processes such as wind-orography interaction (Hines, 1988), thunder storms (Alexander and Pfister, 1995), wind shear (Fritts, 1982) and geographic adjustment (Luo and Fritts, 1993).

Vertically propagating internal gravity waves are thought to transport momentum from the lower to the upper atmosphere, accelerating the upper level mean flow regions of wave breaking, dissipation, and critical absorption (Holton, 1982; Alexander and Dunkerton, 1999).

The perturbation equations useful for the study of gravity waves related to this thesis can be derived from the basic Cartesian equations 1.9 to 1.13. Another useful parameter in the description of gravity waves is the potential temperature θ. The potential temperature is defined as the temperature that a parcel of dry air at pressure p and temperature T would acquire if it were to be expanded or compressed adiabatically to the reference pressure p_0 (Fritts and Alexander, 2003; Dowdy, 2005). Mathematically it can be represented as

$$\theta = \frac{p}{\rho R}\left(\frac{p_0}{p}\right)^{\kappa}. \tag{1.30}$$

The unforced forms of equations from 1.9 to 1.13 (i.e. $X = Y = Q = 0$), linearised about a horizontally uniform hydrostatic basic state with background mean wind ($\bar{u}$,$\bar{v}$,0) , with potential temperature $\bar{\theta}$, density $\bar{\rho}$ and pressure $\bar{p}$ varying only in the z direction, yields the following set of perturbation equations

$$\frac{Du'}{Dt} + w'\frac{\partial \bar{u}}{\partial z} - fv' + \frac{\partial}{\partial x}\left(\frac{p'}{p}\right) = 0 \tag{1.31}$$

$$\frac{Dv'}{Dt} + w'\frac{\partial \bar{v}}{\partial z} - fu' + \frac{\partial}{\partial y}\left(\frac{p'}{p}\right) = 0 \tag{1.32}$$

$$\frac{Dv'}{Dt} + \frac{\partial}{\partial z}\left(\frac{p'}{p}\right) - \frac{1}{H}\left(\frac{p'}{p}\right) + g\frac{\rho'}{\rho} = 0 \tag{1.33}$$

$$\frac{D}{Dt}\left(\frac{\theta'}{\theta}\right) + w'\frac{N^2}{g} = 0 \tag{1.34}$$

$$\frac{D}{Dt}\left(\frac{\rho'}{\rho}\right) + \frac{\partial u'}{\partial x} + \frac{\partial v'}{\partial y} = \frac{\partial w'}{\partial z} - \frac{w'}{H} = 0 \tag{1.35}$$

$$\frac{\theta'}{\theta} = \frac{1}{c_s^2}\left(\frac{p'}{\bar{p}}\right) - \frac{\rho'}{\bar{\rho}}. \tag{1.36}$$

Here, D/Dt is the linearised form of the time derivative given by

$$\frac{D}{Dt} = \frac{\partial}{\partial t} + \bar{u}\frac{\partial}{\partial x} + \bar{v}\frac{\partial}{\partial y}, \tag{1.37}$$

c_s is the speed of sound with c_v the specific heat at constant volume give by

$$c_s = \sqrt{\frac{c_p}{c_v}RT_0} \tag{1.38}$$

and the buoyancy frequency N, given by

$$N = \left(g\frac{\partial \ln \theta}{\partial z}\right)^{\frac{1}{2}}. \tag{1.39}$$

The buoyancy frequency is a measure of static stability in an atmosphere region as well as being the frequency of the gravity wave oscillations. The WKB approximation which assumes $\bar{u}$,$\bar{v}$ and N vary only slowly over a wave cycle in the vertical direction (e.g. Gille and Russell III (1984)) was used. The background shear terms in equations 1.31 and 1.32 were neglected. It was also assumed that the gravity wave solution has the form

$$\left(u', v', w', \frac{\theta'}{\bar{\theta}}, \frac{p'}{\bar{\rho}}, \frac{\rho'}{\bar{\rho}}\right) = \left(\tilde{u},\tilde{v}, \tilde{w}, \tilde{\theta}, \tilde{p}, \tilde{\rho}\right) \exp\left[i\left(kx + ly + mz - \omega t\right) + \frac{z}{2H}\right], \tag{1.40}$$

where (k, l, m) are wavenumbers, and ω is the ground based wave frequency. Substituting the wave solution into equation 1.31 to 1.36 and setting the imaginary coefficients to zero gives

$$\frac{g}{c_s^2} = \frac{1}{H} - \frac{N^2}{g} \tag{1.41}$$

$$\hat{\omega}^2 \left(k^2 + l^2 + m^2 + \frac{1}{4H^2} - \frac{\hat{\omega}^2 - f^2}{c_s^2} \right) = N^2(k^2 + l^2) + f^2 \left(m^2 + \frac{1}{4H^2} \right), \tag{1.42}$$

where $\hat{\omega} = \omega - ku - lv$ is the intrinsic frequency (i.e. the frequency that would be observed in a frame of reference moving with the background wind $(\bar{u}, \bar{v})$). The above equation is 4^{th} order in $\hat{\omega}$ and supports both acoustic and gravity waves. The acoustic wave can be removed by letting $c_s \rightarrow \infty$, giving the gravity wave dispersion relation,

$$m^2 = \frac{\left(k^2 + l^2\right)\left(N^2 - \hat{\omega}^2\right)}{\left(\hat{\omega}^2 - f^2\right)} - \frac{1}{4H^2}. \tag{1.43}$$

Using the approximation that $m^2 \gg 1/4H^2$ the term $-1/4H^2$ can neglected. This approximation is known as Boussinesq approximation, and when $\hat{\omega}^2 \gg f^2$, the dispersion relation can be rewritten as

$$\hat{\omega}^2 = \frac{N^2\left(k^2 + l^2\right)}{k^2 + l^2 + m^2}. \tag{1.44}$$

1.3 The Sudden Stratospheric Warming

The sudden stratospheric warming (SSW) is a dramatic thermo-dynamical event which involves considerable changes of the background wind, temperature and circulation of the winter high latitude middle atmosphere (∼20 – 100 km). During such an event the temperature changes are far too high to be explained by radiative heating. This event was first reported in the 1950s, where a massive increase of temperature over a period of several days in the Arctic was recorded (see the history in Labitzke and Van Loon (1999)). The first ever detailed explanation of the SSW was given by Matsuno (1971), who introduced a simple model of wave-mean-flow interaction induced by planetary waves.

There are four different types of SSW, namely, minor SSW, major SSW, Canadian warming, and final Warming. A study by Labitzke and Naujokat (2000) classified the SSW as a minor warming if there is a significant increase of temperature (at least by 25 K per week) below 10-hPa levels in any area of the winter hemisphere. This temperature increase can be intense and sometimes also reverse the temperature gradient, but they may not lead to wind reversal at/below the 10-hPa pressure level. On the other hand, the SSW is classified as a major warming if at 10-hPa height or below the latitudinal mean temperature increases poleward from 60° latitude and an associated wind circulation reversal leads to a change from the usual dominant eastward directed flow to westward directed flow, and hence to a splitting of the polar vortex.

The Canadian warmings have no counterpart in the Southern Hemisphere, but can only occur in the early winter in the stratosphere of the Northern Hemisphere. During Canadian warmings a warm Aleutian High advects eastward within a few days from its usual position over the dateline (an imaginary line on the surface of the earth following the 180^{th} meridian) towards the 90°W line of longitude over Canada. This leads to a strong distortion and displacement of the polar vortex, but not the splitting of the polar vortex. On the other hand, the final warmings occur when the latitudinal temperature gradient changes sign at the end of winter (spring time) and westward winds remain at middle and high latitudes. They mark the transition between winter eastward and summer westward winds which does not occur smoothly, as it would be driven purely by radiative heating, but in a sporadic manner owing to SSW. This type of stratospheric disturbance leads to polar vortex breakdown. For the purpose of this thesis, only the major SSW will studied.

1.3.1 The Eliassen-Palm (E-P) Flux

A method which is useful in analysing the zonal mean circulation in the troposphere and middle atmosphere, and which provides clear diagnostics of eddy forcing and a more direct view of the transport in the meridional plane, is the Eliassen-Palm (E-P) theory (Eliassen and Palm, 1961). In this thesis, this approach will be very important as it will provide the understanding of the dynamical processes during the SSW event in terms of planetary waves vertical propagation, wave drive, and wave breaking.

Thus, this section intends to present the basic E-P theoretical formulation, with most of the treatment based on the E-P flux. In order to treat the theory of E-P flux, it is important to consider the equations of motion (equation 1.1 to 1.5). But, in their general form they will be complicated if applied to large- and medium-scale meteorological phenomena which are encountered in the atmosphere. Thus several assumptions can be made in order to simplify them. Some of the important assumptions include replacing the vertical momentum equation by the hydrostatic balance, neglecting the Coriolis force associated with the horizontal component of the Earth's rotation vector, and replacing the distance r from any point in the atmosphere to the centre of the Earth by a mean radius a. Hence the resulting approximate set of equations, commonly referred to as the primitive equations, which can be expressed in spherical coordinate form (Holton, 1975)

$$\frac{Du}{Dt} + \left(f + \frac{u\tan\phi}{a}\right)v + \frac{\Phi_\lambda}{a\cos\phi} = X \tag{1.45}$$

$$\frac{Dv}{Dt} + \left(f + \frac{u\tan\phi}{a}\right)u + \frac{\Phi_\phi}{a} = Y \tag{1.46}$$

$$\Phi_z = H^{-1} R\theta e^{-kz/H} \tag{1.47}$$

$$\frac{\mid u_\lambda + (v\cos\phi)_\phi \mid}{a\cos\phi} + \frac{(\rho_0 w)}{\rho_0} = 0 \tag{1.48}$$

$$\frac{D\theta}{Dt} = Q. \tag{1.49}$$

where u is the zonal velocity, v the meridional velocity, w the vertical velocity given by dz/dt, t is the time, ϕ the latitude, λ the longitude, z the log-pressure height given by $(-H\ln(p/p_0))$, Φ the geopotential, a the radius of the Earth, f Coriolis force, Q the heating rate per unit mass, and X and Y the horizontal components of unspecified non-conservative forcings. In many phenomena occurring in the middle atmosphere there is a contribution by interaction of mean flow with disturbances (e.g. wave/eddies) that are superimposed on it. This interaction may bring significant changes in mean flow through nonlinear effects, and can also modify the propagation of the disturbances. In the Eulerian mean flow, the mean is a zonal mean (donated by over-bar) and the departure from the zonal mean (denoted by prime). Thus, these two can be mathematically represented as

$$\overline{u}(\phi, z, t) = (2\pi)^{-1} \int_0^{2\pi} u(\lambda, \phi, z, t)\, d\lambda \tag{1.50}$$

$$u'(\lambda, \phi, z, t) = u - u'. \tag{1.51}$$

It is important to note that the separation of the mean and disturbance parts is primarily a mathematical device and may not be the most natural physics separation in all cases. If one substitutes the separated variables that are the zonal mean part (equation 1.50) and the disturbance part (equation 1.51) into the primitive equations (equation 1.45 to 1.49), perform some manipulation and average the basis equation, the following set of primitive equations for the Eulerian-mean flow in spherical coordinates are obtained

$$\overline{u} + \overline{v}\left[(a\cos\phi)^{-1}(\overline{u}\cos\phi)_\phi - f\right] + \overline{wu} - \overline{X}$$

$$= -\left(a\cos^2\phi\right)^{-1}\left(\overline{v'u'}\cos^2\phi\right)_\phi - \rho_0^{-1}\left(\rho_0\overline{w'u'}\right)_z \tag{1.52}$$

$$\bar{v}_t + a^{-1}\overline{v}\overline{v}_\phi + \overline{w}\bar{v}_z + \bar{u}\left(f + \bar{u}a^{-1}\tan\phi\right) + a^{-1}\overline{\Phi}_\phi - \overline{Y}$$

$$= -\left(a\cos^2\phi\right)^{-1}\left(\overline{v'^2}\cos\phi\right)_\phi - \rho_0^{-1}\left(\overline{w'u'}\right)_z - \overline{u'^2}a^{-1}\tan\phi \tag{1.53}$$

$$\overline{\Phi}_z - H^{-1}R\bar{\theta}e^{-kz/H} = 0 \tag{1.54}$$

$$(a\cos\phi)^{-1}\left(\bar{v}\cos\phi\right)_{\phi}+\rho_0^{-1}\left(\rho_0\overline{w}\right)_z=0 \tag{1.55}$$

$$\overline{\theta}+a^{-1}\overline{v}\overline{\theta}_{\phi}+\overline{w}\overline{\theta}_z-\overline{Q}=(a\cos\phi)^{-1}\left(\overline{v'\theta'}\cos\phi\right)_{\phi}+\rho_0^{-1}\left(\rho_0\overline{w'\theta'}\right)_z. \tag{1.56}$$

With the primitive equations in the current form, it is difficult to predict how the zonal mean flow will respond to parameters such as eddy momentum flux ($\overline{v'u'}$) or eddy heat flux ($\overline{v'\theta'}$) in the quasi-geostrophic set of equations. Thus, in order to solve this problem, it is necessary to transform the mean flow equations to an alternative form. In the spherical case, a residual mean meridional circulation $(0,\overline{v}^{*},\overline{w}^{*})$ is defined by

$$\overline{v}^{*}\equiv\bar{v}-\rho_0^{-1}\left(\rho_0\overline{v'\theta'}/\bar{\theta}_z\right)_z \tag{1.57}$$

$$\overline{w}^{*}\equiv\overline{w}+(a\cos\phi)^{-1}\left(\cos\phi\overline{v'\theta'}/\bar{\theta}_z\right)_{\phi}. \tag{1.58}$$

Performing the substitution for $(\overline{v},\overline{w})$ in the primitive equations for the Eulerian-mean flow in equations 1.52 to 1.56, using the equations 1.57 and 1.58 and rearranging yields the transformed Eulerian-mean (TEM) set of equations given by

$$\bar{u}_t+\overline{v}^{*}\left[(a\cos\phi)^{-1}\left(\bar{u}\cos\phi\right)_{\phi}-f\right]+\overline{w}^{*}\bar{u}_z-\overline{X}=\left(\rho_0 a\cos\phi\right)^{-1}\nabla.F \tag{1.59}$$

$$\bar{u}\left(f+\bar{u}a^{-1}\tan\phi\right)+a^{-1}\overline{\Phi}_{\phi}=G \tag{1.60}$$

$$\overline{\Phi}_z-H^{-1}R\overline{\theta}e^{-kz/H}=0 \tag{1.61}$$

$$(a\cos\phi)^{-1}\left(\bar{v}\cos\phi\right)_{\phi}+\rho^{-1}\left(\rho_0\overline{w}^{*}\right)=0 \tag{1.62}$$

$$\bar{\theta}_t+a^{-1}\overline{v}^{*}\bar{\theta}_{\phi}+\overline{w}\overline{\theta}_z^{*}-\overline{Q}=-\rho_0^{-1}\left[\rho_0\left(\overline{v'\theta'}\overline{\theta'_{\phi}}/a\bar{\theta}_z+\overline{w'\theta'}\right)\right]_z. \tag{1.63}$$

Equations 1.59 to 1.63 comprise a complete set of equations for the mean state described in terms of the quantities $\left\{\overline{u},\overline{v}^{*},\overline{w}^{*},\overline{\theta}\right\}$. In the above new set of equations the E-P flux appears naturally , and it is given by the Eliassen-Palm vector **F**= $\left(0,F^{(\phi)},F^{(z)}\right)$. Its divergence $(\nabla.F)$ can be given by

$$F=\left\{F_{(\phi)},F_{(z)}\right\}=\left\{-\rho_0\cos\phi\left(\overline{v'u'}\right),f\rho_0\cos\phi\left(\frac{\overline{v'\theta'}}{\overline{\theta'}}\right)\right\} \tag{1.64}$$

and,

$$\nabla.F = \frac{1}{a\cos\phi}\left(F_{\phi}\cos\phi\right)_{\phi} + \left(F_{(z)}\right)_{z}. \tag{1.65}$$

The E-P flux is a useful and dynamically fundamental quantity among various representations of waves, and has been used by many atmospheric scientists in studies of the dynamics of the troposphere and middle atmosphere (e.g. Holton (1975); Andrews et al. (1987); Holton (2004)). It has also proved to be useful in studying the planetary wave propagation in the meridional plane during the SSWs (e.g. Limpasuvan et al. (2005); Charyulu et al. (2007)). The focusing direction of E-P flux vectors, which results from the intense convergence of E-P flux, indicates the forcing of planetary waves on the mean flow. The convergence of the E-P flux decelerates or even reverses (e.g. during the major SSW) the mean zonal wind and the poleward residual mean meridional flow in the stratosphere during the winter period. The reversal of the mean circulation leads to the split of the polar vortex, and hence the split of the ozone hole.

1.3.2 The Role of Planetary Waves in the SSW Formation

As mentioned earlier, the primary cause of the sudden stratospheric warming is thought to be planetary waves originating from the troposphere and propagating upwards to the stratosphere and mesosphere lower-thermosphere (MLT) region (Matsuno, 1971; Holton, 1976; Andrews et al., 1987). These planetary waves are zonally travelling wind perturbations of a global scale resulting from the meridional gradient in the Coriolis parameter. According to the Matsuno model (Matsuno, 1971), sudden stratospheric warmings result when the angular momentum deposition from planetary waves suddenly switches from its climatological location of the mid-latitudes and subtropics to a polar location. These planetary waves have westward phase speeds and thus carry westward angular momentum; the resulting westward forcing leads to a deceleration of the zonal wind and a warming of the pole below the forcing region, which accounts for the sudden warming phenomenon (Shepherd, 2000). An example of balanced instantaneous response to a westward (negative) mechanical forcing with a maximum value of 6 m/s/day centred at 70°N and 45 km altitude, calculated with a quasi-geostrophic zonal-mean model is shown in Figure 1.5. The response shows the deceleration of the polar night jet and the strong warming in the polar upper stratosphere, characteristic of a stratospheric sudden warming.

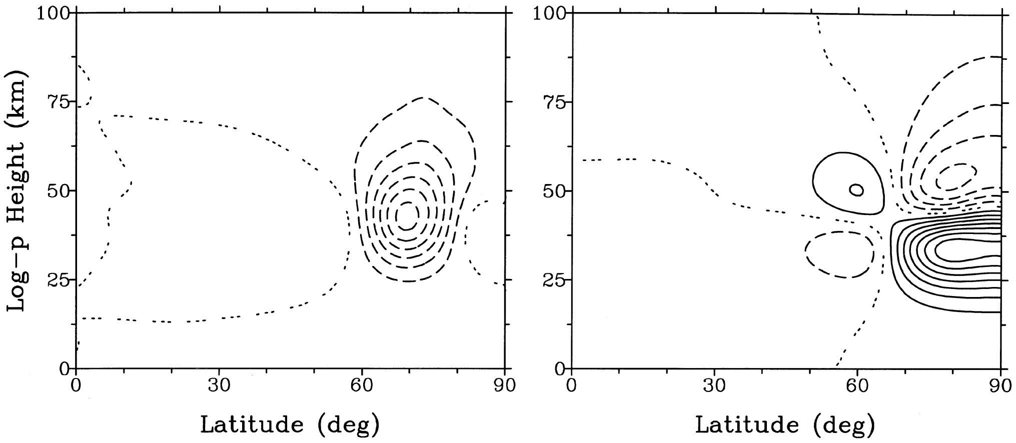

Figure 1.5: On the left is the zonal wind tendency, contour interval 0.5 m.s^{-1}.day^{-1}. On the right is the temperature tendency, contour interval 0.1 K.day^{-1} (from Shepherd (2000)).

The deceleration and reversal of the eastward polar night jet in the high-latitude stratosphere also changes the filtering of internal gravity waves and allows increasing amounts of eastwards propagating gravity waves from the troposphere to penetrate into the mesosphere-lower thermosphere (MLT) and break there, while blocking westward propagating gravity waves (Sathishkumar and Sridharan, 2009). Moreover, this dramatic phenomena induces a downward circulation disturbance in the stratosphere causing adiabatic heating and upward circulation in the mesosphere resulting in adiabatic cooling (Liu and Roble, 2002; Coy et al., 2005; Mbatha et al., 2010b).

Many major and minor SSWs have been observed in the Northern Hemisphere, with a major warming occurring at least once in every two years in the Northern Hemisphere (Hoffmann et al., 2002). A major SSW have never been observed in the Southern Hemisphere since the beginning of the regular monitoring in 1957, until the year 2002. This was always thought to be due to the topography of the Southern Hemisphere, as well as a strong Southern Hemisphere polar vortex. But surprisingly, in late September 2002 a major stratospheric warming occurred, leading to a split of the Antarctica ozone hole (Baldwin et al., 2003; Bencherif et al., 2007).

1.4 Thesis Overview

This thesis uses the SuperDARN HF radar data from SANAE, riometer data, LIDAR data, SABER data, NCEP data, UKMO data, HALOE data, and the CIRA-86 model to study the dynamics and the coupling in the middle atmosphere of the Southern Hemisphere. The thesis focuses mainly on the influence of the late September 2002 major SSW in the middle atmosphere. Planetary waves, gravity waves, mean wind and temperature structure are investigated.

In this thesis, data analysis techniques such as FFT, wavelet and complex demodulation were used to analyse the data. Chapter 2 presents a brief discussion of the theory behind these analysis techniques.

Chapter 3 presents the details regarding the instruments and data sets used in this study, such as observational, assimilated and model data such as SuperDARN HF radars data, LIDAR data, riometer data, SABER data, HALOE data, UKMO data, NCEP data, and the CIRA-86 model are described.

In Chapter 4 the Durban LIDAR temperature monthly distribution, monthly mean and seasonal variation with respect to climatology are discussed extensively, and also compared with observations from satellites and the CIRA-86 model. The seasonal variations from the Durban LIDAR temperature are also compared to Reunion LIDAR observation. Most parts of this chapter are presented in the manuscript by Mbatha et al. (2010a) and Mbatha et al. (2011).

Mean wind and planetary waves as seen by the SuperDARN radars over Antarctica are presented in Chapter 5. The comparison between the mean wind observations from SANAE and Halley SuperDARN radars is also performed in this chapter. The planetary wave coupling between the stratosphere and the MLT is also discussed.

Chapter 6 presents the details of the 2002 major stratospheric warming and its influence in the stratosphere and MLT. Features such as the mean wind, planetary waves activity, E-P flux and temperature structure over the SANAE site, Antarctica, are investigated. Most parts of this chapter have been published by Mbatha et al. (2010b).

Chapter 7 presents the gravity wave activity in the MLT over the Antarctica site during the 2002 major stratospheric warming. The imaging riometer absorption data were used to extract gravity wave parameters such as phase speeds, horizontal wavelength and gravity wave propagation direction during the SSW period. The gravity wave associated potential energy in the Southern Hemisphere during the 2002 SSW event is also presented in this chapter. The results are discussed in relation to the effect of gravity waves in the middle atmosphere wind and temperature.

Chapter 8 presents the summary and conclusions made in this work, including suggestions for future studies.

Chapter 2

Analysis Techniques

In this work, different types of analysis techniques have been used. This chapter presents the theory behind these techniques briefly. The practical applications of these techniques are are also considered, with specific details of such applications mentioned in the relevant sections. A technical computation, MATLAB package was used for the implementation of all the specific procedures used in this thesis, with exception of the wavelet spectral software which was obtained from Torrence and Webster (1999). Specifically, FFT, wavelet analysis, and complex demodulation analysis techniques will be discussed.

2.1 Common Statistical Measures

2.1.1 Mean

In this work both weighted mean and arithmetic mean were used. The arithmetic mean value $\bar{x}$ of a sample of n measured responses $x_i (i = 1, 2, ...n)$ is given by

$$\bar{x} = \sum_{i=n}^{n} \frac{1}{n} x_i \tag{2.1}$$

and for only one measurement made, the arithmetic mean is that measurement. The arithmetic mean can also be given as the weighted mean, a value bias in favour of a more accurately determined data point. The weighted mean is given by

$$\bar{x} = \left(\frac{\sum_{i=1}^{n} w_i x_i}{\sum_{i=1}^{n} w_i} \right), \tag{2.2}$$

where w_i is the weighting factor given by

$$w_i = \frac{1}{(\Delta x_i)^2}. \tag{2.3}$$

The standard deviation of the weighted mean (weighted standard deviation) is given by (Topping, 1972)

$$\Delta x = \sqrt{\frac{\sum_{i=1}^{n} w_i (x_i - \bar{x})^2}{(n-1)\sum_{i=1}^{n} w_i}}. \tag{2.4}$$

2.1.2 Error Propagation

When data variables are experimental measurements they have uncertainties due to measurement limitations such as instrument precision, which propagate to the combination of variables in the function. Thus, it is important to take into account the propagation of the error as computations are made. To perform error propagation, let $m_{1,} m_2 \ldots, m_n$ be the means of variables $i = 1, 2, \ldots, n$ and the corresponding standard errors be $\Delta m_1, \Delta m_2 \ldots m_n$. Then the standard error of any function of $m_1, m_2 \ldots m_n$ i.e., $x = f(m_1, m_{2,} \ldots, m_n)$ can be given by (Topping, 1972)

$$\Delta = \sqrt{\left(\frac{\partial f}{\Delta m_1}\right)^2 (\Delta m_1)^2 + \left(\frac{\partial f}{\Delta m_2}\right)^2 (\Delta m_2)^2 + \ldots + \left(\frac{\partial f}{\Delta m_n}\right)^2 (\Delta m_n)}. \tag{2.5}$$

2.2 Fourier Transforms

The Fourier transform is an operation that transforms one complex-valued function of a real variable into another. In signal processing the domain of the original function is typically time, and is accordingly called the time domain, and the new function is typically called the frequency domain. The frequency domain describes which frequencies are present in the original function. The work by Brook and Wynne (1988) defined the Fourier transform of a signal $x\,(t)$ as

$$X\,(f) = \int_{-\infty}^{\infty} x\,(t)\, e^{-i2\pi f t} dt \tag{2.6}$$

and the inverse Fourier transform as

$$x\,(t) = \frac{1}{2\pi} \int_{-\infty}^{\infty} X\,(f)\, e^{i2\pi f t} d\omega. \tag{2.7}$$

The integral in Equation 2.6 represents the frequency domain of the original signal over the whole duration of the signal without revealing the information regarding the time occurrence of each component. This implies that Fourier transform methods are best suited for stationary time series where the frequency content of the signal does not change with time. However, as most geophysical signals are non-stationary and are typically characterised by transient changes, the above mentioned characteristic of the Fourier transform method limits its use on geophysical data. Analysis of non-stationary signals can be performed by other methods such as wavelet transforms (WT), Short-Time Fourier Transform (STFT) and Complex Demodulation, which will be discussed in the next sections.

2.3 Short-Time Fourier Transform (STFT)

Since the Fourier transform method, as defined above, can only deduce the spectrum of the signal, but cannot give the time of occurrence of the spectral components, it is problematic to use the method on non-stationary signal. However, the Short-Time Fourier Transform (STFT) can be applied in an attempt to localise the frequency in time. The signal is windowed into smaller segments which are assumed to be stationary. The Fourier transform is then applied to the partitioned segments while systematically advancing the window in time along the full length of the signal. The whole procedure can be mathematically represented by (Brook and Wynne, 1988)

$$X(\omega, t) = \int_{-\infty}^{\infty} x(t)\, g(t-k)\, e^{-i\omega t} dt, \tag{2.8}$$

where g is the windowing function which is systematically moved along the length of the signal $x(t)$, and $\omega = 2\pi f$. The result of this above operation is the time frequency representation of the original signal which shows the frequency component present at a given time. The narrower the window the better the time localization of the frequency spectrum, but the poorer the frequency resolution. Therefore, this implies that in a time frequency representation there is a trade-off between time localization and frequency resolution in the sense that good time-frequency resolution of the signal can be achieved by using a narrow window when looking for a high frequency, and vice-versa. Thus, a method resulting in a better time-frequency resolution is needed. In the next section the wavelet transform analysis technique, which has a superior time-frequency resolution, is discussed.

2.4 Wavelet Analysis

2.4.1 Wavelets

Wavelet analysis is becoming a common tool for analysing localised variations of power within a time series. In general the term wavelet is specifically given to a wave-like function $\psi_{ab}(t)$ that is effectively limited in duration and has an average value of zero (Misiti et al., 1996). By decomposing a time series into time–frequency space, one is able to determine both the dominant modes of variability and how those modes vary in time. Wavelets are localised both in frequency and time/space (i.e. their rate of variation is restricted). This is contrary to the Fourier transform method which is only localised in frequency, but not time/space. The wavelet functions $\psi_{ab}\left(t\right)$ are deduced by the translation and dilation or contraction of a particular wavelet prototype $\psi\left(t\right)$, called the mother wavelet or basic wavelet i.e.,

$$\psi_{ab}\left(t\right) = \frac{1}{\sqrt{a}}\psi\left(\frac{t-b}{a}\right), \tag{2.9}$$

where a is the scale and b the position of ψ. The are different types or families of mother wavelets that can be used, which include among others Morlet, Haar, Poul, DOG, Meyer. Each type or family has its own characteristics, properties, advantages and disadvantages. In this work, the Morlet wavelet family have been used because it results in better defined and cleaner waveform than others. Assume that one has a time series, x_n, with equal time spacing δt and $n = 0...N-1$, and also assume that one has a wavelet function, $\psi(\eta)$ that depends on a non-dimensional time parameter η. To be admissible as a wavelet, this function must have zero mean and be localised in both time and frequency space (Farge, 1992). An example is the Morlet wavelet, consisting of a plane wave modulated by Gaussian

$$\psi_0(\eta) = \pi^{-1/4}e^{i\omega_o\eta}e^{-\eta^2/2}, \tag{2.10}$$

where ω_0 is the non-dimensional frequency.

2.4.2 Continuous Wavelet Transform (CWT)

The continuous wavelet transform (Torrence and Compo, 1998) of a signal $x\left(t\right)$ is defined as the sum over time of the signal multiplied by the scaled and shifted wavelets, and is mathematically represented as

$$W\left(a,b\right) = \int_R x\left(t\right)\psi_{a,b}(t) = \int_R x\left(t\right)\frac{1}{\sqrt{a}}\psi\left(\frac{t-b}{a}\right)dt, \tag{2.11}$$

where $\psi\left(\frac{t-b}{a}\right)$ is the wavelet basis function, and the $W\left(a,b\right)$ are wavelet coefficients which depend on the scale and position a and b, respectively. $W\left(a,b\right)$ gives the degree of correction between the wavelet and a portion of the signal $x\left(t\right)$ around position b. The higher the sum of the products of $x\left(t\right)$ and $\psi_{a,b}\left(t\right)$, the higher the wavelet coefficient $W\left(a,b\right)$, and thus, the more closely the scaled wavelet resembles $x\left(t\right)$ around position b. More details about the CWT are discussed by other authors (e.g. Misiti et al. (1996) and Torrence and Compo (1998)). The wavelet power spectrum according to Torrence and Compo (1998) can be mathematically represented by

$$P\left(a,b\right) = \mid W\left(a,b\right)\mid^2 \tag{2.12}$$

and the corresponding phase is given by

$$\phi\left(a,b\right) = \arctan\left[\frac{Im\left(W\left(a,b\right)\right)}{Re\left(W\left(a,b\right)\right)}\right]. \tag{2.13}$$

The wavelet software that was used for spectral analysis in this work was downloaded from the web site: http://paos.colorado.edu/research/wavelets/software.html (Torrence and Compo, 1998).

2.4.3 Time-Frequency Localization

It was mentioned in the subsection above that the wavelet analysis tool has the ability to deduce the spectrum of a signal with good time-frequency resolution. Thus, in this subsection more details of time-frequency resolution will be explained under what is referred to as time-frequency localisation. The above theory of wavelets has showed that the wavelet transforms have good time-frequency resolution due to the fact that it uses a variable 'window' function by performing both the correlating and windowing process. This is unlike the window function used in the STFT technique.

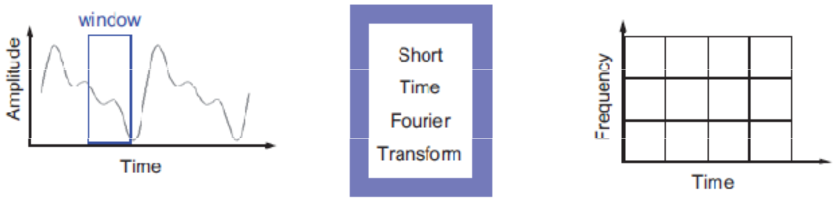

(a)
STFT

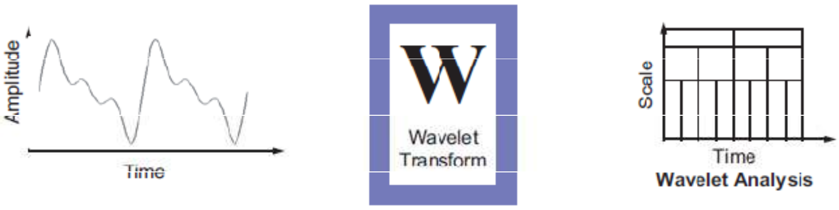

(b)
Wavelet

Figure 2.1: Comparison between STFT (a) and wavelet (b) window function (Misiti et al., 1996).

Figure (2.1) illustrates the different widths of the window functions implemented in the STFT and wavelet analysis. It clearly indicates that the STFT represents a sort of compromise between the time- and frequency-based views of a signal. It provides some information about both when and at what frequencies a signal event occurs, but with limited precision, and that precision is determined by the size of the window (Misiti et al., 1996). On the other hand, wavelet analysis allows the use of long time intervals where more precise low-frequency information in needed, and shorter regions where high-frequency information is needed (Misiti et al., 1996).

2.5 Cross-Spectral Density

In signal processing, some cases require the determination of the relationship or the dominant spectra component in two time series signals. This is achieved by using the cross-spectral density (CSD) technique. Considering two time domain signals $x(t)$ and $y(t)$, and applying the Fourier transform method mentioned above, their Fourier transforms are given by $X(\omega)$ and $Y(\omega)$, respectively. The corresponding CSD can be represented mathematically as

$$CSD = S_{xy}(\omega) = \frac{X_n .^{*} Y_n}{\omega_0}. \tag{2.14}$$

The cross-spectrum is a complex quantity that can be written in the form (Priestley, 1981)

$$S_{xy}(\omega) = c_{xy}(\omega) - iq_{xy}(\omega) = A_{xy}(\omega)\, exp\left[i\phi_{xy}(\omega)\right], \tag{2.15}$$

where $c_{xy}(\omega)$ and $q_{xy}(\omega)$ are co-spectrum and quadrature spectrum, representing the covariance between the coefficients of the in-phase and the quadrature components of the original signals $x(t)$ and $y(t)$, respectively. The cross-amplitude spectrum is given by

$$A_{xy}(\omega) = \sqrt{c_{xy}^2(\omega) + q_{xy}^2(\omega)} \tag{2.16}$$

and it represents the average of the product of the amplitudes of the components in $x(t)$ and $y(t)$ that have frequency ω. The phase spectrum is expressed as

$$\phi_{xy}(\omega) = \arctan\left(\frac{q_{xy}(\omega)}{c_{xy}(\omega)}\right) \tag{2.17}$$

and it represents the average value of the phase-shift $\{\phi_x(\omega) - \phi_y(\omega)\}$ between the components of two signals $x(t)$ and $y(t)$ with frequency ω. To quantify the degree of correction between the two signals at a frequency ω we use the squared coherency which is mathematically represented as (Chatfield, 1989)

$$C(\omega) = \frac{A_{xy}^2(\omega)}{S_{xx}(\omega)\, S_{yy}(\omega)}. \tag{2.18}$$

The coherency is the measure of the square of the linear correlation between the two signals ($x(t)$ and $y(t)$) at a frequency ω. The less the coherency the less the correlation between the two signals at frequency ω, and vice-versa.

2.6 Complex Demodulation

In this work, a method called complex demodulation has been used to extract the amplitude and phase of a periodic signal. The theory in this section is based on the work by Priestley (1981), and also explained by Malinga (2001). A non-stationary process is considered, consisting of a signal and noise in the mathematical form of

$$x\left(t\right)=\sum_{j=1}^{m}A_{j}\left(t\right)\exp\left(i\omega t\right)+z\left(t\right), \tag{2.19}$$

where the complex amplitude $A_j\left(t\right)$ shifts over time indicating the variation of the amplitude and phase of the j^{th} harmonic component with time. The complex demodulation method is a 'local' form of harmonic analysis that assists in the detection of a particular component in a signal and also estimates its change in amplitude and phase (Priestley, 1981). In complex demodulation analysis the component of interest, which has amplitude A_p and frequency ω_p, is shifted to a frequency near zero by multiplying the original signal $x\left(t\right)$ by $\exp\left(-i\omega_d t\right)$, where $\omega_d \simeq \omega_p$ is the demodulation frequency. The demodulated signal is mathematically represented as

$$x_d\left(t\right)=e^{-i\omega_d t}x\left(t\right)=A_p\left(t\right)e^{i\left(\omega_p-\omega_d\right)}+\sum_{j\neq p}^{m}A_j\left(t\right)e^{i\left(\omega_j-\omega_d\right)}+e^{-i\omega_d t}z\left(t\right). \tag{2.20}$$

The signal $x_d\left(t\right)$ is filtered using an appropriately designed filter so as to remove noise and other signal components and only leave the components of interest, which has now been shifted to $\left(\omega_p-\omega_d\right)\sim 0$. The filtering process can be mathematically represented as

$$x_{df}\left(t\right)=\sum_{u=-\infty}^{\infty}g_u x_d\left(t-u\right)=\sum_{u=-\infty}^{\infty}g_u x_d\left(t-u\right)e^{-\omega_d\left(t-u\right)}, \tag{2.21}$$

where $\{g_u\}$ is a real and symmetric filter (i.e., $g_u = g_{-u}$). It must also be noted that even though $z\left(t\right)$ in Equation 2.6 has a continuous spectrum, it can be assumed that it has no component at ω_p because such a component would be indistinguishable from $A\left(t\right)\exp\left(-i\omega_p t\right)$. Thus the second and last term in Equation 2.21 have negligible contributions to $x_{df}\left(t\right)$ and therefore one can only consider the term with ω_p in Equation 2.21 in the form

$$x_p\left(t\right)=A_p\left(t\right)cos\left(\omega_p\left(t\right)+\phi_p\right)=\frac{1}{2}A_p\left(t\right)\left[e^{i\left(\omega_p t+\phi_p\right)}+e^{-i\left(\omega_p t+\phi_p\right)}\right], \tag{2.22}$$

where $A_p\left(t\right)$ changes slowly such that it can be considered to be constant in the effective range of $\{g_u\}$. If Equation 2.22 is substituted into Equation 2.21 and rearranged, the following equation is obtained,

$$x_{df} = \frac{1}{2}A_p(t)\left[H(\omega_d - \omega_p)\, e^{-i[(\omega_d+\omega_p)t-\phi_p]} + H(\omega_d - \omega_p)\, e^{-i[(\omega_d+\omega_p)t+\phi_p]}\right], \tag{2.23}$$

where H is a real and symmetric transfer function given by

$$H(\omega) = \sum_{u=-\infty}^{\infty} g_u e^{-i\omega u}. \tag{2.24}$$

Noting that $\omega_d \sim \omega_p$, and also using a filter designed such that the transfer function $H(\omega) \sim 0$ for $|\ \omega\ | > 2\omega_d$, the second term of Equation 2.23 becomes negligible and therefore,

$$\alpha_t \sim \frac{1}{2}A_p(t)\, H(\omega_d - \omega_p)\cos[(\omega_d - \omega_p)\, t - \phi_p] \tag{2.25}$$

and

$$\beta_t \sim \frac{1}{2}A_p(t)\, H(\omega_d - \omega_p)\sin\left[(\omega_d - \omega_p)\, t - \phi_p\right]. \tag{2.26}$$

From the two equations (Equation 2.25 and 2.26), one can deduce instantaneous Amplitude

$$A_p(t) \sim \frac{2\sqrt{\alpha_t^2 + \beta_t^2}}{H(\omega_d - \omega_p)} \tag{2.27}$$

and instantaneous phase

$$\psi(t) = \arctan\left(\frac{\beta_t}{\alpha_t}\right) \sim (\omega_d - \omega_p)\, t - \phi_p. \tag{2.28}$$

Chapter 3

Instruments and Data Sets

Since the beginning of the investigation of the vertical structure of the Earth's atmosphere in the 18^{th} century, there has been increasing of interest among researchers in atmospheric studies. Thus, many different techniques are currently used to study the atmosphere, e.g. light detections and ranging (LIDARs), radio detection and ranging (radars), satellites, rockets, riometers, balloons and models, each with its own advantages and disadvantages. Ground based remote sensing techniques such as LIDARs and radars have superiority when compared to the other instruments due to their continuous measurements as well as good height and time resolution. However, it is always a better option to study the atmosphere using different types of instruments such as ground based and space based instruments. Thus, the data used in this thesis was obtained from LIDAR, radars, satellite (HALOE and SABER), riometer, NCEP, UKMO, ECMWF, and the CIRA-86 model. The following sections present a brief description of the instruments and data used in this study.

3.1 Observational Data

3.1.1 SuperDARN HF Radars

SuperDARN (Greenwald et al., 1995) is a network of HF radars originally designed to study plasma flow in the high-latitude ionosphere. But, studies such as Hall et al. (1997) which proved that echoes at ranges close to the SuperDARN radars are actually due to scatter from meteor trails near 94 km altitude, except during periods of high k_p (an indication of geomagnetic disturbance), led to the use of this network of HF radars to study neutral wind and waves in the MLT region. Greenwald et al. (1995) reviewed the SuperDARN radars and their operation, thus, in this work only a brief description of the SuperDARN radars is given. The SuperDARN radar network consist of a total of about 17 radars in the Northern Hemisphere and 9 in the Southern Hemisphere (see Figure (3.1)). A list showing all SuperDARN radars and their locations is shown in Table 3.1. The Southern Hemisphere radars marked with a red font are used in this study.

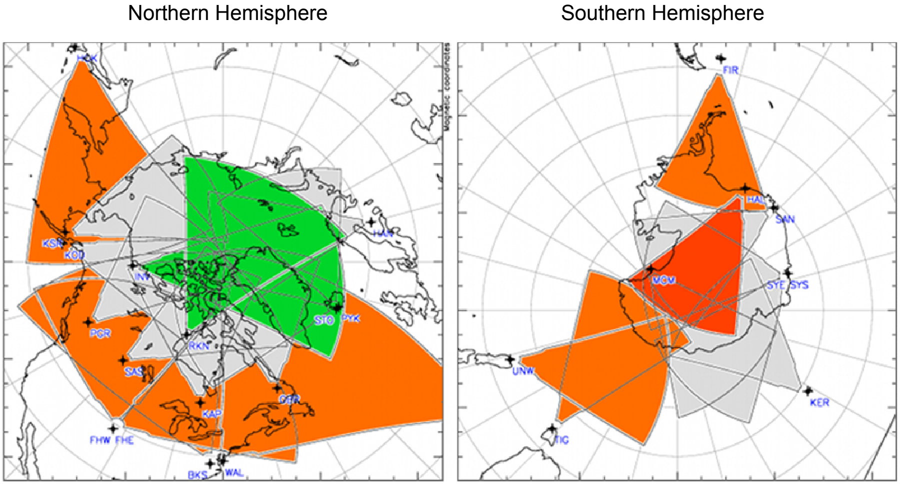

Figure 3.1: Schematic diagram showing SuperDARN radar locations and their field-of-view in the Southern and Northern Hemisphere (http://vt.superdarn.org/).

Table 3.1: List of all SuperDARN radars and their locations.

Northern Hemisphere SuperDARN Radars					**Southern Hemisphere SuperDARN Radars**			
Radar name	**Latitude**	**Longitude**	**Code**		**Radar name**	**Latitude**	**Longitude**	**Code**
Blackstone	37.10	-77.95	bks		**Falkland Island**	-51.83	-58.98	fir
Christmas Valley East	43.27	-120.36	cve		***Halley***	-75.52	-26.63	hal
Christmas Valley West	43.27	-120.36	cvw		**Kerguelen**	-49.22	70.14	ker
Fort Hays East	38.86	-99.39	fhe		**McMurdo**	-77.88	166.73	mcm
Fort Hays West	38.86	-99.39	fhw		***SANAE***	-71.68	-2.85	san
Goose Bay	53.32	-60.46	gbr		**Syowa East**	-69.00	39.58	sye
Hankasalmi	62.32	26.61	han		**Syowa South**	-69.00	39.58	sys
Hokkaido	43.33	143.61	hok		**Tiger**	-43.40	147.20	tig
Kapuskasing	49.39	-82.32	kap		**Unwin**	-46.51	168.38	unw
King Salmon	58.68	-156.65	ksr					
Kodiak	57.62	-152.19	kod					
Pykkvibaer	63.77	-20.54	pyk					
Prince George	53.98	-122.59	pgr					
Rankin Inlet	62.82	-93.11	rkn					
Saskatoon	52.16	-106.53	sas					
Stokkseyri	63.86	-22.02	sto					
Wallops Island	37.93	-75.47	wal					

SuperDARN radars operate at frequencies between 8 and 20 MHz. Each radar site consist of a 16-antenna array connected to a phasing matrix which permits the single beam to be swept through 16 successive positions in increments of 3.25°, covering a sector with a nominal azimuth of 52°. The azimuthal resolution depends on the operating frequency and it ranges from 2.5° at 20 MHz to 6° at 8 MHz. The peak power is about 10 kW and the range resolution is 30-45 km with a typical pulse width of 200-300 µs. Measurements are taken every 7 s at each of the 16 beam positions. Back-scatter information from these pulses are sampled and then processed giving multi-lag auto-correlation functions (ACFs). The ACFs are thereafter used to deduce back-scatter power, mean Doppler velocity and the width of the Doppler power spectrum for each range with significant returns. The pulse sequence is about 40 ms in duration, and pulse sequences are separated by 60 ms, resulting in 60 ACFs in each of the 7 transmitting seconds, which are averaged for each measurement. Measurements can be taken for up to 75 range gates along the beam where each range gate is equal to 45 km. Thus, this means that the measurements can be made from a few kilometres to more than 3000 km in range. For example, Figure (3.2) illustrates the back-scatter power, mean Doppler velocity, and the spectral width for beam number seven for 30 September 2002 as seen by the SANAE SuperDARN radar.

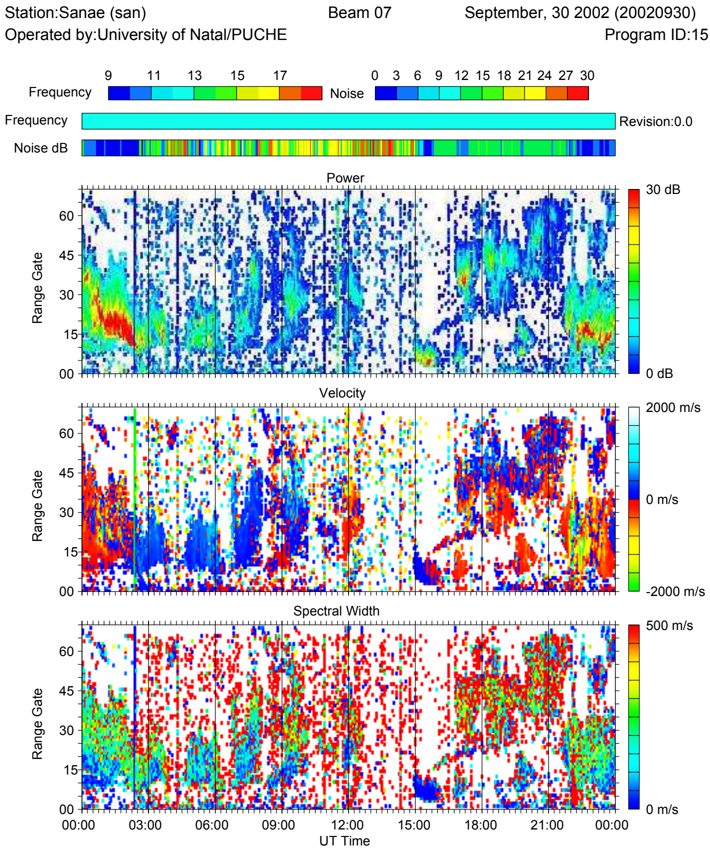

Figure 3.2: Contour plots showing the back-scatter power (top), line of sight Doppler velocity (middle), and the spectral width (bottom) plotted for data from the SANAE SuperDARN radar.

As mentioned above, the SuperDARN radars were primarily designed to study the convection patterns in the high-latitude ionosphere. However, there are several studies which have proved that SuperDARN radars can also be used to study the dynamics of the MLT region. For example, Hussey et al. (2000) performed a comparison of Northern Hemisphere winds using SuperDARN meteor trail and Saskatoon (52.2°N, 106.6°W) MF radar wind measurements. In their results they found good agreement between the two radar systems at an altitude of ~95 km. Bristow et al. (1999) also compared SuperDARN wind results with those of High Resolution Doppler Imager (HRDI) aboard the Upper Atmosphere Research Satellite (UARS) and found that both instruments observed a 2-day wave with wave number-3. Malinga and Ruohoniemi (2007) used the SuperDARN radar network in the Northern Hemisphere to study the characteristics of the quasi-two-day wave (QTDW) at meteor heights. In their work the period of the QTDW were observed to vary in the range of ∼42–56 h, with the most dominant period being ∼48 h and secondary peaks at ∼42- and ∼52-h.

The meteor trail echoes occur predominantly in and below the lower E region (∼95 km). Thus, acquisition of the winds in the meteor region is accomplished by using data from the first several range gates of the radar. The back-scatter at this distance is primarily due to meteors and thus a nominal height of 90-95 km is assumed. Hourly wind averages are computed for each beam direction giving a line of-sight wind velocity (zonal and meridional components). In this work, both the zonal and meridional wind components are used.

3.1.2 Imaging Riometer

The Imaging riometer at SANAE is a 64-element imaging riometer based on the design by Detrick and Rosenberg (1990). The instrument was constructed by the Department of Electronic Services, Potchefstroom University, South Africa, with continuous operation starting on the 10^{th} of April 1997. This design of imaging riometer is an advance on the basic riometer as it utilizes narrow beams antenna arrays to sample the region of interest spatially in contrast to a specially isolated measurement from a single wide beam.

Riometers measure the intensity of the cosmic radio noise received at the surface of the Earth. As radio noise propagates through the atmosphere to the Earth's surface it suffers absorption as the radio waves excite the ionised plasma of the ionosphere, which then loses energy by electron-neutral air collisions. Riometer frequencies are usually between 28 and 40 MHz, and these frequencies result in a maximum absorption peak around an altitude of 90 km in the D-region of the atmosphere (Friedrich and Torkar, 1983). If absorption occurs in the atmosphere the intensity of the cosmic radio noise received at the surface of the Earth decreases and hence the absorption can be determined. However, if no absorption occurs, the intensity of the cosmic radio signal received at the surface of the Earth is cyclic, with the period of a sidereal day; this signal is known as a quiet day curve.

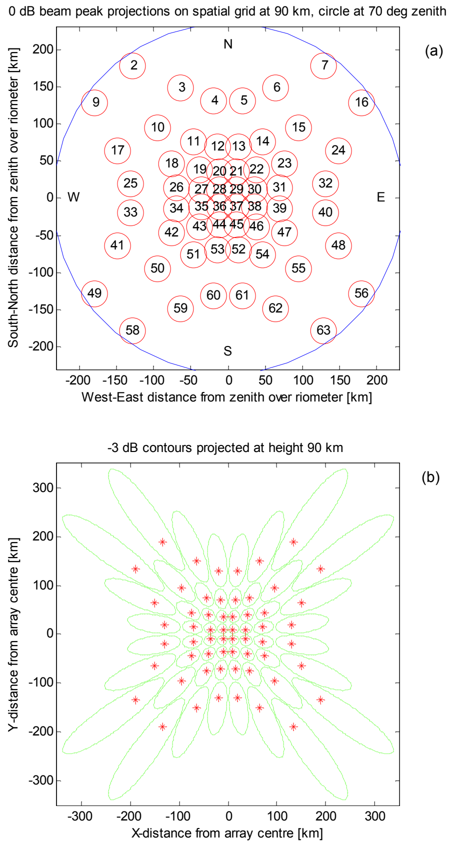

Figure 3.3: Riometer beam projections.

As mentioned above, riometers are primarily used to measure the enhancement of the D-region ionosphere by energetic charged particle precipitation driven by magnetospheric electrodynamics (Stauning, 1984). The imaging riometer for ionospheric studies (IRIS) at SANAE has the 8x8 antenna arrays consists of 64 half-wavelength crossed-dipole (turnstile) antennas mounted one quarter of wavelength above an artificial ground plane (Wilson and Stoker, 2002). Similar to the imaging riometer at Halley, the riometer at SANAE operates on 38.2 MHz and samples a region of over 200 km x 200 km at 90 km altitude with its 49 beams every 1 second (Detrick and Rosenberg, 1990). The details of the imaging riometer at SANAE are well explained by Wilson (2000). The projection of the riometer beams at 90 km altitude as defined by 0 dB beam peak projections as well as 3 dB beam projections are shown in Figure (3.3). The directions of the maxima of the directivities for the north-west quadrant were calculated (Wilson, 2000) and the respective zenith and azimuth angles are shown in Table 3.2. The azimuth angle is taken westwards from the north-south line.

Table 3.2: Directions for the 16 beams in the north-west quadrant.

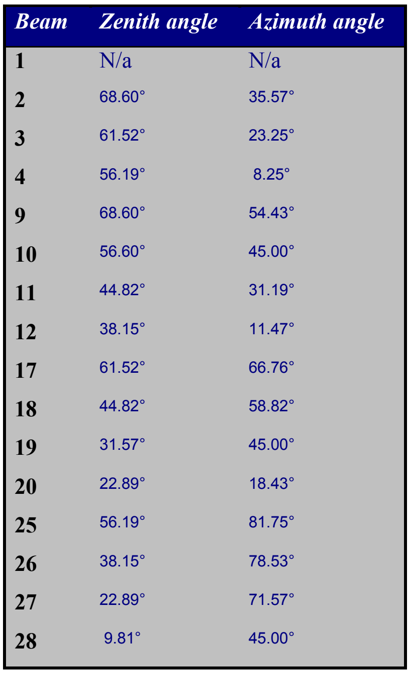

Beam	Zenith angle	Azimuth angle
1	N/a	N/a
2	68.60°	35.57°
3	61.52°	23.25°
4	56.19°	8.25°
9	68.60°	54.43°
10	56.60°	45.00°
11	44.82°	31.19°
12	38.15°	11.47°
17	61.52°	66.76°
18	44.82°	58.82°
19	31.57°	45.00°
20	22.89°	18.43°
25	56.19°	81.75°
26	38.15°	78.53°
27	22.89°	71.57°
28	9.81°	45.00°

The overall operation of the riometer is controlled by a dedicated computer, located at the SANAE base. The voltage signals received from the eight riometers, every 1/8 of a second, are converted to frequency signals. The conversion is done on a scale of 1 V/10 kHz. These pulses are conveyed with eight coaxial cables to the processing laboratory inside the base, located 500 meters away. A GPS is used for accurate timing. The output signals of all 64 beams are sampled at 1 Hz, and written to a file every hour. A file containing one minute values is also created by calculating the mean of every 60 seconds of data sampled. The digital data is then stored on an optical CD.

Since noise is always present on the riometer output, several filter options are available in software to remove or minimise the noise. The details on the available filters are also well explained by Wilson (2000). The noise on the riometer signals originate from several sources. Apart from the internal white noise from the electronics, the major contributor to noise at SANAE is wind. During winter months, the everlasting wind charges the dipoles statically, contributing to most of the noise visible on the signals. Other noise contributors may be side bands transmitted from the other instrumentation at SANAE, or distant radio signals reflected by the ionosphere overlapping the 38.2 MHz band.

3.1.3 LIDAR Instrument

The Light Detection and Ranging (LIDAR) data used in this study was collected over Durban (29.9°S, 31.0°E) and Reunion (20.8°S, 55.5°E). The two Rayleigh LIDAR systems are identical, thus the following brief discussion refers to both of them. The atmospheric

LIDAR/laser radar instrument employs a laser as the source of pulse energy with useful magnitude and suitable short duration. The laser beam is transmitted vertically into the sky and interacts with air molecules and aerosols in the lower and middle atmosphere. The back-scattered photons are collected by parabolic mirrors and transmitted to the photomultiplier tube detector. The data acquisition is carried out in the photon counting mode. The returning signal is integrated to generate a count versus altitude profile. Figure (3.4) illustrates a general schematic diagram of the LIDAR system.

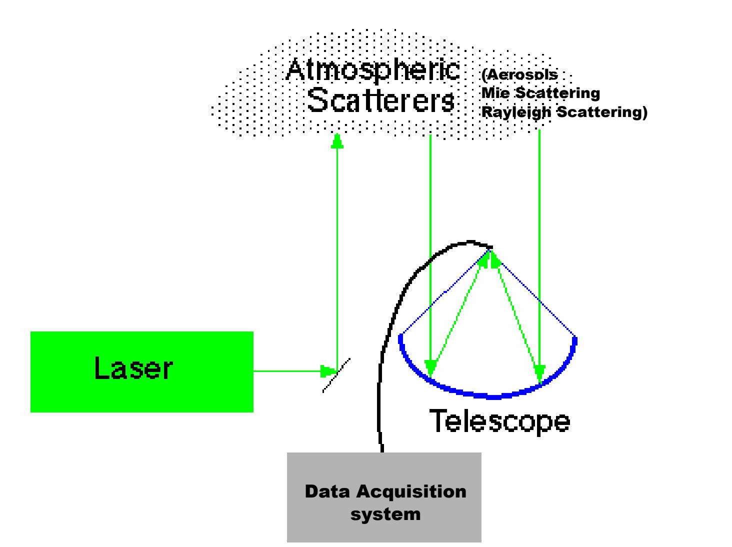

Figure 3.4: General block diagram of a LIDAR system

Despite having similar operating principles to radar, LIDAR uses much shorter wavelengths in the electromagnetic spectrum, typically in the ultraviolet, visible, or near infrared region. LIDARs are capable of producing 2-dimensional coverage, 3-dimensional coverage and 3-dimensional spectrum variation with a function of time. With their shorter pulses, they provide continuous measurements and the possibility to measure temporal variation of the altitude-resolved atmospheric variables studied by the scientific community. The above mentioned instruments are highly sensitive to aerosol and cloud particles. Laser beam densities and its high coherency give a LIDAR more accurate measurements. The shorter wavelengths of the laser are reflected very well by small objects. Different types of scattering are associated with LIDAR and its applications, e.g. Rayleigh scattering, Mie scattering and Raman scattering, as well as fluorescence. The operational wavelengths are different for different types of measurements (i.e. clouds, air molecules, and aerosols). Rayleigh scattering is associated with the scattering of laser light by air molecules, while scattering from aerosols, clouds, smog, and dust particles depends weakly on wavelength and is described by Mie scattering theory. Both Rayleigh and Mie scattering are examples of elastic scattering processes, where the scattered radiation is at the same wavelength as that of the transmitted one. For the purpose of measuring water vapor up to 10 km and nitrogen up to 30 km the Raman LIDARs are used. Raman LIDAR employ the Raman (in-elastic) scattering process. Since Raman scattered signals are free from contribution by aerosols, the method also allows measurements of temperature below 30 km (Keckhut et al., 1990).

3.1.3.1 LIDAR Equation

The LIDAR equation represents the power of the light received by the detector of the instrument. The received signal intensity is described in terms of the LIDAR equations as given by (Fiocco, 1984)

$$P(r) = P_0\eta\left(\frac{A}{r^2}\right)\left(\frac{c\tau}{2}\right)\beta(r)exp[-2\int\alpha(r)dr], \tag{3.1}$$

where $P(r)$ is the instantaneous power received at time t from an altitude r, P_0 is the transmitted power, η is the system constant which depends on the transmitter and receiver efficiencies. A is the area of primary mirror of the receiving telescope. The term $\left(\frac{A}{r^2}\right)$is the solid angle subtended by the primary mirror at the range r. The term $\left(\frac{c\tau}{2}\right)$ gives the length of illuminated path, which contributes to the received power, where c is the speed of light, and τ is the pulse duration of the laser beam. Given a scatter number density N_j of kind j at range r and the differential back-scatter cross section of particles $d\sigma_{j,sca}\left(\pi,\lambda\right)/d\Omega$, $\beta(r,\lambda)$ (the volume back-scatter coefficient) of the atmosphere at range r is given by

$$\beta\left(r,\lambda\right) = \sum_j N_j\left(r\right)\frac{d\sigma_{j,sca}\left(\pi,\lambda\right)}{d\Omega}. \tag{3.2}$$

As the laser light propagates through the atmosphere it is scattered by both particles (index "*aer*") and molecules (index "*mol*"), thus

$$\beta\left(r,\lambda\right) = \beta_{mol}\left(r,\lambda\right) + \beta_{aer}\left(r,\lambda\right). \tag{3.3}$$

The volume attenuation coefficient of the atmosphere $\alpha\left(r,\lambda\right)$ is given by

$$\alpha\left(r,\lambda\right) = \sum_j N_j\sigma_{j,ext}, \tag{3.4}$$

where $\sigma_{j,ext}$ is the extinction cross section. The extinction is obtained due to absorption (index "*abs*") and scattering (index "*sca*") of laser light by particles and molecule, and is given by

$$\alpha(r,\lambda) = \alpha_{mol,sca}(r,\lambda) + \alpha_{mol,abs}(r,\lambda) + \alpha_{aer,sca}(r,\lambda) + \alpha_{aer,abs}(r,\lambda)\,. \tag{3.5}$$

The temperature profile is derived from relative density profile using the hydrostatic equations and ideal gas law by taking an upper level pressure value from the model (Hauchecorne and Chanin, 1980).

3.1.3.2 The Durban LIDAR

The Durban LIDAR is a Rayleigh-Mie system capable of measuring vertical profiles of relative density, temperature and aerosol scatter . The laser is a pulsed Nd:YAG with a repetition rate of 30 Hz and a fundamental wavelength of 1064 nm. The emitting light source is a frequency-double (using potassium dihydrogen phosphate, (KDP) crystal) laser at 532 nm, with a power of ∼500 mJ/s. The system started operating in April 1999 with a Spectra Physics Nd:YAG laser at a repetition rate of 10 Hz delivering an average power of 3 W (Bencherif et al., 2000). In early 2002, the 10 Hz laser was replaced with a more powerful Nd:YAG operating at a frequency of 30 Hz and delivering at least 5 times more power. The instrument uses a dichroic mirror at the emission point of the laser to separate the second harmonic from the fundamental laser beam.

3.1.4 TIMED/SABER data

In this study, the vertical temperature profiles are derived from the Sounding of the Atmosphere using Broadband Emission (SABER) level 2A data version 1.07 (downloaded from the web site http:/saber.gats-inc.com), which is one the four instruments on board Thermosphere–Ionosphere–Mesosphere-Energetics and Dynamics (TIMED) satellite. The primary goal of SABER has been to obtain profile measurements of parameters and species related to the thermal structure and energetics of the upper mesosphere and lower thermosphere (UMLT) region of the atmosphere (Remsberg et al., 2008). The TIMED satellite was launched on 7 December 2001 and it flies in a nadir-pointing orientation from its 625 km circular orbit at a 74.1 inclination angle and has a period of about 102 min. The SABER instrument began measurements during late January 2002. By step-scanning the atmosphere limb, SABER measures height profiles of kinetic temperature and selected chemical species in the 10-180 km altitude range with a vertical resolution of ∼2 km. The kinetic temperature profiles are derived from broadband measurements of CO_2 15 μm limb emission. This emission separates from local thermodynamic equilibrium (LTE) conditions in the rarefied mesosphere and thermosphere, making it necessary to consider the CO_2 vibrational state non-LTE populations in the retrieval algorithm above 70 km. The accuracies of the measurements are 1.5 K for 15– 80 km and 4 K for 80–100 km, while the precisions are 0.5, 1 and 2 K for 15–70 km, 70–80 km and 80–100 km, respectively.

More details regarding errors in SABER kinetic temperature caused by non-LTE model parameters are well explained by García-Comas et al. (2008).

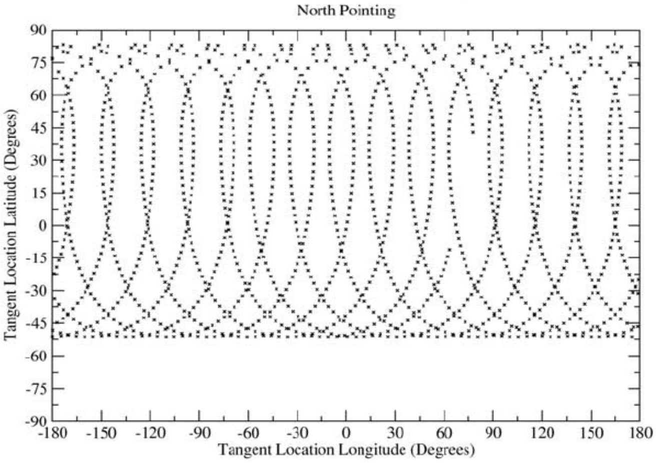

Figure 3.5: Latitude-versus-longitude tangent point locations for one day of observations from SABER in its north looking viewing mode (83° N to 52° S).

SABER obtains profiles from 52°S to 83°N during its north-looking mode for about 60 days, switches to an analogous south-looking mode, and then repeats that sequence for subsequent months (see Figure (3.5)). Nearly continuous coverage is achieved equatorward of the 52° latitude in each hemisphere. Vertical scans are measured every 52 s, giving a profile spacing along the orbit of 3° of latitude for 15 orbits per day. Its north viewing mode extends for 60 to 63 days. The spacecraft is turned to its south viewing mode for another 60+ days, and then the entire viewing sequence is repeated. The details of the SABER instrument are well explained by Remsberg et al. (2003).

3.1.5 HALOE/UARS Satellite Data

The Halogen Occultation Experiment (HALOE) instrument is on board the Upper Atmosphere Research Satellite (UARS) launched on 12 September 1991. The instrument uses a solar occultation measurement technique, providing 15 sunrise and 15 sunset vertical measurement profiles of Ozone (O_3), Hydrogen Chloride (HCl), Hydrogen Fluoride (HF), Methane (CH_4) water vapor (H_2O) Nitric Oxide (NO), Nitrogen Dioxide (NO_2), Temperature and Aerosol Extinction at 4 infrared wavelengths per day with each daily sunrise or sunset group near the same latitude on a given day. The instrument uses the atmospheric transmission measurements in the 2.8 μm CO_2 band for the retrieval of temperature profiles. The retrieval of temperature profiles involves removal of aerosol contamination, assuming that at the height above 30 km the aerosol concentration is negligible. It provides temperature in the altitude range ∼45-85 km (Hervig et al., 1996; Remsberg et al., 2002). A detailed discussion related to the validation of HALOE data can be found in a number of papers (e.g.Russell III et al. (1993); Singh et al. (1996); Hervig et al. (1996); Remsberg et al. (2002)).

3.2 Assimilated Data and Models

3.2.1 UK Met Office Data

The United Kingdom Meteorological Office (UKMO) assimilation system (Swinbank and O'Neill, 1994) is an outcome of assimilation of in-situ and remotely sensed data into a numerical forecast model of the stratosphere and troposphere. The outputs of the assimilation are global fields of daily temperature, geopotential height, and wind components (meridional and zonal) at pressure levels from the surface up to 0.1-hPa. The assimilation system uses a global 42-level configuration of the Unified Mode, with a horizontal resolution of 2.5° and 3.75° steps in latitude and longitude, respectively, and have been run daily since October 1991 to produce near real-time global stratospheric analyses at 12 UTC every day. The analyses are output on the UARS standard levels from 1000-hPa to 0.316-hPa. The description of the original data assimilation system can be found in the work published by Swinbank and O'Neill (1994); the updated version which uses a three-dimensional variational data assimilation system is found in the work by Lorenc et al. (2000) and also Swinbank and Ortland (2003).

3.2.2 NCEP/NCAR Re-analysis Data

Temperature and wind fields used in this work are obtained from the National Centre for Environmental Prediction and National Centre for Atmospheric Research (NCEP/NCAR) reanalysis project available on the National Oceanic and Atmospheric Administration (NOAA) Climate Diagnostics Centre web page (http:/www.cdc.noaa.gov/). This cooperational project between NCEP an NCAR provides daily meteorological values on 2.5° latitude by 2.5° longitude resolution for 17 pressure levels (such as 1000, 925, 850, 700, 600, 500, 400, 300, 250, 200, 150, 100, 70, 50, 30, 20, and 10-hPa). The NCEP/NCAR re-analysis data is formed by the combination of the assimilated data from different meteorological instruments which are scattered globally. The collection of data for reanalysis includes different observations at various countries over the land surface, ocean surface, upper-air such as Global radiosonde data, Comprehensive Ocean Atmosphere Data Set (COADS) marine surface data, Aircraft data, Surface landscape synoptic data, and satellite sounder. The project began in 1991 as a spin off from the NCEP Climate Data Assimilation System (CDAS) project. The details of the NCEP/NCAR reanalyses execution method, data analysis, data assimilation and comprehensive output variables are well explained in work published by Kalnay et al. (1996).

3.2.3 ECMWF ERA-40 Re-analysis Data

In this thesis the European Centre for Medium-Range Weather Forecast Re-Analysis for 40 years (ECMWF ERA-40) horizontal wind fields extracted on a 1.125° by 1.125° grid from 1000 to 1-hPa pressure levels have been used to study the prevailing meteorological and dynamical conditions during the Southern Hemisphere major SSW by deriving the Eliassen-Palm (E-P) flux. The ECMWF ERA-40 data and its documentation can be downloaded from the ECMWF website, http://www.ecmwf.int/research/era/.

The ECMWF ERA-40 is a re-analysis of the meteorological field variables starting from September 1957 to August 2002 by the ECMWF in collaboration with a number of other institutes. The ERA-40 is an improved version of ERA-15, with one of the most important improvements being that the ERA-40 directly assimilates the Television Infrared Observation Satellites (TIROS) Operational Vertical Sounder (TOVS) and Advanced TOVS radiances, as opposed to retrieved temperature and wind profiles. The data is available at 23 standard pressure levels spanning from 1000 to 1-hPa, and as well as at each of the 60 levels of the assimilation model.

3.2.4 CIRA-86 Model

The COSPAR International Reference Atmosphere (CIRA-86) climatological model is a compilation of experimental and theoretical data. The CIRA-86 reference climatologies extend from 0 to 120 km. The model is based mainly on the nadir (SCR) experiment on board the NIMBUS-6 satellite from 1975 to 1978 . The detail of the CIRA-86 zonal mean temperature, geopotential height, and zonal wind has been described in a study published by Barnett and Corney (1985) and Fleming et al. (1990).

Chapter 4

LIDAR Observations

4.1 Introduction

Temperature monitoring in the atmosphere is important as it controls the rate of chemical reactions and thus ozone abundance. The middle atmospheric temperature is an important parameter because it is a combined manifestation of the dynamical, radiative, and chemical processes occurring in the middle atmosphere (Singh et al., 1996). The study of the middle atmospheric thermal structure is also important for understanding the coupling between different regions of the atmosphere. The temperature structure in the middle atmosphere has been studied for several decades using a variety of techniques. The first studies used rocketsondes and falling spheres to measure temperature profiles up to 60-90 km, but with relatively poor accuracy due to uncertain radiative and aerodynamic heating corrections (Schmidlin, 1981). However, the first experimental (Kent and Wright, 1970) and systematic (Hauchecorne and Chanin, 1980) temperature profiles derived from Rayleigh LIDAR measurements of the relative density of the middle atmosphere provided improved accuracy and vertical resolution.

Although many instruments are used to study the middle atmospheric temperature (e.g. rockets, satellite, radiometers), LIDARs are found to be more accurate and efficient compared to the other instruments. They also provide long-term data series relatively devoid of instrumental drift. Integration of the measurements over several hours filters away most of the gravity wave-like short scale disturbances. Thus, the Rayleigh LIDAR has emerged as the most important ground based technique to study the structure and dynamics of the middle atmosphere (Hauchecorne and Chanin, 1983; Chanin, 1991; Leblanc et al., 1998; Whiteway and Carswell, 1994; Sivakumar et al., 2003).

The climatology of the middle atmospheric temperature has been studied over the past decades using LIDARs and other instruments [Wang et al. (1992); Namboothiri et al. (1999a); Labitzke and Naujokat (2000); Sivakumar et al. (2003); Chang et al. (2005); Argall and Sica (2007); and references therein]. Hauchecorne et al. (1991) used the Rayleigh

LIDAR from two stations in France (OHP, 44°N, 6°E; BIS, 44°N, 1°W) for the first time to study the climatology of the mid-latitude middle atmosphere temperature. Sivakumar et al. (2003) studied the thermal structure of the middle atmosphere over Gadanki (13.5°N 79.2°E), India, using Rayleigh LIDAR data and also compared the LIDAR results with Halogen Occultation Experiments (HALOE) on board the Upper Atmosphere Research Satellite (UARS), the CIRA-86 model and the Mass Spectrometer Incoherent Scatter Extended-1990 (MSISE-90) model. More recently, Li et al. (2008) applied the linear regression analyses to a 13.5-year long (January 1994 to June 2007) de-seasonalized monthly mean temperature time series for each 1 km altitude bin between 15 and 85 km, measured by the Jet Propulsion Laboratory Rayleigh-Raman LIDAR at Mauna Loa Observatory, Hawaii (19.5°N, 155.6°W). Their regression analysis included components representing the Quasi-Biennial Oscillation (QBO), the El Niño-Southern Oscillation (ENSO) and the 11-year solar cycle. The analyses revealed the dominance of the QBO (1-3 K) in the stratosphere and mesosphere, and a strong winter signature of ENSO in the troposphere and lowermost stratosphere ($\sim$1.5 K/MEI).

Comparisons between LIDAR temperature observations and observations made using other well established methods/techniques provide a very good opportunity to understand the middle atmosphere thermal structure better. Satellite measurements offer the best method for providing the temperature structure over the globe with satisfactory temporal coverage. However, their height resolution is poor compared to most ground-based instruments. Thus, comparing and quantifying the differences between space-based and ground-based instruments can compensate for the limitations. There have been a number of studies which report on comparisons between Rayleigh LIDAR observations and other instruments (Clancy et al., 1994; Sivakumar et al., 2003; Xu et al., 2006; Argall and Sica, 2007; Dou et al., 2009). Namboothiri et al. (1999a) compared LIDAR measured temperature profiles with rockets, satellite measured profiles and the COSPAR International Reference Atmosphere 1986 (CIRA-86) model. They found that the LIDAR profiles are in fair agreement with the rockets, satellite measurements and the CIRA-86 model. Recently, Dou et al. (2009) studied the seasonal oscillations of the middle atmosphere temperature observed using Rayleigh LIDARs at six different locations from low to high latitudes within the Network for the Detection of Atmosphere Comparison Change (NDACC). They performed comparisons with the results derived from the Sounding of the Atmosphere using Broadband Emission Radiometry (SABER) on board the Thermosphere–Ionosphere–Mesosphere-Energetics and Dynamics (TIMED) satellite observations, and found good agreement at similar latitudes.

The most recent studies which employed the Durban LIDAR temperature data include a study by Moorgawa et al. (2007) which describes the Durban LIDAR system for temperature measurements, and also reported a good agreement between the LIDAR and South African Weather Service (SAWS) radiosonde temperature for the lower stratosphere, ($\sim$20-27 km). Bencherif et al. (2007) used data from the Durban Rayleigh-Mie LIDAR, MeteoSat, SAGE-2 experiments, and ECMWF meteorological analysis to study the lower stratospheric aerosols over South Africa and their link to large scale transport across the southern subtropical barrier. Also, Bencherif et al. (2000) performed the first validation of the stratospheric temperature profiles obtained by the Durban Rayleigh LIDAR.

In this, the Rayleigh LIDAR measurements made over Durban (29.9°S, 31.0°E) were used to study the stratosphere-mesospheric thermal structure over Durban. LIDAR monthly temperature mean profiles are also compared with SABER observations, temperature data from HALOE, and the CIRA-86 model. Seasonal variations of temperature climatology of the Durban LIDAR are obtained and compared with a similar Rayleigh LIDAR system situated in Reunion (20.8°S, 55.5°E). The results obtained in this work are also discussed and compared with results available in the literature. Most part of this chapter content has been published in a study by Mbatha et al. (2010a) and Mbatha et al. (2011).

4.2 LIDAR Data

The Durban Rayleigh LIDAR data used in this study was collected over 277 nights during the period from April 1999 to July 2004. The vertical resolution of this data is 150 m. The histogram in Figure (4.1)(a) represents the year-to-year monthly distribution of the Durban LIDAR data. Due to occasions when the observing conditions are not favourable (i.e. convective and cloudy conditions over the Durban), the observations are necessarily restricted to shorter periods or even no observations at all. These periods are noticeable during the rainy summer months of January, February and December where there will be little or no observations during the entire month (see Figure (4.1)(a)). The histogram in Figure (4.1)(b) illustrates the monthly distribution of the Durban LIDAR (Dur) data plotted along Reunion LIDAR (Reu) data, HALOE data, and SABER data irrespective of the year. For the purpose of comparing the Reunion Rayleigh LIDAR observations with the Durban LIDAR, data which has been measured from 1999 to 2007 (277 night profiles) was used.

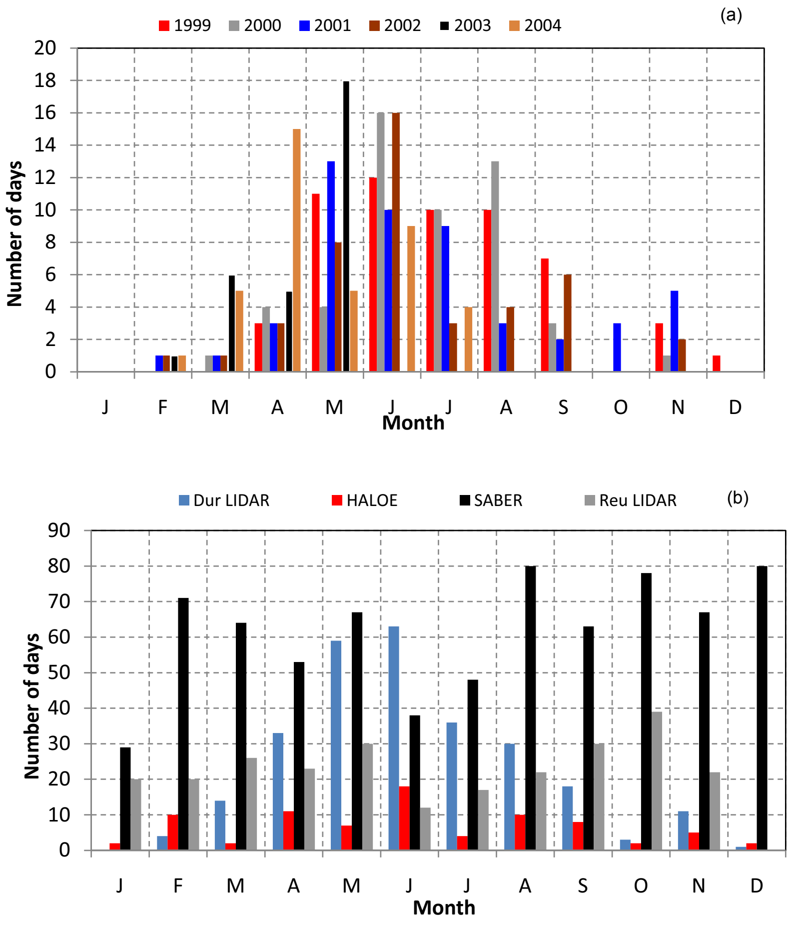

Figure 4.1: The top panel (a) is the year-to-year monthly distribution of the Durban LIDAR data. The bottom panel (b) is the monthly distribution of Durban LIDAR (Dur), Reunion LIDAR (Reu), HALOE data, and SABER data. The LIDAR (Durban and Reunion) and HALOE data is for the period from 1999 to 2004, while the SABER data is for the period from 2002 to 2005.

The measurements from all the instruments, except the SABER instrument, are for the period from 1999 to 2004. The SABER instrument aboard the TIMED satellite started taking measurements in early 2002, thus only data from 2002 to 2005 were used. Both the HALOE and SABER temperature profiles are the closest day and night overpasses of the UARS and TIMED satellite, respectively, over Durban (29.9° S, 31.0° E, South Africa), within ±5° in latitude and ±10° in longitude.

4.3 Climatological Comparison

4.3.1 Year-to-Year Monthly Mean Temperature

Figure (4.2) show the contour plots of the Durban LIDAR monthly mean temperature versus height for each year from 1999 to 2004. Blank spaces indicate the instances where there was no data available. The data gaps are prominent during the summer season, as summer is a rainy season in the Durban region. During all the years, high temperatures are recorded at a height region between ~40 km and 55 km due to the absorption of the ultraviolet radiation from the sun by ozone. It is noticeable that during the summer seasons there are more data gaps due to weather conditions which are not favourable for LIDAR measurements. Other data gaps are due to problems such as the malfunctioning of the system. In some months it is observed that the LIDAR instruments took measurements only in the stratosphere and could not measure up to the lower mesosphere, due to the fact that most of the Durban LIDAR profiles were taken using the 10 Hz-laser transmitter, which does not have a good stratosphere-lower mesosphere range. Even though there are many visible data gaps, the general characteristics of the middle atmosphere appear to be the same for all the years, with the stratopause characterised by peaks at the equinoxes or summer. The data gaps also make it difficult to confidently identify any signatures of annual and semiannual variations in the middle atmosphere.

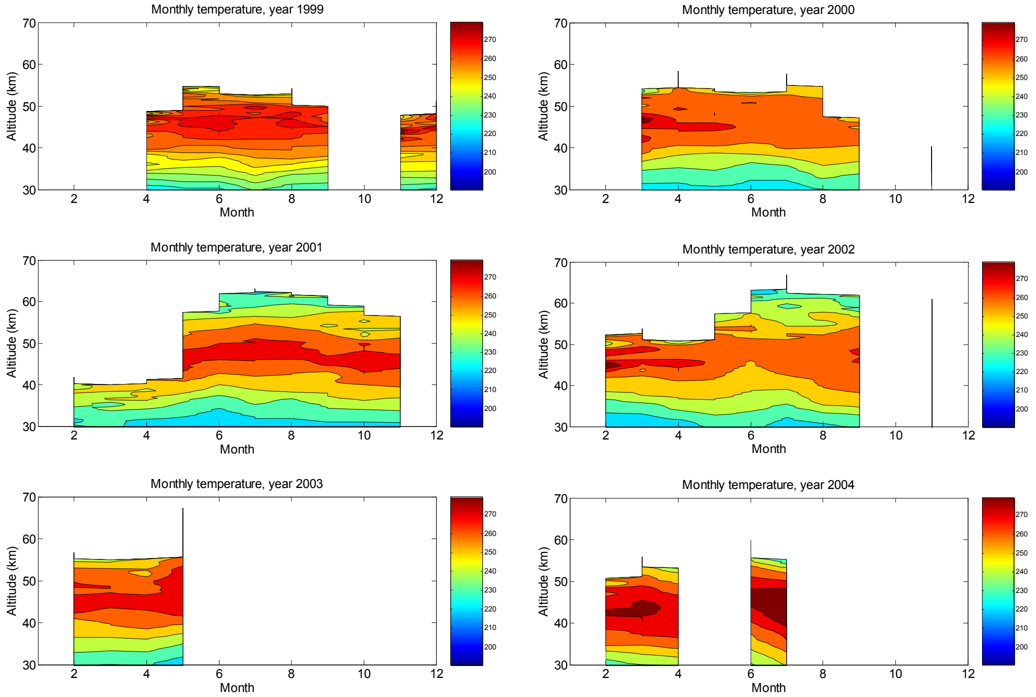

Figure 4.2: Durban LIDAR temperature variation as a function of month and height for each year from 1999 to 2004. The blank areas are due to missing data.

Comparisons of the Durban LIDAR temperature profile with the closest overpass measured by the SABER satellite temperature profile was also performed in this study. Figure (4.3) illustrates the SABER temperature profile (dotted line) and the Durban LIDAR temperature profile for the night of 27-28 November 2002. The LIDAR profile shows the fluctuations in temperature due to vertical propagating planetary and gravity waves. However, the figure indicates a good agreement between the LIDAR and the SABER. In the region between 46 km and 53 km the SABER temperature profile seem to be about 5-7 K warmer than the LIDAR profile. Conversely, in the region between 34 km and 45 km the SABER temperature seem to be about 4 K colder than the LIDAR temperature.

The observed differences in the middle atmosphere over Durban are understandable due to the two different techniques used by the instruments and actual observation time, and also due to some middle atmospheric dynamics which can be identified by the LIDAR, but not the satellite.

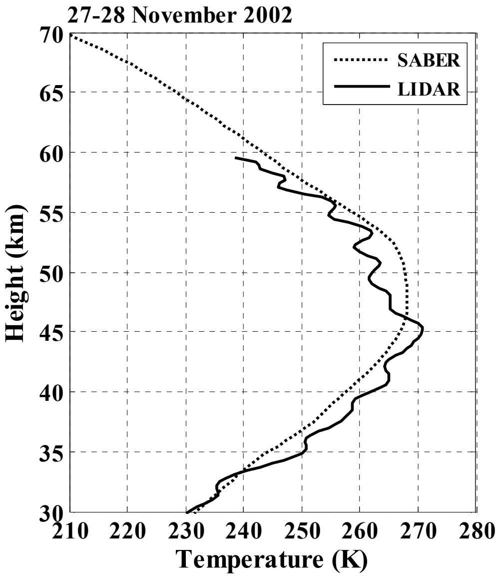

Figure 4.3: A Quasi-simultaneous height profile of the temperature observed by Durban LIDAR and SABER satellite for the night of 27-28 November 2002 over Durban, South Africa.

4.3.2 Overall Monthly Temperature Variations

The contour maps of monthly mean temperature distributions obtained from the Durban LIDAR, SABER (3041 day and night profiles), and HALOE (81 day and night profiles) data plotted in a grid of month versus altitude are shown in Figure (4.4). In all three contour plots high temperatures at a height region between ∼40 km and 55 km can be clearly seen due to the absorption of the ultraviolet radiation from the sun by ozone. The LIDAR, SABER, and HALOE temperatures do not show a significant change with month below about 40 km altitude in the monthly mean distributions. This observation is similar to the findings by Chandra et al. (2005) on their middle atmospheric temperature study over Mt. Abu (24.5°N, 72.7°E), India. However, it should be mentioned that in their study, no measurements were made during July and August due to the monsoon season. The thermal structure observed by the LIDAR over Durban at the stratopause (∼42-50 km) shows two distinct maxima, with one during the period from February to July and the other during the period from September to December. This maximum temperature is about 270 K. The minimum temperature (about 260 K) is observed during August to September in the stratopause.

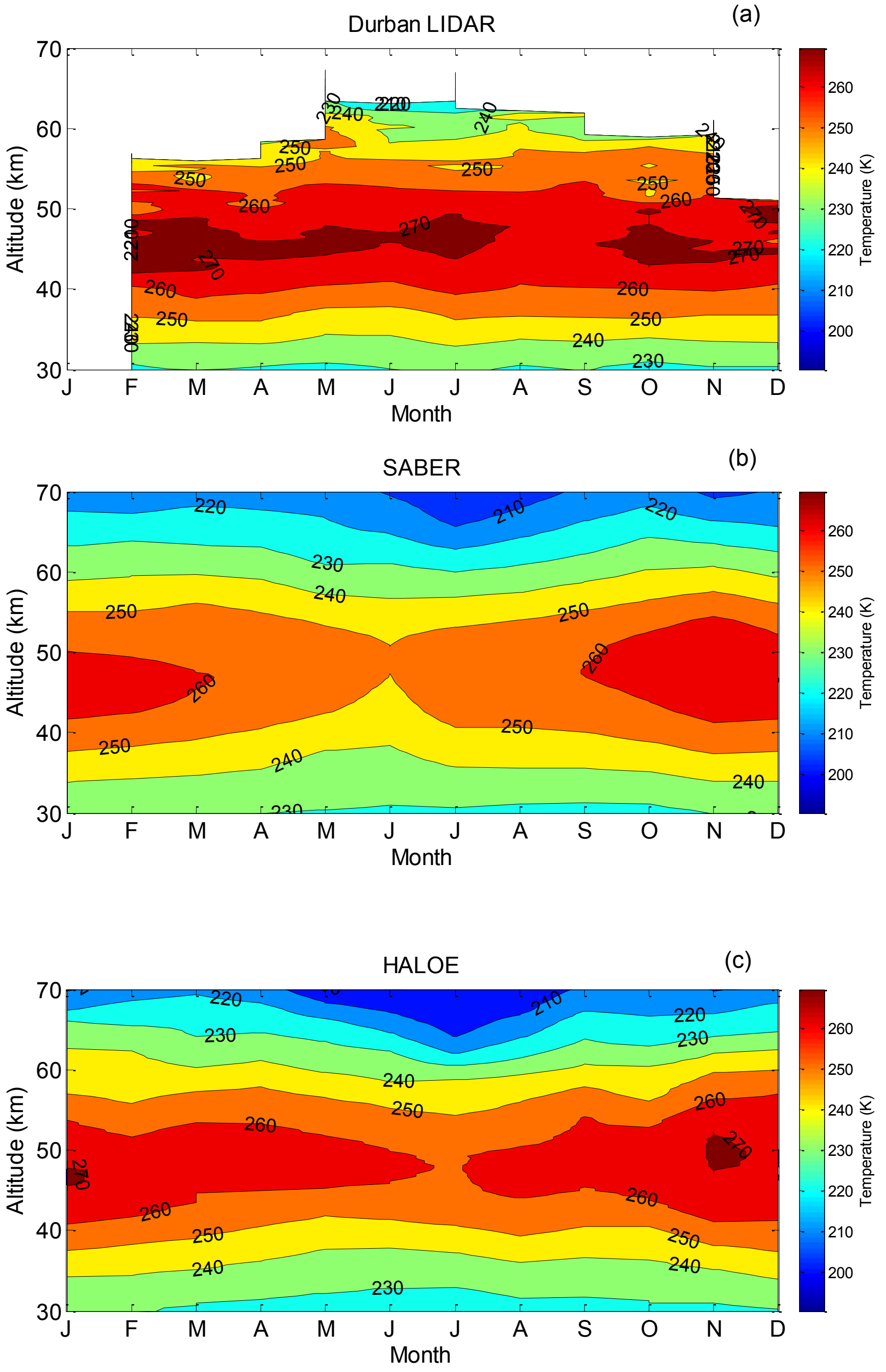

Figure 4.4: The contour plots of temperature variation with altitude and month for the LIDAR (top panel), SABER (middle panel), and HALOE (lower panel) observations.

The SABER stratopause temperature during the spring/summer season (from October to February) has a maximum temperature of 260 K. During the winter period the stratopause temperature is found to be ~250 K. For HALOE the summer and equinoxes stratopause is observed with a maximum of 260 K. Thus, the stratosphere structure as seen by the three instruments (LIDAR, SABER, and HALOE) depicts a familiar feature (annual oscillation) in the mid-latitude regions. Previous studies have also shown a strong presence of annual oscillation in the mid-latitudes and high latitudes (e.g. Chanin (1991); Hauchecorne et al. (1991); Gobbi et al. (1995)). Batista et al. (2009) reported a domination of annual oscillation in the stratosphere in their study using Rayleigh LIDAR measurements obtained from 1993 to 2006 at São josé dos Campos, Brazil (23.2°S, 45°W). In contrast to the annual oscillation in stratosphere of the midlatitudes and high-latitudes, the low-latitude observations show a strong semi-annual oscillation (e.g. Sivakumar et al. (2003)). The Durban station is situated at ∼29°S, and the middle atmosphere at this latitudinal position can be influenced by the subtropical and mid-latitude dynamical patterns. The observation of maximum temperatures during the summer and minimum temperatures during the winter stratosphere is in phase with the solar flux.

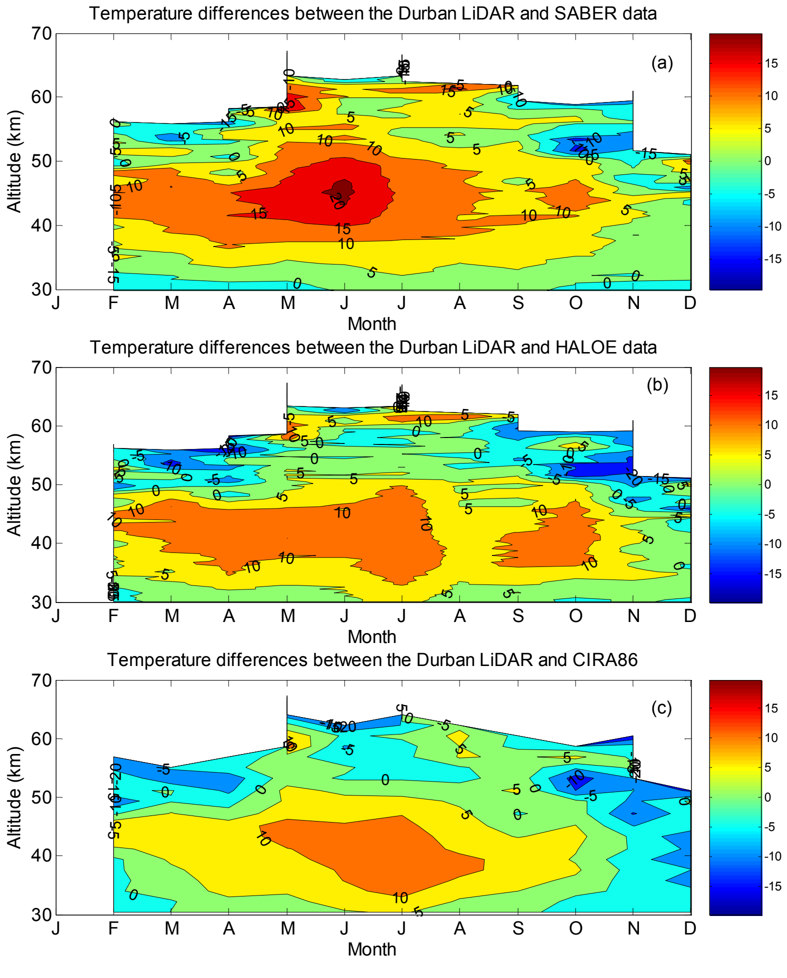

Figure 4.5: Contour plot of temperature differences between the LIDAR and SABER (a), LIDAR and HALOE (b), and LIDAR and CIRA-86 model (c).

Fluctuations observed in the LIDAR temperature climatology are due to dynamical events which are smoothened in the satellite (SABER and HALOE) observations. The LIDAR observations are about 10 K warmer in the height regions between 40 and 55 km compared to the satellites observations for most of the months. This can be associated with the dynamical activities which could not be detected by the satellites. In fact, the ground-based LIDAR experiment allows a better vertical resolution (150 m) than the satellite observations. The calibration of the instrument may also play a role, as, for example, LIDAR instrument assumes the ideal gas law. Furthermore, LIDAR measurements are more sensitive to small-scale dynamical disturbances, such as gravity waves and atmospheric tides than satellite measurements. The SABER and HALOE show almost the same thermal structure of the middle atmosphere over Durban. Both instruments (SABER and HALOE) show cold mesospheric winter above ∼63 km. Similar results were also reported by Batista et al. (2009) in their study of monthly climatology and trend in the 35-65 km altitude over São josé dos Campos, Brazil.

For a better comparison between LIDAR observations and satellite observations it is necessary to calculate temperature differences between the instruments. The contour plots in Figure (4.5) show the temperature differences between the LIDAR (a) and SABER (b) and HALOE (c) and CIRA-86 model, plotted as a function of month versus altitude. These differences were obtained by subtracting the satellite (SABER and HALOE) and model (CIRA-86) climatology from the LIDAR climatology. The differences between LIDAR and SABER and LIDAR and HALOE and CIRA-86 are observed to be similar. Generally, all contour plots are dominated by higher LIDAR temperature values throughout the middle atmosphere, except at a height above 50 km during the equinoxes. The differences between LIDAR and SABER show evidence of higher values (20 K) located in the height range ∼40-50 km during March to July. The differences between LIDAR and HALOE show the highest values (10 K) in the height range ∼35-45 km during February to July. Another peak of 10 K is noticed during September to August. The differences between LIDAR and CIRA-86 model show the highest values (10 K) in the height range ∼35-45 km during April to September. The same feature is observed in all three figures. The double lobe structure of minimum temperature in February to April and September to November over 50 km could possibly reflect the presence of semi-annual oscillation. Another factor which could lead to the formation of the double lobe structure could simply be a general reflection of the larger discrepancies between the systems during the equinoxes. This is confirmation of a semi-annual oscillation which was observed in this study. The smaller differences in SABER, HALOE, and CIRA-86 during November and December may be associated with lack of LIDAR observations during these months.

Studies such as Leblanc et al. (1995) made a comprehensive comparison of the LIDAR and HALOE satellite observations and found differences to be as large as 15 K between the two instruments in the mesospheric inversion region. Hervig et al. (1996) compared the LIDAR temperature measured at different stations in the Northern Hemisphere to that of HALOE and rockets and found that the measurements typically have random differences less than 5 K for the latitude below ∼60 km. The differences shown in Figure (4.5b) exhibit the highest values (10 K) in the height range ∼35-45 km during February to July. Another peak of 10 K is noticed during September-August.

4.3.3 Monthly Mean Comparisons

The monthly mean LIDAR temperature profiles were computed by averaging the individual available night profiles obtained for each month (for April 1999 to December 2004) over Durban (see Figure (4.6)). The LIDAR monthly mean was recorded when data were recorded for at least nine nights. The monthly mean profiles (bold black line) are compared with monthly averaged profiles from SABER (dotted black line), HALOE (dashed black line) instruments, CIRA-86 model (solid black line) and also the mean of all LIDAR data available. Figure (4.6) indicates only the months from February to November as the LIDAR measurements were not possible during January and December due to the rainy summer season. The data from the two satellite instruments were taken as the satellite overpasses closest to Durban.

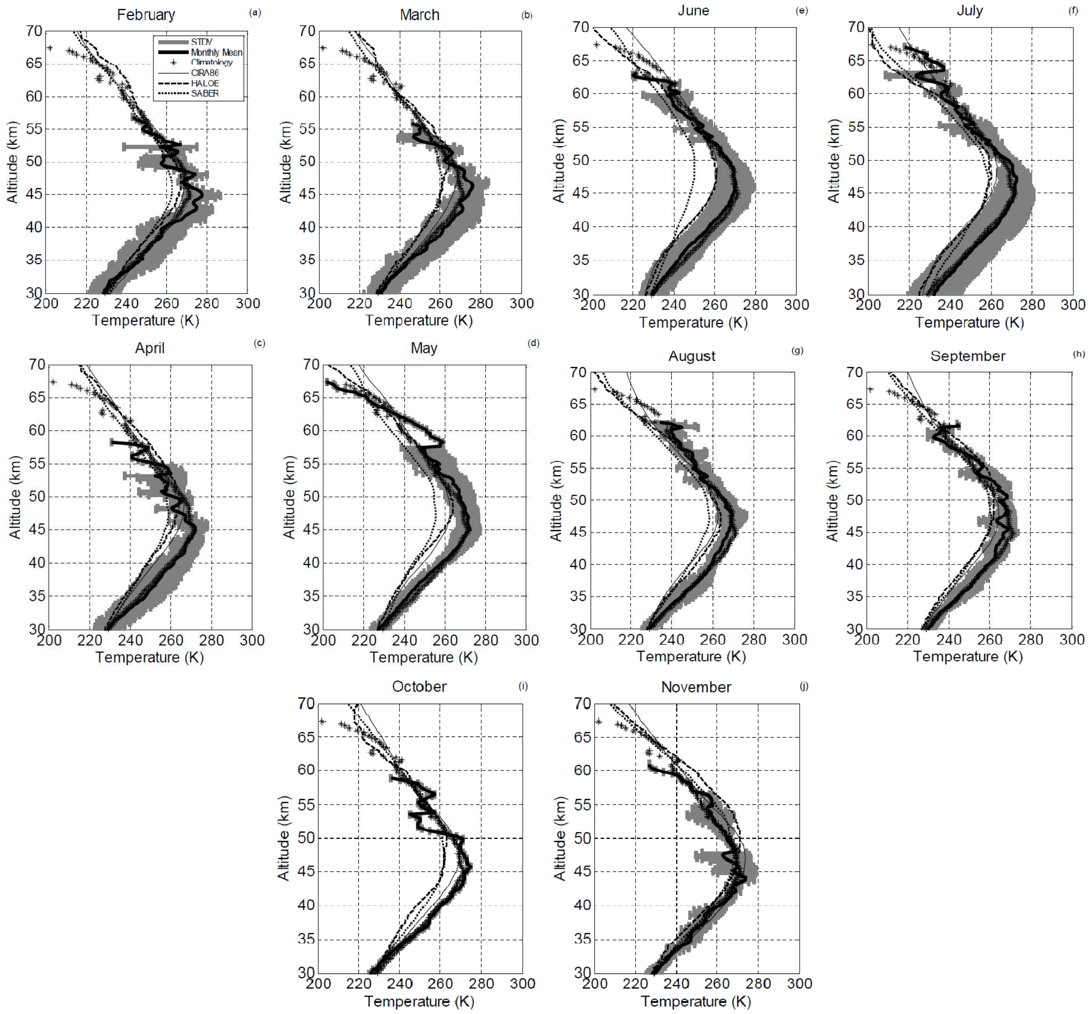

Figure 4.6: Monthly mean temperature profiles for each month (February to November) averaged over the period from February 1999 to November 2004 for Durban LIDAR, February 1999 to November 2004 for HALOE and March 2002 to November 2005 for SABER

The LIDAR monthly means do not appear to be smooth as fewer observations were made due to frequent cloudy conditions over Durban hindering the LIDAR operation. Generally, the LIDAR observed monthly values are in fair agreement with the two satellite instruments and the model. However, a clear difference was found in the stratosphere with warmer LIDAR temperature (both Climatology and monthly mean) below 50 km compared to the satellite instruments, except for the month of November. These observations of the warm LIDAR stratosphere are found to be in good agreement with the recent study by Dou et al. (2009) where Rayleigh LIDARs at six different locations from low to high latitude within the Network for the Detection of Atmosphere Composition Change (NDACC) were used.

It is also worthwhile mentioning that in all months the LIDAR climatology and monthly mean show better agreement with the CIRA-86 modes. The LIDAR climatology and monthly mean temperatures are ∼10-15 K warmer during May and June than SABER and HALOE temperature between 35 and 50 km. The differences of mean temperature between LIDAR and the satellites (SABER and HALOE) in the stratosphere may be due to a bias in satellite temperatures, or tidal aliasing introducing a difference in the temperatures from these instruments (Dou et al., 2009). The differences could also be due to the length of the data set, the difference in data sampling between ground and space-based instruments, and the LIDAR temperature analysis algorithms. 2. This implies that the temperature difference from these instruments can either be due to dynamical events or the difference in resolution or even both. There is a good agreement between the LIDAR, SABER, HALOE, and CIRA-86 model at the height above 50 to 55 km for most of the months.

4.3.4 Seasonal Variations

In order to examine the seasonal characteristics of temperature over Durban and to compare the LIDAR seasonal means against satellites, the temperature profiles derived from LIDAR, HALOE, and SABER observations over Durban have been grouped per season. The summer, autumn, winter and spring temperature profiles are derived from daily profiles averaged for the December-January-February (DJF), March-April-May (MAM), June-July-August (JJA) and September-October-November (SON) periods, respectively. Figure (4.7) illustrates the seasonal averaged LIDAR temperature profiles with standard deviation, superimposed on the seasonal averaged closest overpasses temperature profiles of HALOE and SABER satellite instruments.

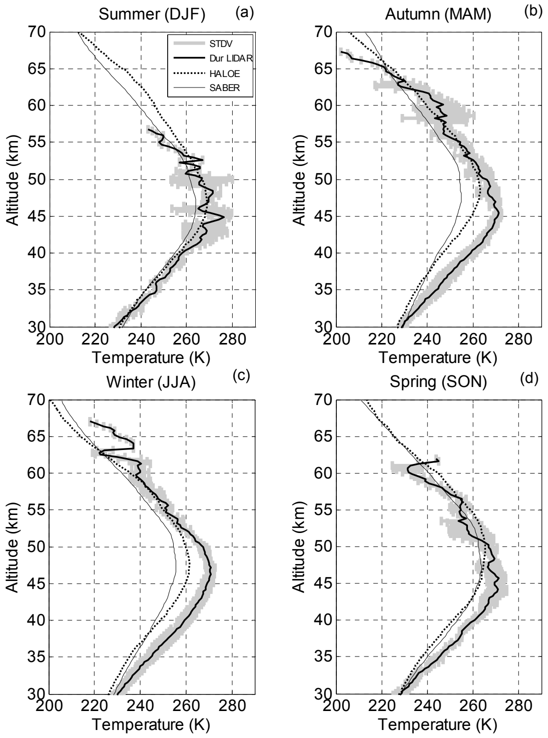

Figure 4.7: Seasonal mean temperature profiles obtained from Durban LIDAR, HALOE, and SABER: (a) Summer (DJF), (b) Autumn (MAM), (c) Winter (JJA), and (d) Spring (SON).

Generally, the LIDAR temperature profiles are found to be systematically warmer than the two satellite observations in the stratospheric height region between 33 km and 55 km. The stratopause is depicted at the same height in the LIDAR, SABER, and HALOE profiles in summer and winter. However, during the equinoxes the LIDAR stratopause height is found to be ∼5 km lower than the two satellite profiles. The HALOE temperature profiles are found to be systematically colder than the SABER temperature profiles for the height region below 40 km in autumn, winter and spring. Above 50 km the three instruments seem to have good agreement with LIDAR observed values apart from visible fluctuations of LIDAR profiles, which can be associated with some middle atmospheric unusual spectacular events which cannot be detected by satellites (e.g. upwards propagating gravity/planetary wave braking, stratospheric warmings, and tidal waves) (Chanin and Hauchecorne, 1981), or even possible measurement errors. The stratospheric temperature differences between the LIDAR and the two satellites are found to be very low during summer (DJF) and spring (SON) seasons compared to the winter (JJA) and autumn (MAM) seasons. The observed differences are consistent with the findings by Sivakumar et al. (2011) in their study on the climatology and comparisons of Rayleigh LIDAR measurements and satellite (HALOE, SABER, GPS-CHAMP and COSMIC) measurements of the stratosphere and mesosphere temperature over southern sub-tropical site, Reunion (20°S, 55.5°E).

The temperature difference between LIDAR and SABER measurements seem to be larger than the differences between LIDAR and HALOE measurements. The temperature differences between LIDAR and SABER are found to be 5-12 K at the height region between 40 km and 50 km in autumn and 5-10 K at the height region between 40 km and 50 km in winter. However, the difference between LIDAR and HALOE are found to be 3-6 K at the height region between 35 km and 50 km in both autumn and winter. The observed differences between LIDAR and the two satellites may be due to the difference in the techniques used to retrieve the temperature, the observational time differences, as well as the poor height resolution of SABER measurements (∼2 km) and HALOE measurements (3.7 km) in comparison with the LIDAR measurements (150 m). Dynamical events can also be the contributor to these differences. It is evident that there are some events which appear to be detected by the LIDAR but smoothened out in the satellite observations. Generally, during the autumn and winter seasons there is usually a large formation of stationary planetary waves, thus this could be a significant reason for larger difference between the satellites and the LIDAR during these seasons. Similar results were also reported by Randel et al. (2004) in the Northern Hemisphere where data sampled at four LIDAR sites to Met Office stratospheric analyses (METO) observations were compared. The HALOE and SABER satellite data represent day and night time observations while the LIDAR measurements were made during the night only. Hervig et al. (1996) compared the sunrise and sunset observations of HALOE temperature and found sunrise values to be 1-5 k colder than the sunset values. HALOE (sunrise and sunset) measured temperature profiles were also compared to that of LIDAR and rocket-sonde, and the measurements typically had differences less than 5 K for the height region below 60 km. Thus, the differences between the LIDAR and HALOE reported in this study are in agreement with results from Hervig et al. (1996). Earlier results on an inter-comparison study by Randel et al. (2004) based on different middle atmospheric temperature measurements also showed that the LIDAR measured temperature profiles are differing by ±5 K. Recently, a study by Sivakumar et al. (2011) on climatology and comparison of Rayleigh LIDAR and satellites measured temperature over a southern subtropical site (Reunion) reported a difference of 5-10 K in the stratosphere.

4.4 Comparison between Reunion and Durban Rayleigh LIDAR Temperature Measurement

The Reunion (20.8°S, 55.5°E) Rayleigh LIDAR instrument has a similar design to the Durban Rayleigh LIDAR. However, the instrument started working in May 1994, about 5 years earlier than the Durban LIDAR system. A description of the improvement made to the Reunion LIDAR system has been detailed by Baray et al. (1999). For the purpose of this work only data for the years 1999-2004 have been used. During this period about 270 nights of Reunion Rayleigh LIDAR temperature profiles were obtained.

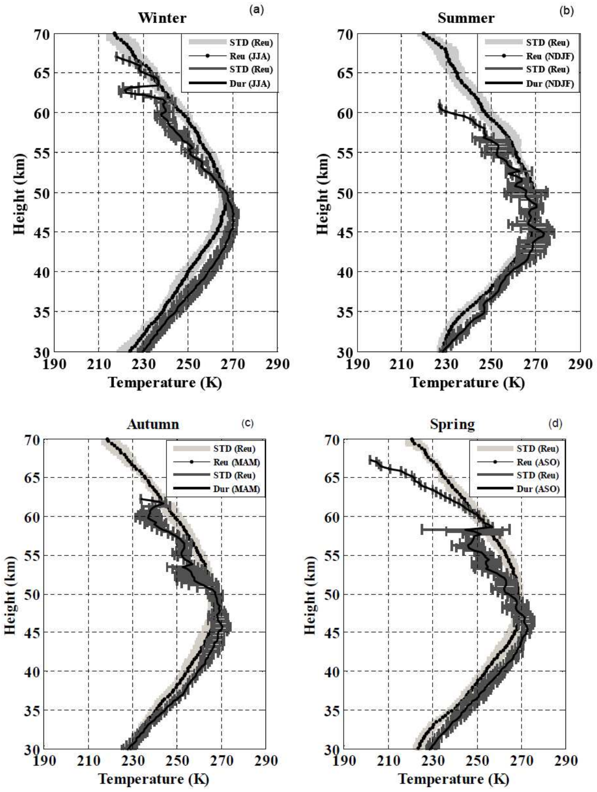

Figure 4.8: Seasonal mean temperature profiles during (a) winter, (b) summer, (c) Autumn, and (d) spring obtained form Durban and Reunion LIDAR data for the period from 1999 to 2004.

Figure (4.8) illustrates a comparison of the average Durban and Reunion LIDAR profiles for different seasons, namely winter (JJA), summer (DJF), autumn (MAM) equinox, and spring (SON) equinox. In this figure, the standard deviation associated with the mean profile is indicated by the horizontal spread in the case of Reunion profiles and horizontal bars in the case of the Durban profiles. The seasonal profiles are found to be within the standard deviation for the height below 50 km, and thus there is a fairly good agreement between the two instruments for all the seasons. However, the Durban LIDAR observations are seen to be slightly higher (about 3 to 8 K) than the Reunion LIDAR observations up to the stratopause for all the seasons. The Durban LIDAR profiles show high standard deviations in comparison to the Reunion profiles. Since the installation of the Durban LIDAR in April 1999, it operated with a Spectra Physics Nd:YAG laser at a repetition rate of 10 Hz delivering an average power of 3 W. During 2002, the 10 Hz laser was replaced with a more powerful Nd:YAG delivering 5 times more power and operating at a frequency of 30 Hz (Moorgawa et al., 2007). A comparative analysis of the backscatter signals obtained separately from each laser (10 Hz and 30 Hz) showed that the 30 Hz laser has a larger stratospheric range (Moorgawa et al., 2007). Thus, the fact that the Durban LIDAR climatology study was dominated by data measured using the 10 Hz laser cannot be ignored in the observation of higher standard deviations in the upper stratosphere. The Reunion profiles are warmer by ∼3 to 10 K above 50 km. Furthermore, the difference in temperature values at Durban and Reunion could be due to the latitudinal and longitudinal variation in the temperature, time difference and the changes in instrumental specifications.

4.5 Discussion and Summary

Based on 5 years of Rayleigh LIDAR measurements over Durban, a tropical latitude station in South Africa in the Southern Hemisphere, the climatology of the temperature between 30 and 70 km was studied and compared to the observations from SABER and HALOE instruments. The LIDAR temperature in the stratopause (altitude ∼42-50 km) shows two distinct maxima of 270 K, one during February to July and the other during September to December. All instruments indicate a presence of annual oscillation in the stratosphere, and in the mesosphere the semi-annual oscillation seems to dominate in some levels (see Figure (4.4b and c)). These findings are consistent with previous observations (e.g. Chanin (1991); Hauchecorne et al. (1991); Gobbi et al. (1995); Batista et al. (2009). SABER and HALOE show almost the same thermal structure of the middle atmosphere over Durban.

Generally, there is a fair agreement between LIDAR observed monthly mean values and the two satellite instruments and the model. However, a clear difference was found in the stratosphere with warmer LIDAR temperatures (both in the climatology profile and monthly mean profiles) below 50 km compared to the satellite instruments, except during November. These differences in the stratosphere may be associated with bias in satellite temperatures, or tidal aliasing introducing a difference in the temperatures from these instruments. Differences may also be caused by the length of the data sets, the difference in height resolution, the difference in data sampling between ground and space-based instruments, and the LIDAR temperature analysis algorithms. All in all, the temperature difference from these instruments might be due to dynamical events or the difference in resolution or even both. The observed warm LIDAR stratosphere is found to be in agreement with the recent study by Dou et al. (2009) where Rayleigh LIDAR was used at six different locations from low to high latitude within the Network for the Detection of Atmosphere Composition Change (NDACC). There is a good agreement between the LIDAR, SABER, HALOE, and CIRA-86 model at the height above 50 to 55 km for most months.

The seasonal temperature means from the Durban LIDAR observations with HALOE and SABER seasonal temperature means are in good agreement. However, during autumn and winter the differences are found to be 5-12 K higher for the LIDAR measurements in the height region between 40 and 55 km. The stationary planetary waves usually observed in the middle atmosphere winter seasons may be the main cause of the higher difference between the LIDAR and satellite observations in winter and autumn. The difference in methods of data retrieval between the ground-based and space-based instruments, as well as the location and time of measurements, might also contribute to the overall differences between the LIDAR measurements and satellite measurements. In all seasonal profiles above 50 km the LIDAR temperature fluctuated, indicating a wave-like structure which may be due to gravity and tidal waves. Gravity waves and tidal waves over Durban will be studied in detail in a future study.

A comparison between Durban and Reunion LIDAR seasonal profiles was also performed in this work, and good agreement was found between the two stations. However, Durban LIDAR profiles showed higher standard deviations in comparison to the Reunion profiles. Furthermore, the Reunion profiles are warmer by ∼3 to 10 K above 50 km. Studies by Sharma et al. (2006) and Dou et al. (2009) included comparisons of LIDAR profiles from different stations. Sharma et al. (2006) compared seasonal LIDAR measurements from the Indian sub-continent in the tropics (Gadanki; 13.5°N, 79.2°E) and in the sub-tropics (Mt. Abu; 24.5°N, 72.7°E), and reported that the mean profiles were within the standard deviations for the heights below 50 km, however, the Mt. Abu profiles were warmer by 4-8 K above 50 km. In this thesis, the middle atmospheric differences between the Durban LIDAR and Reunion LIDAR can be associated with the topography of the two stations, and thus the formation of stationary planetary waves, difference in transportation and mixing in the middle atmosphere above the two stations. Another contributor to the differences, especially in the upper stratosphere, is the use of the 10 Hz-laser for most of the measurements in the Durban station. In future it is important to study the planetary waves, gravity waves, concentration, mixing, and transportation in the lower and middle atmosphere over Durban, so as to understand the atmospheric structure over this region better.

Chapter 5

Mean Wind and Planetary Waves

5.1 Introduction

Understanding the patterns of general circulation of the middle atmosphere is an important subject in trying to understand the middle atmospheric dynamics. Different observational techniques as well as theoretical studies have been used to understand the circulation in the middle atmosphere (Fleming et al., 1996; Namboothiri et al., 1999b; Malinga et al., 2004; Jacobi et al., 2009, etc). The circulation of the middle atmosphere (commonly known as mean flow) is governed by momentum deposition from various atmospheric motions including propagating atmospheric waves such as planetary waves, gravity waves and tides. Some of the above mentioned atmospheric motions interact with the mean flow producing processes such as filtering, wave breaking, mean wind reversal and even MLT heating and cooling (Fritts et al., 1999; Dowdy et al., 2004; Dowdy, 2005; Mbatha et al., 2010b, etc). Apart from other atmospheric waves mentioned above, this chapter focuses on the dynamics of the middle atmosphere on the basis of mean wind and planetary waves of periods between ~2 and 20 days. The MLT has a strong presence of waves with periodicities of 2-, 5-, 10-, 14-, and 16-days, and these waves are reported to be similar to those in the troposphere (Forbes et al., 1995). Investigating variability at time scales known as typical for tropospheric, stratospheric and solar variability may provide insight into possible sources for upper atmospheric variability and interactions between different layers of the atmosphere (Jacobi et al., 2005). The variations of winds as well as temperature in the MLT is thought to be due to the solar variations (Jacobi, 1998), major SSW in the winter months, and quasi biennial oscillation (Namboothiri et al., 1994). The long term trends can be due to atmospheric CO_2 increase or O_3 decrease (Bremer and Berger, 2002).

In Antarctica there are many different ground based MF radar instruments that can be used to study wind in the MLT, and to separate and characterise wave components and the mean flow for climatology and phenomenological studies. However, at SANAE the dynamics of the MLT can only be studied with a SuperDARN HF radar, as the other instruments are not available. As it was mentioned in Chapter 3, the SuperDARN HF radars were primarily designed to study the convection patterns in the high-latitude ionosphere. However, there are several studies which have proved that SuperDARN radars can also be used to study the dynamics of the MLT region. Hussey et al. (2000) compared horizontal wind data from near co-located MF and SuperDARN radars at Saskatoon, Canada (52°N, 107°W). In their work, they observed good agreement between the SuperDARN radar wind and those recorded by the MF radar at around 95 km. They thus concluded that the two systems complement each other effectively. A study by Espy et al. (2005) combined simultaneous data recorded by SuperDARN and MF radars over Antarctica and studied the periods, wavenumber, and propagation direction of the planetary waves in the MLT. A study by Hibbins and Jarvis (2007) compared wind and tidal measurements in the upper mesosphere recorded with an imaging Doppler interferometer (IDI) and a SuperDARN radar at Halley, Antarctica, and observed good correlation between the SuperDARN meridional wind and tides with the IDI at 90-95 km height. Recently, Mbatha et al. (2010b) studied the 2002 major SSW influence on the MLT using the SuperDARN radar wind data recorded at SANAE. Furthermore, Hibbins et al. (2010) studied the inter-annual variability of the non-migrating (s=1) and migrating (s=2) components of the semidiurnal tide in the Antarctica MLT using twelve years of horizontal wind data recorded at the Scott base MF radar and Halley SuperDARN radar.

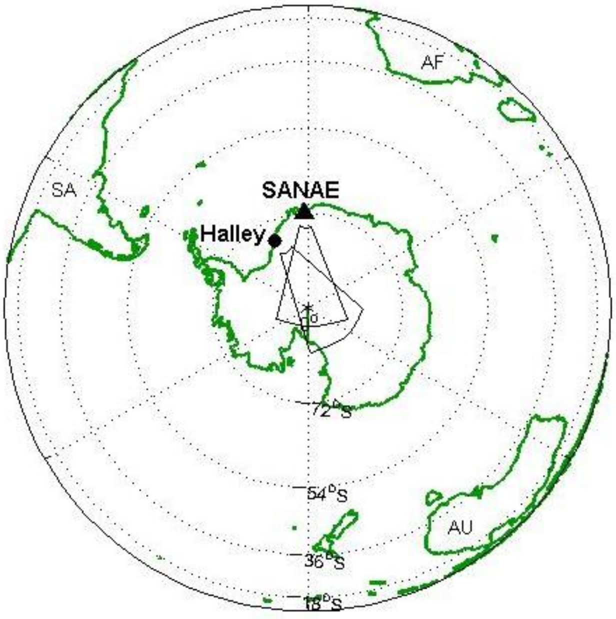

Figure 5.1: Map of Antarctica with the locations of the SANAE and Halley stations denoted by a triangle and a dot, respectively. Also shown are the fields-of-view of the two SuperDARN coherent HF radars.

In this thesis, the climatology of zonal and meridional mean winds is presented based on nine years of meteor wind data recorded with a SuperDARN radar at SANAE (72°S, 3°W) and Halley (76°S, 27°W) sites located in Antarctica (see Figure (5.1)). The results obtained from the two stations are also compared. The climatology of planetary wave activity in the MLT using the SANAE HF radar wind data is studied, and the coupling between the MLT (∼94 km SuperDARN HF radar wind data) and the stratosphere (1-hPa) is assessed using the UKMO assimilated wind data over SANAE. Meteorologists and atmospheric physicists sometimes prefer to use pressure in hectoPascals (hPa) to distinguish different heights of the atmosphere instead of the altitude in km. In this thesis, pressure (in-hPa) is used to describe the altitude wherever the UKMO data is used. For simplicity, a table summarising different pressure levels (in hPa) and their relevant altitude in km is given in Table 5.1.

Table 5.1: Pressure levels (in hPa) and their relevant altitudes in km.

Pressure (hPa)	Altitude (km)
1000.0	0.0
700.0	3.0
500.0	5.5
300.0	9.5
200.0	12.0
150.0	14.0
100.0	16.5
70.0	19.0
50.0	21.0
30.0	24.5
20.0	27.0
10.0	32.0
7.0	34.5
5.0	37.0
3.0	41.0
2.0	44.0
1.0	49.5
0.5	55.0
0.3	59.0

5.2 Mean Wind and its Seasonal Trends

In this study, the mean wind and its seasonal trends and climatology is studied for the first time using SANAE and Halley SuperDARN radar wind data. Figure (5.2) depicts the evolution of hourly averaged zonal (a) and meridional (b) wind observed by SANAE HF radar during September 2002. In this study, the daily mean wind was deduced by averaging the 4-day time sequences of hourly averaged horizontal (zonal and meridional) wind velocities measured by the SANAE and Halley HF radars at ∼ 94 km. The average mean wind measured by the SANAE and Halley SuperDARN radar per day is approximately ±8 $\mathrm{m.s^{-1}}$ and ±3.5 $\mathrm{m.s^{-1}}$ for zonal and meridional component, respectively, depending on the season. The 4-day data window was advanced by 1 day at a time, and the average of the data window was attributed to the second day of the interval. There are some periods where the instruments did not take measurements due to problems with the system. Thus, the four day mean was considered to be acceptable if at least 60% of the possible hourly wind values were recorded. The monthly means were also deduced from the daily means.

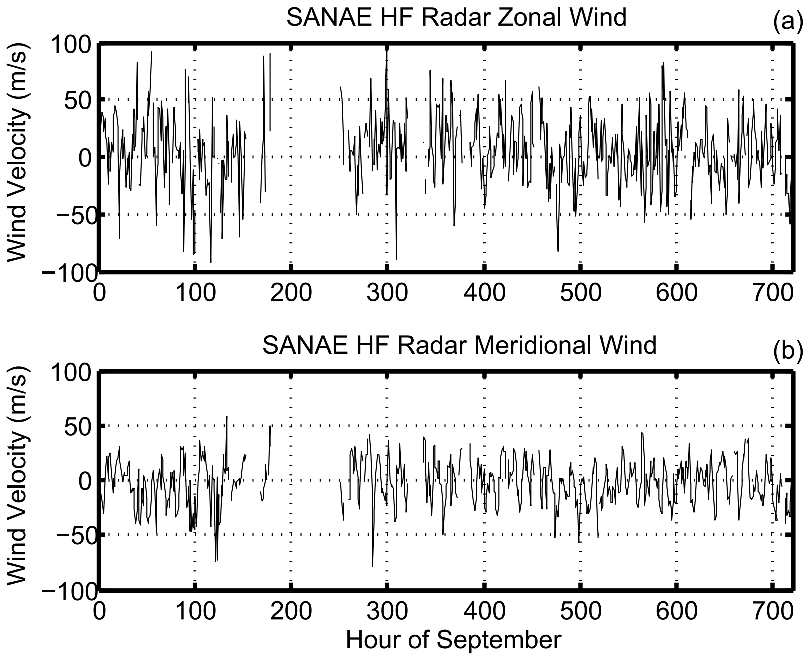

Figure 5.2: Hourly averaged zonal (a) and meridional (b) wind as observed by the SANAE HF radar during September 2002.

Figures (5.3) and (5.4) illustrateone-to-one comparisons of the zonal and meridional mean flow at SANAE (black line) and Halley (blue dotted line) hourly wind for the years from 1998 to 2006, respectively. There is general agreement between the two stations in both zonal and meridional mean flow. The two figures clearly indicate that the zonal wind is consistently stronger than the meridional wind. This is similar to results noted by others (e.g. Malinga and Poole, 2002; Jacobi, 1998). A strong MLT mean flow reversal, which is associated with the unprecedented stratospheric warming in the late winter of year 2002 (late September) is also clearly detected by both HF radars. The details regarding the 2002 stratospheric warming and MLT zonal wind reversal will be discussed later.

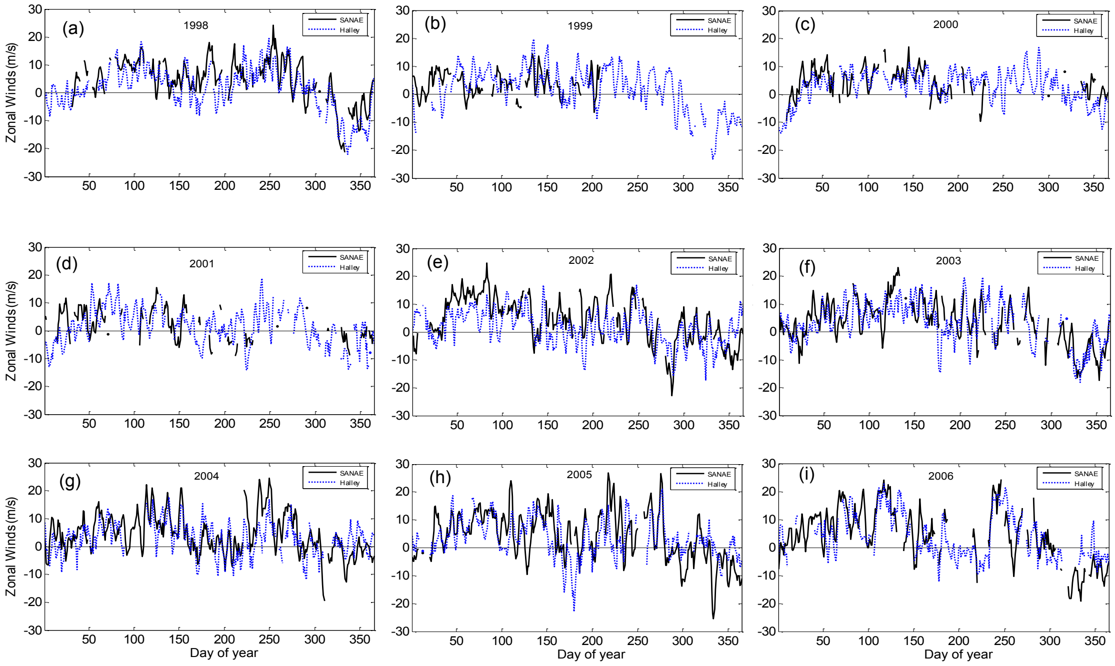

Figure 5.3: The zonal wind at SANAE (solid black line) and Halley (blue dotted line) for the years from 1998-2006.

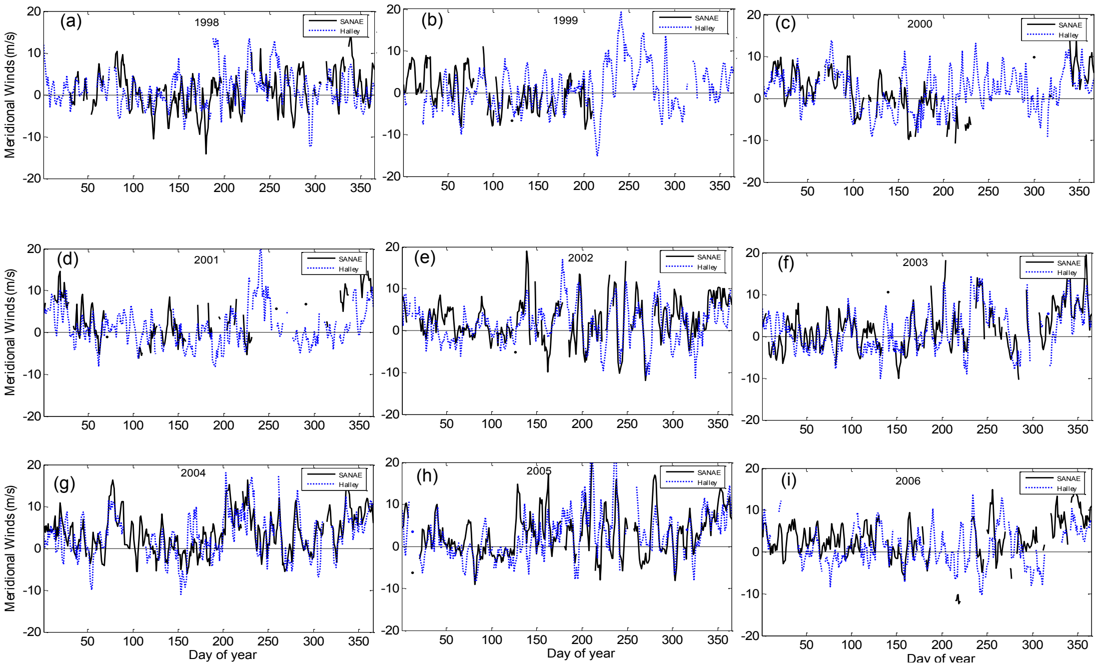

Figure 5.4: Same as Figure (5.3) but for the meridional wind.

A one-to-one comparison of the zonal and meridional monthly mean wind from SANAE and Halley is shown in Figures (5.5) and (5.6). Corresponding inter-annual averages (IA) are shown in Figure (5.7a and b). The error bars represent one standard error of the mean, which in some cases is too small to be seen under the symbol used to represent the data points. In both monthly means and inter-annual variation figures it is clearly indicated that the zonal wind is consistently larger than the meridional wind. This is similar to results noted by others (e.g. Jacobi (1998) and Malinga and Poole (2002)). Generally the zonal mean flow seems to show stronger seasonal variability (with changes up to a maximum of 14 m.s^{-1}) than does the meridional mean flow. In both sites (SANAE and Halley) the zonal mean wind seems to be dominated by an eastward (positive) mean flow. However, there are cases where it also turns to the westward direction (especially during summer and winter seasons). In 2003, the SANAE zonal mean flow was abnormally strong, reaching about 15 m.s^{-1} in May, in contrast to weaker meridional mean flow observed in the same month. Overall, there is good agreement between the zonal mean flow monthly means from the two stations. The meridional mean flow is also observed to be in the northward/equatorward (positive) in both stations, but also shows some southward/poleward (negative) motions in some cases.

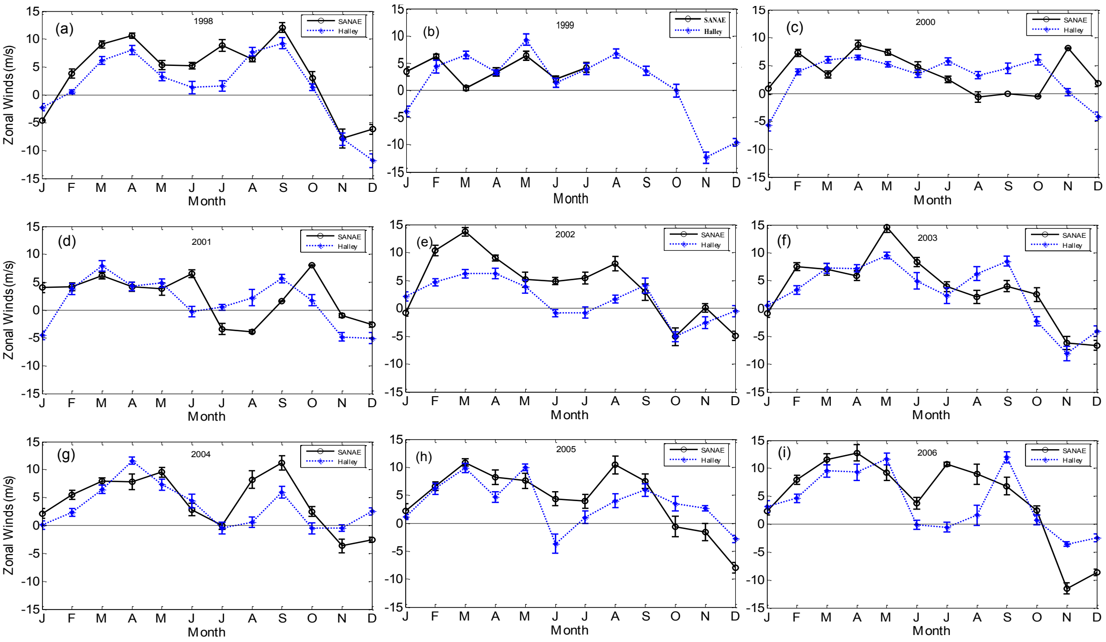

Figure 5.5: The monthly zonal wind at SANAE (solid black line) and Halley (blue dotted line) for the years from 1998-2006. The error bars represent one standard error of the mean.

Generally, there is a sequence of strong westward mean flow which begins in October and reaches its maximum in November for most of the years. However, in the year 2002 this reversal of wind reached its maximum a month early compared to the other years, which may be associated with the disturbance of the MLT mean circulation by the unprecedented 2002 major stratospheric warming event. The weaker mean flow in late winter 2002 is presumably due to the deposition of gravity waves of tropospheric origin (Liu and Roble (2005); Dowdy (2005)). Another outstanding feature is observed in the year 2004 monthly mean flow in Figure (5.6g) where it indicates a good agreement between the two instruments throughout the year, while in year the 2000 (Figure (5.6c)), there was a difference of approximately 10 m.s^{-1} observed in August.

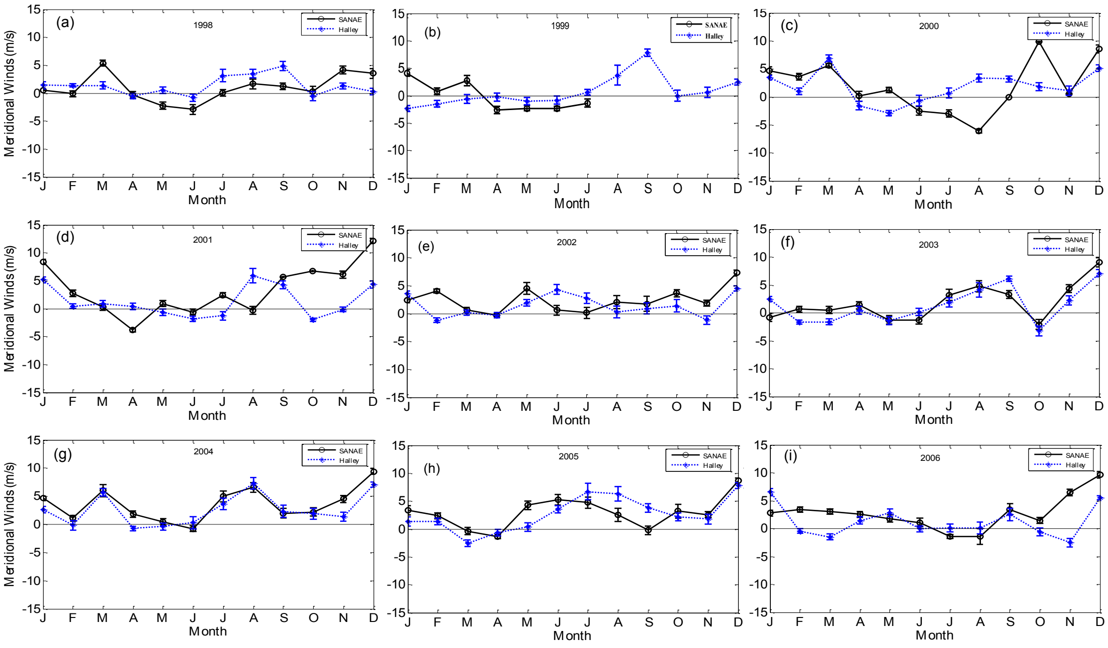

Figure 5.6: Same as Figure (5.5) but for meridional wind.

To complement the visibly good agreement between the wind components measured by the SANAE and Halley HF radars, the correlation between IA obtained from the two instruments was calculated. Figure (5.8) shows the correlation between the SANAE and Halley zonal component and meridional component, respectively. The zonal wind IA and meridional wind IA show a correlation coefficient of R=0.97 and R=0.71, respectively. The correlation of R=0.97 observed in the zonal component is at a 95% confidence level, and this shows a good agreement between the two instruments. The correlation of R=0.71 observed in the meridional component is also fairly significant. The summary of statistics and seasonal variation of the mean flow observed by SANAE and Halley HF radars is shown in Table 5.2. In the table, summer is represented by months from December to February), autumn by months from March to May, winter by months from June to August and spring by months from September to November.

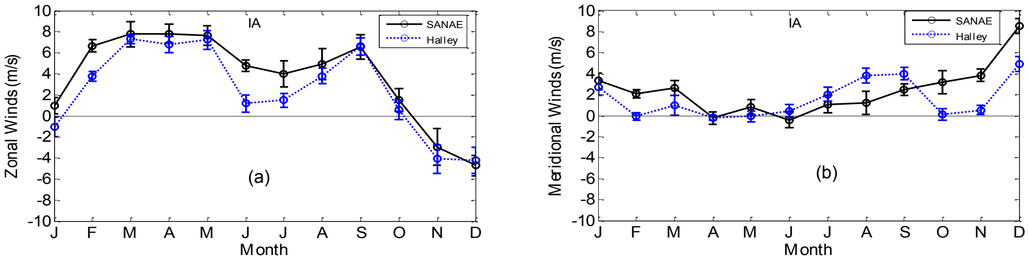

Figure 5.7: Inter-annual averages (IA) at SANAE and Halley for the years from 1998-2006. The error bars represent one standard error of the mean.

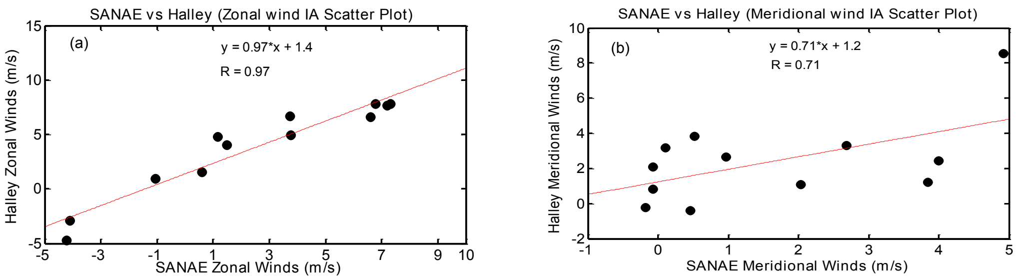

Figure 5.8: Correlation of SANAE and Halley IA zonal (a) and meridional (b) wind.

Table 5.2: Statistics of the monthly mean flow variables at SANAE and Halley for the period of 1998-2006. The values in the brackets represent one standard error of the mean.

Component	Variable	SANAE	Halley
Zonal wind	Speed (m/s)	3.8(1.0)	2.5(1.0)
	Eastward Speed (m/s)	5.2(0.2)	4.2(0.9)
	Westward Speed (m/s)	0	0
	Maximum Speed (m/s)	7.8	7.3
	Summer (m/s)	1.1	0
	Spring (m/s)	1.7	1.1
	Winter (m/s)	5.1(0.7)	3.1
	Autumn (m/s)	7.7(0.1)	7.1(0.1)
Meridional wind	Speed (m/s)	2.4(0.6)	1.6(0.5)
	Northwards Speed (m/s)	2.9(0.7)	2.2(0.5)
	Southwards Speed (m/s)	0	0
	Maximum Speed (m/s)	8.5	5.9
	Summer (m/s)	4.7(1.8)	2.54
	Spring (m/s)	3.2(0.4)	1.5
	Winter (m/s)	1.1	2.2
	Autumn (m/s)	1.1	0.2

The correlation between the SANAE and Halley meridional wind data indicates that there is a longitudinal difference between the two sites. Longitudinal differences have also been observed at other sites in latitudinal proximity. A study by Portnyagin et al. (1993) suggested that mean flow difference between Molodezhnaya (68°S) and Mawson (67°S), which are 1000 km apart, could be due to the relative displacement of the mean flow cells over spatial scales on the order of 1000 km. Forbes et al. (1995) observed a 10 m.s^{-1} difference in the mean flow at Obninsk (54°N, 38°E) and Saskatoon (52°N, 107°W) at about 95 km, and suggested that it could be a thermospheric signature of the zonal wavelength s=1 planetary wave that has been detected in the stratosphere (Smith, 1985). The longitudinal differences between two stations and thus difference in the occurrence of stationary planetary wave activity could also contribute in the difference observed in the meridional mean flow. Kazimirovsky et al. (1988) suggested a possible link between the stationary planetary waves and the longitudinal difference in the mean flow.

There seem to be a significant seasonal variation in the zonal mean flow. The zonal mean flow seasonal trend at both SANAE and Halley tends to have a primary maximum that can go up to ∼14 10 m.s^{-1} during the solstices. The high latitude summer zonal mean flow at ∼95 km is weaker and more variable compared to the eastward winter mean wind circulation owing to tropospherically forced planetary waves propagating through the middle atmosphere. This pattern of the mean flow variation in the MLT corresponds to observations reported by others (e.g. Baumgaertner et al., 2005). The influence of upwards propagating planetary waves also seem to influence the mean wind in winter. During the autumn equinox both instruments show a strong eastward mean flow which may have impelled through thermal wind balance by cold polar region and a strong latitudinal temperature gradient in the troposphere and stratosphere.

The mid-latitude region is reported to show a strong eastward zonal mean wind in summer, and weak and variable zonal mean wind in winter compared to the relatively quiescent summer eastward mean flow (e.g. Fleming et al. (1996); Malinga et al. (2004)). The low latitude MLT zonal mean flow is reported to exhibit a predominant westward wind due to westward momentum deposition from the breaking of diurnal tides (e.g. Fleming et al., 1996). A strong eastward zonal mean flow in the mid-latitudes may also be impelled through thermal wind balance by cold polar region and the associated strong latitudinal temperature gradient in the region below the underlying 70 to 95 km layer characteristic of summer middle and high latitudes (Fleming et al., 1996).

The meridional mean flow seasonal pattern at both SANAE and Halley stations seem to be characterised by a strong northward flow in the months of November to February, and a weaker northward mean flow in the months from April to June (See Figure (5.7)). Similar results were also reported by Malinga et al. (2004) in their study on long term variation of the mesospheric mean flow observed at Grahamstown (South Africa) and Adelaide (Australia). These results are also somewhat similar to annual cycle observation in the climatological mean of the year 1967-1986 at Molodezhnya (68°S, 45°E) (Portnyagin et al., 1993).

5.3 Planetary Waves Activity

5.3.1 Climatology

In order to examine the wave characteristics in the MLT region from the SANAE HF radar data, it is necessary to determine the dominant spectral components within the frequency band of interest. In this thesis, the wavelet power spectrum (Torrence and Compo, 1998) of the SANAE SuperDARN HF wind components (zonal and meridional) for approximately 94 km altitude were calculated for the period range from 2 to 20 days and time interval from January 1998 to December 2006. In particular, the Morlet family of wavelets were used because it has a well defined relationship between its scales and the Fourier periods, and thus suitable for spectral analysis. The contour plots of the wavelet power spectrums obtained are shown in Figures (5.9) and (5.10) for zonal and meridional wind components, respectively.

In this thesis, the wavelet analysis covers the total investigated time interval (1998 to 2006) in order to demonstrate how the character of the planetary wave activity changes with season, and also to identify the dominant periods in the respective years. Specifically, the wavelet analyses was applied to the daily mean data shown in Figure (5.3) and (5.4).

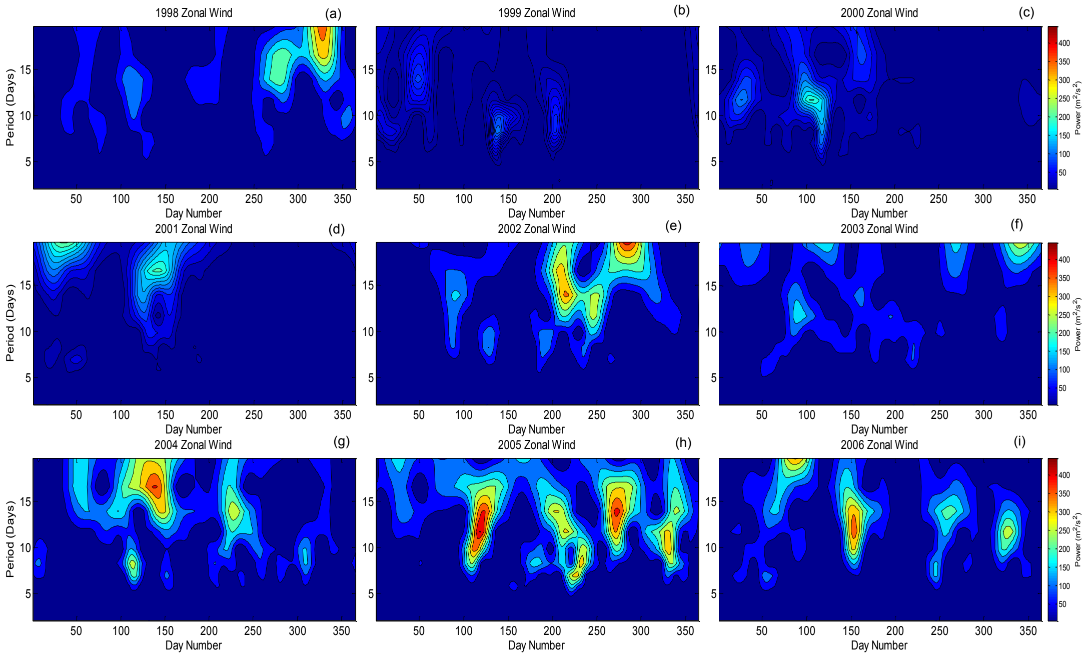

Figure 5.9: Wavelet power spectrum versus time (for years from 1998-2006) and period (2–20 days) calculated for the zonal component of the SuperDARN HF radar wind at SANAE. The white doted lines indicate features that exceed the 95% confidence level.

When comparing Figure (5.9) to Figure (5.10), it can be observed that the meridional winds exhibit weaker planetary wave activity than the zonal winds, especially at longer periods. Moreover, power peaks in zonal winds do not usually coincide in period and/or time with those in meridional winds. This is possibly due to the differing Hough mode structures, and hence latitudinal variabilities of the two wind components of planetary waves (**?**Chshyolkova et al., 2006).

In general, winter months at the mesospheric height are known to have a strong presence of planetary waves over a wide frequency range. The wavelet power spectrum of both zonal and meridional wind components in this study also indicate an amplification of planetary waves especially in early and late winter. In some cases planetary waves with long periods (e.g. quasi 16-day wave) can be seen in summer and equinox months. However, during summer months the long period oscillations which are dominant in winter usually disappear, and oscillations with shorter period (e.g. <10 days) becomes dominant. One of the most noticeable features is the appearance of strong quasi 14-day wave activity in winter

2002 both in the zonal and meridional wind components (see Figure (5.9e) and Figure (5.10e)). This quasi 14-day wave activity was never detected before, and it is responsible for the deceleration of the zonal mean wind in late winter 2002 (see Figure (5.3)). A strong wave activity of waves of periods between 8 and 16 days is also observed in the year 2005 winter. However, this wave activity did not trigger the wind reversal and stratospheric warming in the Southern Hemisphere. The quasi 10-day wave activity observed in the winter of year 2002 will be discussed in detail later on.

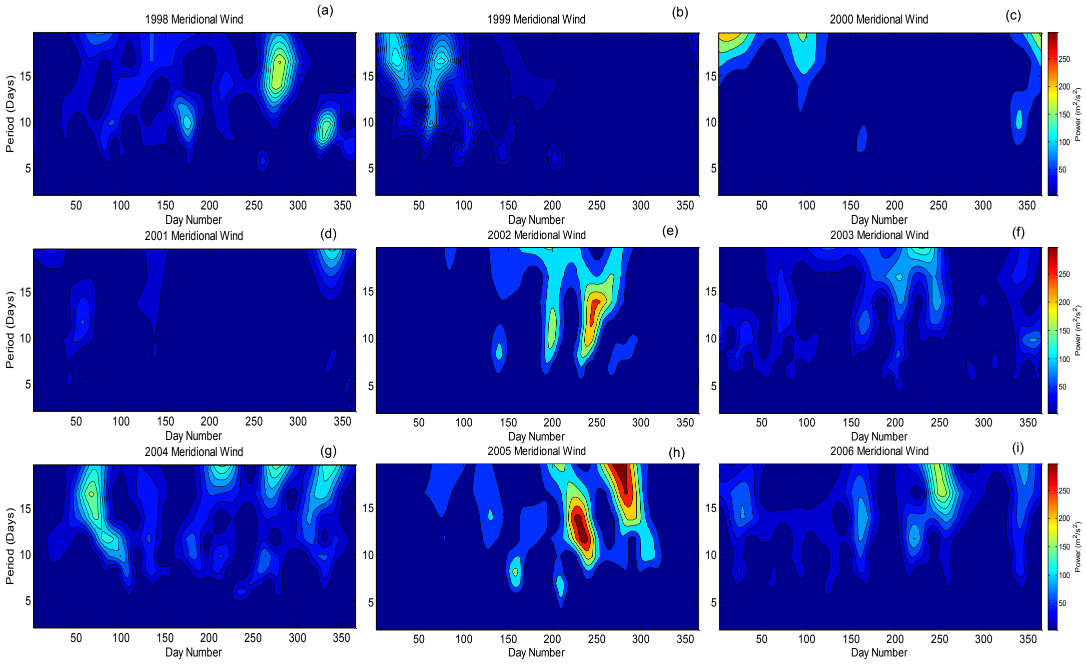

Figure 5.10: Same as Figure (5.9) but for meridional wind.

The spring and autumn seasons seem to be a period where there is a strong wave activity with a planetary wave period of around 8-12 days in the zonal component. This is understandable because this period is a transition time with strong trends in mean wind (e.g. Chshyolkova et al. (2006)).

Important characteristics of the waves are their amplitude, direction of propagation and the zonal structure (zonal wavenumber). Thus, in this thesis, the data range from 2001 to 2003 was selected for the purpose of deducing these characteristics, for wave periods of 5-day, 10-day, and 16-day. In this data range, the years 2001 and 2003 represent quiet years, and the year 2002 represents a disturbed year due to the stratospheric warming occurrence. To study the 5-, 10-, and 16-day waves in detail during the above mentioned three year period, the complex demodulation method was used. The complex demodulation method provides a sensitive measure of the frequency variations of the time series and allows the amplitude and phase of an oscillation to be described as a function of time. The correct choice of demodulation period will prevent the occurrence of phase trends. In order to define the predominant period of the wave activity the correloperiodogram spectra was calculated in the period range between 3 and 7 days for the 5-day wave, 8 and 12 for the 10-day wave, and 14 and 18 for the 16-day wave, where the wave period of interest was a centre frequency. An effective FFT band-pass filter was used to investigate the instantaneous wave characteristics. The figures from Figure (5.11) to Figure (5.13) illustrate the instantaneous amplitude (top panels) and their corresponding instantaneous phases (bottom panel) for the 5-, 10-, and 16-day wave for zonal (right panel) and meridional (left panel) components.

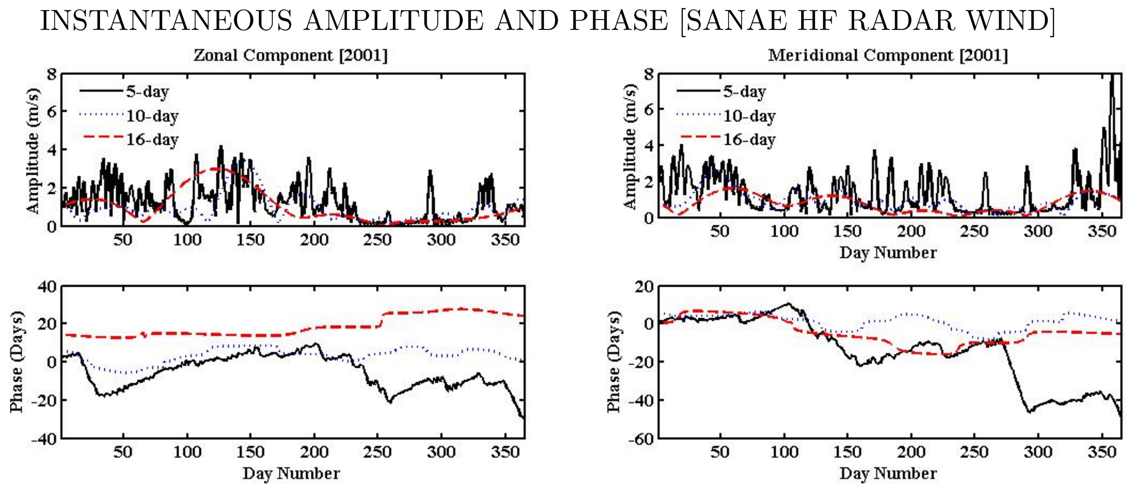

Figure 5.11: Instantaneous amplitude (top panels) and phase (bottom panels) of the 5-, 10-, and 16-day waves for year 2001 zonal (right panel) and meridional (left panel) components obtained by complex demodulation.

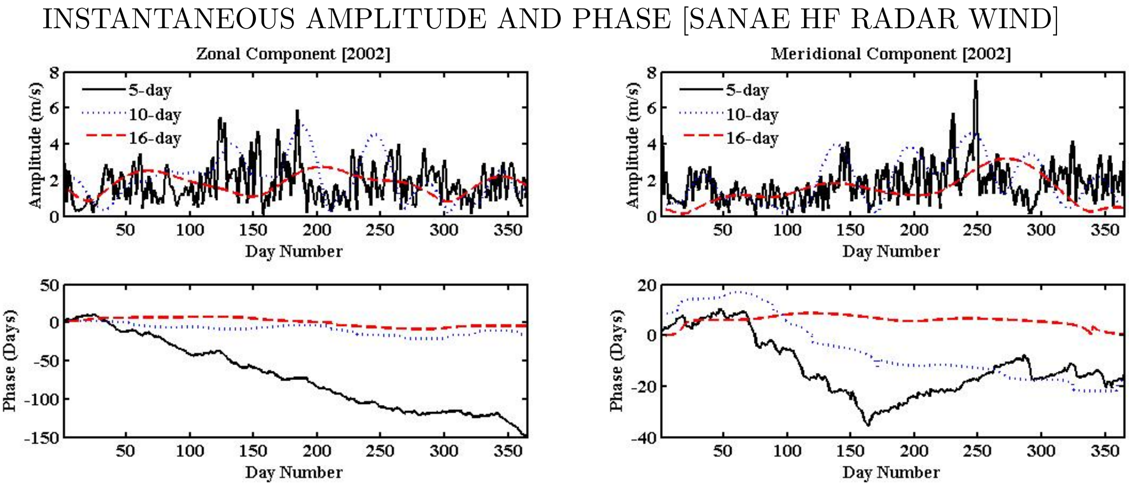

Figure 5.12: Same as Figure (5.11) but for year 2002.

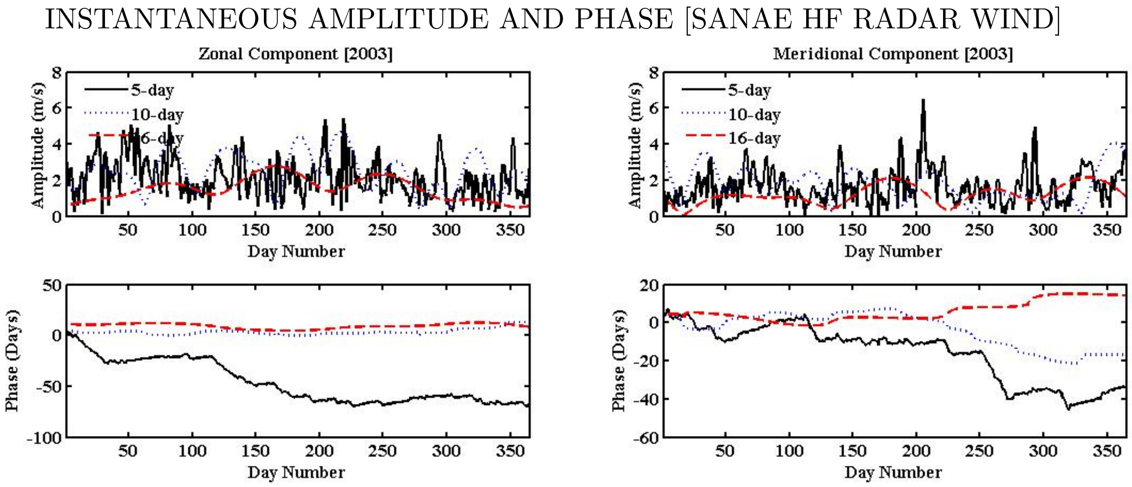

Figure 5.13: Same as Figure (5.11) but for year 2003.

There seems to be amplification of all three wave periods (5-, 10-, and 16-day) during the winter period in all the year, but in some cases there is a significant increase of amplitudes during the summer season. The amplification of the three wave periods in winter is understandable because the winter months are known for their strong planetary wave activity over a wide period (e.g. Chshyolkova et al. (2006)). The 5-day and 10-day wave seems to be the most dominant wave period in summer, possibly long period (>10 days) oscillations which are prominent in winter may disappear in the summer months, and oscillations with shorter period (<10 days) becomes dominant. In some cases the 5-day wave reaches a maximum of 8 m.s^{-1} (e.g. in the month of December 2001, meridional wind component).

In general, the reliability of the phase measurement for a given instrument decreases as the wave amplitude (Clark et al., 2002). However, this effect is not easy to quantify but depends on other components contained in the wind. The zonal component in Figure (5.11) shows that the 5-, 10-, and 16-day waves had increased amplitudes during day numbers from 100 to 250, and during this time the phase of all the wave periods was less variable. In the meridional component (Figure (5.11)), the best time to compare phase with phase in December where the 5-day wave increased to approximately 8 m.s^{-1}. During this period the phase decreased to about 30 days. The zonal component in Figure (5.12) shows that the the 5- and 10-day waves had strong amplitudes during the winter period, presumably due to the Southern Hemisphere 2002 major stratospheric warming effect. The meridional component of year 2002 also shows strong amplitudes of all wave periods excluding the 16-day wave, which only becomes strong in the autumn season. The phases of 5- and 10-day waves are observed to decrease as the amplitude increases in the winter period. While the 16-day wave seems to be weak during the winter months of 2002, its phase also seems to be less variable. The zonal component in Figure (5.13) shows that the 5-day wave has large amplitudes in both summer and winter, and its phase seem to have a negative slope. The 10-, and 16-day waves were also observed to be dominant in the winter period, with less variable phases throughout the year. The meridional wind component for year 2003 (Figure (5.13)) shows a strong 5-day wave in day 205, which reaches a maximum of ∼6 $\mathrm{m.s^{-1}}$. Another noticeable feature is the 10-day wave in the December, which reaches a maximum of 4 $\mathrm{m.s^{-1}}$, while its phase is observed to decrease gradually during this month.

5.3.2 Zonal Wavenumber

For the purpose of estimating the zonal wavenumber, the data from SANAE and Halley SuperDARN radar sites was used. These two stations are separated by ∼24 degrees longitude, which is a good enough separation to estimate reliable zonal wavenumbers. The zonal wavenumbers were derived from the slope of the linear regression of the 5-, 10-, and 16-day wave phases as a function of longitude during the winter and summer seasons. The phase obtained in this analysis was from the 28-day Fourier spectral analysis method because only phases that are well resolved in frequency are needed. This Fourier spectral analysis method is a dynamic Fourier spectra which uses a 28-day data window that is shifted forward by 1-day at a time. The deduced phase for a given data window was attributed to a central day given by day 14 of that particular 28-day data interval. This long data window results in the desired frequency resolution of 0.0357 cycles per day (cpd). The phases used here are only those for the central days which fall within the winter and summer seasons a time at which the spectral power tends to be above the 95% confidence level. The wavenumbers presented in this work are those at which both sites (SANAE and Halley) had data, and the coefficient of determination was 60%. In the results negative wavenumbers represent the westward propagating wave. The technique use to analyse zonal wavenumber in the present work was also used in the study of the quasi-two-day wave studied using the Northern Hemisphere SuperDARN HF radars by Malinga and Ruohoniemi (2007).

ZONAL WAVENUMBER EVENTS IN WINTER.

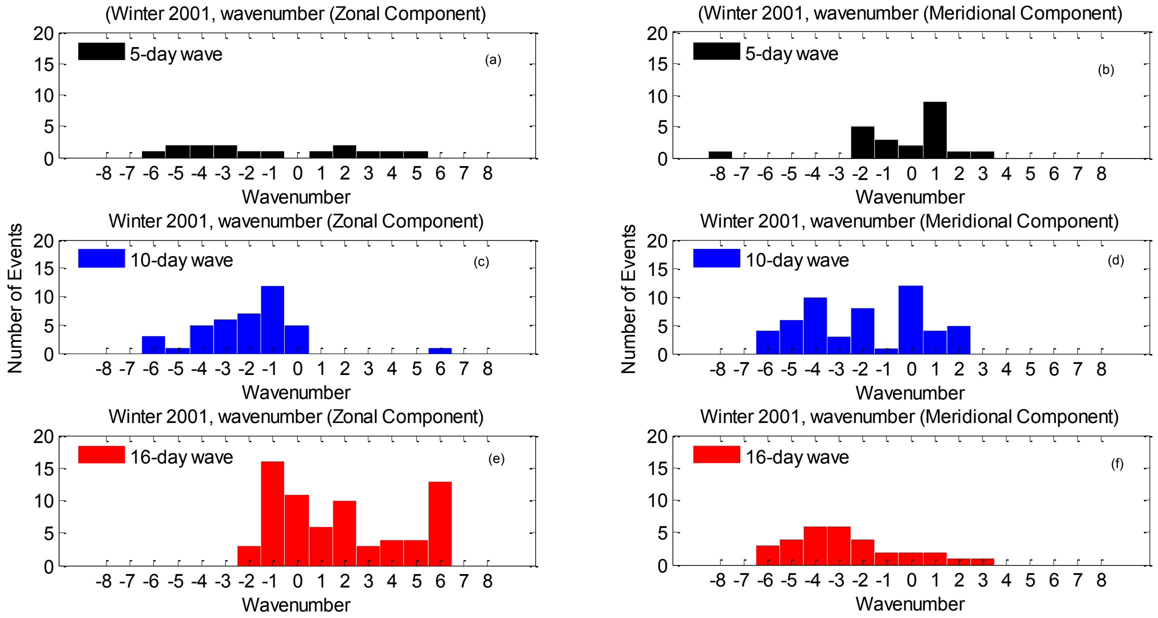

Figure 5.14: The distribution of the zonal wavenumbers for the zonal and meridional 5-, 10-, and 16-day components in winter. The negative wavenumbers represent the westward propagating wave.

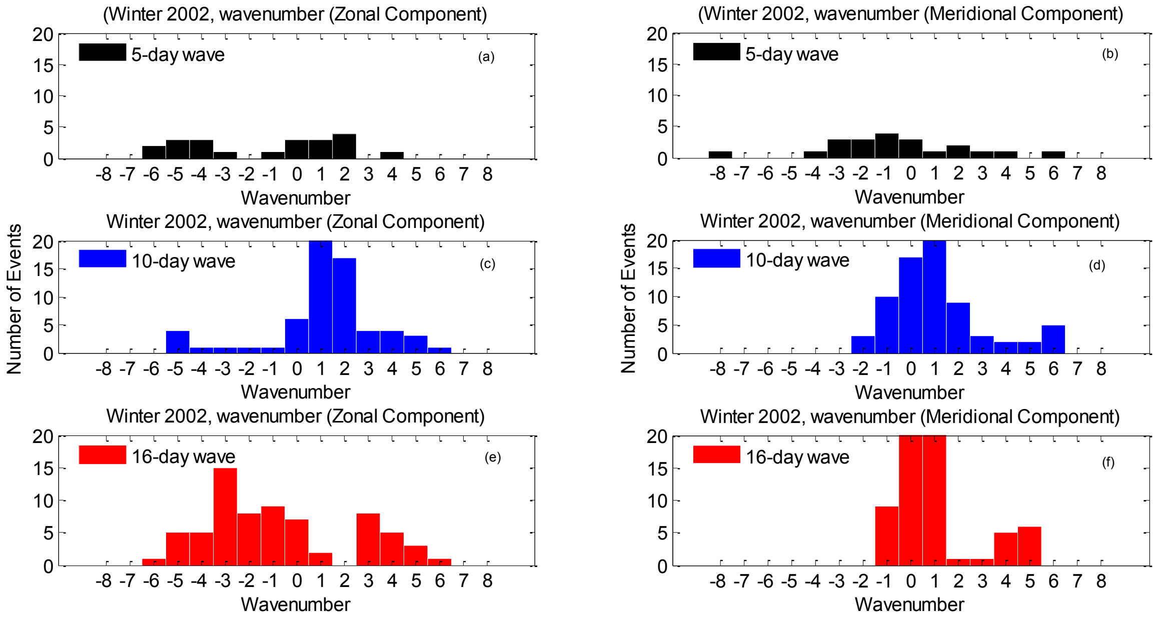

Figure 5.15: Same as Figure (5.14) but for the year 2002.

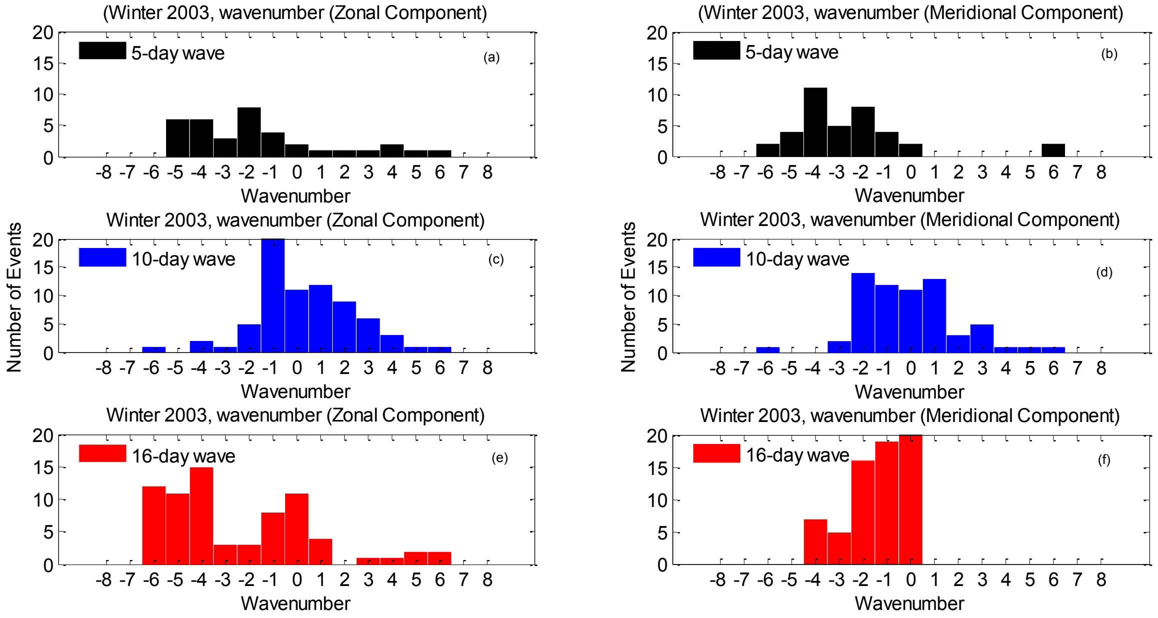

Figure 5.16: Same as Figure (5.14) but for the year 2003.

ZONAL WAVENUMBER EVENTS IN SUMMER.

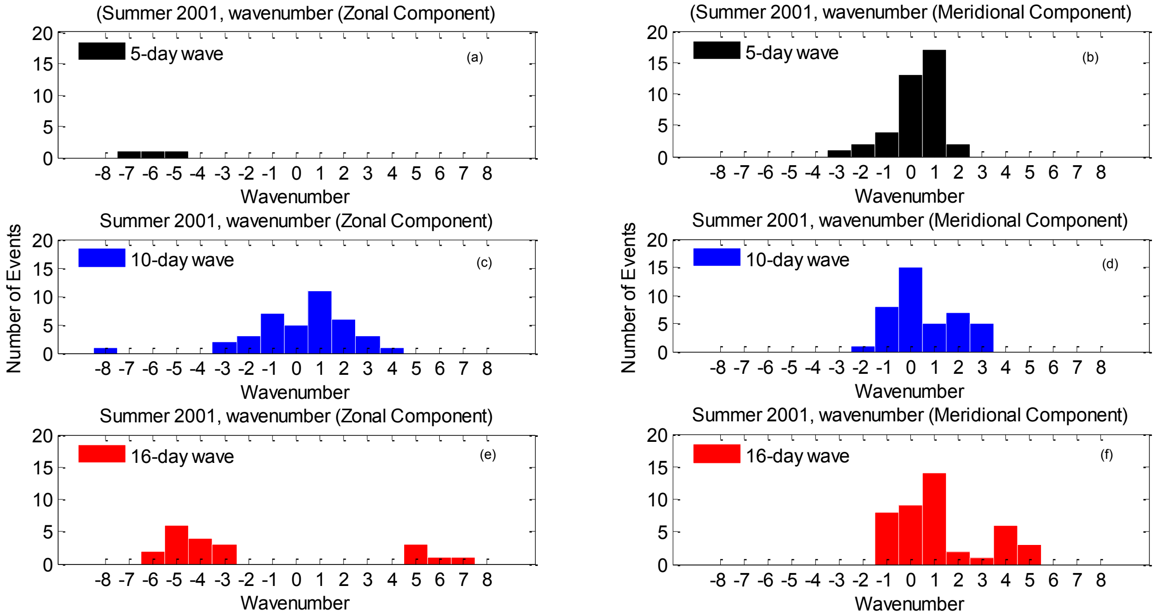

Figure 5.17: Distribution of the zonal wavenumbers for the zonal and meridional 5-, 10-, and 16-day components in summer. The negative wavenumbers represent the westward propagating wave.

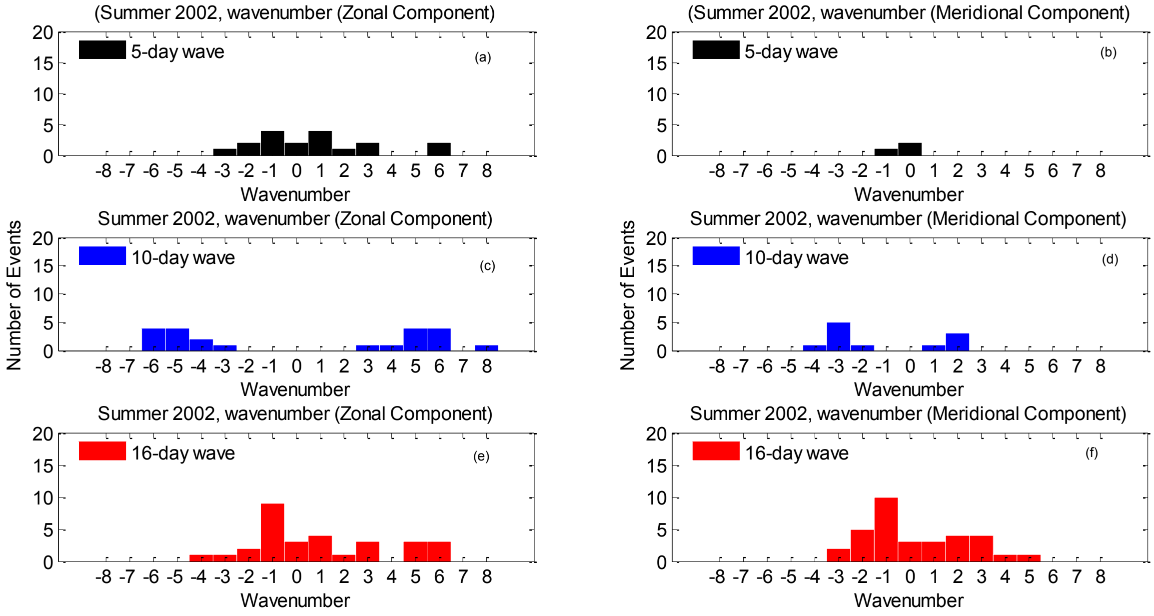

Figure 5.18: Same as Figure (5.17) but for the year 2002.

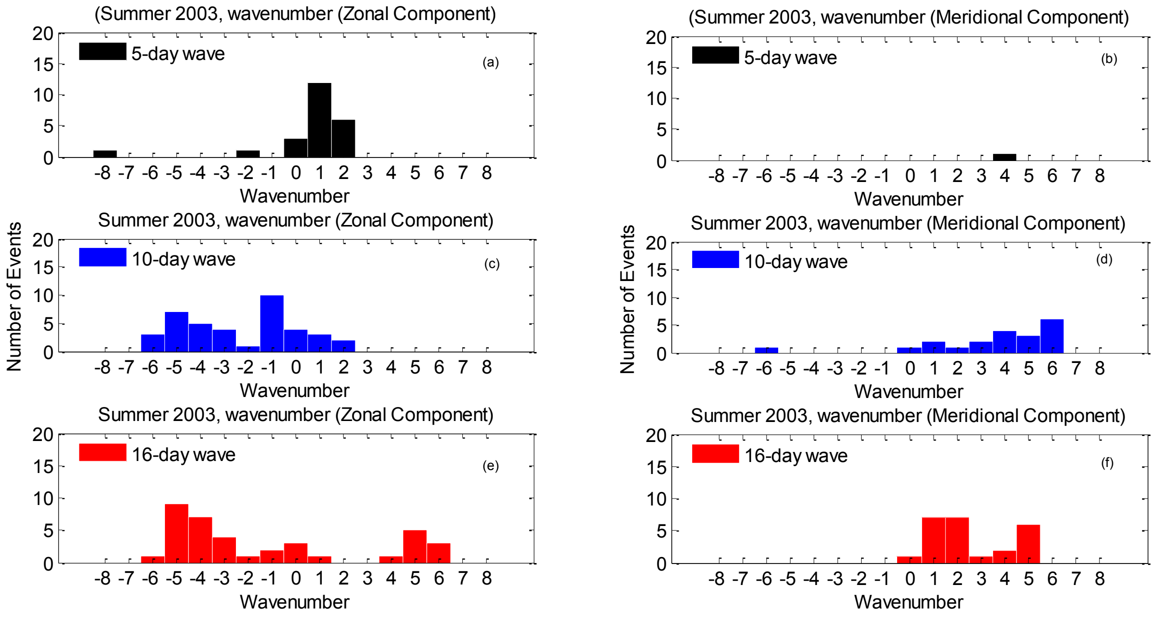

Figure 5.19: Same as Figure (5.17) but for the year 2003.

The above figures (Figure (5.14) to (5.19)) illustrate the distribution of the zonal wavenumbers for the zonal (right panel) and meridional (left panel) 5-, 10-, and 16-day components in winter and summer season, respectively. In the results, the negative wavenumbers represent a westward propagating wave. When comparing the two seasons, the winter season tends to be dominated by planetary wave activity of the 10-day and 16-day wave of shorter zonal wavenumbers (s=±3) both in the zonal and the meridional wind components. The observation of longer period planetary waves ($\geq$ 10 days) having shorter wavenumbers during the winter season is in agreement with the observations by Shiotani et al. (1993), Palo et al. (2005), and Pancheva et al. (2008). In summer, there is a wide distribution of wavenumbers, with shorter wavenumbers weaker compared to the winter seasons. The 5-day wave tends to have stronger shorter wavenumbers during the summer season. The observation of the 5-day wave wavenumbers seem to indicate that a 5-day wave is a wave characterised by bursts of wave activity that is variable on scales of several days (e.g. Pancheva et al. (2004); Malinga and Ruohoniemi (2007)). The dominant shorter wavenumbers of longer period observed in the winter period are understandable because the winter months are known for their strong planetary wave activity over a wide period (e.g. Holton (2004); Chshyolkova et al. (2006)). The 5-day wave in the middle atmosphere has also been shown to increase in amplitude during seasonal transitions.

For the meridional component of year 2001 summer, the 5-day wave zonal wavenumber s=0 and s=1 tend to be dominant when compared to the other years. For both the zonal and meridional flow of the year 2002 winter, there is a strong presence of s=0, s=1 and s=2, in the 10-day component. The 16-day component of the year 2002 winter meridional wind also tend to have dominant s=0 and s=1 component. Planetary waves of wavenumber s=0 and s=1 are believed to be responsible for the deceleration of the mean flow and the mesospheric cooling in the MLT during the major SSW in the Southern Hemisphere (e.g. Cho et al. (2004); Mbatha et al. (2010b)).

5.3.3 Planetary Wave Coupling in the Antarctica Middle Atmosphere

The climatology of planetary wave presented early in this work has shown that there is some sort of seasonal trend in the activity that can be seen in the MLT. The variation of planetary waves in the MLT can be related to the variation in planetary waves sources and source strength, to the critical level filtering in the stratosphere that can prevent waves from propagating through the level where their intrinsic frequency goes to zero, and to seasonal variation in the middle atmospheric parameters such as density and stability (Holton and Alexander, 2000). The stratosphere background wind and stability fields have important effects on the planetary wave activity in the stratosphere as well as their upwards propagation.

In this thesis the UKMO zonal mean zonal winds and meridional winds at 1-hPa ($\sim$49.5 km) was used to study the wave activity taking place in the stratosphere. The UKMO reanalyses data has proved to be very useful in understanding troposphere/stratosphere dynamical processes, and it has been used in many middle atmospheric research (e.g. Dowdy et al. (2004); Dowdy (2005); Chshyolkova et al. (2006); Pancheva et al. (2008)). The data period from January 2001 to December 2003 was used in this study, with years 2001 and 2003 serving as quiet years and 2002 a disturbed year (because of the major stratospheric warming in late winter). Thus, the data interval from 2001 to 2003 was selected in order to study planetary wave activity before, during and after the SSW even. Figure (5.20a and b) illustrate the UKMO zonal mean zonal wind and meridional wind, respectively, for the period from January 2001 to December 2003. The zonal mean zonal wind and meridional mean wind values were calculated by averaging over all longitudes at 70°S.

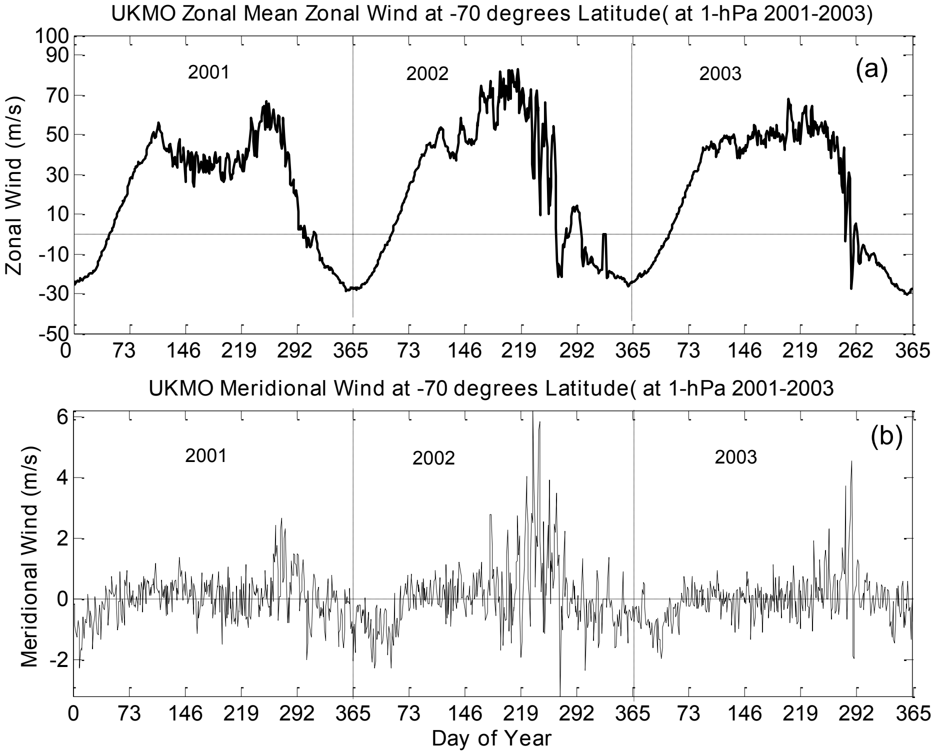

Figure 5.20: UKMO zonal mean zonal wind (a) and meridional winds plotted for the period from January 2001 to December 2003 for the 70°S latitude at 1-hPa (49.5 km).

The stratosphere region has temperatures which are generally lower over the winter hemisphere and higher during summer, and large meridional temperature gradients during solstice seasons which create strong stratospheric winds according to the thermal wind equation. In Figure (5.20a) the zonal mean zonal winds indicates a typical stratospheric circulation with strong eastward flow in winter and westward flow in summer at high latitudes. Generally, temperatures over the winter south pole are lower than over the winter north pole (e.g. Chshyolkova et al. (2006)). This creates stronger temperature gradients leading to stronger eastward winds in the Southern Hemisphere winter. The strong eastward winds are observed during the entire winter of year 2001 and 2003. In contrast, the year 2002 exhibits a very unusual variability in the dynamical sense for the Southern Hemisphere owing to the major stratospheric warming. This major stratospheric warming also had an influence in an unusual variability in the meridional wind (see Figure (5.20b)). The details of the year 2002 Southern Hemisphere major stratospheric warming are given in Chapter 6 of this thesis, and it has been studied by others (e.g. Baldwin et al. (2003); Dowdy et al. (2004); Dowdy (2005); Mbatha et al. (2010b)).

To investigate the planetary wave activity in both the stratosphere and MLT, the wavelet power spectrum for the duration from year 2001 to year 2003 and period between 2 and 20 days was performed. Figure (5.21) shows the wavelet power versus time (January 2001 to December 2003) and period (2–20 days) calculated for the zonal component of the (a) UKMO wind (49.5 km) for 70°S latitude and (b) SANAE HF radar ($\sim$ 94 km). The white dashed line in (b) indicates features that exceed the 95% confidence level. Figure (5.22) is same as Figure (5.21), but for the meridional component.

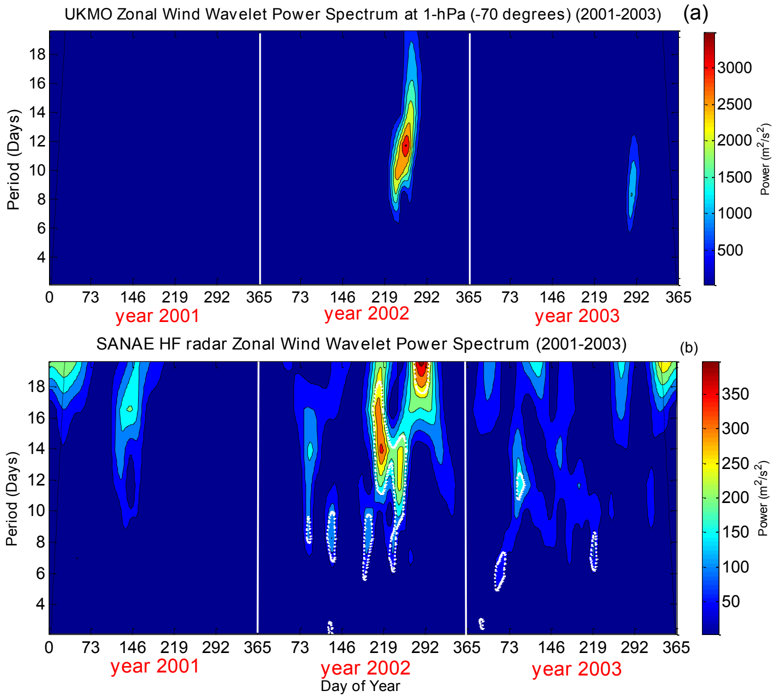

Figure 5.21: Wavelet power versus time (January 2001 to December 2003) and period (2–20 days) calculated for the zonal component of the (a) UKMO winds (1-hPa or 49.4 km) for 70°S latitude and (b) SANAE HF radar. The white dashed line in (b) indicates features that exceed the 95% confidence level.

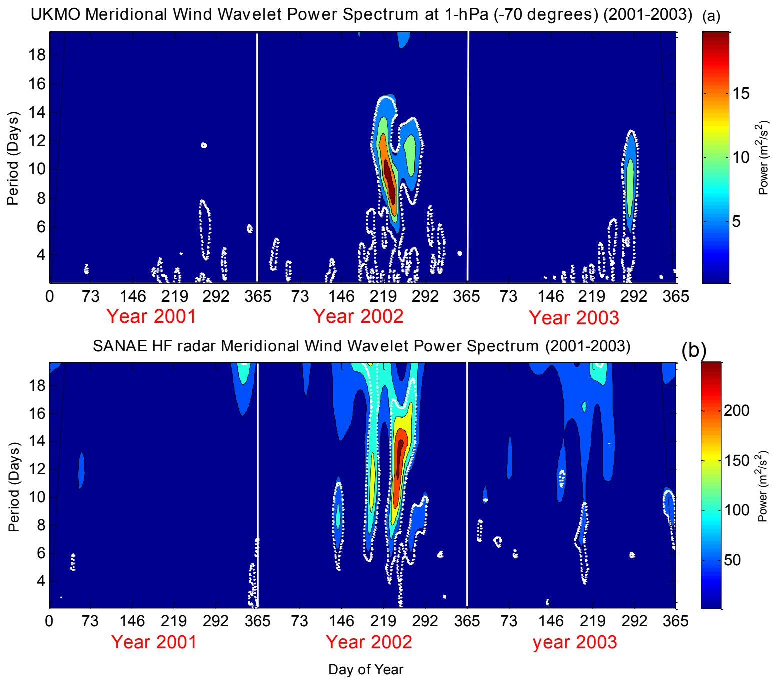

Figure 5.22: Same as Figure (5.21) but for meridional component.

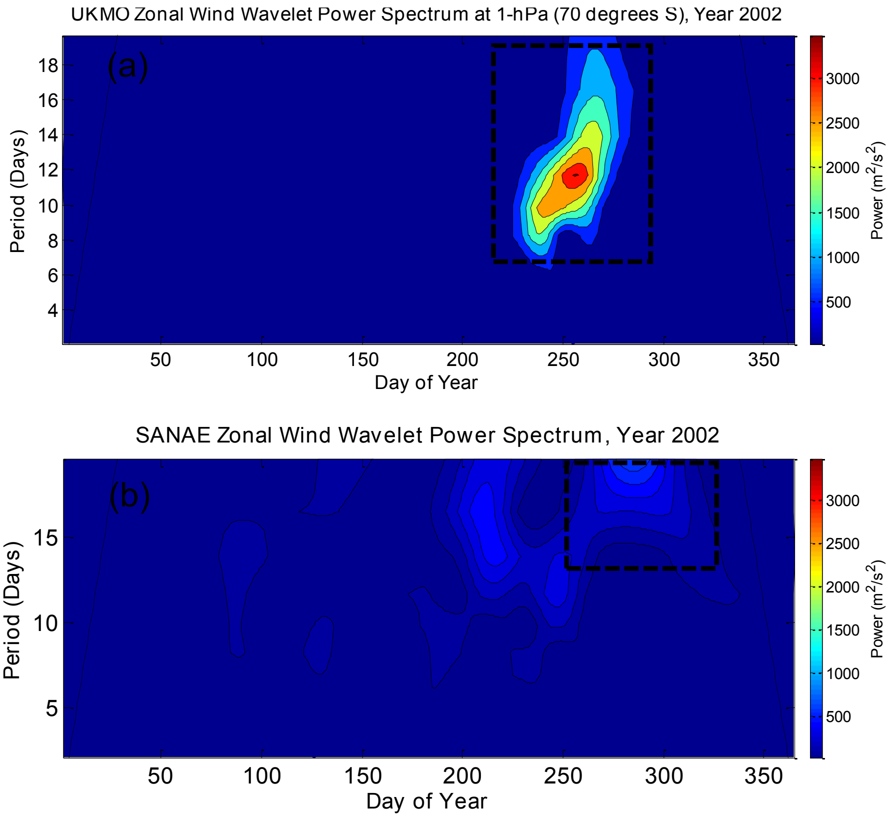

Figure 5.23: Wavelet power versus time (January 2002 to December 2002) and period (2–20 days) calculated for the zonal component of the (a) UKMO winds (1-hPa or 49.4 km) for 70°S latitude and (b) SANAE HF radar.

In contrast to the winter months where planetary wave activity in the year 2002 and 2003 exists in the winter at ∼94 km (see Figure (5.21b) and Figure (5.22b)), the UKMO stratospheric observations shows that the austral winter exhibits less planetary wave activity. There seem to be a weak planetary wave activity in particular in the middle of the austral winter, which is thought to be due to a consequence of the inability of planetary waves to propagate through the strongest zonal wind (Andrews et al., 1987). A planetary wave peak of period between 6 and 12 days is seen in the late 2003 austral winter in both the zonal and meridional component. The meridional component has a strong activity of planetary waves of periods less than 6 days in all the three years.

The year 2002 austral winter exhibits an obvious difference when compared to the year 2001 and 2003. Figure (5.23) illustrates the Wavelet power versus day number (January 2002 to December 2002) and period (2–20 days) calculated for the zonal component of the (a) UKMO winds (1-hPa or 49.4 km) for 70°S latitude and (b) SANAE HF radar. During 2002 winter, there are strong peaks around 10-15 days which are clearly seen in both wind components in the stratosphere (1-hPa) and MLT (∼94 km). This figure was plotted order to intensively investigate the wave activity in the stratosphere and the mesosphere, and also because the zonal wind is an important parameter to study planetary waves because of its power. Figure (5.23a) shows that there was a presence of wave which has a period between 8 and 20 days in the stratosphere. This planetary wave seems to begin at approximately day number ∼220 and it reach maximum power of 3500 m^2/s^2 during day number 250. As days goes by, this planetary wave is observed to reach periods above 14 days, and it also loses its power. The observations from this figure indicates that during the winter months of year 2002, the stratosphere was dominated by a quasi 10-day planetary wave which modified into larger periods as the days got closer to the occurrence of the SSW.

Figure (5.23b) illustrates that at the mesosphere there was presence of planetary waves prior and during the occurrence of the Major SSW. However, these planetary waves are observed to be weaker than in the stratosphere. Moreover, the mesosphere seems to have a wide range of planetary waves which were not observed in the stratosphere. But this is understandable because not all disturbances seen in the mesosphere are due to have propagated from the stratosphere (Chshyolkova et al., 2006). A noticeable future is a planetary wave with periods from 14 to 20 observed from mid September (see the rectangle in Figure (5.23b)). This planetary wave is observed to have maximum power of ∼550 m^2/s^2. This planetary wave seems to be related to the quasi 10-day wave which was observed in the stratosphere earlier. The 10-day wave may have increase with period as it propagates upwards. At the ∼94 km altitude this wave was observed to have periods between 14 and 20 days. The observations from these results agree with other studies that involve both the lower and the middle atmosphere (Liu and Roble, 2005; Chshyolkova et al., 2006). In the SANAE HF radar zonal wind data (∼94 km), the planetary wave observed to have periods ranging from 14 to 20 days in the late winter 2002, whiles other studies observed this wave to have periods of 14 to 16 days at the ~80 to 86 km altitude (Dowdy et al. (2004); Espy et al. (2005)). There is also a signature of a quasi 10-day wave in the mesosphere which is observed at around the same time with the quasi 10-day wave in the stratosphere. The signature maybe presumable due to the lower atmosphere originated gravity waves which are modulated by a strong quasi 10-day wave in the stratosphere, and carrying their momentum to the MLT region.

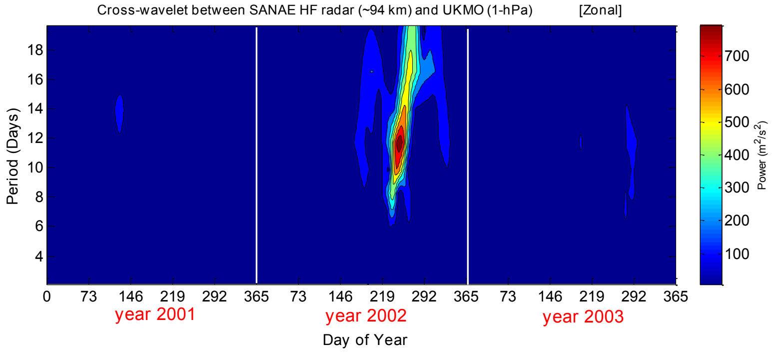

Figure 5.24: Cross-wavelet power versus time (January 2001–December 2003) and period (2–20 days) calculated for the UKMO (1-hPa) and SANAE HF radar zonal winds.

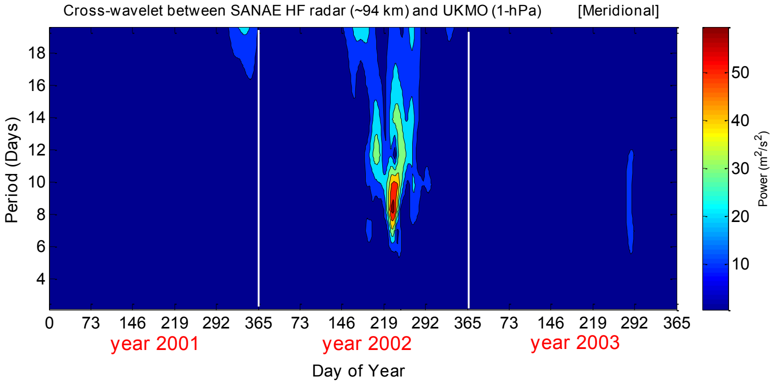

Figure 5.25: Same as Figure (5.24) but for meridional wind component.

In order to demonstrate a possible coupling between the stratospheric and the MLT heights in the Southern Hemisphere, cross-wavelets of UKMO winds at 70°S (1-hPa) and SANAE HF radar (~94 km) winds for the time interval from 2001 to 2003 were calculated. The cross-wavelet (Torrence and Compo, 1998) power spectrum was calculated as

$$W_{XY} = \widetilde{X}\widetilde{Y}^{*}, \tag{5.1}$$

where $\widetilde{X}$ and $\widetilde{Y}$ are the wavelet transforms for the time series data $X(t)$ and $Y(t)$, respectively, and the asterisk superscript indicates the complex conjugate. Figure (5.24) and Figure (5.25) illustrate the zonal wind (SANAE HF radar and UKMO) and meridional wind (SANAE HF radar and UKMO) cross-wavelets power spectrums, respectively. As expected the largest planetary wave activity is observed during the winter season (especially in year 2002), and almost nothing observed during summer period for the entire data range (January 2001 to December 2003).

There seem to be a strong wave coupling between the stratosphere and MLT which is observed in the winter season of year 2002. During this period there are strong peaks of about 8 to 20 days in September 2002 observed in the stratosphere and the MLT. Interestingly, these peaks are clearly indicated in the zonal and the meridional components. Beside the observation of strong vertical coupling between the stratosphere and the MLT especially during major events such as SSW, other authors have also reported a horizontal coupling between the Southern Hemisphere and the Northern Hemisphere (e.g. Chshyolkova et al. (2006)). Chshyolkova et al. (2006) investigated the possibility of the inter-hemispheric planetary waves propagation by calculating the cross-wavelet of the UKMO (1-hPa) zonal winds in the Southern Hemisphere and the Northern Hemisphere , and found some evidence of planetary wave coupling between the Southern and the Northern Hemisphere. They have also observed a coupling between the stratosphere and the MLT in the Northern Hemisphere.

There are indications of weak coupling between the stratosphere and MLT in year 2001 because the cross-wavelet spectrum indicated a quiet year. However, there is a quasi 14-day peak during the autumn season in the zonal component, which seem to be strong in the zonal wind component at ∼94 km. There are also indications of 1-hPa to 94 km coupling in late winter of 2003, in a form of weak planetary wave peaks near 8-12 days observed in both the zonal (Figure (5.24)) and meridional (Figure (5.25)) components. The peaks can be found in the both the stratosphere and MLT in the zonal and meridional components in Figure (5.21) and 5.22.

Planetary waves which are upward propagating from the troposphere depend crucially on the zonal mean flow, in such a way that only waves with phase velocities westward compared to the mean flow, or waves whose intrinsic phase velocities are less than some critical value (u_c) can propagate upwards (Andrews et al., 1987). In this work, in order to understand the strong planetary wave coupling in the stratosphere observed in the year 2002 winter, the background wind in the stratosphere was assessed in order to study the conditions of filtering. This would clarify whether the 14 to 18-day planetary wave that is observed in the MLT by the HF radar is indeed the quasi 10-day planetary wave observed in the stratosphere by the UKMO assimilated data. Thus, the UKMO assimilated stratospheric data was used. In addition, only the zonal wind component was considered because the meridional winds are relatively weak in the stratosphere, and thus can have only minor effect on the upward propagating planetary waves. Figure (5.26) shows the UKMO zonal mean zonal wind for the year 2001 (a) and 2002 (b) winter days at 70°S latitude. For comparison purposes, the panel on the left (year 2001) serves as a quiet year away from strong planetary wave activity, while the panel on the right is the year where there was a strong planetary wave coupling observed in the middle atmosphere.

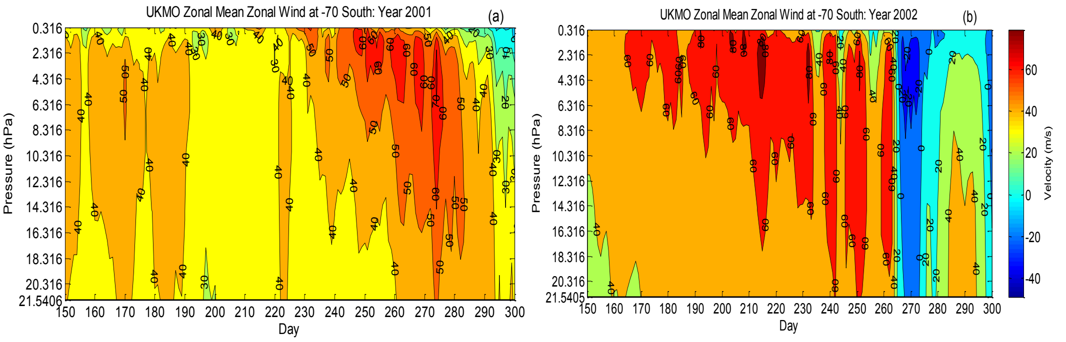

Figure 5.26: UKMO zonal mean zonal wind for the year 2001 (a) and 2002 (b) winter days at 70°S.

Figure (5.26a) illustrates strong eastward winds during the year 2001 winter days which are observed at the height region above 10-hPa (30 km). In contrast, the year 2002 winter (Figure (5.26b)) has periods (between day 230 and 260) where the zonal wind is very weak (<20 m.s^{-1}), before a major reversal of the zonal wind observed in the late September.

In the present thesis, the role of the above observed planetary waves in the transport circulation of the middle atmosphere was also discussed based on the planetary wave theory work by Andrews et al. (1987) and Holton and Alexander (2000). In the case of middle atmosphere, vertically propagating planetary waves linear wave theory based on the conservation of potential vorticity (e.g. Andrews et al. (1987)) shows that for waves stationary relative to the ground, the vertical wavenumber m satisfies the relation

$$m^2 = \frac{N^2}{f^2}\left[\frac{\beta}{\overline{u}} - \left(k^2 + l^2\right)\right] - \frac{1}{4H^2}, \tag{5.2}$$

where l is the meridional wavenumber, N^2 is the buoyancy frequency squared, and H the scale height. If the parameters such as $\overline{u}$, k, and l are known, Equation 5.2 gives the vertical structure of the wave. Therefore, for topographically forced solutions $m^2 > 0$ only if $0 < \overline{u} < u_c$ where

$$u_c = \left[k^2 + l^2 + \frac{f^2}{(4N^2H^2)}\right]^{-1}, \tag{5.3}$$

u_c is the critical zonal wind for which $m = 0$. For $m^2 > 0$, the planetary waves can propagate vertically, while for $m^2 \leq 0$ the planetary waves are trapped. Thus, it is now clear that for the stationary waves, vertical propagation is possible only in the presence of eastward winds that are less than the critical value, u_c. This is referred to as the Charney-Drazin criterion. In explaining the Charney-Drazin criterion, Holton and Alexander (2000) used an example of a wave with a meridional scale 12,000 km, and planetary wavenumber s=1 and showed that the above theory gives $u_c \approx 60$ m.s^{-1}. If the same calculation is performed more accurately using the spherical geometry and realistic winds give $u_c = 100$ m.s^{-1}. The critical value equation (Equation 5.3) clearly indicates that the u_c decreases as k and l increases. Basically, this means that the critical value is determined largely by horizontal wave scales. Practically, only zonal waves with wavenumber s=1 and s=2 can propagates significantly into the stratosphere, and this happens only in the winter hemisphere where $u_c > 0$ (Holton and Alexander, 2000). Thus, the Charney-Drazin criterion provides an approximate explanation of the absence of the stationary planetary waves in stratosphere during the summer months, and the dominance of planetary waves with wavenumber s=1 and s=2 during the winter months.

Using the Charney-Drazin criterion, one can explain the weak or no coupling in the middle atmosphere observed in year 2001 and 2003 as primarily due to the strong winter eastward zonal mean circulation. In contrast, in the year 2002 winter the weakening of the stratospheric eastward zonal mean flow may have allowed the eastward quasi 10-day planetary wave of wavenumber s=1 to propagate upward until it was detected in the MLT.

5.4 Discussion and Summary

Using SuperDARN HF radar wind data (zonal and meridional components) measured from SANAE and Halley, the mean wind mean wind and its seasonal trends and climatology over Antarctica at ˜94 km altitude has been studied. The seasonal and inter annual behaviour of the mean wind at the two SuperDARN stations was also compared. The climatology of planetary wave activity over SANAE was also studied. Using selected years, the vertical coupling between the MLT and the stratosphere was investigated. The findings of this study can be summarised as follows:

There is a good agreement between the two stations in both zonal and meridional mean flow. The zonal wind is observed to be consistently larger than the meridional wind. The zonal wind is consistently more eastwards at both stations with maxima occurring during the solstice months. The high latitude summer zonal mean flow at ∼94 km is observed to be weaker and more variable compared to the eastward winter mean wind circulation owing to tropospherically forced planetary waves propagating through the middle atmosphere. This pattern of the mean flow variation in the MLT is in line with observations reported by others (e.g. Baumgaertner et al. (2005)).

The meridional winds are observed to have a strong northward flow in the months of October to March, which is weaker in the months from April to June. Similar results were also reported by Malinga et al. (2004) on their study on long term variation of the mesospheric mean flow observed at Grahamstown (South Africa) and Adelaide (Australia). These results are also somewhat similar to annual cycle observation in the climatological mean of the year 1967-1986 at Molodezhnya (68°S, 45°E) reported by Portnyagin et al. (1993). Although the meridional wind component is observed to be weaker than the zonal wind component, it also indicated a good agreement between the observations from the two SuperDARN stations.

The wavelet power spectrum for both zonal and meridional wind components indicate an amplification of planetary waves especially in early and in late winter. In most cases, during summer months the long period oscillations which are dominant in winter disappear, and oscillations with shorter periods (e.g. <10 days) becomes dominant. Using complex demodulation method, the details of planetary waves with period 5-, 10-, and 16-days were studied during the time period between 2001 and 2003. The amplification of all the three wave periods in the winter months is observed, and it is understandable because the winter months are known for their strong planetary wave activity over a wide period. The 5-day wave seems to be the most dominant wave period in summer. This may be mainly because during the summer months long period (>10 days) oscillations which are prominent in winter may disappear, and oscillations with shorter period (<10 days) becomes dominant. In some cases the 5-day wave reaches a maximum amplitude of 8 m.s^{-1} (e.g. in the month of December 2001, meridional wind component). The zonal wavenumbers of the 5-, 10-, and 16-day wave during the summer and winter of year 2001, 2002 and 2003 were also calculated in this study. The results show that the winter season tends to be dominated by planetary wave activity of the 10-day and 16-day wave of shorter zonal wavenumbers ($s=\pm3$) both in the zonal and the meridional wind components. Whiles, the 5-day wave tends to have stronger shorter wavenumbers during the summer season. The 16-day component of the year 2002 winter meridional wind also tends to have dominant $s=0$ and $s=1$ component.

Chshyolkova et al. (2006) used the cross-wavelet analyses methods to study the coupling between Southern and Northern Hemisphere at 1-hPa, and the coupling between the MLT and the stratosphere using UKMO (1-hPa) and MF radar data (80 km) in the Northern Hemisphere. In the present work, the same method was used in order to study the coupling between the MLT (SANAE HF radar data at ∼94 km) and the stratosphere (UKMO data at 1-hPa) during the time period between 2001 and 2003. There is indication of weaker planetary wave coupling between the stratosphere and MLT in year 2001 and 2003, but in the year 2002 a strong planetary wave coupling between the stratosphere and MLT was observed during winter season. Given the observation of the eastward travelling quasi 10-day wave (Dowdy et al. (2004)) that was detected in the stratosphere (1-hPa) and later observed later as 14 to 20-day wave in the MLT by the SANAE SuperDARN HF radar, it was concluded that planetary waves probably originated from lower atmosphere and was able to propagate to the mesospheric heights.

In contrast to strong stratospheric eastward zonal mean flow in the year 2001, in the year 2002 winter there were periods (between day 230 and 260) where the zonal wind was very weak (<20 m.s^{-1}), before a major reversal of the zonal wind observed in late September. Using Charney-Drazin criterion it is concluded that during the year 2002 winter the weakening of the stratospheric eastward zonal mean flow may have allowed the eastward propagating 14-day planetary wave of wavenumber $s=1$ to propagate upward until it was detected in the MLT. The details about the Charney-Drazin criterion are also well explained in the study by Holton and Alexander (2000).

Chapter 6

The Year 2002 Southern Hemisphere SSW

6.1 Introduction

The first ever detection of a major Sudden Stratospheric Warming (SSW) in the Southern Hemisphere occurred during 2002 Antarctic winter (Baldwin et al., 2003). During this exceptional event the 60°S wind at 10-hPa reversed on the 26^{th} of September, before it returned to a weak flow on about 15^{th} of October (see Figure (6.1)). During this 2002 winter period the circulation in the stratosphere was characterised by a series of planetary wave events that weakened the polar vortex, preconditioning the stratosphere for the major warming in late September (Baldwin et al., 2003; Dowdy et al., 2004).

Due to the vertical coupling that exists in the various regions of the atmosphere, it is expected that the major SSW in the Southern Hemisphere would have influence on other regions of the atmosphere such as mesosphere and lower thermosphere (MLT). In the previous chapter, the vertical coupling in the middle atmosphere was investigated using data time interval from 2001 to 2003 measured by SANAE HF radar and UKMO, respectively. It was observed that this coupling is stronger in the year 2002. The climatology of wind and planetary waves for the year 2002 presented in Chapter 5 was observed to be different when compared to the other years. Thus, this chapter is aimed at reporting on the year 2002 major SSW and its influence in the stratosphere and MLT. Most of the content in this chapter has been published in Mbatha et al. (2010b).

Usually planetary scale waves are generated in the troposphere by topographic and thermal features, and propagate up into the middle atmosphere. The instabilities arising from horizontal and/or vertical gradients in the temperature and wind disturbances can also induce planetary waves. Because of the topography of the Northern Hemisphere, planetary wave energy is significantly large in the Northern Hemisphere compared to the Southern Hemisphere, and hence the usual detection of the SSW in the Northern Hemisphere. Planetary and gravity waves are critical for mixing processes and for the Brewer-Dobson circulation in the middle atmosphere. The winter hemisphere is dominated by large amplitude stationary planetary waves which originate from the troposphere. Intermittently these waves break, stirring air more or less isotropically across large distances of the stratosphere within a region that has become known as the ”surf zone”, bounded by sharp gradient of potential vorticity (PV) and of tracers in the winter subtropics and the edge of the polar vortex (Plumb, 2002; Sivakumar et al., 2004).

A study by Dowdy et al. (2004) used three medium frequency radars located at Davis (69°S, 78°W), Syowa (69°S, 40°W) and Rothera (68°S, 68°W) to study the dynamics of the MLT during the Southern Hemisphere 2002 SSW. In their study, the most noticeable feature was the reversal of the mesospheric zonal winds a week earlier before the reversal in the stratosphere, and a different winter mesospheric wind pattern in 2002 compared to the other years, primarily due to the increase of planetary wave activity during winter. This behaviour shows similarities when compared to studies of the major SSWs in the Northern Hemisphere. Studies of SSW in the Northern Hemisphere usually report events such as mesospheric cooling and zonal wind reversal as a result of the SSW (Whiteway and Carswell, 1994; Pancheva et al., 2000; Labitzke and Naujokat, 2000; Hoffmann et al., 2002; Jacobi et al., 2003; Cho et al., 2004; Hoffmann et al., 2007). Observations by (Hoffmann et al., 2002) and (Hoffmann et al., 2007) showed that mesospheric cooling and MLT zonal wind reversals occur prior to the SSWs.

Although there are a number of MF radars in Antarctica, any available wind measurements, especially from a global network of identical instruments like SuperDARN is a desirable option for studying wind dynamics, atmospheric waves, and associated characteristics in the MLT region, especially during major events such as SSWs. In recent years, there has been an increase in a number of studies which utilise the HF radar wind data to study the MLT dynamics (e.g. Bristow et al. (1999); Hussey et al. (2000); Espy et al. (2005); Malinga and Ruohoniemi (2007); Mbatha et al. (2010b)). Dowdy et al. (2004) used MF radars with operation frequencies between 1.94 and 2.40 MHz in their study. In this study, the SANAE SuperDARN HF radar with operating frequency between 8 and 20 MHz has been used. The procedure used to retrieve wind data from SuperDARN (Greenwald et al., 1995) is different from the MF radars. To study the unprecedented 2002 September SSW influence in the MLT using SuperDARN radar wind data also contributes to the understanding of the dynamics of the MLT in September 2002. Espy et al. (2005) proved the capabilities of SuperDARN HF radars to study the SSW events by examining meridional winds from Syowa, SANAE and Halley stations and also the Rothera MF radar in order to assess whether long quasi-periodic oscillations in 2002 has a longitudinal phase progression characteristic of planetary waves.

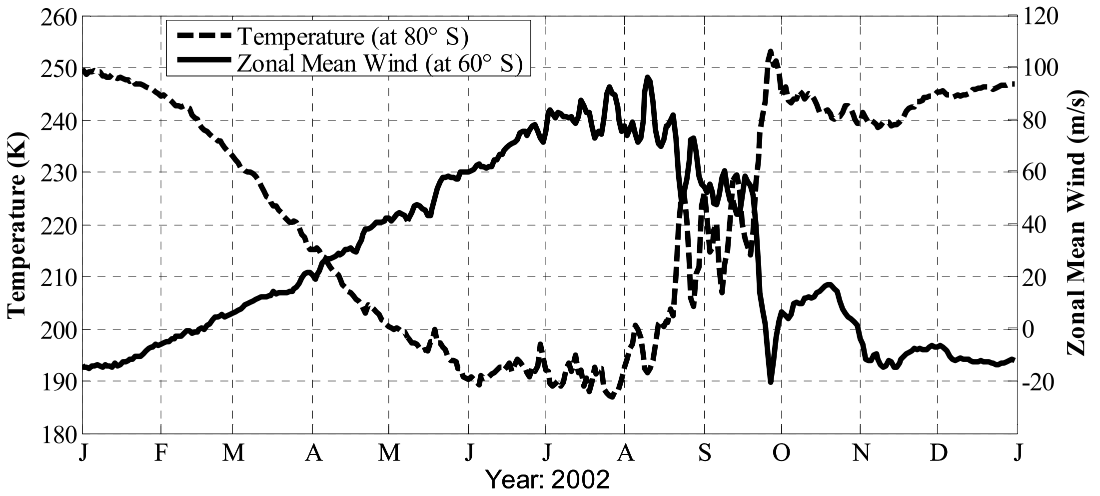

Figure 6.1: 2002 records of daily zonal mean wind at 60°S (solid line) and temperature at 80°S (dotted line) from NCEP reanalysis at the height of 10-hPa (32 km).

Apart from using the SuperDARN HF radar wind data, the UKMO wind and temperature data was also used to study the wind, temperature, and planetary wave activity during the year 2002 winter period. The Eliassen-Palm (E-P) flux diagnostics was used to interpret planetary waves in terms of their propagation and trajectory in the meridional plane. The E-P divergence and vector was calculated using the ECMWF ERA-40 reanalyses data. The SABER instrument data on board the TIMED satellite measurements, is used to examine temperature structure in the middle atmosphere during the 2002 SSW event.

6.2 The 2002 SSW (Wind and Temperature)

6.2.1 Mean Wind at the MLT

Figure (6.2) shows the daily averaged zonal (a) and meridional (b) wind derived from SANAE HF radar observations from the start of July until the end of November 2002 (black dashed line), superimposed on the average wind and its standard deviation values based on the same observations from 2003 to 2006 (Gray line). SANAE HF radar data is smoothed by a 4-day running mean. The years from 2003 to 2006 were identified as the period where there is no SSW observed. Therefore the 2003-2006 averages represent background wind patterns.

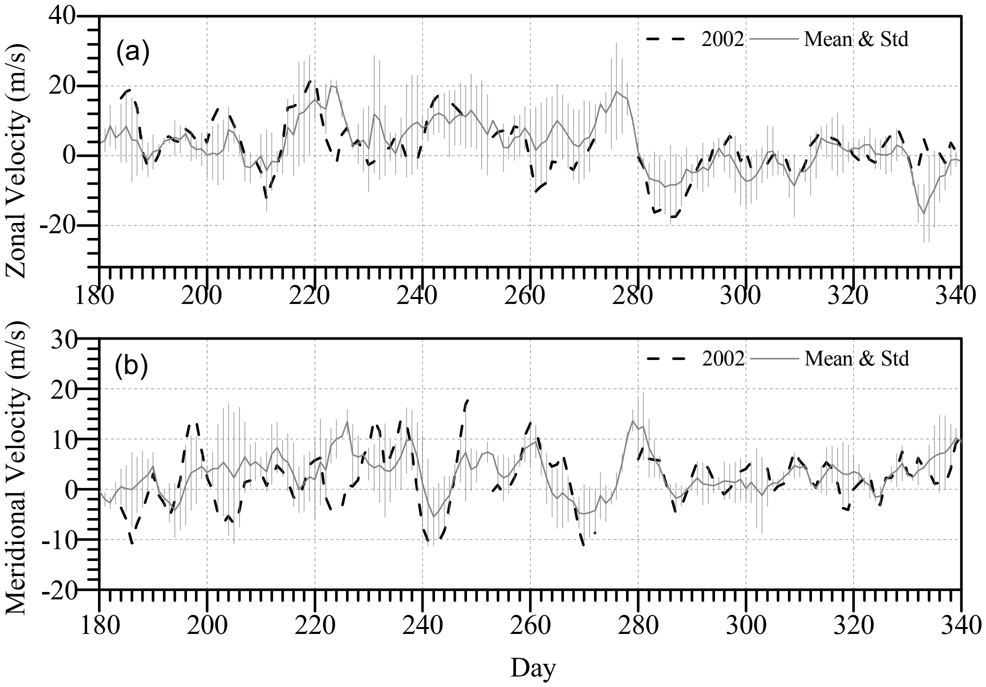

Figure 6.2: Time evolution of daily averaged (a) zonal and (b) meridional velocities obtained from SANAE HF radar observations from 1 July to late November 2002. Each figure is superimposed with the 2003-2006 mean profile with standard deviation.

During the period of July to November, one can see from Figure (6.2a) that eastward winds are primarily dominant in the polar winter in the MLT region particularly during August and September. The reversals of mean wind begin at around the beginning of July, which is approximately two months before the occurrence of the SSW in late September. The reversal of the zonal wind which is associated with the SSW event is well outside the standard deviation of the 2003 to 2006 average, and starts on the 18 September (day 261, from Figure (6.2a)). The reversal persisted for a few days before it returned to eastward direction on 27 September (day 270). However, in the stratosphere the zonal wind reversed on the 25^{th} of September 2002 (Figure (6.1)) leading to the unprecedented major SSW in the Southern Hemisphere. This is consistent with results from Dowdy et al. (2004). Dowdy et al. (2004) used MF radars at polar locations to study the 2002 SSW and reported that the zonal wind in the mesosphere became westward on day 261 (18 September), approximately a week earlier than the 10-hPa (∼32 km) winds turned westward. The meridional mean winds during 2002 also show an enhancement during the period of the occurrence of the SSW event and this feature is not seen in the other years (see Figure (6.2)). Maximum reversals of meridional mean winds are seen on day 242 (30 August 2002) and 270 (27 September 2002).

6.2.2 Mean Wind Reversal at the Stratosphere and MLT

Figure (6.3) shows the time evolution of the zonal wind at 10-hPa (∼32 km) derived from the NCEP at 60°S during the period from 250 to 300 Julian days in 2002. The zonal wind observations from SANAE HF radar (for ∼94 km MLT height) are superimposed with a solid black line. The SANAE HF radar data is smoothed by a 4-day running mean.

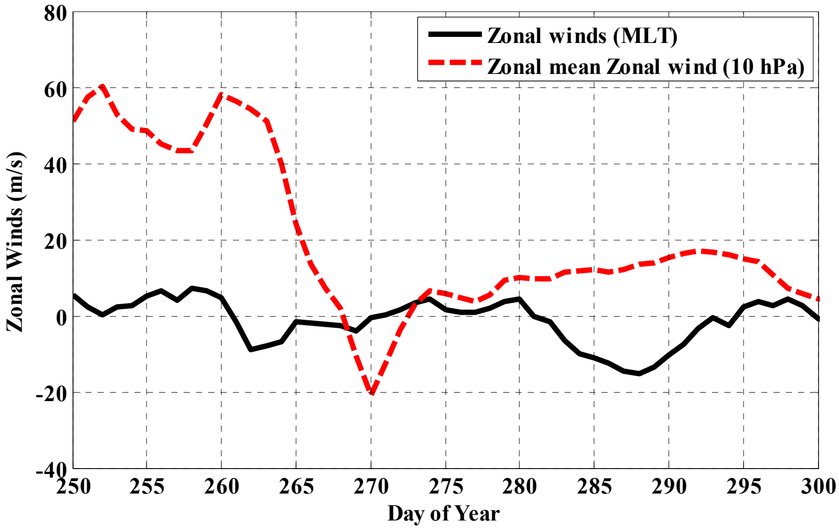

Figure 6.3: Zonal wind evolution in the MLT region (∼94 km) obtained by SANAE HF radar (solid black line) during the period from 250 to 300 of 2002-Julian days. The red dashed line illustrates the zonal-mean zonal wind variation at 10-hPa (∼32 km) derived from NCEP reanalyses at 60°S for the same period of time.

The figure shows that the zonal wind started to reverse (became westward) in the MLT region on the 261th 2002-Julian day (18 September), i.e., about a week earlier than the reversal of the zonal wind in the polar stratosphere at ∼10-hPa pressure level. The reversal in the MLT reaches a maximum magnitude of about -10 m/s on day 263 (20 September 2002). The MLT zonal winds reversal lasted for a few days and thereafter returned to the eastward direction for more than 7 days, before another reversal which starts on day 282 (9 October 2002) and persists until the beginning of summer. The reversal in the stratosphere began on the 268th day and reached its maximum amplitude of -20 m/s on day 270 before it turns back to the eastward direction on day 273. It is noted here that the daily variability of the zonal wind may vary from day-to-day and time-to-time, but it is found to be within ±8 m/s.

6.2.3 Potential Temperature (∼32 km)

Figure (6.4) shows the Southern Hemisphere NCEP potential temperature maps at 10-hPa (∼32 km) for selected days in August and September 2002 leading up to the major SSW of late September (Azeem et al., 2010). This figure clearly indicates that at the start of the sequence the basic cyclonic polar vortex is well established and is centred just off the pole at 60°S. Thereafter, the distortion of the polar vortex can be seen to commence on 18 August due to minor warmings. Other distortions are also seen in early September due to the presence of minor warmings. On 25 September the polar vortex splits into two cyclonic cells indicating the commencement adapted from a major stratospheric warming.

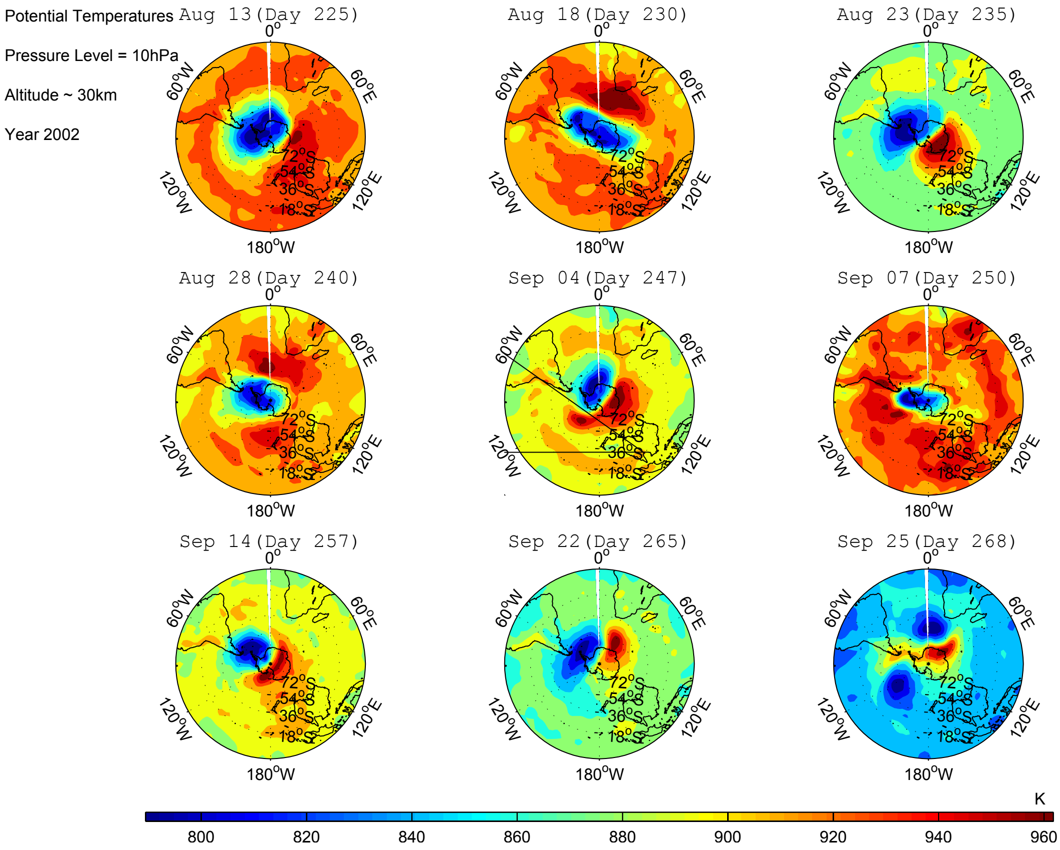

Figure 6.4: Southern Hemisphere potential temperature maps at 10-hPa pressure level for selected days in August and September of year 2002 (from Azeem et al. (2010)).

6.3 The Eliassen-Palm (E-P) Flux Cross Sections

Planetary waves associated with wavenumber 1, 2, and to a lesser extent, 3 seem to be the most prominent wave patterns in the troposphere and the middle atmosphere during the winter seasons (Hartmann et al., 1984; Bencherif et al., 2007). As mentioned earlier, these planetary waves are generated in the troposphere through processes tied to large-scale geographical features. Most notably, most of the wave-mean flow interaction diagnostics studies have been applied in the Northern Hemisphere data, primarily due to many occasions of strong wave-mean flow interactions during the common occurrence of the major stratospheric warmings. In order to understand processes behind the unprecedented state of the middle atmosphere in the late Southern Hemisphere winter of year 2002, it is essential to study the wave-mean flow interaction in the Southern Hemisphere. Details of previous studies of the wave-mean flow interaction in the Southern Hemisphere are given by Hartmann et al. (1984) and Semane et al. (2006). The Eliassen-Palm (E-P) flux diagnostics is used to interpret planetary waves in terms of their propagation and trajectory in the meridional plane. In this study, the theoretical formulation given by Edmon et al. (1980) was used to deduce the E-P vector ($\mathbf{F}$) and its divergence ($\nabla.\mathbf{F}$) from the ECMWF ERA-40 reanalyses data. The E-P flux vector and its divergence is defined by the following equation (Edmon et al., 1980; Andrews et al., 1987)

$\mathbf{F} = \left\{\mathrm{F}_{(\phi)}, \mathbf{F}_{(z)}\right\} = \left\{-\rho_0 a \cos\phi \left(\overline{v'u'}\right), f\rho_0\theta a \cos\phi \left(\frac{\overline{v'\theta'}}{\overline{\theta'}}\right)\right\}$ and

$$\nabla.\mathbf{F} = \frac{1}{a\cos\phi}\left(\mathbf{F}_{\phi}\cos\phi\right)_{\phi} + \left(\mathbf{F}_{(z)}\right)_{z}. \tag{6.1}$$

where ϕ represents latitude, (u, v, w) the 'velocity' in (longitude, latitude, pressure) coordinates, θ the potential temperature, a the Earth's radius.The over-bars denote the zonal mean and the primes denote the deviations with their respective means. Parameters. The other symbols have their usual meaning. Further explanations are given in Chapter 1, section 1.31, and also by other authors (e.g. Edmon et al. (1980); Andrews et al. (1987)). The orientation of the the E-P flux vector indicates the direction of the planetary wave propagation (Andrews et al. (1987)). Generally, in the mid-latitudes and high-latitudes, planetary wave activity is usually observed to propagate from the winter troposphere up into the stratosphere and mesosphere and towards the equator (Eliassen and Palm, 1961). In some cases the wave planetary activity originating from the winter troposphere is observer to propagate up into the stratosphere and mesosphere and towards the pole (Eliassen and Palm, 1961).

For the purpose of studying the year 2002 SSW dynamics, the days before and during the onset of the SSW were selected. The E-P cross-section diagrams for the Southern Hemisphere plotted for the dates of 1, 11, 20, 21, 23, and 25 September 2002 are shown in Figure (6.5). The E-P flux vectors ($\mathbf{F}$) are represented with arrows. The contours represent $\nabla.\mathbf{F}$ in m.s^{-1}; negative values are shaded. The contour interval is 2 m.s^{-1} per day, and the dashed contours correspond to the values of more than 10 m.s^{-1} per day or less than -10 m.s^{-1} per day. The zero line has been overlaid (thick black contour). The direction of the E-P flux vectors indicate the active vertical propagation of the wave flux for planetary wave propagation with height and from one latitude to another. Planetary wave breaking is identified by the convergence of the E-P flux (i.e. negative values). The 2002 major stratospheric warming started approximately on 18 September 2002 and persisted for about a week, thus the 1st and 11th of September represents the days before the SSW whiles the 20th, 21st, and 25th of September represents the days during the SSW.

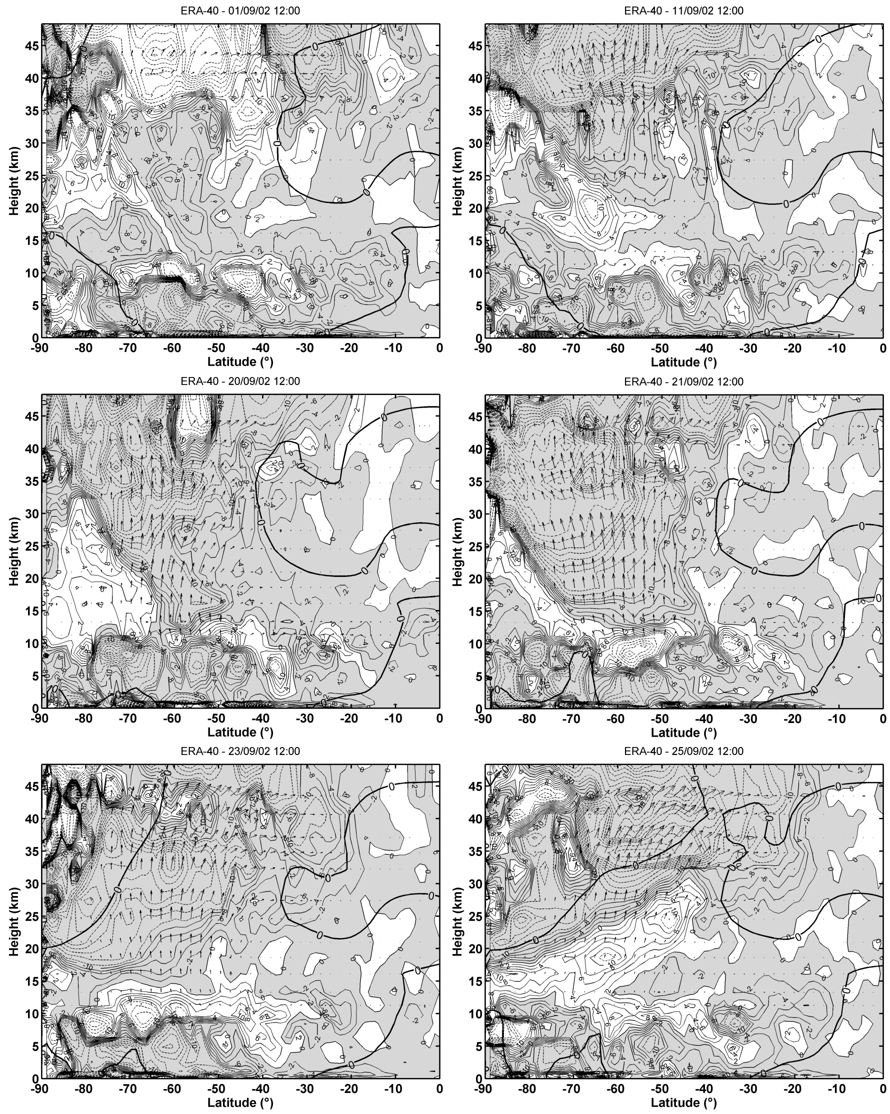

Figure 6.5: Eliassen-Palm cross-sections in the meridional plane for selected days of 1, 11, 20, 21, 23, and 25 September 2002.

During 1 September 2002 it is evident that there are few E-P arrows in the troposphere, indicating less planetary wave activity propagating from the troposphere. However, at the stratospheric heights the E-P arrows with a strong equatorward component are observed. This E-P flux component seems to be responsible for the minor SSW observed in late August 2002 (see Figure (6.1)). On 11 September there seem to be a strong activity of upward propagating waves indicated by longer length of E-P arrows. During the few days of the beginning of the major stratospheric warming (20 and 21 September), there is strong upward movement in the mid-latitudes lower stratosphere and upper stratosphere, with longer E-P arrows.

On the 21^{st} of September, the driving of the mean flow in the stratosphere seems to exhibit a dipole structure with some wave flux vectors indicating acceleration of the mean flow on the poleward flank of the stratospheric jet and deceleration equatorward of the jet ore.

On 25 September a strong equatorward E-P flux component was observed in the upper stratosphere. When comparing all the figures, there seems to be a tendency of an increase of the stratospheric wave activity during the period from 1 to 25 September. The strong upward planetary wave propagation seem to be dominant over the mid- and high-latitude regions. The E-P flux vectors are observed to have a tendency of bending equatorward with height. The equatorward directed E-P flux vectors are known to generate convergence of the E-P flux (e.g. Semane et al. (2006)). In this study, the convergence of the E-P flux is observed to be dominant over the high-latitudes, mid-latitudes and subtropics, indicating intense wave penetration and enhance wave driving in stratosphere. The convergence associated with the wave penetration and wave driving is observed to reach minimum values lower than -8 m.s^{-1} during the period from the 11 to 25 September.

The E-P flux figures above illustrate that much of the acceleration of the zonal wind in troposphere during the year 2002 winter was provided by strong planetary wave activity. The planetary waves of zonal wavenumber s=1 have previously proved to produce almost all of the upward wave flux at approximately 20 km and above, and all eddy-driving of the mean flow in the upper stratosphere (e.g. Hartmann et al. (1984)). The lowest wavenumbers (e.g. wavenumber 1, 2 and 3) are most likely to produce rapid deceleration of zonal mean circulation and associated increase of temperature in stratosphere, which is thereafter referred as the major SSW. The middle atmosphere wave activity during the 2002 winter SSW is discussed in details in the next sections.

6.4 Planetary Waves

6.4.1 Planetary Waves in the Stratosphere and Lower Mesosphere

As mentioned in previous sections, planetary waves play a huge role in the formation of the major SSW events. The analysis of the Southern Hemisphere stratospheric data by Kruger et al. (2005) during the 2002 major SSW demonstrated the role of planetary wave forcing in preconditioning the atmosphere prior to this event. Studies such as Kruger et al. (2005) and Palo et al. (2005) reported the wave interaction between eastwards propagating waves with periods near 10 days, quasi-stationary planetary waves, and the zonal mean atmospheric state that was eventually driven towards total break-down of the polar vortex and a major SSW on the stratosphere. In the Southern Hemisphere winter the coexistence of eastward propagating waves with periods between 7 and 23 days (usually with zonal wavenumbers s=2) and quasi-stationary planetary waves (predominantly zonal wave number s=1) is a common feature (Shiotani et al., 1993; Fedulina et al., 2004; Palo et al., 2005). The above mentioned scenario is the analog of the more familiar midwinter warmings in the Northern Hemisphere where travelling waves are primarily westward propagating, and is reminiscent of the minor Southern Hemisphere midwinter warming during 1988 which involved eastward propagating wave of a 10-day period (Hirota et al., 1990).

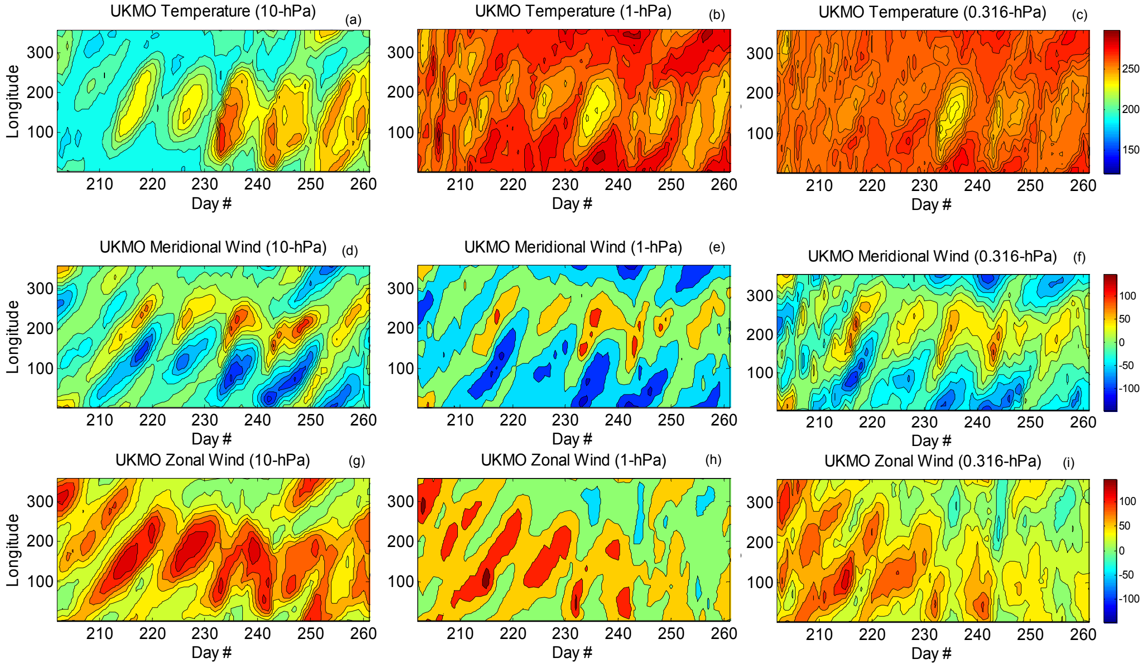

Figure 6.6: Longitude-time UKMO temperature, meridional wind and zonal mean zonal wind at 10-hPa (∼32 km), 1-hPa (∼49 km), and 0.316-hPa (∼60 km) and at 70°S.

Figure (6.6) illustrates the evolution of UKMO temperature, meridional wind, and zonal mean zonal wind prior to the onset of the year 2002 Southern Hemisphere major SSW, for 10-hPa (∼32 km), 1-hPa (∼49 km), and 0.316-hPa (∼60 km) altitudes. In this figure, it can be clearly observed that there is a domination of the eastward propagating wave with zonal wavenumber s=1 with a period near 10-days in the stratosphere. This wave seems to be clearer at 10-hPa (∼32 km) than at other altitudes. Basically, this figure clearly indicates the eastward phase progression of the quasi 10-day wave. The feature indicating strong temperature because of absorption of solar radiation by ozone is observed at altitudes between 50 km and 60 km (see Figure (6.6) (b) and (c)). A stronger winter eastward stratospheric zonal wind is also clearly observed, while, the meridional wind is observed to be systematically weaker than the zonal wind.

To examine the presence and temporal evolution of long period waves in the MLT region before, during and after the onset of the stratospheric warming event, the wavelet power spectra of the UKMO zonal mean zonal wind component for 10, 1, and 0.316-hPa pressure levels were also calculated for the period range from 2 to 20 days and the time interval from 1 June 2002 to 31 October 2002. The contour plots of the power spectra obtained are shown in Figure (6.7). It is clearly observed that there is a very strong presence of a quasi 10-day wave just before the major SSW occurrence begins. The observed intensification of planetary wave activity in UKMO zonal wind in the Southern Hemisphere prior to the onset of the SSW event is consistent with the results of Espy et al. (2005) and Pancheva et al. (2008) and Azeem et al. (2010). There is also a strong quasi 16-day wave observed in late October which coincides with the final warming which took place during this period (e.g. Dowdy et al. (2004)).

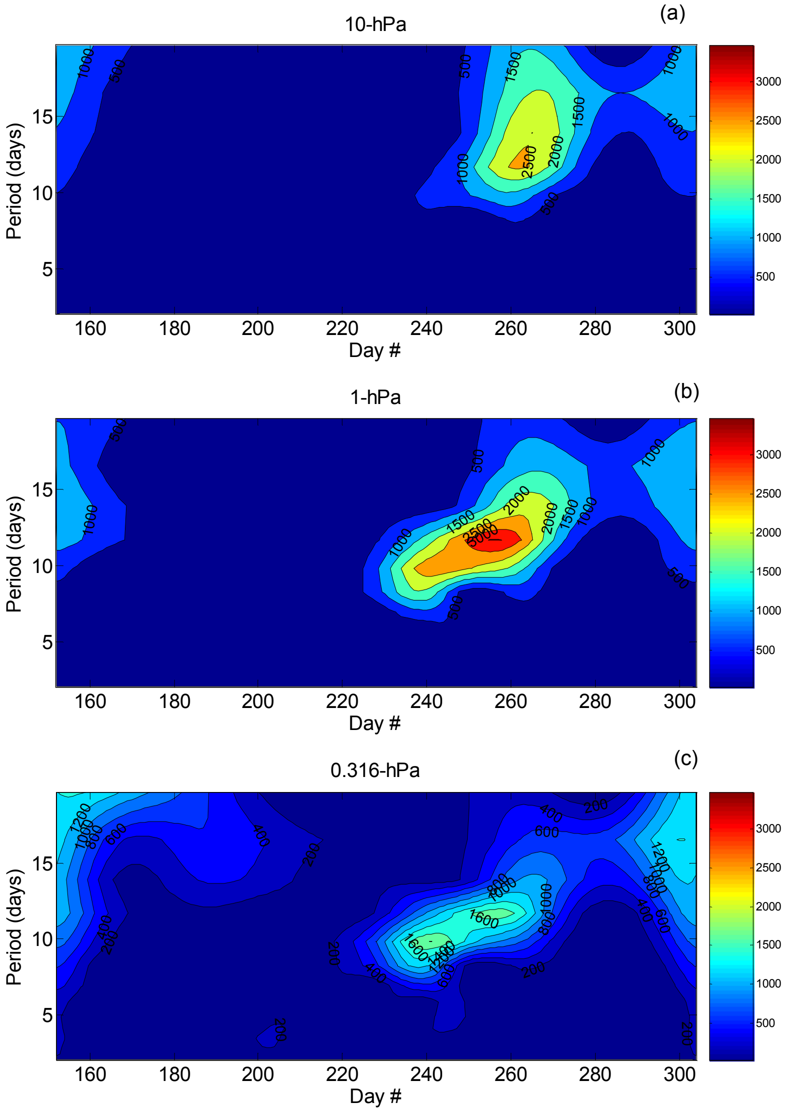

Figure 6.7: Wavelet power spectra of UKMO zonal mean zonal wind showing the amplification of the quasi 10-day wave activity.

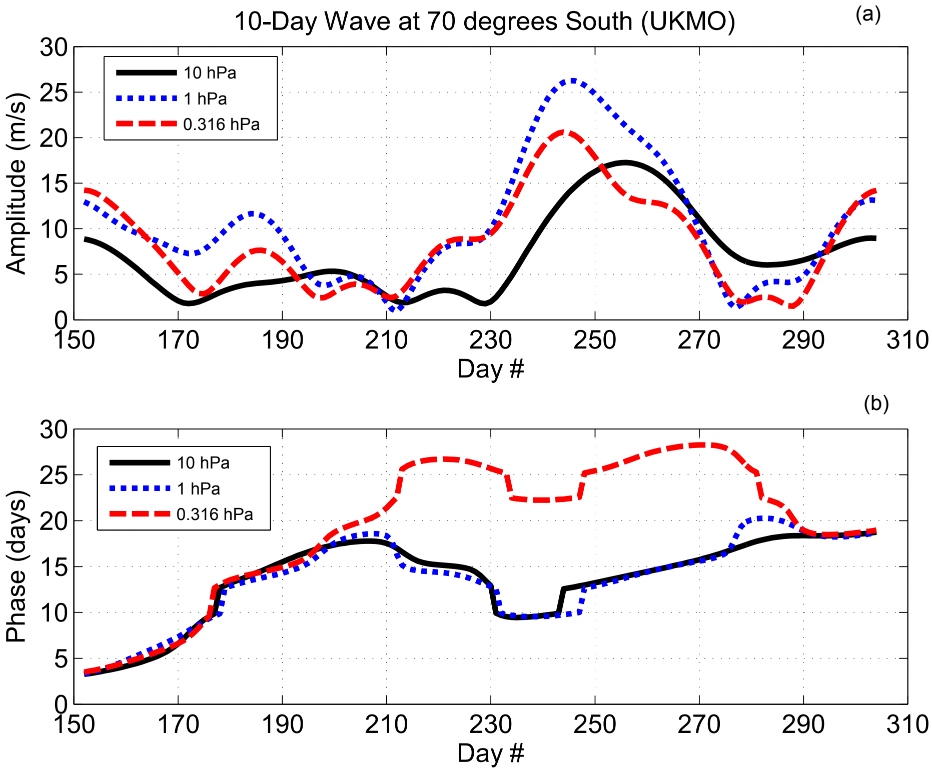

Figure 6.8: Instantaneous amplitudes (a) and phases (b) of the 10-day wave at 10-hPa (solid black line), 1-hPa (dotted blue line), and 0.316-hPa (red dash line) extracted from the UKMO zonal mean zonal wind data at 70°S using complex demodulation.

A 10 day demodulation period and an effective FFT band-pass filter at 8 and 14 days were used to investigate the instantaneous quasi 10-day wave characteristics during the period before, during, and after the major SSW. Figure (6.8) shows the instantaneous amplitudes (a) and phases (b) of the 10-day wave calculated from the zonal mean zonal wind at 70°S and at 10, 1, and 0.316-hPa pressure levels, obtained by complex demodulation. The 10-day wave instantaneous amplitudes are observed to be strong during the 30 days proceeding the major SSW occurrence days in the stratosphere and lower mesosphere. However, this 10-day wave seems to be stronger at the upper stratosphere and lower mesosphere, which seems to follow a usually reported downwards circulation disturbance in the middle atmosphere during major SSWs (e.g. Dowdy et al. (2004); Lee et al. (2009)). The instantaneous amplitudes at 0.316-hPa reaches a maximum of 27 $m.s^{-1}$ in day 248, and at 1-hPa it reaches a maximum of 20 $m.s^{-1}$ in day 248. But, at 10-hPa the 10-day instantaneous amplitude reaches its maximum approximately one week later.

Figure (6.8b) shows the instantaneous phases of the quasi 10-day wave in the zonal wind at 10-hPa (black solid line), 1-hPa (blue doted line), and 0.316-hPa (red dashes line) for the time period from 1 June 2002 to 31 August 2002 at 70°S latitude. It can be noted here that the phase behaviour at the stratosphere (10-hPa), upper stratosphere (1-hPa), and lower mesosphere (0.316-hPa) is similar. However, there is a 10-12 days average phase difference between the phase at 0.316-hPa and the phases at 10 and 1-hPa, for the days corresponding to the days when the 10-day waves amplifies (between day 210 to day 275). The phase difference between the phases at 10 and 1-hPa is very small.

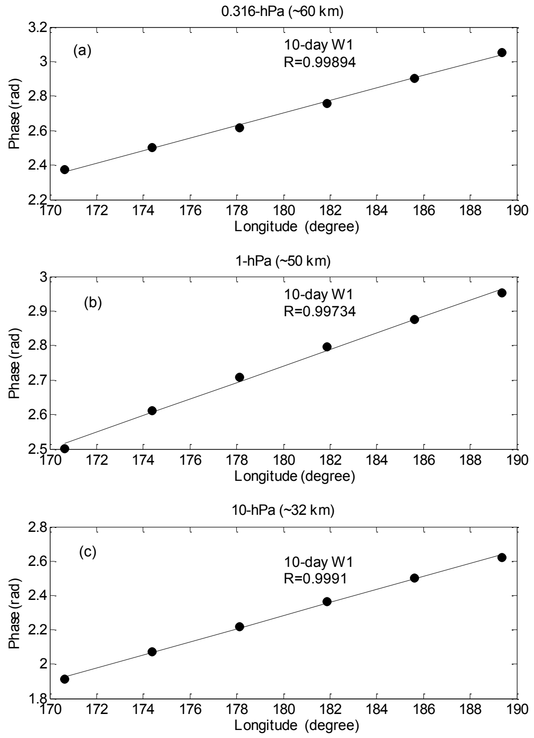

Figure 6.9: Phase slopes of the 10-day wave at 0.316, 1, and 10-hPa.

Using FFT the calculation of the longitudinal distribution of phases at 70°S, which defines the zonal wavenumber and the propagation direction of the wave was performed. Figure (6.9) shows the longitudinal distribution of the 10-day wave phases for 0.316, 1, and 10-hPa pressure levels, calculated using the UKMO zonal mean zonal wind data at 70°S, for days from 1 June to 31 October 2002. In all the three pressure levels it is observed that the 10-day wave is a eastward propagating wave with a zonal wavenumber s=1. This calculation is in agreement with the visualisation of the wave in Figure (6.6).

The E-P flux cross section figures in Figure (6.5) has shown that planetary waves detected in the stratosphere in the year 2002 winter originated from the troposphere. Moreover, the conditions of the stratospheric zonal mean zonal wind in the winter of the year 2002 seem to be in favour of upward propagating planetary waves (see subsection 5.3.3 in Chapter 5). In theory, the vertical propagation of quasi-stationary planetary waves is only possible when

$$0 < \hat{u} < \frac{\beta}{k^2 + l^2} = u_c, \tag{6.2}$$

where u_c is a critical wind speed, and $\beta = \partial f / \partial y$ results from the simplification known as the $\beta - plane$ approximation by setting the Coriolis parameter, f, equal to

$$f = f_0 + \beta y, \tag{6.3}$$

where $\beta y = \partial f / \partial y$ is a constant resulting in a linear relationship between f and latitude y.

Theoretical and observational studies have shown that only zonal waves with wavenumber s=1 and s=2 can propagate significantly into the stratosphere, and this happens only in the winter hemisphere where $u_c > 0$ (Holton and Alexander, 2000). In the Southern Hemisphere, the stratosphere is dominated by longer period eastward propagating waves which are prevailing (e.g. Fedulina et al. (2004)). Azeem et al. (2010) studied the daily evolution of the amplitudes of zonal wavenumber s=1 using the year 2002 NCEP temperature data averaged over the latitudes between 70°S and 85°S at 10-hPa. In their study, they noted that during the months of August and September 2002 the wave events with large daily zonal wavenumber s=1 amplitudes were present. Baldwin et al. (2003) showed that these amplitudes in 2002 were the largest amplitudes of wavenumber s=1 ever recorded in the Southern Hemisphere and were associated with the 2002 SSW event.

Unlike the longer period westward propagating waves which frequently precondition the Northern Hemisphere stratosphere for the occurrence of the major stratosphere, the dominant eastward propagating waves in the Southern Hemisphere are not strong enough to trigger the major SSW. Furthermore, the polar vortex in the Southern Hemisphere is stronger compared to the Northern Hemisphere. However, the results of this study show that during the year 2002 winter the eastward propagating planetary waves had the largest amplitude, which was large enough to precondition the stratosphere for the occurrence of the unprecedented year 2002 major SSW. Thus, it will not be a surprise if the quasi 10-day wave of wavenumber s=1 travelling in the eastward direction, which is shown above and in Chapter 5 can also be detected in the MLT. In the following subsection the planetary wave activity in the MLT is investigated using HF radar data.

6.4.2 Planetary Waves in the MLT (SuperDARN radar)

In order to examine wave characteristics in the MLT region from the HF radar data, it is necessary to determine the dominant spectral components within the frequency band of interest. For the purpose of this work, we have opted to use the FFT and also compare the power of dominant wave periods. Thus, to do this, we performed dynamic Fourier spectra using a 28-day data window that is shifted forward by 1-day at a time. The deduced power for a given data window was attributed to a central day given by day 14 of that particular 28-day data interval. This long data window results in the desired frequency resolution of 0.0357 cycles per day (cpd). However, the problem with this frequency resolution is that it is at the expense of time resolution. This is important because planetary waves with short periods, e.g. quasi-two-day waves which are characterised by bursts of wave activity that varies on scales of several days (Pancheva, 2006; Malinga and Ruohoniemi, 2007). Nevertheless, for the purpose of deducing the signature of planetary waves, the 28-day data window is a suitable compromise and has been used where proper in the present study.

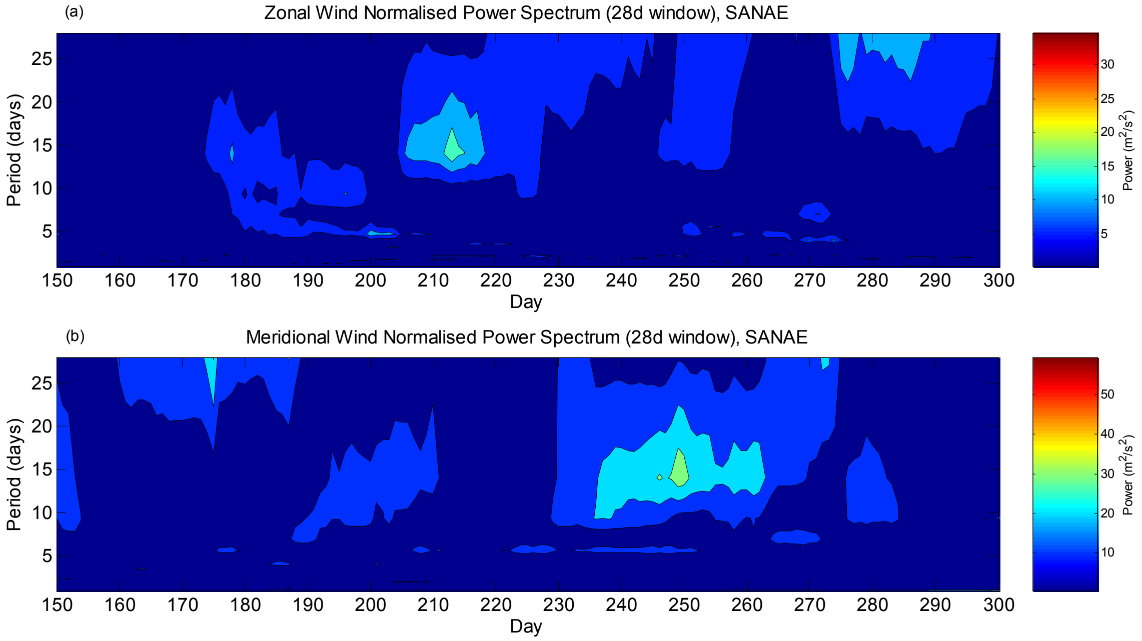
(a) Zonal Wind Normalised Power Spectrum (28d window), SANAE

(b) Meridional Wind Normalised Power Spectrum (28d window), SANAE

Figure 6.10: Normalised Power spectra of daily zonal (a) and meridional wind (b) derived for the MLT region Climatology (~94km) from SANAE HF radar for the period from 30 May to 27 October 2002 (150-300 Julian days).

The contour plots in Figure (6.10) illustrates the dynamic spectra analysis applied to the zonal and meridional wind components of SANAE HF radar wind data. Here, only the normalised power for the period from May to late October (150 to 300 Julian days) was plotted. The sampled height is ~94 km. The power spectra has been normalised by σ^2/N, where N is the number of data points and σ^2 is the variance of the time series. Using this normalization, white noise would have an expectation value of one at all frequencies (Torrence and Compo, 1998). In Figure (6.10a), it can be clearly seen that the zonal wind power spectra is characterised by dominant peaks near to periods of 5-day, 10-day and 14- to 16-day waves in the mid-winter. The 5-day and 14- to 16-day waves are also seen around the 250^{th} of 2002 Julian day (7 September), and this period is about 2 weeks prior to the occurrence of the SSW. When comparing the year 2002 spectra to the other years (see Chapter 5), it is observed that other years do not have a strong presence of the above mentioned planetary waves. The spectrum for the meridional wind component which is shown in Figure (6.10b) also shows the presence of a 14- to 16-day wave around 7 September (250^{th} of Julian days). There is also some evidence of a 5-day wave on the spectrum.

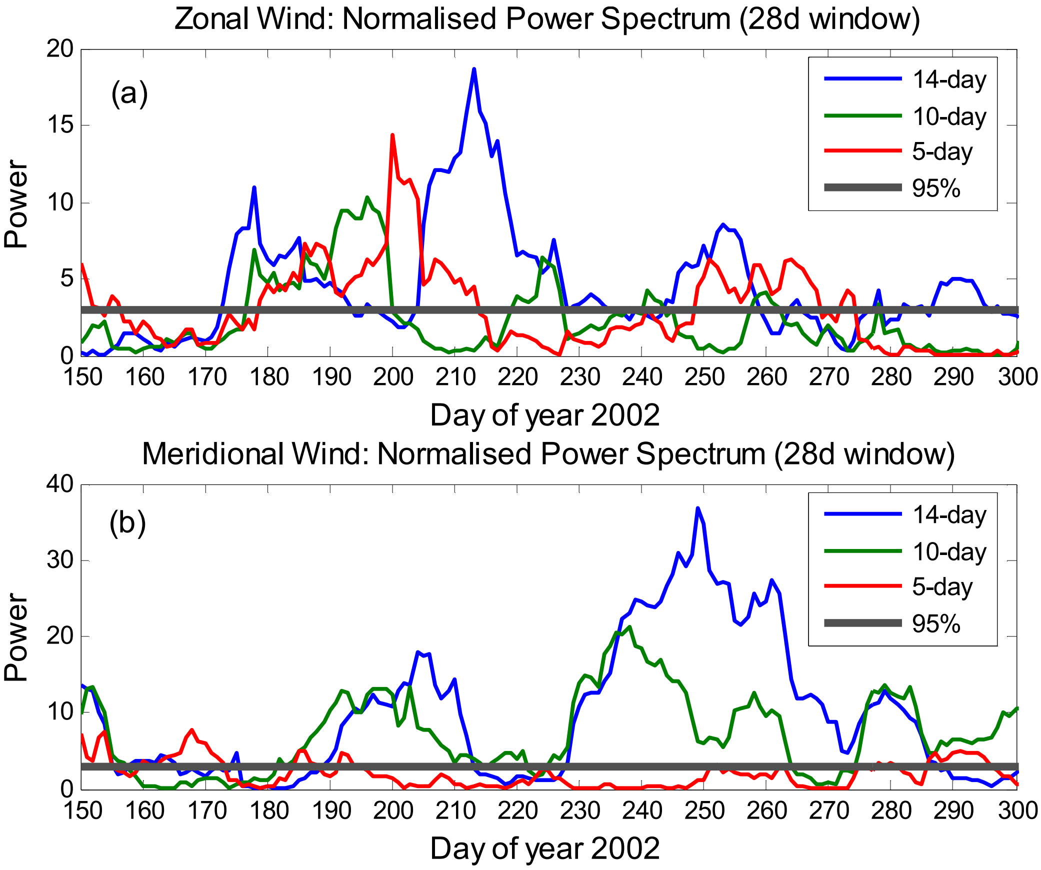

Figure 6.11: Normalised power spectrum of the zonal wind (a) and meridional wind (b) 14-, 10-, and 5-day wave components for SANAE HF radar. The horizontal grey line represents the 95% confidence level.

In Figure (6.11) the normalised power spectra of the 14-, 10-, and 5-day waves for (a) zonal and (b) meridional components was plotted. The horizontal grey thick line indicates the 95% confidence level using a chi-square test, assuming white noise as background spectrum (Torrence and Compo, 1998). From the figure, it is clear that zonal 14-, 10- and 5-day waves have a seasonal pattern characterised by enhanced wave activity in winter superimposed by short-term fluctuations. The winter wave activity tends to be above the 95% confidence level. A burst of wave activity was observed from around day 173 to 229. The zonal 14-day wave activity has the strongest peak in day 213. The meridional component has a strong presence of wave activity with an exception of the 5-day wave which is always under the 95% confidence level. The meridional 14-day wave activity reaches its peak on day 250.

The statistics of the wavenumber contributions of a strong quasi 14-day wave observed in the year 2002 winter was also performed in this study. The zonal wavenumbers were derived from the slope of the linear regression of the 14-day wave phase as a function of longitude during the winter season. A method similar to the one described in Chapter 5 (subsection 5.3.2) was also used here to deduce the zonal wavenumber events both in the meridional and zonal wind components.

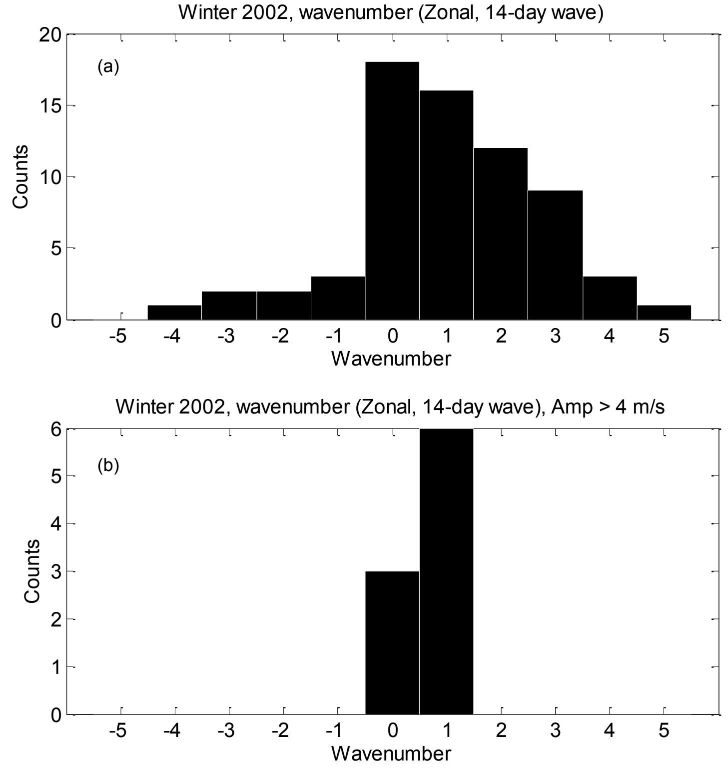

Figure 6.12: The distribution of the zonal wavenumber for the zonal 14-day components in winter. The negative wavenumbers represent the westward propagating wave.

Figure (6.12a and b) shows the histograms of distribution of the zonal wavenumber for the zonal quasi 14-day components in year 2002 winter. The difference between the two figures is that in Figure (6.12a) wavenumbers contributed by all amplitudes of the 14-day wave were included, while in Figure (6.12b) all wavenumbers contributed by amplitudes less than 4 m.s^{-1} (Average between SANAE and Halley) were omitted. This is primarily because only planetary waves with larger amplitudes are known to have strong influence in the middle atmosphere (Pancheva et al., 2008). In Figure (6.12a) it is observed that for the zonal component, the zonal wavenumbers s=0, s=1, s=2, and s=3 tend to be dominant. In Figure (6.12b), the wavenumbers contributed by smaller wave amplitudes (4 m.s^{-1}) were filtered out. In this figure, the zonal wavenumbers s=0 and s=1 tend to be dominant, indicating that the MLT was characterised by stationary planetary wave and a strong 14-day wave of wavenumber s=1 travelling in the eastward direction.

In extracting the zonal wavenumber contribution from the meridional wind component, a method similar to the one used above was followed. Figure (6.13a) shows the histogram of wavenumbers contributed by all amplitudes of the quasi 14-day wave in the meridional component, while in Figure (6.13b) the wavenumbers contributed by amplitudes less than 4 m.s^{-1} (Average between SANAE and Halley wind data) were omitted. The meridional component (Figure (6.13a)) also shows evidence of the presence of a wide distribution of wavenumbers because of the inclusion of the wavenumbers with smaller amplitudes. However, after filtering out the wavenumber contributed by amplitudes less than 4 m.s^{-1}, the dominance of wavenumbers s=0, and s=1, is observed. There is clear evidence that meridional component also detected the quasi 14-day oscillation with zonal wavenumber s=1 travelling in the eastward direction.

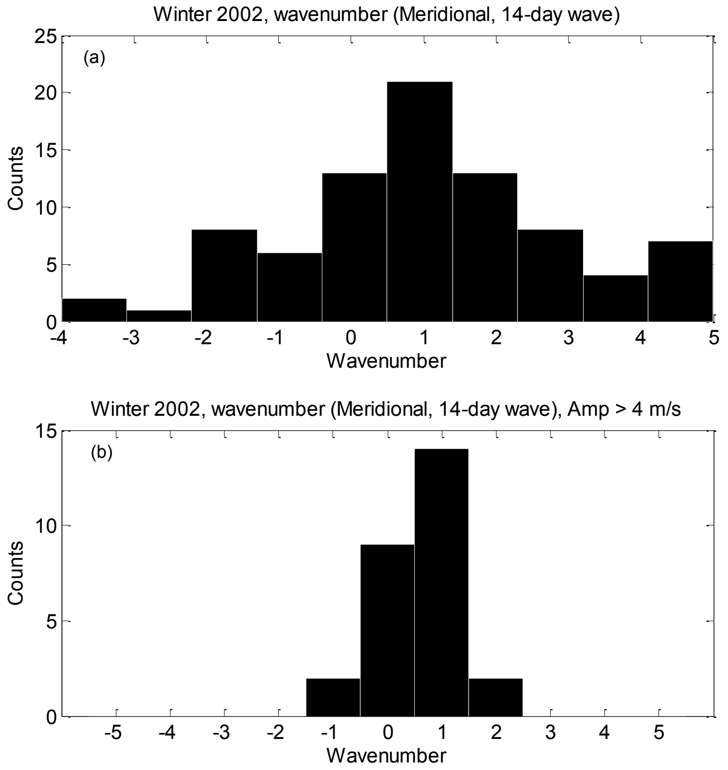

Figure 6.13: The distribution of the zonal wavenumbers for the meridional 14-day components in winter. Negative represents westward propagating waves.

Statistics of the wavenumber contributions during the winter of year 2002 showed that both the zonal and meridional wind components were dominated by a 14-day oscillation having a eastward phase progression and a zonal wavenumber of s=1. This finding is consistent with a study by Dowdy et al. (2004), where they used MF radars from Davis, Syowa, and Rothera and observed a 14-day oscillation having a eastward phase progression and a zonal wavenumber of s=1. A strong contribution by stationary wave in both the zonal and meridional components could be presumably due to the longitudinal difference between the two SuperDARN sites. But, it should also be considered that in the southern hemisphere winter there is usually a coexistence of eastward propagating waves with periods between 7 and 23 days, and quasi-stationary planetary waves (Shiotani et al., 1993; Palo et al., 2005). Espy et al. (2005) also observed a strong 14-day planetary wave peak from the meridional wind data measured by SuperDARN radars at Syowa, SANAE and Halley and Rothera MF radar. They thereafter extracted more information about this wave by utilising the Fourier amplitudes to obtain the cross-spectra and cross-correlations of each station relative to Syowa. They plotted the phase delay with respect to longitude, and observed the 14-day oscillation consistent with a eastward phase progression and zonal wavenumber s=1 at the lower thermosphere. Using observations from the SABER instrument, Palo et al. (2005) presented the first comprehensive view of the above observed 10-14 day disturbances showing the vertical coupling from the lower stratosphere through to the lower thermosphere. In their study, they showed that the 10-day eastward propagating wave of zonal wavenumber s=1, zonal wavenumber s=2, and the stationary planetary wave originated from the lower atmosphere and propagated upwards causing disturbance through the middle atmosphere. In this study, the observation of a quasi 10-day wave of wavenumber s=1 in the stratosphere (using UKMO data) and MLT regions (using SANAE HF radar data) prior to the onset of the major SSW also suggest a coupling between the MLT and the stratosphere.

6.5 Link with Temperature Variations

Previous studies have associated the occurrence of SSW events with the cooling of the MLT temperature (e.g. Walterscheid et al. (2000); Hernandez (2003); Liu and Roble (2005)). Hernandez (2003) reported a cooling of the mesopause region over the South Pole during the 2002 southern hemisphere stratospheric sudden warming. Liu and Roble (2005) used a Global Circulation Model (GCM) extending from 30 to 500 km to examine the interaction between planetary wave forcing and the evolving zonal mean state during the same event. They found significant mesospheric effects which included a cooling and reversal of the zonal wind prior to the SSW event.

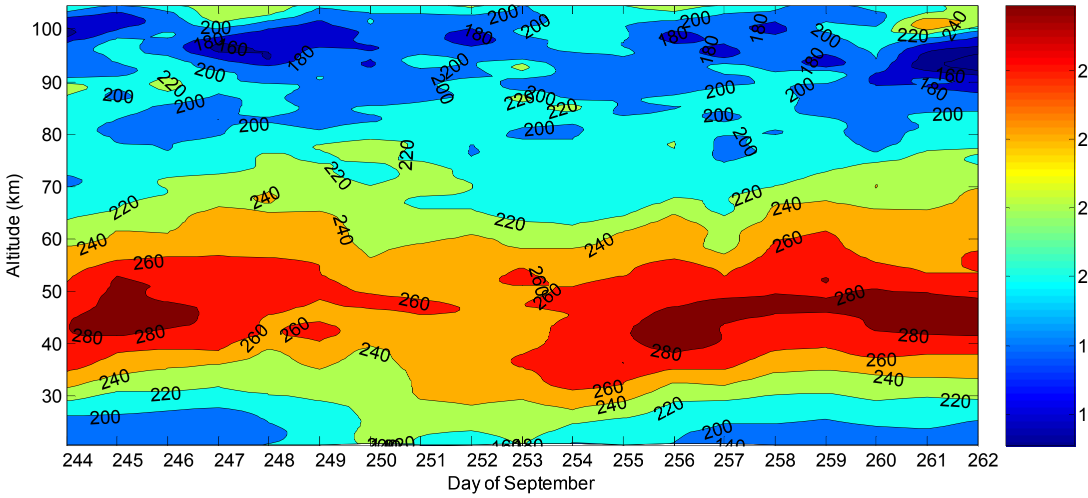

Figure 6.14: Altitude–temperature contour map obtained from the SABER data for successive days from 244 to 262 year 2002 (1 to 19 September 2002) . The data corresponds to the satellite closest overpass above SANAE site.

Figure (6.14) shows temperature contour maps obtained from SABER satellite data plotted for successive days from 1 to 19 September 2002 (244 - 262 Julian days). The main idea was to use those SABER temperature data which are closer to the SANAE base during

September 2002. However, SABER obtains profiles from 52°S to 83°N during its north-looking mode for 60 days before switching to an analogous south-looking mode and then repeating that sequence for the subsequent months (Remsberg et al., 2003). In this way, the polar cap data is available only in 60-day segments, with no information from the preceding 60 days. Thus, only the first 19 days of September 2002 are closer to the SANAE site. The 19 profiles used in this work are the closest as the satellite overpasses over the SANAE site.

The figure (Figure (6.14)) shows the structure of the variation of vertical temperature prior to the occurrence of the major SSW which only reaches its maximum on the 26th of September 2002. In fact, such warming drives an unusual dynamical situation resulting in the split of the polar vortex (Baldwin et al., 2003) and transportation of air-masses from pole to mid- and low-latitudes (Bencherif et al., 2007). The most noticeable feature in these temperature profiles is a substantial increase of temperature (at the rate of 5 K/day) throughout the stratosphere which is visible on the 13^{th} to the 19^{th} of September. Baldwin et al. (2003) illustrated the daily variation of temperature for the stratosphere at the south pole using NCEP/NCAR reanalysis from 1979 to 2002. They showed that the polar temperature in late September 2002 was extremely high, indicating that this is an unprecedented event at least in the past 24 years. Thus, the increase of temperature which reaches a maximum of 240 K at around 32 km and 280 K at around 40 km is uncommon and is associated with a SSW.

Moreover, it can be mentioned that before this major warming event, which reached its peak on 26 September, a few minor warmings can be seen during the 2002 winter period primarily in mid-July, mid- and late-August onwards, until the beginning of September (see. Figure (6.1)).

6.5.1 Mesospheric Inversion Layer During the 2002 SSW

The temperature profiles in Figure (6.15) illustrates the structure of the vertical temperature prior to the occurrence of the major SSW. At mesospheric heights, the vertical temperature profiles illustrate the persistence and the variability of the mesospheric temperature inversion layer during the continuous series of SABER measurements. These inversion layers are primarily observed between 70 and 110 km and in all profiles with a stronger signature on the 17^{th}, 18^{th} and 19^{th} of September. Thus, there are signatures of mixing and viscous dissipation associated with turbulence generated by the breaking upward propagating gravity waves in the MLT region. Although according to Meriwether and Gerrard (2004), the mesospheric inversion layers can appear in the MLT region of the low-latitude and mid-latitude at any time of the year, the mesospheric inversion layers observed over SANAE in the present study indicate an interesting future which still need to be investigated in details. In the following chapter, the gravity wave activity in the middle atmosphere will be studied.

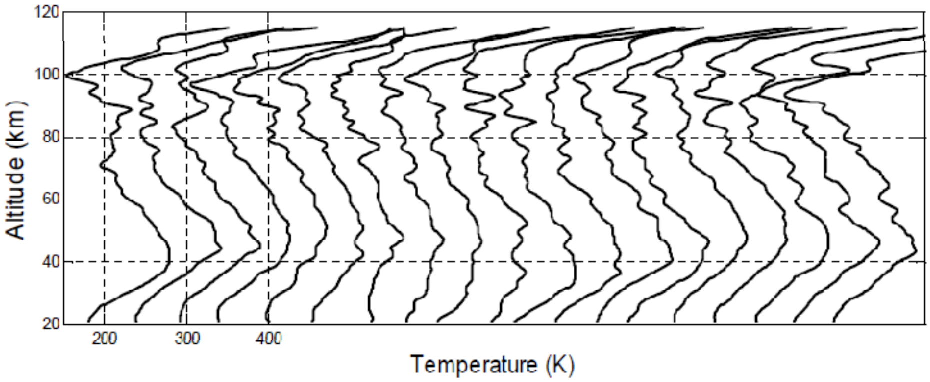

Figure 6.15: Vertical temperature profiles from the SABER data for successive days from 1 to 19 September 2002 (244-262 Julian days), which are shifted by 100 K from each other. These profiles were obtained as the satellite closest overpass above SANAE site.

6.6 Discussion and Summary

In this chapter, the HF radar data set measured at the SANAE site in Antarctica was used to examine the dynamical structure of the MLT region during the unprecedented major SSW in late September 2002. Previously, only MF radars are usually used for this purpose, both in the Southern and Northern Hemisphere. In the results, it was shown that the mean zonal and meridional wind (from SANAE HF radar) throughout 2002 winter at ∼94 km, displayed an enhancement due to a series of large planetary waves amplification. The large amplitude planetary wave produced strong westward forcing in the high-latitude winter stratosphere. In general, eastward zonal winds dominate the winter MLT, but the 2002 winter elucidates clear differences when compared to other years, with many brief periods of westward winds observed. The normalised Fourier power spectra in Figures (6.10a) and (6.11a) depicts the presence of planetary waves (5-day, 10-day and 14- to 16-day waves) during the 2002 austral winter. In addition, Figures (6.10b) and (6.11b) also showed the presence of a 14- to 16-day wave in the meridional wind component during winter. The observation of a strong 14-day wave of wavenumber s=1 travelling in the eastward direction is consistent with observations reported by Dowdy et al. (2004) and other authors.

In Figure (6.3), the zonal winds at ∼94 km from SANAE HF radar were compared to the zonal mean zonal winds from NCEP stratospheric data (at 10-hPa), and the results showed that the reversal event in the MLT took place in a few days (about a week) prior to the reversal in the stratosphere. This behaviour indicates that there may be a downward propagation of circulation disturbance in the middle atmosphere. Similar results were also reported by Dowdy et al. (2004). The SANAE HF radar results showed similarities to the previous observations of the major SSWs both in the Southern and the Northern Hemisphere. Lee et al. (2009) also reported the same behaviour of the middle atmosphere, where they studied the vertical structure and evolution of the wintertime

Northern Hemisphere Annular Mode (NAM). In their study, they concluded that the time evolution of NAM suggested that significant NAM anomalies typically appear first in the mesosphere and progress downwards.

The E-P flux vectors (**F**) and divergence ($\nabla.\mathbf{F}$) clearly indicate that there was a strong planetary wave activity of tropospheric origin in the stratosphere during the year 2002 winter period. The circulation in the stratosphere was characterised by a series of planetary wave events in 2002 winter that weakened the polar vortex and triggered the SSW in late September. Specifically, a quasi 10-day wave of wavenumber s=1 travelling in an eastward direction was identified as responsible for triggering the occurrence of the 2002 major SSW. The analyses of the wave activity in the middle atmosphere using the NCEP, UKMO and SANAE HF radar data revealed a number of features suggestive of the vertical linkage between the stratosphere and the MLT region during SSW events.

The response of the MLT region to the stratospheric warming depends on many different factors that still require more investigation. Mesospheric cooling is usually reported and associated with the major warmings in the Northern Hemisphere . Explaining the mesospheric cooling generally observed over Arctic SSWs, Holton (1983) suggested that eastwards gravity waves drag anomalies are consequences of a change in the filtering of parameterized gravity wave momentum fluxes when the stratospheric winds change from eastward to westward. Ren et al. (2008) observed mesospheric cooling over Antarctica during the period of occurrence 2002 major SSW, and associated it with a net gravity wave drag induced upwelling rather than a suppression of dawn-welling.

In this study, the SABER temperature data was used to examine a response of the thermal structure to the SSW in the stratosphere and MLT region. The stratosphere displayed an unusual increase of temperature which started in the mid September, whilst the MLT region showed a cooling and temperature signature of inversion layers few days before the SSW occurrence. This behaviour of the MLT region is associated with energy deposition due to gravity wave breaking in the mesosphere. Gravity wave momentum deposition drives the pole-to-pole meridional wind circulation that in turn causes the departure of mesospheric temperature from radiative equilibrium, keeping the winter MLT warmer and summer MLT colder (Holton, 1983). Liu and Roble (2002) suggested that the penetration of gravity waves during the SSW can drive meridional circulation leading to adiabatic cooling and heating. The above reported behaviour of the middle atmosphere strengthens the idea of coupling between the stratosphere and the MLT region. Figure (6.14) also showed a signature of minor warming in early September. Moreover, this work also highlights and strengthens the idea that HF radars enable us to investigate dynamical processes in the MLT region.

Chapter 7

Influence of Gravity Waves during the SSW

In Chapter 5 and 6 it was observed that the occurrence of the major SSW can have a strong influence on the mean circulation in the polar regions. In particular, during the occurrence of this phenomena the deceleration and reversal of the eastward polar night jet in the high-latitude stratosphere also changes the filtering of internal gravity waves and allows increasing amounts of eastward propagating gravity waves from the troposphere to penetrate into the MLT, and break there, while blocking westward propagating gravity waves (Sathishkumar and Sridharan, 2009). Thus, this chapter investigates the gravity waves activity in the middle atmosphere during the year 2002 major stratospheric warming. A special attention is paid mainly to the gravity wave phase speeds, horizontal wavelengths, propagation direction, and potential energy before, during, and after the occurrence of the SSW.

The interaction of gravity waves and wind during stratospheric warmings has a significant impact on the structure and general circulation in the mesosphere. There are several observational studies that examine gravity waves during the SSW period in the past decade (e.g. Ratnam et al. (2004b); Wang and Alexander (2009); Azeem et al. (2010)). Using temperature profile measured by Challenging Minisatellite Payload Global Positioning System (CHAMP/GPS), Ratnam et al. (2004b) analysed the gravity wave activity in the stratosphere during the 2002 late winter/spring SSW in the southern hemisphere. In their study, they showed that during the SSW period the gravity wave energy (potential energy, E_p) became three times higher than usual in the stratosphere. This enhancement mostly occurred near the edge and outside the cold polar vortex, but not inside the vortex.

Wang and Alexander (2009) used temperature retrievals from the Constellation Observation System for Meteorology, Ionosphere and Climate (COSMIC)/Formosa Satellite Mission 3 (FORMOSAT-3), CHAMP/GPS radio occultation profiles and independent temperature retrievals from the Earth Observing System (EOS) satellite High Resolution

Dynamics Limb Sounder (HIRDLS) and SABER temperature data to investigate the SSW event and accompanying gravity wave temperature amplitude in the 2007-2008 Northern Hemisphere winter. They reported the enhancement of gravity wave amplitudes in the stratosphere and subdued gravity wave amplitudes in the mesosphere. Recently, a study by Yamashita et al. (2010) showed that gravity waves forcing controls the pattern and strength of residual circulation and thereby the characteristics of the cooling and warming regions. They also showed that the planetary wave forcing in the MLT affects the vertical depth and magnitude of the MLT temperature anomalies through further modification of the residual circulation.

A technique for extracting gravity waves parameters which is used in this work was first described by Jarvis et al. (2003), where for the first time they performed observations of gravity waves using an imaging riometer located at Halley, Antarctica (76°S, 27°W). This technique uses fluctuations in ionospheric absorption as a tracer for gravity waves. Imaging riometers respond to changes in the absorption of the cosmic radio noise in the ionospheric D-region which enables them to detect the compression and rarefaction at ∼90 km altitude, generated by the propagation of gravity waves (Jarvis et al., 2003). Jarvis et al. (2003) demonstrated that a single wave observed in a co-located airglow imager was also present in the central beams of the Halley imaging riometer. The wave first appeared in the airglow imager at 07:25 UT on 7 June 2000, whilst it was not apparent in the imaging riometer data until 08:00 UT. The work by Jarvis et al. (2003) was further extended by Moffat-Griffin et al. (2008), where they also showed the capabilities of the imaging riometer to detect short period mesospheric gravity waves using the fluctuation of the ionospheric absorption of cosmic radio noise. Moffat-Griffin et al. (2008) presented a detailed analysis technique for quantifying these signatures. They demonstrated the extraction of the wave period, horizontal phase speeds, horizontal wavelengths, and the propagation direction by applying wavelet analysis to synthetic imaging riometer absorption data. They also performed comparisons between the gravity wave parameters extracted from imaging riometer data with those derived from a co-located airglow imager and found good agreement between the two instruments.

In the past the SANAE imaging riometer has not been used to study short period gravity waves. In fact, this instruments has only been used for other studies such as observation of energetic electron precipitation at SANAE IV, Antarctica, by Wilson and Stoker (2002), and spatial structures in enhanced ionisation of the ionosphere observed by absorption of cosmic radio waves by Wilson et al. (2001). In this thesis, the above mentioned technique is used to extract parameters of gravity waves of periods between 40 and 50 minutes during the 2002 major SSW event (from the 11 September 2002 to the 10 October 2002) in the southern hemisphere. The 2002 results are also compared to 2003 observations (a year without a stratospheric warming). The imaging riometer used in this study is located at the SANAE, Antarctica (72°S, 3°W). This is the first time that this imaging riometer is being used to study mesospheric gravity wave signatures. In fact it is the first time that any imaging riometer is used to study gravity waves during the SSW. The details of the SANAE imaging riometer are given in Chapter 3. The results obtained in this study are also discussed and compared with results available in literature.

7.1 Gravity Wave Detection using an Imaging Riometer

As gravity waves have periods which are not discrete, it is necessary to first determine the dominant spectral components within a frequency band of interest. For this purpose, techniques such as Fourier transform analyses of the time-series is performed. In this study, the Fourier cross-spectrum was specifically used to determine the dominant spectral components in two time series. The Fourier cross-spectra phase (Priestley, 1981) which is given by the average value of the phase-shift between the two time series is the key parameter required for the extraction of gravity wave parameters. With the knowledge of the phase difference, the distance between the imaging riometer beams projected at an altitude of 90 km, period of the wave feature, horizontal phase speeds and wavelengths are calculated using a method outlined by Moffat-Griffin et al. (2008). The horizontal phase speed is determined by equation (7.1) and the horizontal wavelength is determined by equation (7.2).

$$V_p = \frac{2\pi\Delta x}{\Delta\phi T} \tag{7.1}$$

$$\lambda = \frac{2\pi\Delta x}{\Delta\phi}, \tag{7.2}$$

where Δx is the distance between the beams, $\Delta\phi$ is the phase difference between the beams in radians and T is the observed Doppler shifted wave period in seconds.

Jarvis et al. (2003) and Moffat-Griffin et al. (2008) showed that the spatial resolution of the imaging riometer puts limitations on the resolvable horizontal wavelength of $2\Delta x$. This is the primary reason for choosing to use only the central riometer beams when extracting the gravity waves parameters. For the central beams, the spatial resolution limitations result in a lowest resolvable limit of 45 km for the horizontal wavelength. This means that any waves that pass through the field of view with horizontal wavelengths shorter than this limit would be subjected to spatial aliasing. This could result in obtaining unreliable gravity wave parameters. Therefore, in order to eliminate this effect, Moffat-Griffin et al. (2008) also developed a method that requires a wave feature to be detected in three linearly adjacent beams over the same period and time range. Figure (7.1) shows the separation between five SANAE imaging riometer central beams.

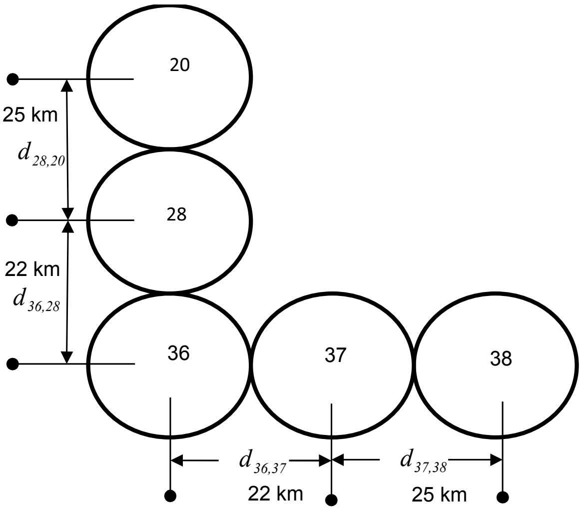

Figure 7.1: The SANAE imaging riometer central beams and their beam separations.

By using simple wave theory, the following equation is derived,

$$\frac{d_{36,37}}{d_{37,38}} = \frac{\Delta\phi_{36,37}}{\Delta\phi_{37,38}}$$

and

$$\frac{d_{36,28}}{d_{28,20}} = \frac{\Delta\phi_{36,28}}{\Delta\phi_{28,20}}. \tag{7.3}$$

The beam separations and phase difference ratios are known. The right hand side of the above equations, can be adjusted by using $\pm 2n\pi$ until the best match to the beam separation ratio is found, where n is an integer. The adjusted set of phase difference values that form the best match to the beam separation ratios is then taken to represent the actual phase difference. This adjustment can then be applied to the phase differences in equation 7.1 and 7.2 to calculate the true horizontal wavelength and horizontal phase speed of the wave feature. The ability to calculate this necessary adjustment relies on the fact that the beam separations at any fixed altitude are neither equal nor have an integer ratio (Jarvis et al., 2003; Moffat-Griffin et al., 2008).

After obtaining reliable phase difference values, the propagation direction of the wave can be calculated using a method outlined by Donelan et al. (1996). This technique requires using two phase differences of a wave feature, measured in near orthogonal directions (e.g. $\Delta\phi_{36,28}$ and $\Delta\phi_{36,37}$). The SANAE imaging riometer central beam phase differences between the riometer north–south and east–west beams are at exactly 90°, thus the wave direction can be given by

$$\theta = \arctan\left(\frac{\Delta\phi_{36,28}}{\Delta\phi_{36,37}}\right). \tag{7.4}$$

7.1.1 Gravity Waves Parameters

The times series showing imaging riometer absorption for the five central beams labelled in Figure (7.1) are shown in Figure (7.2). These riometer absorption sub-figures are for day number 260 of year 2002 (17 September), and they serve as an example of the SANAE imaging riometer absorption time series used in this work. This day was picked randomly. All the riometer beams show similar behaviour of absorption, with an absorption maximum at approximately 770 minutes.

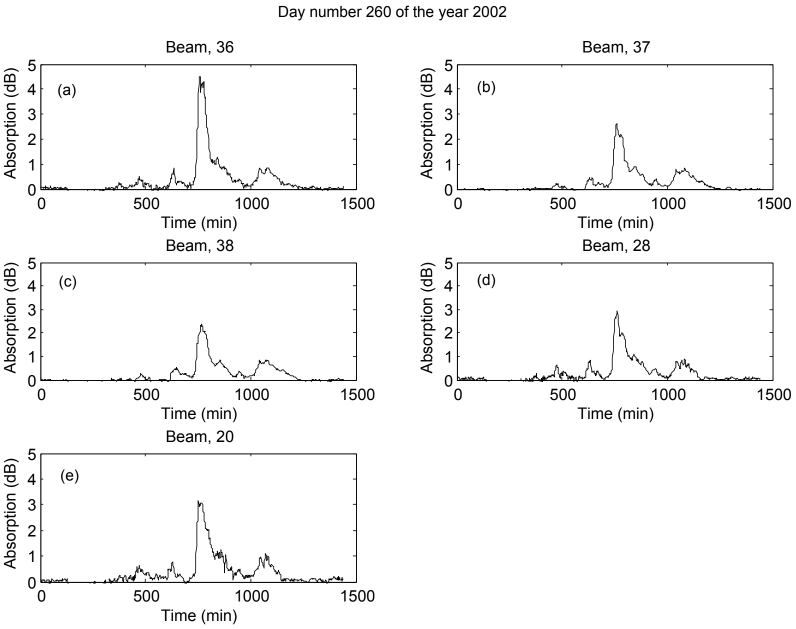

Figure 7.2: Radio absorption measured by the SANAE imaging riometer centre beams (36, 37, 38, 28, and 20) for day number 260 of September 2002.

In Figure (7.3), the normalised Fourier power spectras of the five centre beams were plotted to show the periods of gravity waves available. The horizontal red dashed line indicates the 95% confidence level using a chi-square test, assuming white noise as background spectrum (Torrence and Compo, 1998). The Fourier cross-spectrum of each of the five pairs of beams was generated and the phase differences from the regions of highest coherency were determined. Figure (7.4) shows the cross-spectra amplitude between the central beams, for day number 260 of the year 2002. The same figure (not shown in this thesis) was also generated for days before, during, and after the stratospheric warming for the purpose of extracting gravity wave parameters during these days.

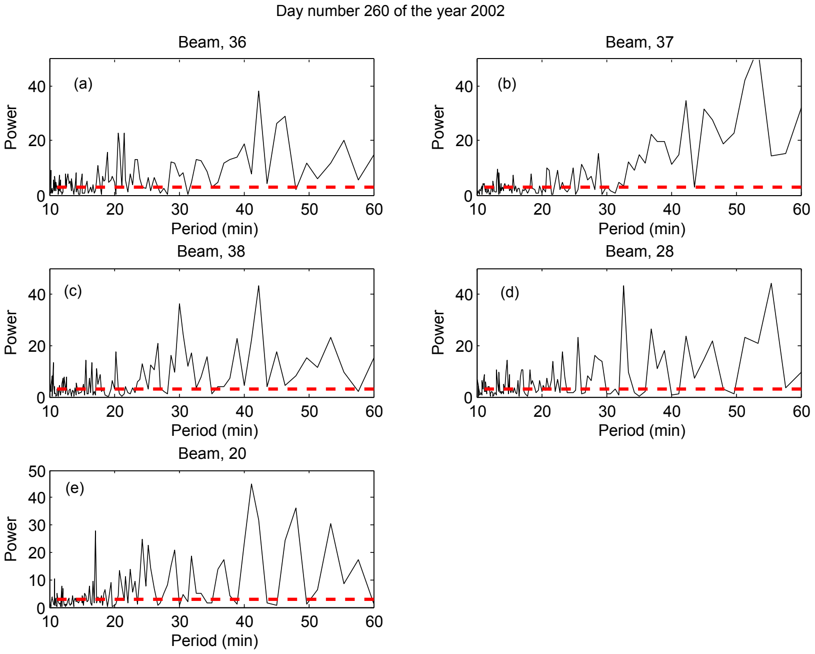

Figure 7.3: Normalised power spectrum of radio absorption measured by the SANAE imaging riometer centre beams (36, 37, 38, 28, and 20) for day number 260 of September 2002. The horizontal red dashed line represents the 95% confidence level.

Because in this study the intention is to focus on short-period gravity waves (e.g. $\leq$60 minutes), a band-pass FFT filter was used to filter gravity waves with periods less than 3 minutes and greater than 60 minutes. What is noticeable is that the spectrums of the five riometer beams in Figure (7.3) illustrates significant gravity waves periods above 18 minutes. This is also observed in the cross-spectra amplitude shown in Figure (7.4). Due to more stronger peaks of periods above 40 minutes, only gravity waves with periods between 40 and 50 minutes are studied in this thesis.

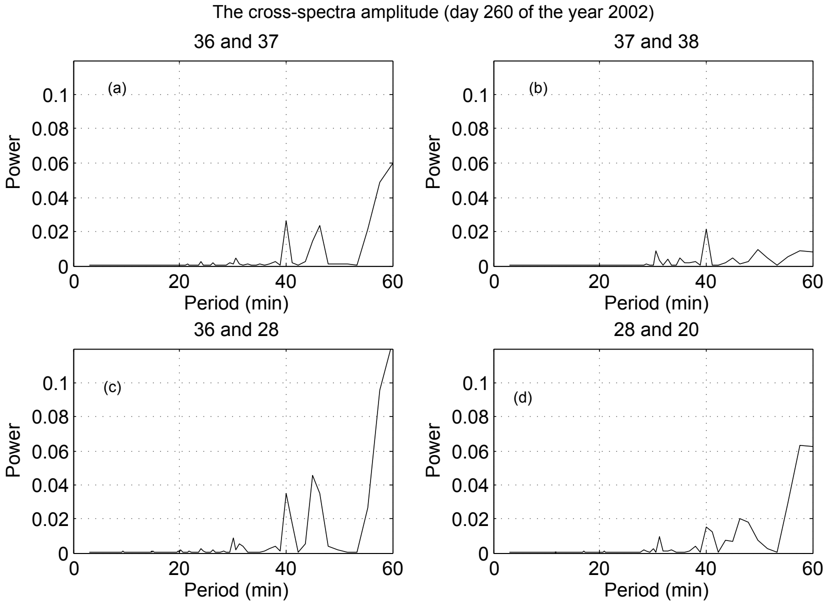

Figure 7.4: The Fourier cross-spectra between the central beams for day number 260 of year 2002.

The reversal of the zonal wind which is associated with the SSW in the mesosphere started on 18 September 2002 (day 261) and persisted for a few days before it returned to the eastward direction on 27 September (day 270), while in the stratosphere the zonal wind reversed on 25 September 2002 leading to the unprecedented major SSW in the southern hemisphere (Baldwin et al., 2003; Dowdy et al., 2004; Mbatha et al., 2010b; Azeem et al., 2010). Thus, in order to study the influence of stratospheric warming in the gravity wave parameters such as phase speed, horizontal wavelength and propagation direction, the gravity wave parameters for days before, during and after the stratospheric warming were extracted. Table 7.1 shows the daily evolution of phase speeds and horizontal wavelength and propagation direction, before, during, and after the major stratospheric warming in late September 2002. The table also indicates whether the phase difference values were adjusted or not, using the equation 7.3, in order to correct the aliasing due to the spatial resolution of the riometer beams. There are days where it was not possible to deduce the gravity wave parameters due to some technical problems with the riometer data.

Table 7.1: Daily evolution of phase speeds, horizontal wavelength, and propagating direction before, during, and after the onset of the major stratospheric warming in late September 2002.

Day #	**Phase Speed(m/s)**	**Horizontal wavelength (km)**	**Direction (˚)**	**Adjust**
254	23.2	64.7	44.5	yes
255	23.7	60.2	44.6	yes
256	22.6	63.0	26.8	yes
257	21.0	53.2	46.4	yes
259	24.7	68.9	38.5	yes
260	25.7	63.3	297.0	yes
261	28.7	68.9	45.3	yes
262	23.5	65.4	316.1	yes
263	19.3	52.1	315.0	yes
264	28.2	71.6	95.5	yes
265	17.4	50.0	123.9	yes
266	10.5	28.4	318.0	yes
267	7.9	22.1	57.2	yes
269	7.3	19.2	307.1	yes
270	11.0	27.9	42.9	yes
271	24.0	57.7	95.0	yes
272	15.2	40.0	71.0	yes
273	23.7	60.3	48.8	yes
274	27.3	67.5	41.6	yes
280	24.4	62.0	44.9	yes
281	26.2	63.0	315.3	yes
282	24.7	66.7	43.6	yes
283	26.0	66.0	42.4	yes

There seem to be no pattern in the propagation direction which can be associated with the major SSW. Thus, the gravity wave parameters presented above will only be discussed in terms of phase speeds and horizontal wavelengths. When examining both the gravity wave horizontal phase speeds and wavelengths, it is observed that the gravity waves of periods between 40 and 50 minutes can go up to a maximum of 29 m.s^{-1} and 69 km, respectively, during the period before and after the major SSW occurrence period. However, an interesting observation is that during the period of the occurrence of the major stratospheric warming (especially from day number 264 to 270) the gravity wave parameters had the lowest values. The primary reason behind the reduced values of gravity wave phase speed and wavelength during the SSW occurrence is presumably due to the fact that during the stratospheric warming gravity waves are thought to be able to propagate into the MLT and break there depositing their momentum. It has been previously shown that the height at which the gravity waves break in the MLT is the height where the MLT cooling and/or warming takes place (e.g. Holton, 1983; Yamashita et al., 2010).

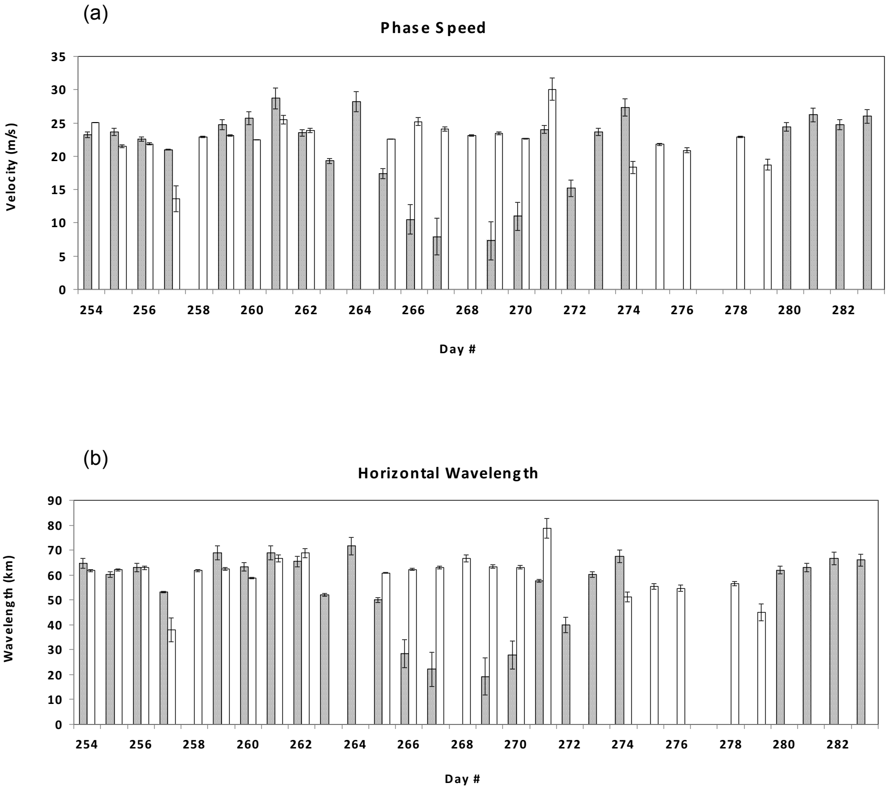

Figure 7.5: Histograms showing gravity wave phase speeds (a) and horizontal wavelengths (b), for year 2002 (dark grey bars) and 2003 (white bars) day number 254 to 283. The standard deviations are also included.

A comparison between the observations of the year 2002 late winter and year 2003 was also performed. The year 2003 was treated as a quite year, and year 2002 as a disturbed year due to the major stratospheric warming event. Figure (7.5) illustrates the histograms of the gravity wave (a) phase speed and (b) horizontal wavelength, for year 2002 (grey bars) and 2003 (white bars), respectively. The observations clearly show that both the phase speed and horizontal wavelength had comparable parameters for most of the days, but there is a difference observed during the period of the stratospheric warming occurrence from day number 264 to 272. During the SSW occurrence, the gravity wave phase speeds and horizontal wavelengths were observed to reach minimum values of about 7 m.s^{-1} and 18 km, respectively. The smaller values of both the gravity wave phase speeds and horizontal wavelengths during the period of the occurrence of SSW as observed by the SANAE riometer absorption data are not a surprise because mesopause region may be the region where the wave breaking occurred, and thus loosing the wave momentum. This wave breaking led to the cooling of the MLT and also the reversal of the mean circulation in the MLT in late September 2002 (Dowdy et al., 2004; Mbatha et al., 2010b).

Although many studies focusing on the gravity wave activity in the stratosphere during the stratospheric warmings (e.g. Ratnam et al., 2004b; Wang and Alexander, 2009), there have been a few studies that focus on the gravity wave activity in the MLT (e.g. Yamashita et al., 2010; Siskind et al., 2010). The observations presented in this study are consistent with both of these studies. Yamashita et al. (2010) examined how the height, vertical depth, and magnitude of the cooling and warming regions in the MLT varies with gravity wave parameters (phase velocity, horizontal wavelength, and momentum flux) in the Thermosphere-Ionosphere-Mesosphere-Electrodynamics General Circulation Model (TIME-GCM) during a minor SSW. They reported that the height, vertical depth and magnitude of the MLT cooling and warming regions vary significantly with gravity wave forcing. Yamashita et al. (2010) used the TIME-GCM, which employs a gravity wave parameterization based on a linear saturation theory. They used the parameters (spectral width, horizontal wavelength and wave amplitude) which are summarized in Table 7.2.

Table 7.2: Gravity wave parameters used in gravity wave parameterization (from Yamashita et al. (2010)).

	Range of Phase Velocities[a] (m/s)	Horizontal Wavelength (km)	Momentum Flux (Pa)
Base Case	±90	100	~1X10^{-5}
Case 1	±30	100	~1X10^{-5}
Case 2	±90	1000	~1X10^{-4}

[a] Spectral width

The most important observation by Yamashita et al. (2010) was that when the horizontal wavelength of the input gravity wave was reduced from 1000 km to 10 km with a constant spectral width (range of phase velocity) of ±90 m.s^{-1}, the magnitude of the gravity wave forcing in the MLT increased. This showed that as the horizontal wavelength decreases the gravity wave forcing becomes stronger, the forcing region expands, and the altitude of the maximum gravity wave forcing increases. A similar case is observed in this study, where the gravity wave horizontal wavelength is observed to decrease during the stratospheric warming period, which implies that there was an increase in gravity wave forcing during this period which led to the mesospheric cooling and mesospheric mean circulation reversal. Moreover, this is because the dispersion relations dictate that for a fixed phase speed, gravity waves with shorter horizontal wavelength have higher frequencies and longer vertical wavelengths, and these waves can propagate to higher altitudes (Holton, 1983; Yamashita et al., 2010).

7.2 Momentum Flux

In the previous sections it has been observed that the influx of wave activity originating from the troposphere and their deposition of wave momentum in the MLT led to many unprecedented processes in the MLT. Thus, it is important to also study the momentum flux ($\overline{u'v'}$) in the MLT during the year 2002 winter. The availability of the zonal and meridional wind components in the SANAE SuperDARN radar wind data is very important because it can help to derive the horizontal momentum flux in the MLT. The only drawback regarding this data is that it cannot be used to derive the vertical momentum flux because it does not have a good height resolution. The vertical momentum flux would be useful because it would identify the height region where the gravity waves started to lose their momentum. Here, u' and v' are zonal and meridional winds and the overbar denotes a time average. Running means of the momentum fluxes plotted together with the zonal mean wind evolution during the year 2002 and 2003, respectively, are presented in Figure (7.6). These running means are made up of a 4-day data window which was advanced by 1 day at a time, and the average of the data window was attributed to the second day of the interval. The four day mean was considered to be acceptable if at least 60% of the possible hourly wind values were recorded. The two panels in Figure (7.6) were plotted in order to compared the evolution of the momentum flux during year 2002 (warming year) and 2003 (quiet year). The period of the occurrence of the stratospheric warming is marked by a rectangle (see Figure (7.6)).

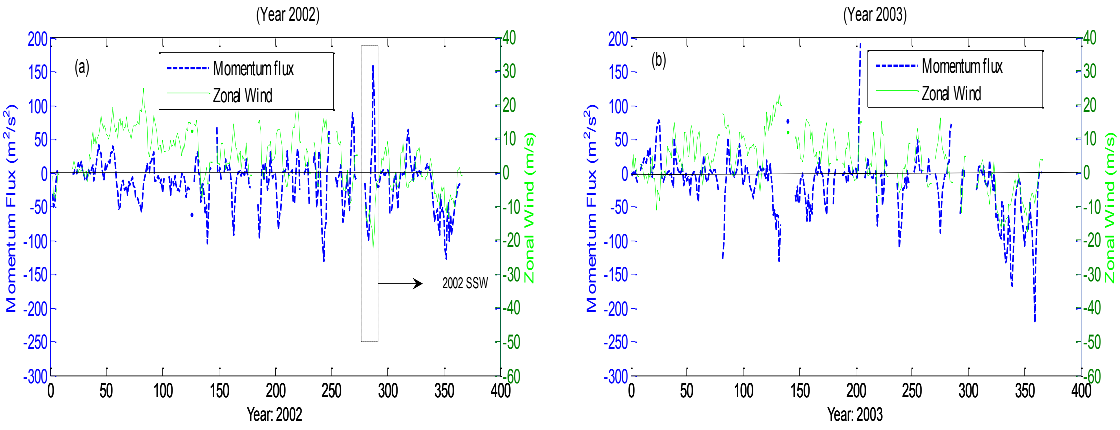

Figure 7.6: The zonal mean wind (green line) and momentum flux (blue line) at ∼94 km during year the 2002 (a) and 2003 (b).

There is a tendency of large negative (south-poleward) momentum flux in the year 2002 winter period (June-August), presumably due to the influx of wave activity of tropospheric origin. During this period, the momentum flux reaches minimum values of approximately -140 $m^2.s^{-2}$. Such intense reversal of the momentum flux is not apparent in the winter period of year 2003. Large positive momentum flux of a maximum value of approximately 100 $m^2.s^{-2}$ is present few days before the onset of the 2002 major stratospheric warming. This large momentum flux is followed by a sudden decrease of the momentum flux which coincides with the reversal of the zonal wind at ∼94 km altitude. The reversal of the momentum flux is associated with the deposition of gravity waves in the MLT. In early October 2002, a large positive momentum flux is again observed. The trend observed in the year 2002 momentum flux calculated using the SANAE SuperDARN radar wind measurements is consistent with the observations by Murphy et al. (2007), which were compiled using MF radar measurements at Davis. The study by Murphy et al. (2007) also utilised the accumulation of the MF radar wind and hydroxyl temperature measurements at Davis from 1997 to 2005 to compile a climatology of long period wave activity in the MLT. There study also presented comparisons of heat and momentum fluxes observed during the year of the southern hemisphere stratospheric warming (2002) to other years.

7.3 Gravity Wave Potential Energy

The estimates of potential energy associated with gravity waves have been studied by other authors (e.g. Sivakumar et al., 2006; Thurairajah et al., 2010). However, these studies usually use LIDAR observations. But, the South African site (SANAE) in Antarctica does not have a LIDAR instrument. Thus, in order to study the potential energy in the middle atmosphere used the SABER temperature data was used. The SABER vertical temperature profiles shown in Figure (6.15) of Chapter 6 clearly indicate that there were some element of gravity wave activity which led to the variation of temperature, as well as some inversion layer observed in the MLT during the occurrence of the major SSW.

A study by Sivakumar et al. (2006) used the Rayleigh LIDAR observations made at Gadanki (13.5°N, 79.2°E) to study the characteristics of atmospheric gravity waves. In their study, they estimated the variation of gravity wave associated potential energy for different seasons. A recent study by Thurairajah et al. (2010) reported on the gravity wave activity in the arctic stratosphere and mesosphere during the 2007-2008 and 2008-2009 stratospheric sudden warming events, using Rayleigh LIDAR measurements. A study by Chanin and Hauchecorne (1981) and Chanin (1991) showed significant dependence of the gravity waves associated potential energy with seasons. In this study, the potential energy in the middle atmosphere is studied using SABER temperature observations taken before and during the 2002 (warming year) southern hemisphere late winter major stratospheric warming. The observations are also compared to the similar period in the year 2003 (normal year). The temperature profiles used here are for the sunrise and sunset passages of SABER/TIMED satellite over the SANAE base, within ±10° in latitude and ±10° in longitude.

7.3.1 Theoretical Consideration of Gravity Wave Energy

Previous studies have shown that the density and temperature fluctuations normalized to their mean values are about the same and either of them can be used to estimate the gravity wave associated potential energy (e.g. Whiteway and Carswell (1994)). Thus in this study, the height profiles of the potential energy associated with gravity waves perturbations were computed using profiles of relative temperature fluctuations $\left(\frac{T'}{T_0}\right)$ obtained from the SABER satellite. The potential energy (E_p) per unit mass is expressed as (Wilson et al., 1990)

$$E_p = \frac{1}{2}\left(\frac{g}{N}\right)^2\left(\frac{T'}{T_0}\right)^2, \tag{7.5}$$

where g is the gravitational acceleration, T_0 and T' are the mean temperature and temperature perturbations, and N is the Brunt Väisälä frequency computed using the expression

$$N^2 = \frac{g}{T_p}\left[\frac{dT_p}{dz} + \Gamma\right], \tag{7.6}$$

where, Γ is the adiabatic lapse rate (=-9.8 km^{-1}), and T_p is the temperature value taken from the 3rd order polynomial fit applied to the mean temperature profile. In general, the total energy associated with gravity wave activity is given by

$$E_0 = \frac{1}{2}\left[\overline{u'^2} + \overline{v'^2} + \overline{w'^2} + \left(\frac{g}{N}\right)^2\left(\frac{T'}{T_0}\right)^2\right] = E_k + E_p, \tag{7.7}$$

where E_k is the gravity wave associated kinetic energy given by

$$E_0 = \frac{1}{2}\left[\overline{u'^2} + \overline{v'^2} + \overline{w'^2}\right]. \tag{7.8}$$

In the above equation, u' and v' correspond to the perturbation components of wind velocity which are aligned or orthogonal to the wave propagation direction, respectively, while w' is the vertical wind velocity. By assuming a uniform azimuthal distribution of wave propagation, the vertical wind velocity (w') may neglected, and thus only zonal and meridional wind components for u' and v', respectively, can be used. It is also worth mentioning that u', v', w' and T' are all coupled to each other through gravity wave polarization equations.

A study by Fritts and Vanzandt (1993) described the energy spectrum of wind velocity and temperature perturbation caused by gravity waves as a product of separable functions in ω, m, and ϕ

$$E(\mu, \omega, \phi) = E_0 A(\mu) B(\omega) \Phi(\phi), \tag{7.9}$$

where,

$$A(\mu) = \frac{A_0 \mu^s}{(1 + \mu^{s+t})} \tag{7.10}$$

$$B(\omega) = B_0 \omega^{-p}. \tag{7.11}$$

where $\mu = m/m_*$, $m = 2\pi/\lambda_z$, with λ_z and m_* being the vertical wavelength and the characteristic wavenumber, respectively, and ϕ is the azimuth angle indicating the direction of the wave propagation, s, t, and p are constants. The parameters E_0 and A_0 and B_0 are, respectively, the total wave energy per unit mass and normalization constraints for vertical wavenumber and frequency spectra $A(\mu)$ and $B(\omega)$. The function $\Phi(\phi)$ depicts the anisotropy of the wave field.

The linear theory of gravity waves predicts that the ratio of the kinetic energy to potential energy is a constant equal to the spectral index p (e.g. VanZandt (1985)). Therefore, under the linear theory it is possible to estimate the total energy E_0 from the temperature observations only (i.e. from equation 7.5).

7.3.2 Results: Measured Gravity Wave Potential Energy

As mentioned earlier, the SABER instrument obtains temperature profiles from 52°S to 83°N during its north-looking mode for 60 days before switching to an analogous south-looking mode and then repeats that sequence for the subsequent months (Remsberg et al., 2003). In this way, the polar cap data is available only in 60-day segments, with no information for the 60 days preceding. Due to this reason, only data from 1 September to 19 September was available. This implies that only data from the first 3-4 days of the occurrence of the major SSW could be obtained over SANAE (72°S, 3°W), because the stratospheric warming started around 15 September and persisted for about 10 days. Figure (7.7) shows the height profiles of mean potential energy with standard error of the mean, for August and September 2002 (warming year) and 2003 (normal year), respectively.

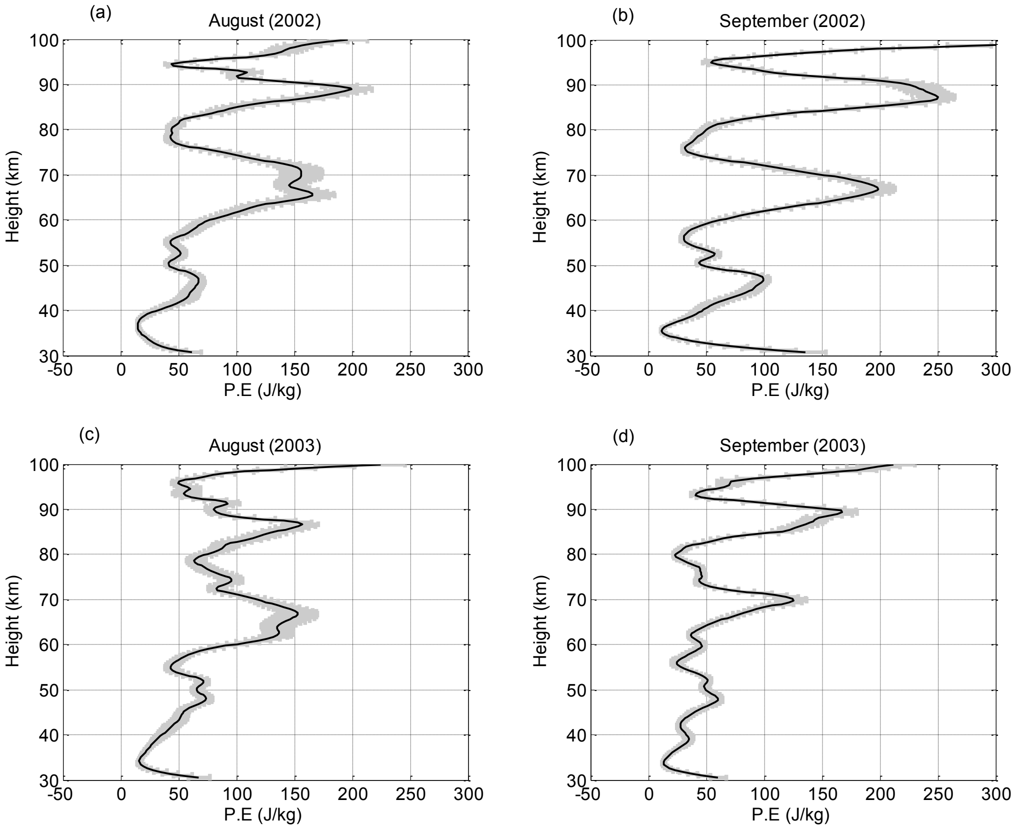

Figure 7.7: Height profiles of monthly mean potential energy per unit mass (black line) and the associated standard error of the mean (grey shading) for the gravity wave perturbations over SANAE.

The variation of the potential energy with height is clearly observed during August and September and in 2002 and 2003 (see Figure (7.7)). The potential energy is observed to be gradually increasing with height up to values of ∼150 J.kg^{-1} at heights above ∼65 km. Even though the September 2002 potential energy mean profile contains only the first 19 days of the month, the enhancement in the potential energy can be clearly observed. The September 2002 potential energy height variation unlike the other panels show three distinct peaks with values of ∼100 J.kg^{-1}, ∼200 J.kg^{-1}, and ∼300 J.kg^{-1} in the height region of 45-50 km, 65-73 km, and 85-93 km.

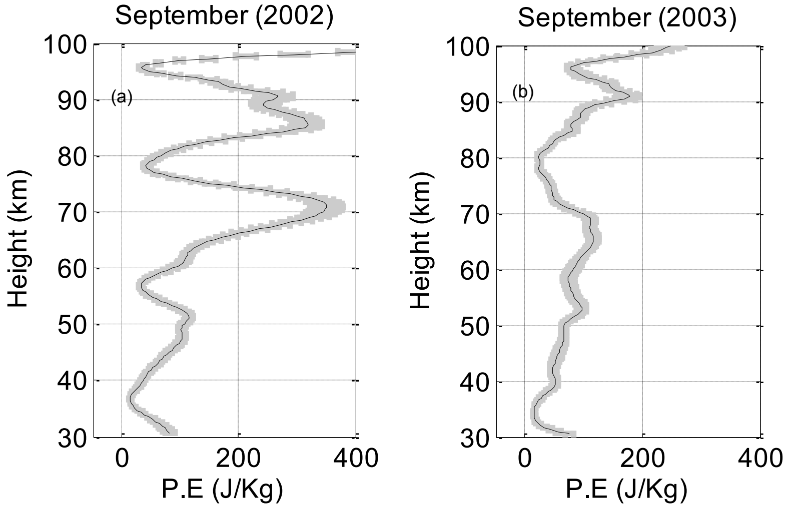

Figure 7.8: Height profiles of monthly mean potential energy per unit mass (black line) and the associated standard error of the mean (grey shading) for gravity wave perturbations over 52°S.

In order study the gravity wave associated potential energy for the whole month of September, those profiles which are closest to -52° latitude were used. Figure (7.8) shows the height profiles of mean potential energy with standard error of a mean, for September 2002 and 2003, respectively. Again when comparing the two years there is a clear enhancement in September 2002 potential energy profile through the middle atmosphere. This enhancement in the potential energy is evidence of the effect of the major SSW. The MLT peaks observed in Figure (7.7b) are also evident in the profile of September 2002 (Figure (7.8a)). However, in this profile, the peak at the height around 70 km seems to be the strongest (∼350 $J.kg^{-1}$).

The values of potential energy observed at a height region below 40 km in the September 2002 profile (Figure (7.7b) and Figure (7.8a)) are consistent with observations by Ratnam et al. (2004b). Ratnam et al. (2004b) studied the dynamics of the potential energy only in the stratosphere during the 2002 major SSW using the CHAMP/GPS temperature profiles, and compared it to the 2003 observations. In their study, they showed that during the 2002 major SSW the potential energy in the stratosphere had higher values outside and in the edges of the polar vortex, while the values were lower inside the polar vortex. The above mentioned observation could explain the reason for observed higher values of potential energy at latitudinal region closest to -52° (Figure (7.8a)) when compare to the potential energy at region closest to -72° latitude (Figure (7.7b)), observed in this study. For more details on the latitudinal and longitudinal variation of potential energy and the causative mechanisms, the reader may refer to Tsuda et al. (2000) and Ratnam et al. (2004a).

Figure (7.8a) indicates clearly that gravity wave amplitudes were increasing with height up to their braking point in the MLT. The observations indicate that during the year 2002 winter, the amplification of planetary waves in the middle atmosphere led to the reversal of the mean wind. This disturbance of the mean wind in the stratosphere allowed more gravity waves of tropospheric origin to propagate to the MLT. Gravity waves propagation in the middle atmosphere depends largely on the background wind. As they propagate upward in the middle atmosphere they undergo a selection process due to critical level filtering (Taylor et al., 1993) owing to the effect of the background wind. Assuming that the background wind varies slowly on the spatial and temporal resolution of the gravity waves, a local dispersion relation holds, and the vertical wavenumber m can be given by

$$m^2 \approx \frac{N^2}{\left(c - \overline{u}\hat{k_h}\right)^2} \tag{7.12}$$

and the vertical group velocity C_{g_z} is given by

$$C_{g_z} \approx \frac{N k_h}{m^2} \tag{7.13}$$

where N is the Brunt Väisälä frequency, $c = \omega/k$ is the horizontal phase speed of the wave with radial frequency ω, k_h is the horizontal wavenumber, and $\overline{u}$ is the background wind. The above two equations show that as a wave travels with the background wind, m increases, the vertical wavelength is shortened, and the vertical group velocity decreases. The shortening of the wavelength and the reduction of the phase speed implies that the viscosity will have a larger effect, and thus the attenuation of the wave (e.g. Stockwell and Lowe (2001)).

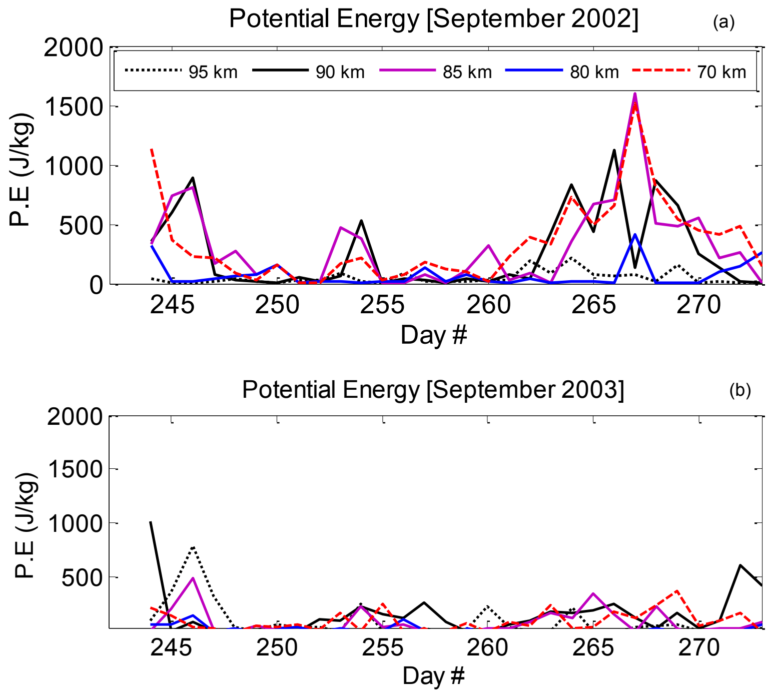

Figure 7.9: Potential energy for the days from 1 to 30 September 2002 (a) and 2003 (b), respectively.

Figure (7.9) shows the daily variation of the potential energy over the altitude region of 70 km, 80 km, 85 km, 90 km, and 95 km, for the days of September 2002 (warming year) and 2003 (normal year), respectively. These profiles were obtained from the SABER temperature profiles which are closest to -52° latitude. When comparing the two figures (Figure (7.9a and b)), it can be clearly observed that there was an enhancement in the year 2002 potential energy in the MLT region during the period of the occurrence of the major SSW. During this period (day 260-273), the potential energy at the height region between 70 km and 90 km is observed to have a maximum peak which reach a value of $\sim$1500 J.kg^{-1} on day number 267 (24 September 2002) at the height region of 85 km and 70 km. At the height region between 90 km and 100 km, the potential energy is observed to be weaker, presumably due to the gravity waves damping their momentum in this region, leading to the MLT cooling which is evident in Figure (6.14).

7.4 Discussion and Summary

By using the SANAE imaging riometer absorption data and vertical temperature profiles from the SABER instruments aboard the TIMED satellite, the effect of the 2002 major SSW in the southern hemisphere on the gravity waves activity in the middle atmosphere is examined in this chapter. In this work, the SANAE imaging riometer was for the first time used to extract gravity wave parameters such as horizontal phase speeds, horizontal wavelength, and the propagation direction.

During the period of the occurrence of the major stratospheric warming, there was a reduction of both the gravity wave horizontal phase speeds and the horizontal wavelengths. This reduction was not observed in the propagation direction of the gravity waves. During the SSW occurrence period, the gravity wave phase speeds and horizontal wavelengths were observed to reach minimum values of about 7 m.s^{-1} and 18 km, respectively, while during the quiet period the average value of the phase speed and propagation direction was approximately 23 m.s^{-1} and 62 km, respectively. This reduction of the above mentioned parameters may be associated with the region where gravity waves break, and thus loosing the wave momentum. This process also leads to the mesospheric cooling (e.g. Cho et al. (2004); Mbatha et al. (2010b); Yamashita et al. (2010)).

Gravity waves are thought to be generated in the troposphere during a variety of meteorological and orographic situations (e.g. Hines (1988)). These waves can have zonal asymmetries resulting from the distribution of orographic features and the flows in the troposphere. Unlike the Northern Hemisphere, the orography of the southern hemisphere limits the generation of gravity wave. However, there have been many studies which have reported gravity wave activity in the lower atmosphere and the stratosphere. In this study, the SABER vertical temperature profiles taken over the SANAE site, within ±10° in latitude and ±10° in longitude was used to study the gravity wave associated potential energy in the middle atmosphere during the southern hemisphere major SSW, and compared it to a normal year (2003).

There is a clear enhancement observed on the vertical profiles of the potential energy during the 2002 September month. The potential energy was observed to have maximum values of about 300 J.kg^{-1} at the height region between 85 to 93 km over SANAE. However, at the -52° latitude the potential energy was observed to be higher when compared to the potential energy observed at the -72° latitude. This is consistent with the observations made by Tsuda et al. (2000) and Ratnam et al. (2004b). The observations indicate that gravity wave amplitudes were increasing with height up until they reach the MLT region where they dump their energy and momentum, and thus leading to the MLT cooling and mean wind reversal.

The major stratospheric warming started on 18 September 2002 and persisted for about 10 days, before the stratosphere returned to its normal state. The observations of this study have shown that during this period there was an enhancement in the potential energy in the MLT. The potential energy reached maximum value of $\sim$1500 J.kg^{-1} during day number 267 (24 September 2002), a value which is about 3 times higher than typical values. At the height above 90 km, the potential energy is observed to decrease presumably due to the breaking of gravity waves and the associated loss of momentum. A strong planetary wave activity in the stratosphere led to the reversal of the mean circulation in the stratosphere, which in turn allowed gravity waves to propagate to the MLT. The amplitude of these gravity waves was observed to increase with height until they broke at the MLT depositing their momentum.

By using fluctuations of the ionospheric absorption of cosmic radio noise measured by SANAE imaging riometer as a tracer of gravity waves, as well as temperature profiles from the SABER/TIMED satellite, this study has shown that gravity waves play an important role in the dynamics of the middle atmosphere. This study seems to indicate that gravity waves observed in the middle atmosphere during the SSW event originate from the troposphere, and propagated upwards. The upward propagating gravity waves are filtered by the stratospheric circulation, which may be zonally asymmetric due to planetary waves (Ratnam et al., 2004b). When these upward propagating gravity waves dissipate, the wave drag forcing will have planetary scale zonal asymmetries. However, a future study shall further investigate in detail the characteristics of gravity waves (gravity wave sources, energy and momentum flux divergence) in order to assess whether they are significant enough to modify the dynamics of the middle atmosphere.

Chapter 8

Summary and Conclusion

This study has investigated the coupling and dynamics of the middle atmosphere using the SuperDARN HF radar system, LIDAR, riometer, satellites, assimilated data and models. In particular, the study focused on the 2002 major stratospheric warming and its role in coupling the middle atmosphere. The SANAE SuperDARN radar meteor wind data was for the first time used to study, in detail, the dynamics of the MLT including the 2002 winter major SSW event.

In Chapter 1, background information relevant to the study presented in thesis was given. A general overview of the structure of the middle atmosphere primarily in terms of the general circulation and the temperature structure was presented in this chapter. Phenomena such as planetary waves, gravity waves and the stratospheric warmings were also described in this chapter. All the analysis techniques applied to analyse data used in this study were described in Chapter 2. These techniques are primarily Fourier transforms, wavelet transforms and complex demodulation.

In this thesis, data from different sources was used in order to study the middle atmospheric dynamics of the southern hemisphere. These instruments include the SuperDARN HF radars, the Durban and Reunion Rayleigh LIDAR, imaging riometer, satellites (SABER and HALOE), modelled and assimilated data (UKMO, NCEP/NCAR, ECMWF and CIRA-86), and were described in Chapter 3. These data sources were chosen on basis of accessibility and relevance. It should also be mentioned that due to the unavailability of a MF radar in the SANAE base, the MLT wind data was very limited. However, this disadvantage also proved to be very useful because this study has also shown that SuperDARN radar meteor wind data can also be a suitable option in studying the dynamics of the MLT, even though it has only one assumed height.

In Chapter 4, the climatology of the temperature between 30 and 70 km altitude based on 5 years (1999-2004) of Rayleigh LIDAR measurements over Durban, South Africa, was investigated. The LIDAR observations were also compared with the 4 year (2000-2004) and 5 year (1999-2004) observations from SABER and HALOE satellite instruments, respectively, and CIRA-86 model, for the first time. Even though there are some differences at some specific heights, in general, the results show that there is a good agreement between the LIDAR instrument, satellites and the model. The difference in methods of data retrieval between the ground-based and space-based instruments as well as the location and time of measurements might contribute in the overall differences between the LIDAR and satellite.

The seasonal temperature profiles measured by the Durban LIDAR were also compared to the temperature profiles measured by the Reunion LIDAR. The seasonal profiles were found to be within the standard deviation at the height below 50 km, and thus there is fairly good agreement between the two instruments for all the seasons. However, for all the seasons the Durban LIDAR observations were seen to be slightly higher (about 3 to 8 K) than the Reunion LIDAR observations up to the stratopause. Moreover, the LIDAR climatology results presented in this thesis should benefit a variety of different middle atmosphere models and reanalyses data (e.g. CIRA and NCEP).

In Chapter 5, the meteor wind data (zonal and meridional component) measured by the SANAE and Halley SuperDARN HF radars was utilised in order investigate the climatology of mean wind and planetary waves of periods between 2 and 20 days for the time interval from January 1998 to December 2006 in the MLT of the southern hemisphere. The study presented in this chapter is pioneering work since it was the first time ever that the measurements from the SuperDARN HF radar in the southern hemisphere is used to study the climatology of the mean wind and planetary waves. The climatology of the mean wind showed good agreement when comparing observations from the two SuperDARN sites (SANAE and Halley). This was expected because the radars are similarly designed and are part of network of SuperDARN radars located both in the southern hemisphere and in the Northern Hemisphere . The climatology of the zonal mean wind as observed by both HF radars seemed to indicate a seasonal dependence, while the opposite is true for the meridional wind component. The zonal mean flow seasonal trend at both SANAE and Halley was observed to have a primary maximum that can go up to 14 m/s in the solstices, while the minimum values were observed during summer and winter months. These results are consistence with observations by other authors (e.g. Fleming et al. (1996); Malinga et al. (2004); Baumgaertner et al. (2005)).

Furthermore, Chapter 5 also investigated the year-to-year variation of planetary waves of period between 2 and 20 days for the time interval from January 1998 to December 2006, as observed by the SANAE HF radar using the wavelet analysis technique. This was done in order to investigate the seasonal variation of planetary waves as well as the trend of planetary wave activity in the MLT. The observations showed that the there is a tendency of the meridional wind component to exhibit weaker planetary wave activity than the zonal wind, especially at longer periods ($\geq$10 days), presumably due to the difference in Hough mode structures, and hence latitudinal variabilities of the two wind components (e.g. **?**Chshyolkova et al. (2006)). The spring and autumn seasons were observed to have strong planetary wave activity of period around 8-12 days in the zonal component, understandably because this period is a transition time with strong trends in the mean wind of the MLT.

The wind data (HF radar and UKMO) for time interval from 2001 to 2003 (with 2001 and 2003 being treated as normal years, and 2002 a disturbed year because of the stratospheric warming) was selected for the purpose of deducing characteristics for planetary wave activity, as well as the coupling in the middle atmosphere. During this period, the zonal wavenumbers of the 5-, 10-, and 16-day waves during the summer and winter were also calculated. It was observed that the winter season tends to be dominated by planetary wave activity of the 10-day and 16-day waves of shorter zonal wavenumbers ($s=\pm3$) both in the zonal and the meridional wind components. The 5-day wave was observed to have shorter wavenumbers during summer seasons. Both the Charney-Drazin criterion and the cross-wavelet analyses between the UKMO ($\sim$49.5 km) stratospheric data and the SANAE HF radar data ($\sim$94 km), show a wave coupling between the MLT and the stratosphere, especially during the stratospheric warming event. There is also a signature of a quasi 10-day wave in the mesosphere which is observed at around the same time with the quasi 10-day wave in the stratosphere. The signature maybe presumable due to the lower atmosphere originated gravity waves which are modulated by a strong quasi 10-day wave in the stratosphere, and carrying their momentum to the MLT region.

In Chapter 6, the SANAE HF radar data was used to examine the dynamical structure of the MLT region during the unprecedented major SSW which occurred in late September 2002. Only MF radars are usually used for this purpose both in the Southern and Northern Hemisphere s. The results showed that at $\sim$94 km, the mean zonal wind (obtained from the SANAE HF radar) displays an enhancement throughout the 2002 winter, due to a series of large planetary wave amplifications in the stratosphere which produce strong westward forcing in the high latitude winter stratosphere. In general, eastward zonal winds dominate the winter MLT. However, the 2002 winter reflect obvious differences when compared to other years, with many brief periods of westward winds observed. Normalised Fourier power spectra reflected the presence of planetary waves of 5-day, 10-day and 14- to 16-day periods during the 2002 austral winter. The observation of the quasi 14-day oscillation is consistence with observations reported by Dowdy et al. (2004) and other authors.

The mean circulation in the stratosphere was characterised by a series of planetary wave events in 2002 winter that weakened the polar vortex and triggered the SSW in late September. The E-P flux also confirmed that a strong planetary wave activity observed in the middle atmosphere originated from the troposphere. Particularly, in the stratosphere there was a presence of a quasi 10-day eastward propagating planetary wave of wavenumber $s=1$, while in the MLT a quasi 14-day eastward propagating planetary wave of wavenumber $s=1$ was observed to be dominant. When investigating the zonal wind at $\sim$94 km (SANAE HF radar data) and the zonal mean zonal winds at the stratosphere (32 km) using the NCEP stratospheric data, the results show that the reversal event in the MLT took place in a few days (about a week) prior to the reversal in the stratosphere. This behaviour indicates that there may be a downward propagation of the disturbances in the middle atmosphere. Similar results were also reported by Dowdy et al. (2004). In general, the SANAE HF radar results show similarities to the previous observations of the major SSWs both in the Southern and the Northern Hemisphere.

In the winter months of year 2002, the stratosphere displayed an unusual increase of temperature which started in mid September, whilst the MLT region showed cooling and temperature signature of inversion layers a few days before the SSW occurrence. This behaviour of the MLT region is associated with energy deposition due to gravity wave breaking in the mesosphere. Gravity wave momentum deposition drives the pole-to-pole meridional wind circulation, that in turn causes the departure of mesospheric temperature from radiative equilibrium, keeping the winter MLT warmer and summer MLT colder (Holton, 1983).

By using the imaging riometer and SABER data, the gravity wave parameters (phase speeds, horizontal wavelength, and propagation direction) and middle atmosphere potential energy associated with gravity wave activity were investigated in Chapter 7. The major SSW and its associated enhanced planetary wave activity were observed to have an influence in the gravity wave activity in the middle atmosphere. During the year 2002 winter there was a tendency of large negative (south-poleward) momentum flux, presumably due to the influx of wave activity of tropospheric origin at the MLT region. A reduction of gravity wave horizontal wavelengths and phase speeds at 90 km in timing of the stratospheric warming and the zonal wind reversal associated with the 2002 stratospheric warming was observed. The conditions of the stratosphere in the year 2002 winter preconditioned the region to allow more gravity waves to propagate upward to the MLT. The potential energy of these gravity waves was observed to increase with height from the stratosphere up until they reach the lower thermosphere. At the MLT they lose their energy and deposit their momentum, and leading to the MLT cooling and mean wind reversal. The above mentioned processes which indicate a strong coupling between the MLT and the stratosphere have also been reported by other authors (e.g. Liu and Roble (2002); Chshyolkova et al. (2006); Dowdy et al. (2004); Mbatha et al. (2010b)).

8.1 Future Work

While this study has shown the presence of vertical coupling middle atmosphere, particularly during the occurrence of the unprecedented 2002 southern hemisphere major stratospheric warming, there are still many unanswered questions. A higher frequency of observations uniformly distributed across Antarctica could be useful in order to comprehensively analyse in more detail the stratospheric warming in the southern hemisphere. The installation of a Rayleigh LIDAR network could provide the much needed temporal measurements of gravity wave activity in the zonally asymmetric Antarctica middle atmosphere.

The analysis technique used in this thesis will be applied to the entire SANAE imaging riometer data set to build up the climatology of mesospheric gravity wave characteristics over this region. The observations from the SANAE riometer will also be compared to other imaging riometers situated across Antarctica, as well as other instruments (e.g. airglow imager). The SABER middle atmospheric temperature data could also be useful in investigating the climatology of the gravity wave associated potential energy, and their latitudinal and longitudinal variations.

References

Alexander, M. J. and Dunkerton, T. J.: A spectral parameterization of mean-flow forcing due to breaking gravity waves, Journal of the Atmospheric Sciences, 56, 4167–4182, 1999.

Alexander, M. J. and Pfister, L.: Gravity wave momentum flux in the lower stratosphere over convection, Geophysical Research Letters, 22, 2029–2032, 1995.

Andrews, D., Holton, J., and Leovy, C.: Middle atmosphere dynamics, Academic Pr, San Diego, Calif, 1987.

Andrews, D. G.: An introduction to atmospheric physics, Cambridge Univ Pr, 2000.

Argall, P. S. and Sica, R. J.: A comparison of Rayleigh and sodium lidar temperature climatologies, in: Annales Geophysicae, vol. 25, pp. 27–35, 2007.

Azeem, S. M. I., Talaat, E. R., Sivjee, G. G., and Yee, J. H.: Mesosphere and lower thermosphere temperature anomalies during the 2002 Antarctic stratospheric warming event, Annales Geophysicae, 28, 267–276, 2010.

Baldwin, M., Hirooka, T., OŠNeill, A., Yoden, S., Charlton, A. J., Hio, Y., Lahoz, W. A., and Mori, A.: Major stratospheric warming in the Southern Hemisphere in 2002: Dynamical aspects of the ozone hole split, SPARC newsletter, 20, 24–26, 2003.

Baray, J. L., Leveau, J., Porteneuve, J., Ancellet, G., Keckhut, P., Posny, F., and Baldy, S.: Description and evaluation of a tropospheric ozone lidar implemented on an existing lidar in the southern subtropics, Applied Optics, 38, 6808–6817, 1999.

Barnett, J. J. and Corney, M.: Middle atmosphere reference model derived from satellite data, in: In International Council of Scientific Unions Middle Atmosphere Program. Handbook for MAP, vol. 16, pp. 47–85, 1985.

Batista, P. P., Clemesha, B. R., and Simonich, D. M.: A 14-year monthly climatology and trend in the 35-65 km altitude range from Rayleigh Lidar temperature measurements at a low latitude station, Journal of Atmospheric and Solar-Terrestrial Physics, 71, 1456–1462, 2009.

Baumgaertner, A. J. G.: Observations of Middle Atmosphere Dynamics over Antarctica, PhD thesis, 2007.

Baumgaertner, A. J. G., McDonald, A. J., Fraser, G. J., and Plank, G. E.: Long-term observations of mean winds and tides in the upper mesosphere and lower thermosphere above Scott Base, Antarctica, Journal of Atmospheric and Solar-Terrestrial Physics, 67, 1480–1496, 2005.

Bencherif, H., Moorgawa, A., Morel, B., Michaelis, M., Leveau, J., Hauchecorne, A., Porteneuve, J., and Faduilhe, D.: First validation of stratospheric temperature profiles obtained by a Rayleigh LIDAR over Durban, South Africa, South African Journal of Science, 96, 487–492, 2000.

Bencherif, H., Amraoui, L. E., Semane, N., Massart, S., Charyulu, D. V., Hauchecorne, A., and Peuch, V. H.: Examination of the 2002 major warming in the southern hemisphere using ground-based and Odin/SMR assimilated data: stratospheric ozone distributions and tropic/mid-latitude exchange, Canadian Journal of Physics, 85, 1287–1300, 2007.

Bremer, J. and Berger, U.: Mesospheric temperature trends derived from ground-based LF phase-height observations at mid-latitudes: comparison with model simulations, Journal of Atmospheric and Solar-Terrestrial Physics, 64, 805–816, 2002.

Brewer, A. W.: Evidence for a world circulation provided by the measurements of helium and water vapour distribution in the stratosphere, Quarterly Journal of the Royal Meteorological Society, 75, 351–363, 1949.

Bristow, W. A., Yee, J. H., Zhu, X., and Greenwald, R. A.: Simultaneous observations of the July 1996 2-day wave event using the Super Dual Auroral Radar Network and the High Resolution Doppler Imager, Journal of Geophysical Research, 104, 12 715, 1999.

Brook, D. and Wynne, R. J.: Signal processing: Principles and applications, Edward Arnold London, 1988.

Chandra, H., Sharma, S., Acharya, Y. B., and Jayaraman, A.: A Rayleigh lidar study of the atmospheric temperature structure over Mt. Abu, India, Journal of Indian Geophysical Union, 9, 2005.

Chang, Q. H., Yang, G. T., and Gong, S. S.: Lidar observations of the middle atmospheric temperature characteristics over Wuhan in China, Journal of Atmospheric and Solar-Terrestrial Physics, 67, 605–610, 2005.

Chanin, M. L.: Lidar study of the structure and dynamics of the middle atmosphere, in: IN: The middle atmosphere and space observations; International Summer School on Space Physics, Marseille, France, Aug. 1990, Proceedings (A92-26731 10-46). Toulouse, France, Cepadues-Editions, 1991, p. 479-495. In French., vol. 1, pp. 479–495, 1991.

Chanin, M. L. and Hauchecorne, A.: Lidar observation of gravity and tidal waves in the stratosphere and mesosphere, Journal of Geophysical Research, 86, 9715–9721, 1981.

Charney, J. G. and Drazin, P. G.: Propagation of planetary-scale disturbances from the lower into the upper atmosphere, Journal of Geophysical Research, 66, 83–109, 1961.

Charyulu, D. V., Sivakumar, V., Bencherif, H., Kirgis, G., Hauchecorne, A., and Rao, D. N.: 20-year LiDAR observations of stratospheric sudden warming over a mid-latitude site, Observatoire de Haute Provence (44 N, 6 E): Case study and statistical characteristics, Atmospheric Chemistry Physics Discussion, 7, 15 739Ű15 779, 2007.

Chatfield, C.: The analysis of time series. An Introduction, Chapman & hall, London, 1989.

Cho, Y. M., Shepherd, G. G., Won, Y. I., Sargoytchev, S., Brown, S., and Solheim, B.: MLT cooling during stratospheric warming events, Geophysical Research Letters, 31, L10 104, 2004.

Chshyolkova, T., Manson, A. H., Meek, C. E., Avery, S. K., Thorsen, D., MacDougall, J. W., Hocking, W., Murayama, Y., and Igarashi, K.: Planetary wave coupling processes in the middle atmosphere (30-90 km): A study involving MetO and MFR data, Journal of Atmospheric and Solar-Terrestrial Physics, 68, 353–368, 2006.

Clancy, R. T., Rusch, D. W., and Callan, M. T.: Temperature minima in the average thermal structure of the middle mesosphere (70–80 km) from analysis of 40-to 92-km SME global temperature profiles, Journal of Geophysical Research, 99, 19 001, 1994.

Clark, R. R., Burrage, M. D., Franke, S. J., Manson, A. H., Meek, C. E., Mitchell, N. J., and Muller, H. G.: Observations of 7-d planetary waves with MLT radars and the UARS-HRDI instrument, Journal of Atmospheric and Solar-Terrestrial Physics, 64, 1217–1228, 2002.

Coy, L., Siskind, D. E., Eckermann, S. D., McCormack, J. P., Allen, D. R., and Hogan, T. F.: Modeling the August 2002 minor warming event, Geophysical Research Letters, 32, 2005.

Detrick, D. L. and Rosenberg, T. J.: A phased-array radiowave imager for studies of cosmic noise absorption, Radio Science, 25, 325–338, 1990.

Dobson, G. M. B.: Origin and distribution of the polyatomic molecules in the atmosphere, Proceedings of the Royal Society of London. Series A, Mathematical and Physical Sciences, 236, 187–193, 1956.

Donelan, M. A., Longuet-Higgins, M. S., and Turner, J. S.: Nonstationary analysis of the directional properties of propagating waves, Journal of Physical Oceanography, 26, 1901–1914, 1996.

Dou, X., Li, T., Xu, J., Liu, H., Xue, X., Wang, S., Leblanc, T., McDermid, I., Hauchecorne, A., Keckhut, P., et al.: Seasonal oscillations of middle atmosphere temperature observed by Rayleigh lidars and their comparisons with TIMED/SABER observations, Journal of Geophysical Research, 114, D20 103, 11 PP, doi:10.1029/2008JD011 654, 2009.

Dowdy, A. J.: Polar Middle Atmosphere Dynamics, Ph.D. thesis, University of Adelaide, 2005.

Dowdy, A. J., Vincent, R. A., Murphy, D. J., Tsutsumi, M., Riggin, D. M., and Jarvis, M. J.: The large-scale dynamics of the mesosphere–lower thermosphere during the Southern Hemisphere stratospheric warming of 2002, Geophysical Research Letters, 31, L14 102, 2004.

Edmon, H. J., Hoskins, B. J., and McIntyre, M. E.: Eliassen-Palm Cross Sections for the Troposphere., Journal of Atmospheric Sciences, 37, 2600–2616, 1980.

Eliassen, A. and Palm, E.: On the transfer of energy in stationary mountain waves, Geofysiske Publikasjoner, 22, 1–23, 1961.

Espy, P. J., Hibbins, R. E., Riggin, D. M., and Fritts, D. C.: Mesospheric planetary waves over Antarctica during 2002, Geophysical Research Letters, 32, 2005.

Farge, M.: Wavelet transforms and their applications to turbulence, Annual Review of Fluid Mechanics, 24, 395–458, 1992.

Farman, J. C., Gardiner, B. G., and Shanklin, J. D.: Large losses of total ozone in Antarctica reveal seasonal C10x/NOx interaction, Nature, 315, 207–210, 1985.

Fedulina, I. N., Pogoreltsev, A. I., and Vaughan, G.: Seasonal, interannual and short-term variability of planetary waves in Met Office stratospheric assimilated fields, Quarterly Journal of the Royal Meteorological Society, 130, 2445–2458, 2004.

Fiocco, G.: Lidar systems for aerosol studies: an outline, in: In International Council of Scientific Unions Middle Atmosphere Handbook, Vol. 13 p 56-68 (SEE N85-17452 08-46), vol. 13, pp. 56–68, 1984.

Fleming, E. L., Chandra, S., Barnett, J. J., and Corney, M.: Zonal mean temperature, pressure, zonal wind and geopotential height as functions of latitude, Advances in Space Research, 10, 11–59, 1990.

Fleming, E. L., Chandra, S., Burrage, M. D., Skinner, W. R., Hays, P. B., Solheim, B. H., and Shepherd, G. G.: Climatological mean wind observations from the UARS high-resolution Doppler imager and wind imaging interferometer: Comparison with current reference models, Journal of Geophysical Research, 101, 10 455, 1996.

Forbes, J. M.: Tidal and planetary waves, The upper mesosphere and lower thermosphere: a review of experiment and theory, p. 67, 1995.

Forbes, J. M., Hagan, M. E., Miyahara, S., Vial, F., Manson, A. H., Meek, C. E., and Portnyagin, Y. I.: Quasi 16-day oscillation in the mesosphere and lower thermosphere, Journal of Geophysical Research, 100, 9149–9163, 1995.

Friedrich, M. and Torkar, K. M.: High-latitude plasma densities and their relation to riometer absorption, Journal of Atmospheric and Terrestrial Physics, 45, 127–135, 1983.

Fritts, D. C.: Shear Excitation of Atmospheric Gravity Waves., Journal of Atmospheric Sciences, 39, 1936–1952, 1982.

Fritts, D. C. and Alexander, M. J.: Gravity wave dynamics and effects in the middle atmosphere, REVIEWS OF GEOPHYSICS-RICHMOND VIRGINIA THEN WASHINGTON-, 41, 1003, 64 PP., 2003 1003, 64 PP, doi:10.1029/2001RG000 106, 2003.

Fritts, D. C. and Vanzandt, T. E.: Spectral estimates of gravity wave energy and momentum fluxes. Part 1: Energy dissipation, acceleration, and constraints, Journal of Atmospheric Sciences, 50, 3685–3694, 1993.

Fritts, D. C., Isler, J. R., Lieberman, R. S., Burrage, M. D., Marsh, D. R., Nakamura, T., Tsuda, T., Vincent, R. A., and Reid, I. M.: Two-day wave structure and mean flow interactions observed by radar and High Resolution Doppler Imager, Journal of Geophysical Research, 104, 3953–3969, 1999.

Garcia, R. R., Lieberman, R., Russell III, J. M., and Mlynczak, M. G.: Large-scale waves in the mesosphere and lower thermosphere observed by SABER, Journal of the Atmospheric Sciences, 62, 4384–4399, 2005.

García-Comas, M., López-Puertas, M., Marshall, B. T., Wintersteiner, P. P., Funke, B., Bermejo-Pantaleón, D., Mertens, C. J., Remsberg, E. E., Gordley, L. L., Mlynczak, M. G., et al.: Errors in Sounding of the Atmosphere using Broadband Emission Radiometry (SABER) kinetic temperature caused by non-local-thermodynamic-equilibrium model parameters, Journal of Geophysical Research, 113, D24 106, doi:10.1029/2008JD010 105, 2008.

Gille, J. C. and Russell III, J. M.: The limb infrared monitor of the stratosphere: Experiment description, performance, and results, Journal of Geophysical Research, 89, 5125–5140, 1984.

Gobbi, G. P., Souprayen, C., Congeduti, F., Donfrancesco, G. D., Adriani, A., Viterbini, M., and Centurioni, S.: Lidar observations of middle atmosphere temperature variability, in: Annales geophysicae, vol. 13, pp. 648–655, Springer, 1995.

Greenwald, R. A., Baker, K. B., Dudeney, J. R., Pinnock, M., Jones, T. B., Thomas, E. C., Villain, J. P., Cerisier, J., Senior, C., Hanuise, C., et al.: DARN/SuperDARN, Space Science Reviews, 71, 761–796, 1995.

Hadley, G.: Concerning the Cause of the General Trade-Winds: By Geo. Hadley, Esq; FRS, Philosophical Transactions, 39, 58, 1735.

Hall, G. E., MacDougall, J. W., Moorcroft, D. R., St-Maurice, J. P., Manson, A. H., and Meek, C. E.: Super dual auroral radar network observations of meteor echoes, Journal of Geophysical Research, 102, 14 603–14 614, 1997.

Hartmann, D. L., Mechoso, C. R., and Yamazaki, K.: Observations of Wave-Mean Flow Interaction in the Southern Hemisphere., Journal of Atmospheric Sciences, 41, 351–362, 1984.

Hauchecorne, A. and Chanin, M. L.: Density and temperature profiles obtained by lidar between 35 and 70 km, Geophysical Research Letters, 7, 565–568, 1980.

Hauchecorne, A. and Chanin, M. L.: Mid-latitude lidar observations of planetary waves in the middle atmosphere during the winter of 1981–1982, Journal of Geophysical Research, 88, 3843–3849, 1983.

Hauchecorne, A., Chanin, M. L., and Keckhut, P.: Climatology and trends of the middle atmospheric temperature (33–87 km) as seen by Rayleigh lidar over the south of France, Journal of Geophysical Research, 96, 15 297, 1991.

Hernandez, G.: Climatology of the upper mesosphere temperature above South Pole (90 S): Mesospheric cooling during 2002, Geophysical Research Letters, 30, 1535, 2003.

Hervig, M. E., Russell III, J. M., Gordley, L. L., Drayson, S. R., Stone, K., Thompson, R. E., Gelman, M. E., McDermid, I. S., Hauchecorne, A., Keckhut, P., et al.: Validation of temperature measurements from the Halogen Occultation Experiment, Journal of Geophysical Research, 101, 10 277, 1996.

Hibbins, R. E. and Jarvis, M. J.: A long-term comparison of wind and tide measurements in the upper mesosphere recorded with an imaging Doppler interferometer and SuperDARN radar at Halley, Antarctica, Atmospheric Chemistry and Physics Discussions, 7, 6573–6601, 2007.

Hibbins, R. E., Marsh, O. J., McDonald, A. J., and Jarvis, M. J.: Interannual variability of the S= 1 and S= 2 components of the semidiurnal tide in the Antarctic MLT, Journal of Atmospheric and Solar-Terrestrial Physics, 72, 794–800, 2010.

Hines, C. O.: A Modeling of Atmospheric Gravity Waves and Wave Drag Generated by Isotropic and Anisotropic Terrain., Journal of Atmospheric Sciences, 45, 309–322, 1988.

Hirota, I., Kuroi, K., and Shiotani, M.: Midwinter warmings in the southern hemisphere stratosphere in 1988, Quarterly Journal of the Royal Meteorological Society, 116, 929–941, 1990.

Hoffmann, P., Singer, W., and Keuer, D.: Variability of the mesospheric wind field at middle and Arctic latitudes in winter and its relation to stratospheric circulation disturbances, Journal of Atmospheric and Solar-Terrestrial Physics, 64, 1229–1240, 2002.

Hoffmann, P., Singer, W., Keuer, D., Hocking, W. K., Kunze, M., and Murayama, Y.: Latitudinal and longitudinal variability of mesospheric winds and temperatures during stratospheric warming events, Journal of Atmospheric and Solar-Terrestrial Physics, 69, 2355–2366, 2007.

Holton, J. R.: The dynamic meteorology of the stratosphere and mesosphere, in: Research supported by the National Science Foundation Boston, American Meteorological Society (Meteorological Monograph. Volume 15, No. 37), 1975. 224 p, vol. 15, 1975.

Holton, J. R.: A semi-spectral numerical model for wave-mean flow interactions in the stratosphere: Application to sudden stratospheric warmings, Journal of the Atmospheric Sciences, 33, 1639–1649, 1976.

Holton, J. R.: The role of gravity wave induced drag and diffusion in the momentum budget of the mesosphere, Journal of the Atmospheric Sciences, 39, 791–799, 1982.

Holton, J. R.: The influence of gravity wave breaking on the general circulation of the middle atmosphere, Journal of the Atmospheric Sciences, 40, 2497–2507, 1983.

Holton, J. R.: An introduction to dynamic meteorology, 4th Edition , Academic press, 2004.

Holton, J. R. and Alexander, M. J.: The role of waves in the transport circulation of the middle atmosphere, Atmospheric science across the stratopause, pp. 21–35, 2000.

Hussey, G. C., Meek, C. E., André, D., Manson, A. H., Sofko, G. J., and Hall, C. M.: A comparison of Northern Hemisphere winds using SuperDARN meteor trail and MF radar wind measurements, Journal of Geophysical Research, 105, 18 053, 2000.

Jacobi, C.: On the solar cycle dependence of winds and planetary waves as seen from mid-latitude D1 LF mesopause region wind measurements, in: Annales Geophysicae, vol. 16, pp. 1534–1543, Springer, 1998.

Jacobi, C., K
"urschner, D., Muller, H. G., Pancheva, D., Mitchell, N. J., and Naujokat, B.: Response of the mesopause region dynamics to the February 2001 stratospheric warming, Journal of Atmospheric and Solar-Terrestrial Physics, 65, 843–855, 2003.

Jacobi, C., Portnyagin, Y. I., Merzlyakov, E. G., Solovjova, T. V., Makarov, N. A., and K ”urschner, D.: A long-term comparison of mesopause region wind measurements over Eastern and Central Europe, Journal of Atmospheric and Solar-Terrestrial Physics, 67, 229–240, 2005.

Jacobi, C., Fr ”ohlich, K., Portnyagin, Y., Merzlyakov, E., Solovjova, T., Makarov, N., Rees, D., Fahrutdinova, A., Guryanov, V., Fedorov, D., et al.: Semi-empirical model of middle atmosphere wind from the ground to the lower thermosphere, Advances in Space Research, 43, 239–246, 2009.

Jarvis, M. J., Hibbins, R. E., Taylor, M. J., and Rosenberg, T. J.: Utilizing riometry to observe gravity waves in the sunlit mesosphere, Geophysical Research Letters, 30, 1979, doi:10.1029/2003GL017 885, 2003.

Kalnay, E. C., Kanamitsu, M., Kistler, R., Collins, W., Deaven, D., Gandin, L., Iredell, M., Saha, S., White, G., Woollen, J., et al.: The NCEP/NCAR 40-year reanalysis project, Bulletin of the American Meteorological Society, 77, 437–471, 1996.

Kazimirovsky, E., Manson, A. H., and Meek, C. E.: Winds and waves in the middle atmosphere at Saskatoon (52ř N, 107ř W), Collm (52ř N, 15ř E) and Badary (52ř N, 105ř E), Journal of atmospheric and terrestrial physics, 50, 243–250, 1988.

Keckhut, P., Chanin, M. L., and Hauchecorne, A.: Stratosphere temperature measurement using Raman lidar, Applied Optics, 29, 5182–5186, 1990.

Kent, G. S. and Wright, R. W. H.: A review of laser radar measurements of atmospheric properties, Journal of Atmospheric and Terrestrial Physics, 32, 917–943, 1970.

Kruger, K., Naujokat, B., and Labitzke, K.: The unusual midwinter warming in the Southern Hemisphere stratosphere 2002: A comparison to Northern Hemisphere phenomena, Journal of the Atmospheric Sciences, 62, 603–613, 2005.

Labitzke, K. and Naujokat, B.: The lower Arctic stratosphere in winter since 1952, SPARC Newsletter, 15, 11–14, 2000.

Labitzke, K. G. and Van Loon, H.: The stratosphere: phenomena, history, and relevance, Springer Berlin, 1999.

Leblanc, T., Hauchecorne, A., Chanin, M. L., Taylor, F. W., Rodgers, C. D., and Livesey, N.: Mesospheric temperature inversions as seen by ISAMS (UARS), Geophysical Research Letters, 22, 1485–1488, 1995.

Leblanc, T., Stuart McDermid, I., Hauchecorne, A., and Keckhut, P.: Evaluation of optimization of lidar temperature analysis algorithms using simulated data, Journal of Geophysical Research, 103, 6177–6187, 1998.

Lee, J. N., Wu, D. L., Manney, G. L., and Schwartz, M. J.: Aura Microwave Limb Sounder observations of the Northern Annular Mode: From the mesosphere to the upper troposphere, Geophysical Research Letters, 36, L20 807, 2009.

Li, T., Leblanc, T., and McDermid, I. S.: Interannual variations of middle atmospheric temperature as measured by the JPL lidar at Mauna Loa Observatory, Hawaii (19.5 N, 155.6 W), Journal of Geophysical Research, 113, D14 109, 2008.

Limpasuvan, V., Hartmann, D. L., Thompson, D. W. J., Jeev, K., and Yung, Y. L.: Stratosphere-troposphere evolution during polar vortex intensification, Journal of Geophysical Research, 110, D24 101, doi:10.1029/2005JD006 302, 2005.

Liu, H. L. and Roble, R. G.: A study of a self-generated stratospheric sudden warming and its mesospheric–lower thermospheric impacts using the coupled TIME-GCM/CCM3, Journal of Geophysical Research, 107, 4695, 2002.

Liu, H. L. and Roble, R. G.: Dynamical coupling of the stratosphere and mesosphere in the 2002 Southern Hemisphere major stratospheric sudden warming, Geophysical Research Letters, 32, L13 804, doi:10.1029/2005GL022 939, 2005.

Lorenc, A. C., Ballard, S. P., Bell, R. S., Ingleby, N. B., Andrews, P. L. F., Barker, D. M., Bray, J. R., Clayton, A. M., Dalby, T., Li, D., et al.: The Met. Office global three-dimensional variational data assimilation scheme, Quarterly Journal of the Royal Meteorological Society, 126, 2991–3012, 2000.

Luo, Z. and Fritts, D. C.: Gravity-aves excitation by geostrophic adjustment of the jet stream,II, Three-dimensional forcing, Journal of the Atmospheric Sciences, 50, 104–115, 1993.

Malinga, S. and Poole, L. M. G.: The 16-day variation in the mean flow at Grahamstown (33.3S, 26.5 E), Annales geophysicae, 20, 2027–2032, 2002.

Malinga, S. B.: A comparative study of atmosphere dynamics in the mesosphere and lower thermosphere (MLT) near Grahamstown (South Africa) and Adelaide (Australia), Ph.D. thesis, Rhodes University, 2001.

Malinga, S. B. and Ruohoniemi, J. M.: The quasi-two-day wave studied using the Northern Hemisphere SuperDARN HF radars, Annales Geophysicae, vol. 25, pp. 1767–1778, 2007.

Malinga, S. B., Poole, L. M. G., and Vincent, R. A.: Long term variations in the mesospheric mean flow observed at Grahamstown (South Africa) and Adelaide (Australia), Journal of Atmospheric and Solar-Terrestrial Physics, 66, 1745–1754, 2004.

Matsuno, T.: A dynamical model of the stratospheric sudden warming., Journal of Atmospheric Sciences, 28, 1479–1494, 1971.

Mbatha, N., Sivakumar, V., Bencherif, H., Malinga, S. B., R., P. S., Moorgawa, A., and Michaelis, M. M.: DURBAN RAYLEIGH LIDAR MEASUREMENTS OF THE STRATOSPHERE-MESOSPHERE TEMPERATURE STRUCTURE, in: 25th International Laser Radar Conference, 2010a.

Mbatha, N., Sivakumar, V., Malinga, S. B., Bencherif, H., and Pillay, S. R.: Study on the impact of sudden stratosphere warming in the upper mesosphere-lower thermosphere regions using satellite and HF radar-[Article], Atmospheric Chemistry and Physics, 10, 1–8, 2010b.

Mbatha, N., Sivakumar, V., Bencherif, H., Malinga, S. B., R., P. S., Moorgawa, A., and Michaelis, M. M.: Observations of a middle atmosphere thermal structure over Durban using a ground-based Rayleigh LIDAR and satellite data, South African Journal of Science, Accepted, 2011.

Meriwether, J. W. and Gerrard, A. J.: Mesosphere inversion layers and stratosphere temperature enhancements, Reviews of Geophysics, 42, 2004.

Misiti, M., Misiti, Y., Oppenheim, G., and Poggi, J.: Wavelet Toolbox 4, User's Guide, 1996.

Moffat-Griffin, T., Hibbins, R. E., Nielsen, K., Jarvis, M. J., and Taylor, M. J.: Observing mesospheric gravity waves with an imaging riometer, Journal of atmospheric and solar-terrestrial physics, 70, 1327–1335, 2008.

Moorgawa, A., Bencherif, H., Michaelis, M. M., Porteneuve, J., and Malinga, S.: The Durban atmospheric LIDAR, Optics & Laser Technology, 39, 306–312, 2007.

Murphy, D. J., French, W. J. R., and Vincent, R. A.: Long-period planetary waves in the mesosphere and lower thermosphere above Davis, Antarctica, Journal of Atmospheric and Solar-Terrestrial Physics, 69, 2118–2138, 2007.

Namboothiri, S., Sugimoto, N., Nakane, H., Matsui, I., and Murayama, Y.: Rayleigh lidar observations of temperature over Tsukuba: winter thermal structure and comparison studies, Earth Planets and Space, 51, 825–832, 1999a.

Namboothiri, S. P., Meek, C. E., and Manson, A. H.: Variations of mean winds and solar tides in the mesosphere and lower thermosphere over time scales ranging from 6 months to 11 yr: Saskatoon, 52 N, 107 W, Journal of Atmospheric and Solar-Terrestrial Physics, 56, 1313–1325, 1994.

Namboothiri, S. P., Tsuda, T., and Nakamura, T.: Interannual variability of mesospheric mean winds observed with the MU radar, Journal of Atmospheric and Solar-Terrestrial Physics, 61, 1111–1122, 1999b.

Palo, S. E., Forbes, J. M., Zhang, X., Russell III, J. M., Mertens, C. J., Mlynczak, M. G., Burns, G. B., Espy, P. J., and Kawahara, T. D.: Planetary wave coupling from the stratosphere to the thermosphere during the 2002 Southern Hemisphere pre-stratwarm period, Geophysical Research Letters, 32, L23 809, 2005.

Pancheva, D., Mukhtarov, P., Mitchell, N. J., Beard, A. G., and Muller, H. G.: A comparative study of winds and tidal variability in the mesosphere/lower-thermosphere region over Bulgaria and the UK, in: Annales Geophysicae, vol. 18, pp. 1304–1315, Springer, 2000.

Pancheva, D., Mitchell, N. J., Manson, A. H., Meek, C. E., Jacobi, C., Portnyagin, Y., Merzlyakov, E., Hocking, W. K., MacDougall, J., Singer, W., et al.: Variability of the quasi-2-day wave observed in the MLT region during the PSMOS campaign of June-August 1999, Journal of atmospheric and solar-terrestrial physics, 66, 539–565, 2004.

Pancheva, D., Mukhtarov, P., Mitchell, N. J., Merzlyakov, E., Smith, A. K., Andonov, B., Singer, W., Hocking, W., Meek, C., Manson, A., et al.: Planetary waves in coupling the stratosphere and mesosphere during the major stratospheric warming in 2003/2004, Journal of Geophysical Research, 113, D12 105, 2008.

Pancheva, D. V.: Quasi-2-day wave and tidal variability observed over Ascension Island during January/February 2003, Journal of Atmospheric and Solar-Terrestrial Physics, 68, 390–407, 2006.

Plumb, R. A.: Stratospheric transport, Journal of the Meteorological Society of Japan, 80, 793–809, 2002.

Portnyagin, Y. I., Forbes, J. M., Fraser, G. J., Vincent, R. A., Avery, S. K., Lysenko, I. A., and Makarov, N. A.: Dynamics of the Antarctic and Arctic mesosphere and lower thermosphere regions–I. The prevailing wind, Journal of Atmospheric and Terrestrial Physics, 55, 827–841, 1993.

Priestley, M. B.: Spectral analysis and time series. Volume 2: Multivariate series, prediction and control, Academic Press, 1981.

Randel, W., Udelhofen, P., Fleming, E., Geller, M., Gelman, M., Hamilton, K., Karoly, D., Ortland, D., Pawson, S., Swinbank, R., et al.: The SPARC intercomparison of middle-atmosphere climatologies, Journal of Climate, 17, 986–1003, 2004.

Ratnam, M. V., Tetzlaff, G., and Jacobi, C.: Global and seasonal variations of stratospheric gravity wave activity deduced from the CHAMP/GPS satellite, Journal of the atmospheric sciences, 61, 1610–1620, 2004a.

Ratnam, M. V., Tsuda, T., Jacobi, C., and Aoyama, Y.: Enhancement of gravity wave activity observed during a major Southern Hemisphere stratospheric warming by CHAMP/GPS measurements, Geophysical Research Letters, 31, L16 101, 2004b.

Remsberg, E., Deaver, L., Wells, J., Lingenfelser, G., Bhatt, P., Gordley, L., Thompson, R., McHugh, M., Russell III, J. M., Keckhut, P., et al.: An assessment of the quality of Halogen Occultation Experiment temperature profiles in the mesosphere based on comparisons with Rayleigh backscatter lidar and inflatable falling sphere measurements, Journal of Geophysical Research, 107, 4447, 2002.

Remsberg, E., Lingenfelser, G., Harvey, V. L., Grose, W., Russell III, J., Mlynczak, M., Gordley, L., and Marshall, B. T.: On the verification of the quality of SABER temperature, geopotential height, and wind fields by comparison with Met Office assimilated analyses, Journal of Geophysical Research, 108, 4628, 2003.

Remsberg, E. E., Marshall, B. T., Garcia-Comas, M., Krueger, D., Lingenfelser, G. S., Martin-Torres, J., Mlynczak, M. G., Russell III, J. M., Smith, A. K., Zhao, Y., et al.: Assessment of the quality of the Version 1.07 temperature-versus-pressure profiles of the middle atmosphere from TIMED/SABER, Journal of Geophysical Research, 113, 15–70, 2008.

Ren, S., Polavarapu, S. M., and Shepherd, T. G.: Vertical propagation of information in a middle atmosphere data assimilation system by gravity-wave drag feedbacks, Geophysical Research Letters, 35, 2008.

Russell III, J. M., Gordley, L. L., Park, J. H., Drayson, S. R., Hesketh, W. D., Cicerone, R. J., Tuck, A. F., Frederick, J. E., Harries, J. E., and Crutzen, P. J.: The halogen occultation experiment, Journal of Geophysical Research, 98, 10 777, 1993.

Sathishkumar, S. and Sridharan, S.: Planetary and gravity waves in the mesosphere and lower thermosphere region over Tirunelveli (8.7ř N, 77.8ř E) during stratospheric warming events, Geophysical Research Letters, 36, L07 806, doi:10.1029/2008GL037 081, 2009.

Schmidlin, F. J.: Repeatability and measurement uncertainty of the United States meteorological rocketsonde, Journal of Geophysical Research, 86, 9599–9603, 1981.

Semane, N., Bencherif, H., Morel, B., Hauchecorne, A., and Diab, R. D.: An unusual stratospheric ozone decrease in the Southern Hemisphere subtropics linked to isentropic air-mass transport as observed over Irene (25.5 S, 28.1 E) in mid-May 2002, Atmospheric Chemistry and Physics, 6, 1936, 2006.

Sharma, S., Sivakumar, V., Bencherif, H., Chandra, H., Acharya, Y. B., Jayaraman, A., Rao, P. B., and Narayana Rao, D.: A comprehensive study on middle atmospheric thermal structure over a tropic and sub-tropic stations, Advances in Space Research, 37, 2278–2283, 2006.

Shepherd, T. G.: The middle atmosphere, Journal of Atmospheric and Solar-Terrestrial Physics, 62, 1587–1601, 2000.

Shettle, E. P., Thomas, G. E., Olivero, J. J., Evans, W. F. J., Debrestian, D. J., and Chardon, L.: Three-satellite comparison of polar mesospheric clouds: Evidence for long-term change, Journal of Geophysical Research, 107, 4134, 2002.

Shiotani, M., Shimoda, N., and Hirota, I.: Interannual variability of the stratospheric circulation in the southern hemisphere, Quarterly Journal of the Royal Meteorological Society, 119, 531–546, 1993.

Singh, U. N., Keckhut, P., McGee, T. J., Gross, M. R., Hauchecorne, A., Fishbein, E. F., Waters, J. W., Gille, J. C., Roche, A. E., and Russell, J. M.: Stratospheric temperature measurements by two collocated NDSC lidars during UARS validation campaign, J. Geophys. Res, 101, 10–287, 1996.

Siskind, D. E., Eckermann, S. D., McCormack, J. P., Coy, L., Hoppel, K. W., and Baker, N. L.: Case studies of the mesospheric response to recent minor, major, and extended stratospheric warmings, Tech. rep., 2010.

Sivakumar, V., Rao, P. B., and Krishnaiah, M.: Lidar measurements of stratosphere-mesosphere thermal structure at a low latitude: Comparison with satellite data and models, Journal of Geophysical Research, 108, 4342, 2003.

Sivakumar, V., Morel, B., Bencherif, H., Baray, J. L., Baldy, S., Hauchecorne, A., and Rao, P. B.: Rayleigh lidar observation of a warm stratopause over a tropical site, Gadanki (13.5 N; 79.2 E), Atmospheric Chemistry and Physics, 4, 1989–1996, 2004.

Sivakumar, V., Rao, P. B., and Bencherif, H.: Lidar observations of middle atmospheric gravity wave activity over a low-latitude site (Gadanki, 13.5 N, 79.2 E), in: Annales Geophysicae, vol. 24, pp. 823–834, 2006.

Sivakumar, V., Prasanth, P. V., Kishore, P., Bencherif, H., and Keckhut, P.: Rayleigh LIDAR and satellite (HALOE, SABER, CHAMP and COSMIC) measurements of stratosphere-mesosphere temperature over a southern sub-tropical site, Reunion (20.8? S; 55.5? E): climatology and comparison study, Ann. Geophys, 29, 649–662, 2011.

Smith, A. K.: Wave transience and wave-mean flow interaction caused by the interference of stationary and traveling waves, Journal of the atmospheric sciences, 42, 529–535, 1985.

Stauning, P.: Absorption of cosmic noise in the E-region during electron heating events. A new class of riometer absorption events, Geophysical Research Letters, 11, 1184–1187, 1984.

Stockwell, R. G. and Lowe, R. P.: Airglow imaging of gravity waves. I- Critical layer filtering, Journal of geophysical research, 106, 17, 205Ű17,220, doi:10.1029/2001JD900036, 2001.

Swinbank, R. and O'Neill, A.: A stratosphere-troposphere data assimilation system, Monthly Weather Review, 122, 686–702, 1994.

Swinbank, R. and Ortland, D. A.: Compilation of wind data for the Upper Atmosphere Research Satellite (UARS) reference atmosphere project, Journal of Geophysical Research, 108, 4615, 2003.

Taylor, M. J., Ryan, E. H., Tuan, T. F., and Edwards, R.: Evidence of preferential directions for gravity wave propagation due to wind filtering in the middle atmosphere, Journal of geophysical research, 98, 6047–6057, 1993.

Thurairajah, B., Collins, R. L., Harvey, V. L., Lieberman, R. S., Gerding, M., Mizutani, K., and Livingston, J. M.: Gravity wave activity in the Arctic stratosphere and mesosphere during the 2007–2008 and 2008–2009 stratospheric sudden warming events, Journal of Geophysical Research, 115, D00N06, 2010.

Topping, J.: Topping 1972, error of observation and their treatment, Chaoman and Hall, London, 1972.

Torrence, C. and Compo, G. P.: A practical guide to wavelet analysis, Bulletin of the American Meteorological Society, 79, 61–78, 1998.

Torrence, C. and Webster, P. J.: Interdecadal changes in the ENSO–monsoon system, Journal of Climate, 12, 2679–2690, 1999.

Tsuda, T., Nishida, M., Rocken, C., and Ware, R. H.: A global morphology of gravity wave activity in the stratosphere revealed by the GPS occultation data(GPS/MET), Journal of Geophysical Researcheo Physical rRsearch, 105, 7257–7273, 2000.

VanZandt, T. E.: A model for gravity wave spectra observed by Doppler sounding systems, Radio Science, 20, 1323–1330, 1985.

Volland, H.: Atmospheric tidal and planetary waves, Springer, 1988.

Walterscheid, R. L., Sivjee, G. G., and Roble, R. G.: Mesospheric and lower thermospheric manifestations of a stratospheric warming event over Eureka, Canada (80 N), Geophysical Research Letters, 27, 2897–2900, 2000.

Wang, L. and Alexander, M. J.: Gravity wave activity during stratospheric sudden warmings in the 2007–2008 Northern Hemisphere winter, Journal of Geophysical Research, 114, DOI: 10.1029/2009JD011 867, 2009.

Wang, P. H., McCormick, M. P., Chu, W. P., Lenoble, J., Nagatani, R. M., Chanin, M. L., Barnes, R. A., Schmidlin, F., and Rowland, M.: SAGE II stratospheric density and temperature retrieval experiment, Journal of Geophysical Research, 97, 843–863, 1992.

Whiteway, J. A. and Carswell, A. I.: Rayleigh lidar observations of thermal structure and gravity wave activity in the high arctic during a stratospheric warming, Journal of the atmospheric sciences, 51, 3122–3136, 1994.

Wilson, A.: Imaging riometer observations on energetic electron precipitation at SANAE IV, Antarctica, Ph.D. thesis, Potchefstroomse Universiteit vir Christelike Hoër Onderwys, 2000.

Wilson, A. and Stoker, P. H.: Imaging riometer observations on energetic electron precipitation at SANAE IV, Antarctica, Journal of Geophysical Research, 107, 1268, 2002.

Wilson, A., Nel, J. J., Mathews, M. J., and Stoker, P. H.: Direct measurements on imaging riometer antenna array beam directivities, Radio Science, 36, 1531–1543, 2001.

Wilson, R., Hauchecorne, A., and Chanin, M. L.: Gravity wave spectra in the middle atmosphere as observed by Rayleigh lidar, Geophysical Research Letters, 17, 1585–1588, 1990.

WMO.: Assessment of our understanding of the processes controlling its present distribution and change, World Meteorological Organization, Global Ozone Research and Monitoring Project-Report, 1985.

Xu, J., She, C. Y., Yuan, W., Mertens, C., Mlynczak, M., and Russell, J.: Comparison between the temperature measurements by TIMED/SABER and lidar in the midlatitude, Journal of Geophysical Research, 111, A10S09, doi:10.1029/2005JA011 439, 2006.

Yamashita, C., Liu, H. L., and Chu, X.: Responses of mesosphere and lower thermosphere temperatures to gravity wave forcing during stratospheric sudden warming, Geophysical Research Letters, 37, L09 803, doi:10.1029/2009GL042 351, 2010.